

SYSTEM-ON-CHIP BASED DOPPLER RADAR OCCUPANCY SENSOR WITH
ADD-ON PASSIVE NODE

A DISSERTATION SUBMITTED TO THE GRADUATE DIVISION OF THE
UNIVERSITY OF HAWAII AT MĀNOA IN PARTIAL FULFILLMENT OF THE
REQUIREMENTS FOR THE DEGREE OF

DOCTOR OF PHILOSOPHY

IN

ELECTRICAL ENGINEERING

DECEMBER 2014

By

Chenyan Song

Dissertation Committee:

Olga Boric-Lubecke, Chairperson

Victor M. Lubecke

Gary Varner

Zhengqing Yun

Daniel M. Jenkins

Shigeo Kawasaki

Acknowledgements

First, I gratefully and sincerely thank my advisor, Professor Olga Boric-Lubecke, for her patient guidance and energetic encouragement for the past four years. She is not just a research advisor to me. More often, she has been a mentor to my life.

I would like to express my deep appreciation to my family members without whom this dissertation cannot be done:

- My dearest parents, ShiRong Chen and YuHua Song, who support me to pursue my degree by sacrificing their retired life to take care of my son, my husband and me;
- My beloved husband, ZhaoHui Wang, for his support and forbearance;
- My precious son, YanKai Wang, who brings me unexpected challenges and great experiences as well, and teaches me many things, particularly to be patient and efficient.

I also thank my dissertation committee, Professor Victor M. Lubecke, Professor Gary Varner, Professor Zhengqing Yun, Professor Daniel M. Jenkins and Professor Shigeo Kawasaki for many valuable discussions.

My sincere gratitude goes to the following individuals for their helpful advice and assistance in making this research possible:

- The previous and present members of Dr. Lubeckes' group, particularly Ehsan, Xiaomeng, Adi, and Ashik, for friendship and help in the laboratory;
- Department of Energy for financial support;

- Department of Electric Engineering, University of Hawaii at Manoa for supporting my research.

Abstract

Occupancy sensors can save up to 80% of energy used for lighting and heating ventilation and air conditioning (HVAC) systems, resulting in huge financial savings. However, currently available occupancy sensors --- most commonly passive infrared (PIR) and ultra-sonic (US) sensors --- have significant drawbacks, including high rates of false-positives and failures to detect stationary persons. Newly available high-efficiency Doppler radar transceivers can be used to discern human cardiopulmonary motion thus providing a practical solution for such problems in occupancy sensing. In addition, the advent of the integrated low-power microprocessor/RF-transceivers provides a new platform which combines sensing, processing and communication to form the core of a wireless smart sensor network (WSSN) for applications such as “smart buildings”.

A significant challenge for wide adoption of occupancy sensors is to demonstrate reliable system performance at low power with low cost. This research demonstrates the feasibility of low cost, low power Doppler radar occupancy sensor by building a customized passive sensor node into commercially available SoC's (TI's CC2530 and CC430). Experiments using periodic moving mechanical target illustrate that these SoC based Doppler radar sensors are able to accurately detect the motion of the target under continuous wave (CW), modulated CW and packet operation modes. The study on sensitivity and power consumption under these modes indicates the most cost efficiency and power efficiency can be achieved by operating the sensor under packet mode with an optimum output power level. A comparison between passive sensor node and quadrature receiver shows sensor node does not sacrifice the sensitivity by using simpler and lower-costing configuration. Null-point sensitivity study shows that though the configuration with add-on passive sensor node suffers from the decreased sensitivity, the specific pattern at this point can be used for a decision on occupancy detection. Simulation and experiment demonstrate characteristic pattern of the respiration signal detected by the Doppler radar occupancy sensor by charting how the variation of target position impacts the strength of the real motion frequency and its second harmonic. An algorithm detects the true presence occupancy is developed based on this pattern analysis, and is evaluated

to be effective with human testing. This research also includes a broad-band mixer design for the add-on passive node using 0.18- μm IBM7HP CMOS process. The broad-band performance of this mixer is presented.

Future work will include single channel Doppler radar measuring the displacement of target in periodic motion by making use of the relationship between the detected characteristic pattern and the target location , and harvesting ambient RF energy by the same passive sensor node configured in this dissertation.

Table of Contents

Acknowledgements	i
Abstract	iii
Table of Contents	i
List of Figures	iv
List of Tables	xvi
Chapter 1 Introduction	1
1.1 Background on Current Occupancy Sensors.....	2
1.1.1 Passive Infrared (PIR) Sensors.....	3
1.1.2 Ultrasonic Sensors.....	4
1.1.3 Dual Technology Sensors.....	6
1.1.4 Other Technology Sensors	7
1.2 Occupancy Sensor Using Doppler Radar Detection on Human Cardiopulmonary Motion.....	7
1.3 Scope of the Dissertation.....	8
Chapter 2 Doppler Radar Detection of Cardiopulmonary Signals	10
2.1 Radar Basics	10
2.1.1 The Radar Range Equation	11
2.1.2 Radar Cross Section	16
2.1.3 Doppler Effect.....	17
2.1.4 Continuous Wave (CW) Radar and Pulsed Radar	20
2.2 Doppler Radar Detection of Cardiopulmonary Signals	23
2.2.1 CW Radar Concept of Cardiopulmonary Monitoring.....	24
2.2.2 Single Channel Receiver	26
2.2.3 Quadrature Receiver.....	28
2.2.4 Sensor Node with Air Coupling.....	30

Chapter 3 Doppler Radar Occupancy Sensor Hardware Design	33
3.1 System on Chip (SoC).....	35
3.1.1 CC2530.....	36
3.1.2 CC430.....	39
3.2 Doppler Radar Occupancy Sensor Built with CC2530 and CC430.....	40
3.2.1 Doppler Radar Occupancy Sensor with the CC2530.....	40
3.2.1.1 Experiment Setup	40
3.2.1.2 Experiment Result	42
3.2.2 Doppler Radar Occupancy Sensor with the CC430.....	45
3.2.1.1 Experiment Setup	45
3.2.2.1 Experimental results	46
3.3 CMOS Wideband Passive Mixers.....	51
3.3.1 Circuit design	52
3.3.1.1 Mixer Core.....	52
3.3.1.2 Passive Balun.....	54
3.3.1.3 Mixer with Baluns	56
3.3.2 Measured Results	58
3.3.2.1 Mixer Core.....	59
3.3.2.2 Passive Balun.....	61
3.3.2.3 Mixer with Baluns	62
3.4 Conclusion.....	67
 Chapter 4 Sensitivity Study of Doppler Radar Based Occupancy Sensor	 70
4.1 Detection Sensitivity and Power Consumption vs. Operation Modes	70
4.1.1 Experiment Setup	70
4.1.2 Experiment Result.....	72
4.2 Sensitivity Comparison between Sensor Node and Quadrature Architecture	76
4.2.1 Experiment Setup	76
4.2.2 Experimental Results.....	78
4.3 Sensitivity Comparison between Null Point and Optimum Point.....	86
4.3.1 Experiment Setup	86

4.3.2	Experimental Results.....	88
4.4	Conclusion.....	96
Chapter 5 Algorithm of True Presence Occupancy Detection		97
5.1	Respiration Signal Pattern Analysis of Doppler Radar Occupancy Sensor with SoC and Passive Node	97
5.1.1	Analysis with Sinusoidal model.....	97
5.1.1.1	Simulation.....	97
5.1.1.2	Experiment.....	105
5.1.2	Analysis with complex model	109
5.1.2.1	Simulation.....	109
5.1.2.2	Experiment.....	116
5.2	Algorithm	118
5.3	Human Testing	121
5.3.1	Experiment Setup	121
5.3.2	Experiment Result	122
5.4	Conclusion.....	130
Chapter 6 Future Work and Conclusions		131
6.1	Periodic Motion Measurement with Single Channel Doppler Radar	131
6.2	Harvesting Ambient RF Energy with the Passive Sensor Node	132
6.3	Conclusion.....	134
Appendix A		136
Appendix B		140
References		144

List of Figures

Fig. 1.1 PIR sensor detects human movement with dual elements, generating two successive out of phase signals	4
Fig. 1.2 Ultrasonic sensors detect occupancy via frequency shift of reflected wave	5
Fig. 1.3 Sensor coverage diagram: Ultrasonic sensors can detect motion at any point within the contour lines. PIR sensors see only in the wedge-shaped zones, and they don't generally see as far as ultrasonic units	6
Fig. 2.1 Illustration of a basic radar system, and its working principle.....	10
Fig. 2.2 Illustration of the Doppler Effect. The frequency (wavelength) of reflected wave differs from the transmitted wave due to target movement	18
Fig. 2.3. Relative geometry of a radar and target, illustrating the factors influencing the Doppler frequency shift.	19
Fig. 2.4 Simple CW radar block diagram that extracts Doppler frequency shift from a moving target	20
Fig. 2.5 Block diagram of a simple pulse radar that extracts the Doppler frequency shift from a moving target.....	22
Fig. 2.6 (a) Receive RF echo pulse signals; (b) Base band pulse signals when the Doppler frequency $f_d > 1/\tau$; (c) Base band pulse signals when the Doppler frequency $f_d > 1/\tau$ with the Doppler frequency signal is shown dashed	23
Fig. 2.7 A simple Doppler transceiver architecture denoting transmit and receive antenna, signal source, coupler, circulator and a frequency mixer. Operation Principle of the Doppler radar: the phase shift $\varphi(t)$ of the reflected signal is proportion to the time-varying chest position/displacement $d(t)$ due to heart beat and respiration	26
Fig. 2.8 A simple Doppler transceiver architecture, in which a single channel receiver mixes partial transmitted signal and reflected signal with a mixer to produce baseband signal.	26
Fig. 2.9 A quadrature Doppler transceiver architecture, in which two receiver chains are 90° out of phase.	28
Fig. 2.10 A Doppler radar system with passive sensor node.....	32

Fig. 3.1	The main components of a Doppler radar based occupancy sensor integrated with off-the-shelf SoC and passive sensor node.	34
Fig. 3.2	CC2530 function blocks, including MCU, RF function block, and various useful peripherals	38
Fig. 3.3	The main components of CC430F614x, including MSP430 MCU, CC1101 transceiver, and intelligent peripherals.	39
Fig. 3.4	Diagram of a Doppler Radar occupancy sensor using CC2530 and a passive sensor node.	41
Fig. 3.5	CW mode measurement results at an output power +4.5 dBm: (a) raw data, (b) digital low pass filtered data, and (c) FFT analyzed result: periodic motion rate of the mechanical target at 0.2 Hz.....	43
Fig. 3.6	Modulated CW mode measurement result at output power 4.5 dBm: (a) raw data, (b) digital low pass filtered data, and (c) FFT analyzed result: periodic motion rate of the mechanical target at 0.2 Hz.	43
Fig. 3.7	Algorithm for extracting the target motion rate in packet transmitting mode.	44
Fig. 3.8	Packet mode measurement result at an output power +4.5 dBm: (a) raw data (only show 10000 samples) with detected peaks marked with red star; (b) peaks interpolated with spline technique; (c) FFT analyzed result: periodic motion rate of the mechanical target at 0.2 Hz.....	44
Fig. 3.9	Diagram of Doppler Radar occupancy sensor system using the CC430 and passive sensor node.....	46
Fig. 3.10	CW mode measurement result at an output power +10 dBm and frequency of 868 MHz. (a) raw data, (b) digital low pass filtered data, and (c) FFT analyzed result: periodic motion rate of the mechanical target at 0.2 Hz.....	47
Fig. 3.11	Measurement result for 2FSK modulated CW mode at an output power +10 dBm and carrier frequency of 868 MHz. (a) raw data, (b) digital low pass filtered data, and (c) FFT analyzed result: periodic motion rate of the mechanical target at 0.2 Hz.....	48
Fig. 3.12	Measurement result for 2GFSK modulated CW mode at an output power +10 dBm and carrier frequency of 868 MHz. (a) raw data, (b) digital low pass filtered	

data, and (c) FFT analyzed result: periodic motion rate of the mechanical target at 0.2 Hz.	48
.....	
Fig. 3.13 Measurement result for MSK modulated CW mode at an output power +10 dBm and carrier frequency of 868 MHz. (a) raw data, (b) digital low pass filtered data, and (c) FFT analyzed result: periodic motion rate of the mechanical target at 0.2 Hz.....	49
Fig. 3.14. Measurement result for 2FSK Packet mode at an output power +10 dBm and carrier frequency of 868 MHz. (a) raw data with detected peaks marked with red star; (b) peaks interpolated with spline technique; (c) FFT analyzed result: periodic motion rate of the mechanical target at 0.2 Hz.	49
Fig. 3.15 Measurement result for 2GFSK Packet mode at an output power +10 dBm and carrier frequency of 868 MHz. (a) raw data with detected peaks marked with red star; (b) peaks interpolated with spline technique; (c) FFT analyzed result: periodic motion rate of the mechanical target at 0.2 Hz.	50
Fig. 3.16 Measurement result for MSK Packet mode at an output power +10 dBm and carrier frequency of 868 MHz. (a) raw data with detected peaks marked with red star; (b) peaks interpolated with spline technique; (c) FFT analyzed result: periodic motion rate of the mechanical target at 0.2 Hz.....	50
Fig. 3.17 Schematic of the mixer core - four NMOS transistors in ring configuration..	53
.....	
Fig. 3.18 Simulation results for CL as a function of W/L, and LO power at RF frequency of 2.4 GHz.....	53
Fig. 3.19 Simulated results of CL, RF and LO reflection coefficient magnitude of the mixer core vs. RF frequency, available LO power = +10 dBm.....	54
Fig. 3.20 Schematic of the passive balun, implemented using L-C passive elements. .	55
.....	
Fig. 3.21 Balun transmission coefficient simulation results: magnitude (S21 and S31) and phase difference (DelPhase) between the ports S2 and S3 in Fig. 3.20.....	55
Fig. 3.22 (a) Schematic of the mixer with LO and RF baluns. (b) Block diagram of the mixer core (i) integrated with LO and RF baluns (ii).	56

Fig. 3.23	Simulated CL versus RF frequency. The IF frequency = 10 MHz, and LO power = 13 dBm. The CL is calculated with the power level at each IF port versus the power level at the RF input.....	57
Fig. 3.24	Die photograph of mixer core (a), and the mixer with integrated RF and LO baluns (b). Chip size is $1.01 \times 1.1 \text{ mm}^2$ for mixer core (a) and $1.4 \times 1.3 \text{ mm}^2$ for mixer integrated with balun (b).....	59
Fig. 3.25	Simulated and measured CL of the mixer core vs. LO power. RF frequency is 2.4 GHz, and IF frequency 10 MHz.....	60
Fig. 3.26	Simulated and measured results of CL, RF and LO reflection coefficient magnitude of the mixer core vs. RF frequency, available LO power = 10 dBm.....	60
Fig. 3.27	Measured RF reflection coefficient magnitude of the mixer core with no gate bias, and with a gate bias of 0.5 V, for available LO power = 10 dBm.....	61
Fig. 3.28	Measured IF reflection coefficient magnitude of the mixer core with no gate bias, and with a gate bias of 0.5 V, for available LO power = 10 dBm.....	61
Fig. 3.29	Balun transmission coefficient magnitude and phase difference: measurement vs. simulation.....	62
Fig. 3.30	Simulated and measured CL versus RF frequency. IF frequency = 10 MHz, and LO power = 13 dBm. The CL is calculated with the power level at each IF port versus the power level at the RF input.....	63
Fig. 3.31	RF and LO reflection coefficient magnitude of the mixer with baluns, with available LO power = 13 dBm.....	64
Fig. 3.32	IF reflection coefficient magnitude of the mixer with baluns, available LO power = 13 dBm.	64
Fig. 3.33	Measured LO-RF and LO-IF isolation of the mixer with baluns versus RF frequency. IF frequency = 10 MHz, and LO power = 13 dBm.	65
Fig. 3.34	IP1dB of the mixer with baluns versus RF frequency. IF frequency = 10 MHz, and LO power = 13 dBm.	65
Fig. 3.35	Measured IIP3 of the mixer with baluns versus RF frequency. IF frequency = 10 MHz, and LO power = 13 dBm.....	66
Fig. 3.36	Measured DC offset of the mixer with baluns versus LO frequency. LO power = 13 dBm.	67

Fig. 4.1	Diagram of Doppler Radar system using CC2530 and passive sensor node.	71
Fig. 4.2	Measurement result for CW mode at an output power of -22 dBm. (a) raw data, and (b) FFT analyzed result: periodic motion rate of the mechanical target at 0.2 Hz.	72
Fig. 4.3	Measurement result for modulated CW mode at an output power of -22 dBm. (a) raw data, and (c) FFT analyzed result: periodic motion rate of the mechanical target at 0.2 Hz.....	73
Fig. 4.4.	Measurement result for Packet mode at an output power of -18 dBm. (a) raw data with detected peaks marked with red star; (b) peaks interpolated with spline technique; (c) FFT analyzed result: periodic motion rate of the mechanical target at 0.2 Hz.	73
Fig. 4.5.	The illustration of experiment setup for the sensitivity testing of Doppler radar occupancy sensors with sensor node and quadrature receiver, respectively.	77
Fig. 4.6	Measured result for passive sensor node at an output power of +4.5 dBm and frequency of 2.405 GHz when operated at CW mode. Top: raw data, Middle: digital low pass filtered data, and Bottom: FFT analyzed result: periodic motion rate of the mechanical target at 0.3 Hz.....	79
Fig. 4.7	Measured result for quadrature sensor at an output power of +4.5 dBm and frequency of 2.405 GHz when operated at CW mode. Top: raw data, Middle: digital low pass filtered data, and Bottom: FFT analyzed result: periodic motion rate of the mechanical target at 0.3 Hz.....	79
Fig. 4.8	Measured result for passive sensor node at an output power of +4.5 dBm and frequency of 2.405 GHz when operated at modulated CW mode. Top: raw data, Middle: digital low pass filtered data, and Bottom: FFT analyzed result: periodic motion rate of the mechanical target at 0.3 Hz.	80
Fig. 4.9	Measured result for quadrature sensor at an output power of +4.5 dBm and frequency of 2.405 GHz when operated at modulated CW mode. Top: raw data, Middle: digital low pass filtered data, and Bottom: FFT analyzed result: periodic motion rate of the mechanical target at 0.3 Hz.....	80

Fig. 4.10 Measured result for sensor node at an output power of +4.5 dBm and frequency of 2.405 GHz when operated at packet mode. Top: raw data with detected peaks marked with red star; Middle: peaks interpolated with spline technique; Bottom: FFT analyzed result: periodic motion rate of the mechanical target at 0.3 Hz. 81

Fig. 4.11 Measured result for quadrature sensor at output power +4.5 dBm and frequency of 2.405 GHz when operated at packet mode. Top: raw data with detected peaks marked with red star for I-channel (left) and Q-channel (right); Bottom left: peaks interpolated with spline technique; Bottom right: FFT analyzed result: periodic motion rate of the mechanical target at 0.3 Hz. 81

Fig. 4.12 Measured result for passive sensor node at an output power of -23 dBm and frequency of 2.405 GHz when operated at CW mode. Top: raw data, Middle: digital low pass filtered data, and Bottom: FFT analyzed result: 0.3 Hz periodic motion rate peak is buried in other peaks. 83

Fig. 4.13 Measured result for quadrature sensor at an output power of -22 dBm and frequency of 2.405 GHz when operated at CW mode. Top: raw data, Middle: digital low pass filtered data, and Bottom: FFT analyzed result: 0.3 Hz periodic motion rate peak is buried in other peaks. 83

Fig. 4.14 Measured result for sensor node at an output power of -22 dBm and frequency of 2.405 GHz when operated at modulated CW mode. Top: raw data, Middle: digital low pass filtered data, and Bottom: FFT analyzed result: 0.3 Hz periodic motion rate peak is buried in other peaks. 84

Fig. 4.15 Measured result for quadrature sensor at an output power of -22 dBm and frequency of 2.405 GHz when operated at modulated CW mode. Top: raw data, Middle: digital low pass filtered data, and Bottom: FFT analyzed result: 0.3 Hz periodic motion rate peak is buried in other peaks. 84

Fig. 4.16 Measured result for sensor node at an output power of -20 dBm and frequency of 2.405 GHz when operated at packet mode. Top: raw data with detected peaks marked with red star; Middle: peaks interpolated with spline technique; Bottom: FFT analyzed result: 0.3 Hz periodic motion rate peak is buried in other peaks. 85

Fig. 4.17 Measured result for quadrature sensor at output power -22 dBm and frequency of 2.405 GHz when operated at packet mode. Top: raw data with detected

peaks marked with red star for I-channel (left) and Q-channel (right); Bottom left: peaks interpolated with spline technique; Bottom right: FFT analyzed result: 0.3 Hz periodic motion rate peak is buried in other peaks. 85

Fig. 4.18. The illustration of experiment setup for the sensitivity testing of Doppler radar occupancy sensor with sensor node at null and optimum points..... 87

Fig. 4.19 Measured result for optimum point at an output power of +4.5 dBm and frequency of 2.405 GHz when operated at CW mode. Top: raw data, Middle: digital low pass filtered data, and Bottom: FFT analyzed result: periodic motion rate of the mechanical target at 0.2 Hz..... 89

Fig. 4.20 Measured result for null point at an output power of +4.5 dBm and frequency of 2.405 GHz when operated at CW mode. Top: raw data, Middle: digital low pass filtered data, and Bottom: FFT analyzed result: two peaks appear at original motion rate of 0.2 Hz and 0.4 Hz. 89

Fig. 4.21 Measured result for optimum point at an output power of +4.5 dBm and frequency of 2.405 GHz when operated at modulated CW mode. Top: raw data, Middle: digital low pass filtered data, and Bottom: FFT analyzed result: periodic motion rate of the mechanical target at 0.2 Hz..... 90

Fig. 4.22 Measured result for null point at an output power of +4.5 dBm and frequency of 2.405 GHz when operated at modulated CW mode. Top: raw data, Middle: digital low pass filtered data, and Bottom: FFT analyzed result: two peaks appear at 0.2 Hz original motion rate and 0.4 Hz..... 90

Fig. 4.23 Measured result for optimum point at an output power of +4.5 dBm and frequency of 2.405 GHz when operated at packet mode. Top: raw data, Middle: digital low pass filtered data, and Bottom: FFT analyzed result: periodic motion rate of the mechanical target at 0.2 Hz..... 91

Fig. 4.24 Measured result for null point at an output power of +4.5 dBm and frequency of 2.405 GHz when operated at packet mode. Top: raw data, Middle: digital low pass filtered data, and Bottom: FFT analyzed result: one peak appears at 0.4 Hz. ... 91

Fig. 4.25 Measured result for optimum point at output power -22 dBm and frequency of 2.405 GHz when operated at CW mode. Top: raw data, Middle: digital low pass

filtered data, and Bottom: FFT analyzed result: 0.2 Hz periodic motion rate peak is buried in other peaks.	93
Fig. 4.26 Measured result for null point at output power -10.5 dBm and frequency of 2.405 GHz when operated at CW mode. Top: raw data, Middle: digital low pass filtered data, and Bottom: FFT analyzed result: periodic motion rate of the mechanical target appears at 0.4 Hz.	93
Fig. 4.27 Measured result for optimum point at output power -22 dBm and frequency of 2.405 GHz when operated at modulated CW mode. Top: raw data, Middle: digital low pass filtered data, and Bottom: FFT analyzed result: 0.2 Hz periodic motion rate peak is buried in other peaks.	94
Fig. 4.28 Measured result for null point at an output power of -10.5 dBm and frequency of 2.405 GHz when operated at modulated CW mode. Top: raw data, Middle: digital low pass filtered data, and Bottom: FFT analyzed result: periodic motion rate of the mechanical target appears at 0.4 Hz.	94
Fig. 4.29 Measured result for null point at an output power of -9.5 dBm and frequency of 2.405 GHz when operated at CW mode. Top: raw data, Middle: digital low pass filtered data, and Bottom: FFT analyzed result: 0.2 Hz periodic motion rate peak is buried in other peaks.	95
Fig. 4.30 Measured result for optimum point at output power -22 dBm and frequency of 2.405 GHz when operated at CW mode. Top: raw data, Middle: digital low pass filtered data, and Bottom: FFT analyzed result: 0.2 Hz periodic motion rate peak is buried in other peaks.	95
Fig. 5.1 Simulation results on the amplitude of misinterpreted frequency at 0.5 Hz, with data shown in time domain (Top) and frequency domain (Bottom), at nominal distance of 1m (null point).	102
Fig. 5.2 Simulation results on the amplitude of real motion frequency at 0.25 Hz and misinterpreted frequency at 0.5 Hz, with data shown in time domain (Top) and frequency domain (Bottom), at nominal distance of $1m - \lambda/64$	102
Fig. 5.3 Simulation results on the amplitude of real motion frequency at 0.25 Hz and misinterpreted frequency at 0.5 Hz, with data shown in time domain (Top) and frequency domain (Bottom), at nominal distance of $1m - 2$ of $\lambda/64$	103

Fig. 5.4	Simulation results on the amplitude of real motion frequency at 0.25 Hz, with data shown in time domain (Top) and frequency domain (Bottom), at nominal distance of 1m - 8 of $\lambda/64$ (optimum point).....	103
Fig. 5.5	Simulation results on the amplitude of real motion frequency at 0.25 Hz and misinterpreted frequency at 0.5 Hz, with data shown in time domain (Top) and frequency domain (Bottom), at nominal distance of 1m - 14 of $\lambda/64$	104
Fig. 5.6	Simulation results on the amplitude of real motion frequency at 0.25 Hz and misinterpreted frequency at 0.5 Hz, with data shown in time domain (Top) and frequency domain (Bottom), at nominal distance of 1m - 15 of $\lambda/64$	104
Fig. 5.7	Simulation results on the amplitude of misinterpreted frequency at 0.5 Hz, with data shown in time domain (Top) and frequency domain (Bottom), at nominal distance of 1m - 16 of $\lambda/64$ Null point.....	105
Fig. 5.8	Amplitude of real motion frequency peak at 0.25 Hz and the one at 0.5 Hz changes with the position of the target tells where the target is relative to the null or optimum point.....	105
Fig. 5.9	The illustration of experiment setup for the impact of position of periodic moving target on the phase demodulated output.	106
Fig. 5.10	Comparison between simulation and experiment data for the position impact on the phase demodulated sensor output.....	107
Fig. 5.11	Experimental results on the impact of subject location on phase demodulated sensor output, with raw data shown in time domain (Top), filtered data shown in time domain (Middle) and data in frequency domain (Bottom), at a null point. ..	108
Fig. 5.12	Experimental results on the impact of subject location on phase demodulated sensor output, with raw data shown in time domain (Top), filtered data shown in time domain (Middle) and data in frequency domain (Bottom), at an optimum point.	108
Fig. 5.13	Experimental results on the impact of subject location on phase demodulated sensor output, with raw data shown in time domain (Top), filtered data shown in time domain (Middle) and data in frequency domain (Bottom), at a point between a null point and an optimum point.....	109

Fig. 5.14	Modeled chest wall motion waveform: (a) heartbeat signal; (b) respiration signal; (c) combination of heartbeat and respiration.....	110
Fig. 5.15	Simulation results on the impact of subject location on demodulated output, with demodulated data shown in time domain (Top) and frequency domain (Bottom), at the distance of 1m (null point).....	111
Fig. 5.16	Simulation results on the impact of subject location on demodulated output, with demodulated data shown in time domain (Top) and frequency domain (Bottom), at incremental nominal distance of 1m - $\lambda/64$	112
Fig. 5.17	Simulation results on the impact of subject location on demodulated output, with demodulated data shown in time domain (Top) and frequency domain (Bottom), at the nominal distance of 1m - 2 of $\lambda/64$	112
Fig. 5.18	Simulation results on the impact of subject location on demodulated output, with demodulated data shown in time domain (Top) and frequency domain (Bottom), at incremental nominal distance of 1m - 8 of $\lambda/64$ (optimum point).....	113
Fig. 5.19	Simulation results on the impact of subject location on demodulated output, with demodulated data shown in time domain (Top) and frequency domain (Bottom), at the nominal distance of 1m - 14 of $\lambda/64$	113
Fig. 5.20	Simulation results on the impact of subject location on demodulated output, with demodulated data shown in time domain (Top) and frequency domain (Bottom), at incremental nominal distance of 1m - 15 of $\lambda/64$	114
Fig. 5.21	Simulation results on the impact of subject location on demodulated output, with demodulated data shown in time domain (Top) and frequency domain (Bottom), at incremental nominal distance of 1m - 16 of $\lambda/64$ (null point).	114
Fig. 5.22	Amplitude of real motion frequency peak at 0.25 Hz and the one at 0.5 Hz changes with the position of the target tells where the target is relative to the null or optimum point.....	115
Fig. 5.23	A comparison between simulation and experiment data.....	116
Fig. 5.24	Experimental results on the impact of subject location on phase demodulated sensor output, with raw data shown in time domain (Top), filtered data shown in time domain (Middle) and data in frequency domain (Bottom), at a null point. ..	117

Fig. 5.25	Experimental results on the impact of subject location on phase demodulated sensor output, with raw data shown in time domain (Top), filtered data shown in time domain (Middle) and data in frequency domain (Bottom), at an optimum point.	117
Fig. 5.26	Experimental results on the impact of subject location on phase demodulated sensor output, with raw data shown in time domain (Top), filtered data shown in time domain (Middle) and data in frequency domain (Bottom), in between a null point and an optimum point.	118
Fig. 5.27	Comparison of radar signals between the mechanical target (a) moves at 0.2 Hz and subject (b) breath with rate around 0.2 Hz.	120
Fig. 5.28	Flow chart of the algorithm to detect human presence occupancy.....	121
Fig. 5.29	Human testing with Doppler radar occupancy sensor.....	122
Fig. 5.30	CW Data from Subject #16. The top left trace is the occupancy sensor raw data, the bottom left trace is IR camera raw data, the top right trace is the comparison between sensor and camera after filtering and normalization, and the bottom right trace is the frequency spectrum after FFT.....	123
Fig. 5.31	Packet mode Data from Subject #16. The top left trace is the occupancy sensor raw data (only show 10000 samples), the bottom left trace is IR camera raw data, the top right trace is the comparison between sensor and camera after filtering and normalization, and the bottom right trace is the frequency spectrum after FFT.....	124
Fig. 5.32	Detected dominant frequency and its harmonics for respiration of subject #1 – 20 at CW mode.	126
Fig. 5.33	Detected dominant frequency and its harmonics for respiration of subject #1 – 20 at packet mode.	127
Fig. 5.34	Detected respiration rate vs. time for subject # 1 – 20 at CW mode.....	128
Fig. 5.35	Detected respiration rate vs. time for subject # 1 – 20 at packet mode.....	129
Fig. 6.1	The amplitude ratio between fundamental frequency and second harmonic varies with the position of a periodically moving mechanical target.	132
Fig. 6.2	The basic components which provide cardiopulmonary remote sensing and RF energy harvesting, including the passive sensor node/rectenna.....	133

Fig. 6.3 Block diagram for proposed occupancy sensor unit, consisting of: energy harvester, power management, energy storage, and sensor/load. 133

List of Tables

Table 2.1	The frequencies used in radar systems.....	11
Table 3.1	Summarized performances of this mixer and its comparison with previously published data	69
Table 4.1	Comparison of max. working distance, sensor node number, and power consumption for three modes.....	76

Chapter 1 Introduction

With US demand for electricity forecast to double by 2050 [1], there has been an increasing focus on energy efficiency and energy conservation. Buildings in the U.S. consume 72 % of electricity produced, and 55 % of U.S. natural gas use, accounting for about 40 % of total U.S. energy consumption (costing \$350 billion per year) and greenhouse gas emissions [2]. To truly tackle the issues of associated with dependence on fossil fuels, it is essential to take a hard look at ways to reduce the energy usage associated with buildings. At present, 42% of the energy consumed by buildings is used for heating, ventilation, and air conditioning (HVAC), and 23% is used for lighting. Research has shown that occupancy sensors can cut HVAC costs by as much as 80%, resulting in significant financial savings [2]. According to the U.S. Environmental Protection Agency, using occupancy sensors can save 40% to 46% of energy consumption in classrooms, 13% to 50% in private offices, 30% to 90% in restrooms, 22% to 65% in conference rooms, 30% to 80% in corridors, and 45% to 80% in storage areas [3].

Besides providing a means of minimizing energy consumption, occupancy sensors have found a niche in the rapidly growing demand for “Smart Homes” and “Smart Buildings” with another growing trend in the technology of home and workplace automation. More additional uses of occupancy sensors include security (by indicating that an area is occupied), and minimizing light pollution (by reducing the usage of lighting operating at night), whether it be outdoor lighting or indoor lighting emitting through windows or skylights.

However, currently available occupancy sensors, most commonly passive infrared (PIR) and ultrasonic sensors, have significant drawbacks, including high rates of false positives and failure to detect stationary persons [4,5]. To address the problems in the applications of occupancy sensors, the goal of this dissertation is to develop hardware and software solutions for a novel occupancy sensor for indoor spaces that can detect true human presence, reducing the rates of false alarms.

Newly available high-efficiency Doppler radar transceivers can be used to detect human cardiopulmonary motion [6, 7, 8, 9, 10, 11], thus providing a practical solution for the problems stated above in occupancy sensing. In addition, the advent of integrated low-power microprocessor/RF-transceivers provides a new platform for combination of sensing, processing and communication [12, 13] which can form the core of a wireless smart sensor network (WSSN) for applications such as “smart building” systems.

The work of this dissertation is to develop SoC-based Doppler radar occupancy sensors which can be used to detect and report the true presence and activity of humans, by adding passive nodes on off-the-shelf low-power system-on-chip (SoC) platform. These low-cost high-efficiency occupancy sensors integrate the capabilities of sensing, processing and communications in a single device, thus providing the key to small, low-cost, and low-power wireless sensor unit for zero energy “smart buildings” by reducing the energy consumption and improving the energy efficiency.

Such sensor units can be used to detect and report the true presence and activity of humans whether they are active or lying motionless, even in the presence of other environmental motion. While appliances such as rotating fans may generally falsely set off conventional sensors, these intelligent sensors focus on motion associated with true human presence, thus providing a highly-reliable low-power occupancy sensor for indoor spaces.

In the following sections, the most common used occupancy sensors will be introduced, and a brief overview of the work of this dissertation will be described.

1.1 Background on Current Occupancy Sensors

An occupancy sensor is designed to detect the presence or absence of people in a space, usually in order to determine whether various electrically powered loads in that room (for example, lights, ventilation, and the like) should be turned on or not. This is of particular advantage in hotels, commercial and government facilities such as office complexes, as well as communities such as military housing, college dorms, and public housing. When utilized properly, occupancy sensors can conserve a great deal of energy. This has led many businesses to purchase them voluntarily; and it has also resulted in

laws and regulations mandating the use of occupancy sensors as an energy conservation measure.

The most common occupancy sensors use passive infrared (PIR), ultrasonic, and dual (combination of PIR and ultrasonic) technologies — each of which has its own advantages and disadvantages. Regardless of which sensor type is selected, the goal is to gain the full advantages of occupancy sensor operation while avoiding possible negative outcomes, most notably nuisance switching (for example, lights are switched under false conditions, such as turning off while somebody is still in the room but has been motionless for several minutes).

1.1.1 Passive Infrared (PIR) Sensors

PIR sensors detect the motion of objects by sensing a change of infrared radiation in the form of heat emitted from the bodies including human beings, pets, vehicles, etc. The sensors first set up equilibrium with the background conditions. If the equilibrium state is disturbed due to some intrusion, the sensors perceive it as a change. This change is fundamental to the operation of PIR sensors. PIR sensors are passive devices in that they don't radiate infrared energy, but only detect radiation. They are designed to be maximally sensitive to objects that emit heat energy at a wavelength of around 10 μm , which is the peak wavelength of the heat energy emitted by humans [14].

PIR sensors detect infrared radiation with a pyroelectric transducer, which generates a voltage signal when it experiences temperature change, *e.g.*, infrared energy change in this case. The infrared energy focuses on the surface of the sensor by a multi-faceted Fresnel lens or segmented parabolic mirrors. Since the lens or mirrors gather the infrared energy from a very wide view with a multitude of narrow and discrete beams or cones, these sensors do not view the area in a continuous fashion. As an object moves from one cone of the field of view to another, a change in the infrared energy excites the dual sensing elements in the sensors connected out of phase one after another, resulting two successive signals with 180° phase difference, as shown in Fig. 1.1. In this way, movement of a person in the field of view can be detected. However, if the movement happens in the gaps between discrete cones, the change cannot be detected.

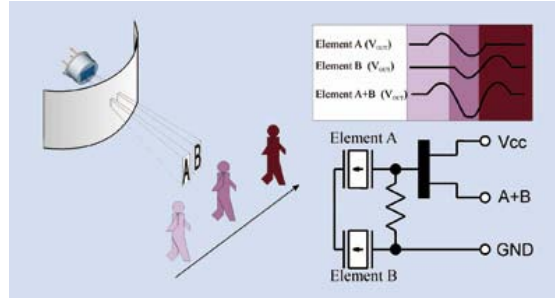


Fig. 1.1 PIR sensor detects human movement with dual elements, generating two successive out of phase signals [15].

Generally speaking, PIR sensors are small, inexpensive, low power, rugged, and easy to use. They are most suitable for smaller, enclosed spaces (wall switch sensors), spaces where the sensor has a view of the activity (ceiling- and wall-mounted sensors), and outdoor areas and warehouse aisles. While they have numerous advantages, challenges still exist.

These sensors detect motion within a field of view that requires a line of sight. They cannot "see" around corners and through obstacles. They are most sensitive to movement laterally across the sensor's field of view, and don't work for detecting a very-slowly-moving entity or one that does not move at all. An entity moving towards the sensor along the line of the view may also not be detected until the entity is in very close proximity to the sensor.

Designed for use at ambient temperatures of 15°C to 20°C, at higher temperatures the field of view narrows, and if below 15°C, the field of view widens and small or distant objects can activate the sensor. For this reason, it is not recommended that the sensors be used in drafty environments, near HVAC equipment, or facing windows where outside temperatures, or even motion, can cause false readings.

1.1.2 Ultrasonic Sensors

Ultrasonic sensors utilize the Doppler principle to detect occupancy, which are similar to radar and sonar. The sensors employ a piezoelectric transducer to convert electrical energy into ultrasonic waves at frequencies of 25 kHz or higher, typically between 40-50 kHz. These sound wave frequencies are at levels far above what human

ears can hear. The sensors then listen to the reflected waves. If there is motion, the reflected waves' frequency will shift slightly. Ultrasonic sensors work by sensing the frequency shift of the reflected ultrasound waves, as shown in Fig. 1.2.

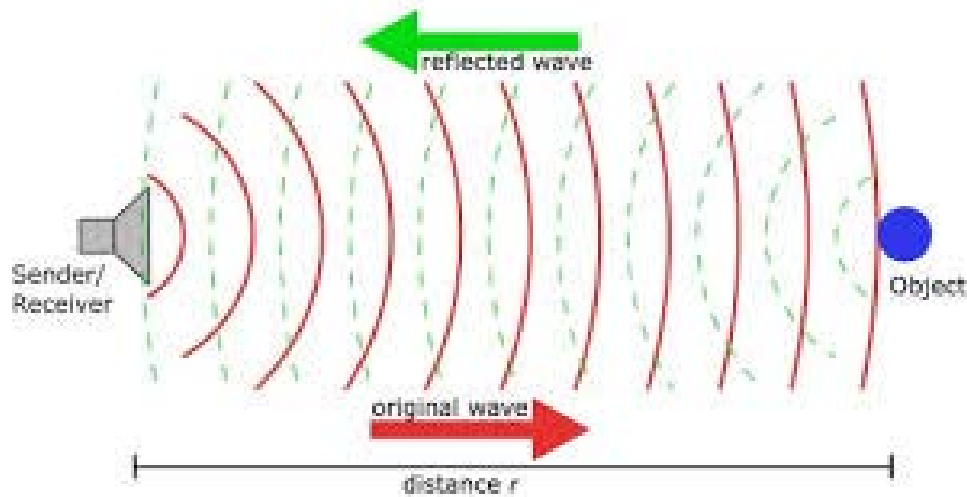


Fig. 1.2 Ultrasonic sensors detect occupancy via frequency shift of reflected wave [16].

Ultrasonic sensors do not require a direct line of sight and instead can “see” around corners and objects. They do not have gaps in the coverage zone like the PIR sensors. They are more effective for low motion activity, and they can be sensitive to slight motion, such as hand movement, typically up to 25 feet, or nearly twice the distance of the PIR sensors. The sensor is most sensitive to movement toward and away from the sensor. Ultrasonic sensors typically have a larger coverage area than PIR sensors. Ultrasonic sensors are best suited to open spaces, spaces with obstacles, restrooms, and spaces with hard surfaces.

One major drawback to ultrasonic sensors is that certain materials, such as cloth or foam, absorb sound waves [17]. This creates problems with occupancy sensing because a person could be covered in multiple layers of clothing and the sensor would not detect motion consistently. Ultrasonic sensors are also highly sensitive to reflective materials such as glass or plastic and could lead to false triggers.

One of the main advantages of the ultrasonic sensors is often one of the main disadvantages as well. Ultrasonic sensors are prone to false triggering and can be set off by air movement, such as that produced by a person running by a door or excessive

motion from a fan or an HVAC system, due to their highly sensitivity. Other incompatible applications include high ceilings (greater than 14 feet), and open spaces that require selective coverage (such as control of individual warehouse aisles).

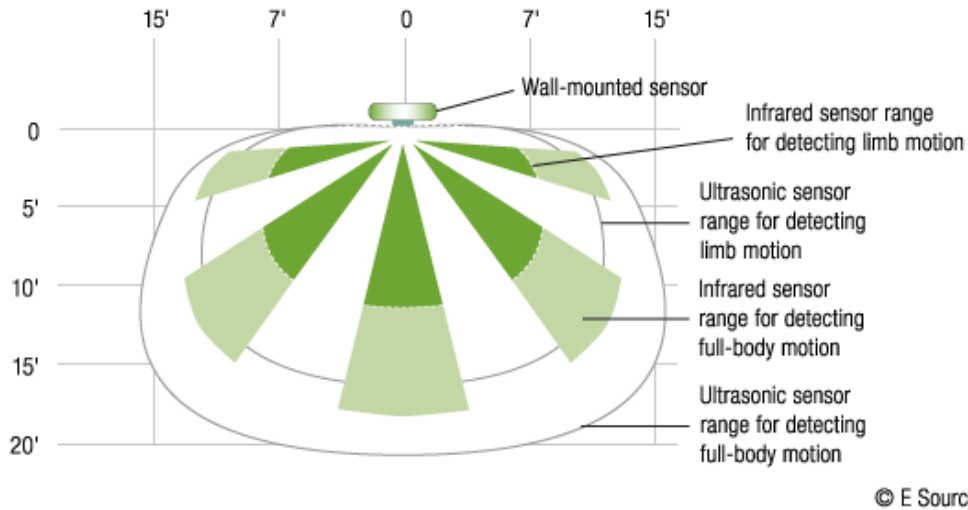


Fig. 1.3 Sensor coverage diagram: Ultrasonic sensors can detect motion at any point within the contour lines. PIR sensors see only in the wedge-shaped zones, and they don't generally see as far as ultrasonic units [18].

1.1.3 Dual Technology Sensors

Dual-technology sensors employ both PIR and ultrasonic technologies for maximum accuracy. The system activates the lights only when both technologies detect motion or when only the PIR detects the motion. By doing so, the system lowers the possibility of false-on by the ultrasonic sensors caused by motions such as air flow. The system deactivates when both technologies no longer sense motion, only requiring either one of the two technologies to hold the lights on. This significantly reduces the possibility of false-off problem of PIR sensors due to the lack of sensitivity to slight motions. Appropriate application of the dual-technology sensors include classrooms, conference rooms, and other spaces where a higher degree of detection may be desirable.

However, both PIR and ultrasonic sensors detect the physical movement of subjects. If the subject is still, such as reading or sleeping, the lights or AC may be shut down due to the sensor's failure to detect relatively slight motion. These shortcomings are well-documented by designers of building automation and facility security systems and have been referenced in trade publications as a major obstacle to the development of

reliable “smart building” systems [5]. In one potentially lucrative market segment, hotel rooms, the use of PIR and ultrasonic occupancy sensors has been all but abandoned due to the common problem of the lights going off automatically when guests are stationary -- - such as when they are using the bathroom.

1.1.4 Other Technology Sensors

Magnetic reed switch and CO₂ sensors are also available, but are less commonly used. Drawbacks of CO₂ sensors are inaccurate readings due to ventilation systems and delayed sensing due to the time it takes for CO₂ to accumulate. Magnetic reed door switches have advantages such as low power consumption and would be useful for contributing an input to the occupancy count of a room.

1.2 Occupancy Sensor Using Doppler Radar Detection on Human Cardiopulmonary Motion

A potential solution to the problems of existing occupancy sensors lies in the emerging technology used for non-invasive monitoring of human cardiopulmonary activity using Doppler radar [9, 10, 11, 19]. Such technology has been developed with Department of Defense funding for through-the-wall sensing of adversaries [19], and by medical device manufacturers for non-contact monitoring of vital statistics [9, 10]. By detecting the associated Doppler shift in a radio signal reflected off the body, cardiopulmonary-related movement can be discerned from a standoff distance of several meters. When a microwave signal illuminates the subject, the reflected signal is phase modulated by the subject’s chest motion due to cardiopulmonary activity. A simple phase demodulation technique of mixing the received signal with the portion of the transmitted signal results in a base-band signal that can be processed to yield the heart and respiration rates of the human subject [9, 11].

Doppler radar detection of respiratory and heart rates has been known for more than three decades [6, 7], but only recently the reduced cost of transceivers and computational components made the technology feasible for human monitoring. The detection of human cardiopulmonary motion with Doppler radar could provide a

promising approach to overcome the problems of false trigger and “dead spots” in conventional occupancy sensors.

With the primary focus on a growing demand for improved human detection sensors in energy-efficiency applications, the objective of this research is to develop an SoC-based, low-cost, and low-power Doppler radar occupancy sensor. This new occupancy sensor would be capable of reporting the true presence of humans by detecting human activity via cardiopulmonary motion. Therefore, the high level objectives include:

1. To develop the SoC-based Doppler radar occupancy sensor hardware platform.
2. To study the developed sensor operation condition for optimum energy efficiency.
3. To develop an algorithm for true presence detection of human.

The following section will describe the scope of this research work in details.

1.3 Scope of the Dissertation

This dissertation focuses on development of new Doppler radar occupancy sensor hardware by adding a passive node into commercially available SoCs and software, which identifies the occupancy or vacancy of a person by using the spectrum characteristics of respiratory movement.

Chapter 1 has introduced the most common technologies employed in the current occupancy sensors, defined the problems of these technologies, addressed the importance of solving these problems, provided the solution by briefly describing the SoC-based Doppler radar detection of respiratory movement, and its background.

Chapter 2 presents the Doppler radar systems in cardiopulmonary monitoring in depth. Several system architectures, and demodulation and signal processing methods are introduced, and performance trade-offs are analyzed.

Chapter 3 focuses on the hardware design of the proposed occupancy sensor. The two main components, off-the-shelf SoC and passive sensor node are introduced. The feasibility of building an Doppler radar occupancy sensor with off-the-shelf SoC and custom passive node is proved by accurately extracting the motion rate of a mechanical

target programmed to simulate human respiration with such sensor unit. In this chapter, a CMOS passive mixer intended used for the passive sensor node with unique characteristics of both narrow band and broad band is designed, fabricated, and tested. The mixer demonstrates excellent conversion loss, LO-to-IF isolation, and DC offset performance, which makes it extremely suitable in the use of Doppler radar cardiopulmonary sensing.

Chapter 4 reviews the operation parameters of the proposed occupancy sensor. The sensor is operated in three modes: continuous wave, modulated continuous wave and packet mode. The sensitivity and power consumption of its three operation modes have been measured and compared. Though packet mode is slightly inferior to CW and modulated CW mode in sensitivity, it demonstrates greatly superior power efficiency to the other two modes. This chapter also compares the sensitivity between the configuration employed in the proposed sensor and the sensor system using quadrature receiver when a target is at non-null points, as well as the sensitivity of the proposed sensor at a null point against an optimum point. The sensor built with a passive node shows similar sensitivity to the quadrature receiver at non-null points. At null points, the sensitivity of this sensor is decreased as well as the frequency information is distorted. Yet the distorted information is useful, due to the fact that the incorrect frequency is double that of the authentic one.

Chapter 5 proposes an algorithm for true occupancy detection based on human respiratory movement. In Chapter 5, the spectral pattern of the human respiration is characterized with simulation and experiment, using both simplistic and more complex but realistic models. Based on this pattern, an algorithm to detect human occupancy is developed. The algorithm is tested and validated with 19 stationary subjects, sitting in front of the proposed occupancy sensor.

Chapter 6 summarizes the work done in this dissertation and draws the conclusions of this dissertation. Future work to improve the system is also discussed in this chapter.

Chapter 2 Doppler Radar Detection of Cardiopulmonary Signals

2.1 Radar Basics

RADAR is an acronym for Radio Detection And Ranging. The radar operation principle is similar to the sound-wave reflection. If a person shouts towards an object which reflects sound, he will hear an echo. The general direction, distance and the time required for an echo to return can be estimated if the speed of a sound wave traveling in air is known. Instead of sound waves, radar transmits electromagnetic waves and uses its echo to determine the direction, distance, and speed of the reflecting object.

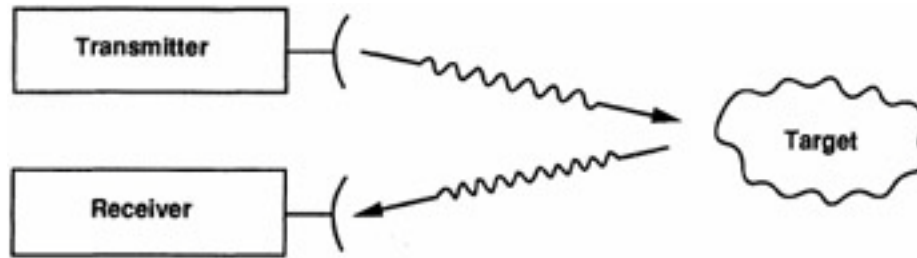


Fig. 2.1 Illustration of a basic radar system, and its working principle.

As shown in Fig. 2.1, a basic radar system usually consists of a transmitter and a receiver. The transmitter is a device to generate an electromagnetic signal. The receiver is a highly sensitive device which can pick up the relatively weak signal reflected by a target. The transmitting signal normally travels through space at approximately the speed of light in a straight line, and will vary only slightly because of atmospheric and weather conditions. When it meets an electrically disruptive surface, it is reflected in a variety of directions. A portion of the reflected signal travels in the opposite direction to the incident rays. It can be sensed by the receiver. The time delay between the transmitted signal and received echo implies the distance to the target. The velocity of a target can be derived from the frequency shift of the received signal with respect to the transmitted signal. The strength of the signal gives information about the target's radar cross section, which indicates its size, geometry, and composition. Depending on the application, the

frequency of the radar signals varies from MHz to GHz, as shown in Table 2.1 [20]. A major advantage of radio and microwave frequency radar system is that the waves in this range can penetrate through some objects that light cannot penetrate, resulting in detection of the objects which are not visible [21].

Table 2.1 The frequencies used in radar systems.

Radar Band	Frequency (GHz)	Wavelength (cm)
Millimeter	40 to 100	0.75 to 0.30
Ka	26.5 to 40	1.1 to 0.75
K	18 to 26.5	1.7 to 1.1
Ku	12.5 to 18	2.4 to 1.7
X	8 to 12.5	3.75 to 2.4
C	4 to 8	7.5 to 3.75
S	2 to 4	15 to 7.5
L	1 to 2	30 to 15
UHF	0.3 to 1	100 to 30

Radar is used in many fields for scientific, military, and civilian applications. The first use of radar was for military purposes: detecting and searching for air, ground and sea targets. It rapidly evolved into civilian applications for monitoring aircraft, ships, and roads.

In aviation, Air Traffic Control (ATC) radars are used for safely controlling the air traffic en route and close to the airports. High resolution radars are used to monitor air and ground vehicles in large airports. Also, they have been used with ground control approach systems to guide aircrafts to a safe landing in bad weather [21]. In ship-borne applications, marine radars are used to measure the distance of ships to prevent collision with other ships, to navigate, and to fix their position at sea. Also shore-based radars are used to monitor and regulate ship movements for surveillance of harbors [22]. In scientific applications, meteorologists use radar to monitor weather patterns. Geologists use specialized ground-penetrating radars to map the composition of the Earth's crust. As an example of law enforcement application, police use radar to monitor vehicle speeds.

2.1.1 The Radar Range Equation

The radar equation [21] specifies the physical dependence of the transmit power. Furthermore, one can assess the performance of a given radar with the radar equation.

The radar equation relates the range for a radar to the characteristics of the transmitter, receiver, antenna, target, and the environment. It takes into account the maximum target detection distance for a specific radar system, as well as the factors affecting radar performance. This is very helpful for understanding the overall characteristics of a particular radar system. This section derives the basics of the radar range equation, under the free space assumption, which imposes that the following conditions are fulfilled:

(a) No large obstacles lie between antenna and the target, along an optical line of sight.

(b) No alternative transmission path, via any reflecting surface, can be followed by a substantial fraction of the total radiated energy.

(c) The intervening medium is transparent, *i.e.*, it does not absorb energy from the electromagnetic waves at the frequency used.

(d) The intervening medium is homogeneous, with respect to the refractive index at the radar frequency

To derive the maximum range which a target can be detected by a radar system, the link budget, *i.e.*, an accounting all of the gains and losses from the transmitter through the medium to the receiver, shall be considered for the radar-to-target and target-to-radar paths, together with target characteristics.

Assuming the power of a radar transmitter, P_t , is transmitted through an *isotropic* antenna, which radiates isotropically. The transmitted power P_t , at a range R from the transmitter, is uniformly distributed over the surface of a sphere of radius R . The surface area can be expressed as:

$$A = 4\pi R^2 . \quad (2.1)$$

Assuming the distance between the transmitting antenna and target is R_l , in meters, the power density of the transmitted power P_t , in Watts, on the spherical surface with radius R_l can be expressed as:

$$S_u = \frac{P_t}{4\pi R_l^2} , \quad (2.2)$$

where S_u is the power density, in W/m^2 .

While we assumed isotropic emission, in reality, an directional antenna is used in radar systems to provide directivity, *i.e.*, to concentrate or focus the radiated power in a directional sector of space. This redistribution of the transmitted power results in an increase power density in the direction of the radiation. This directional power density can be calculated by omni-directional power density S_u and antenna gain G . Antenna gain is the measure of the antenna effectiveness in concentrating the radiated energy in the direction of interest. Hence,

$$S_g = S_u \cdot G, \quad (2.3)$$

where S_g is directional power density and G is the transmitting antenna gain.

Directional power density S_g is derived where the target is located. As the transmitted electromagnetic wave reaches the target, some of the power in it will be radiated back toward the radar by the target. Target detection depends on both the power density at the location of the target and the amount of power reflected from the target. The radar cross section (RCS) is a measure of how detectable a target is with a radar. A larger RCS indicates that a target is more easily detected. The RCS quantity depends on several factors, which will be explained in following section. Here, we simply use the concept of RCS to calculate the reflected power, together with the power density S_u , the antenna gain G :

$$P_{rf} = \frac{P_t \cdot G \cdot \sigma}{4\pi R_1^2} \quad [W], \quad (2.4)$$

where P_{rf} is reflected power, and σ is RCS.

Similar to the transmitted power, P_t , emitted from the radar transmitting antenna to the target, the reflected power, P_{rf} , can propagate back from the target to the radar receiving antenna. Since the radiation from the target can be considered under the same conditions as the transmitted power, the power density observed at the receiver is given by:

$$S_e = \frac{P_{rf}}{4\pi R_2^2} [W/m^2], \quad (2.5)$$

where S_e is power density at the receiver, P_{rf} is reflected power in Watts, and R_2 is the distance between target and antenna in meters.

The signal is collected by the receiving antenna proportionally to its *effective area*, which can be expressed as:

$$P_r = S_e \cdot A_e, \quad (2.6)$$

where P_r is power at the receiver in Watts, and A_e effective antenna area in m^2 .

The effective antenna area arises from the fact that an antenna suffers from losses, therefore, the received power at the antenna is not equal to the incident power. As a rule for reference, the efficiency of a typical antenna, K_a , is around 0.6 to 0.7. The effective antenna area can be calculated from the geometric antenna area as:

$$A_e = K_a \cdot A_a, \quad (2.7)$$

where A_e is effective antenna area in m^2 , and A_a is geometric antenna area in m^2 .

From equations (2.6) and (2.7), the power received, P_r , can be expressed as:

$$P_r = S_e \cdot A_a \cdot K_a \quad (2.8)$$

Combining equations (2.8) and (2.5), P_r can be derived as:

$$P_r = \frac{P_{rf} A_a K_a}{4\pi R_2^2} [W] \quad (2.9)$$

In the analysis above, the transmitted and reflected signals have been considered separately. Now, consider both transmitted and reflected power, we have

$$P_{rf} = \frac{P_t \cdot G \cdot \sigma}{4\pi R_1^2} [W] \quad (2.4)$$

$$P_r = \frac{P_{rf} A_a K_a}{4\pi R_2^2} [W] \quad (2.9)$$

$$P_r = \frac{P_t G \sigma A_a K_a}{(4\pi)^2 R_1^2 R_2^2} \text{ [W]} \quad (2.10)$$

Assuming the distance traveled by the transmitted signal from the transmitting antenna and target, and the distance traveled by the reflected signal from the target and receiving antenna are equal,

$$R_1 = R_2, \quad (2.11)$$

We conclude the power P_r at receiver is

$$P_r = \frac{P_t G \sigma A_a K_a}{(4\pi)^2 R^4} \text{ [W]}. \quad (2.12)$$

If the same antenna is used for both transmit and receive, we can apply the formula relating the effective area A_e , and hence to antenna geometry area A , to the gain G in terms of the wavelength λ ,

$$G = \frac{4\pi A_a K_a}{\lambda^2}. \quad (2.13)$$

The echo power returning to the receiver will then be:

$$P_r = \frac{P_t G^2 \sigma \lambda^2}{(4\pi)^3 R^4} \text{ [W]}. \quad (2.14)$$

Solving for range R , we obtain the classic radar range equation

$$R = \sqrt[4]{\frac{P_t G^2 \lambda^2 \sigma}{P_r (4\pi)^3}}. \quad (2.15)$$

From this radar range equation, the factors that influence the wave propagation of radar signals can be seen. The most important feature of this equation is the fourth-root dependence.

The smallest signal that can be detected by the radar is called Minimum Discernible Signal, $P_{r,min}$. Received power smaller than $P_{r,min}$ are not detectable since they are lost in the noise of the receiver and its environment. The minimum power can be

detected by a given radar system corresponds to the maximum detectable range R_{max} , which can be expressed as

$$R_{max} = \sqrt[4]{\frac{P_t G^2 \lambda^2 \sigma}{P_{r,min} (4\pi)^3}} \quad [\text{m}]. \quad (2.16)$$

2.1.2 Radar Cross Section

As mentioned in previous section, when a target is illuminated by electromagnetic waves generated by a radar, it will back-scatter portion of the energy towards the radar. The size and reflectivity of the target can be summarized into a single term, σ , the radar cross section (RCS). This is a measure of a target's ability to reflect radar signals in the direction of the radar receiver, *i.e.* it is a measure of the ratio of backscatter power per unit solid angle in the direction of the radar (from the target) to the power density that is intercepted by the target:

$$\sigma = \frac{\text{power reflected toward source/unit solid angle}}{\text{incident power density}/4\pi} = 4\pi R^2 \frac{|E_r|^2}{|E_i|^2} \quad (2.17)$$

where R is the range to the target, E_r is the electric field strength of the echo signal back at the radar, and E_i is the electric field strength incident on the target. It is assumed in the above derivation that the target intercepts power from an incident wave and radiates that power uniformly in all directions, although most real targets do not scatter energy uniformly in all directions, and the target is far enough from the radar that the incident wave can be considered to be planar rather than spherical. This radar cross section can be calculated by Maxwell's equations with the proper boundary conditions or can be measured based on the radar equation.

The RCS of a target can also be viewed as a comparison of the strength of the reflected signal from a target to the reflected signal from a perfectly smooth sphere of cross section area of 1 m^2 , as implied in the derivation of the simple form of the radar equation in (2.15):

$$\text{Reradiated power density back at the radar} = \frac{P_t G}{4\pi R^2} \cdot \frac{\sigma}{4\pi R^2}. \quad (2.18)$$

The factors that influence a target RCS include:

- the target's physical geometry and exterior features;
- the direction of the illuminating radar;
- the frequency of radar transmitters;
- the material used on the reflecting surface of the target.

2.1.3 Doppler Effect

The fundamental function of radar is to measure the range of a target from the radar by measuring signal round trip time. However, it can be difficult to distinguish returning signals from the target of interest with other objects or background located at similar distances. In this case, radar can be used to measure another characteristic of the returning signals, relative velocity, due to Doppler effect or Doppler shift – a phenomenon that the radar transmitted wave frequency is modified by the process of being reflected by a moving object. By measuring the relative velocity of all objects returning echoes to the radar system, the radar can discriminate between objects moving at different relative velocities.

Consider a radar that transmits a sinusoidal wave of a certain frequency f , the number of oscillations per unit time. The distance from the rest of each wave to the next is the wavelength λ , which is inversely proportional to the frequency. The relationship between wavelength and frequency is:

$$\lambda = \frac{v}{f}, \quad (2.19)$$

where:

f = wave frequency (Hz or cycles per second),

λ = wavelength (meters),

and v = speed of light (approximately 3×10^8 meters/second).

Each successive wave is reflected from the target of interest. When the target and radar are both relatively still, the echo will have the same wave frequency as the original signal. Each part of the signal is reflected when it reaches the target, mirroring the

original signal exactly. When either the target or the radar or both move away from each other, the next wave crest travels a longer round trip distance, from the radar to the target and from the target to the radar. In the interval time, the target has moved closer to the radar between the previous and current wave crest. This has the effect of “stretching out” the wave, resulting in a longer wavelength. Since frequency is inversely proportion to wavelength, the frequency of the reflected wave appears to have decreased. On the contrary, if the target or the radar or both of them are moving towards each other, then the opposite happens. Each successive wave crest has a shorter round trip distance to travel, so the time between arrival of receive wave crests is shortened, resulting in a shorter wavelength and a lower frequency. In all cases, the frequency of the sinusoidal wave produced by the radar remains constant. The Doppler effect principle is illustrated in Fig. 2.2.

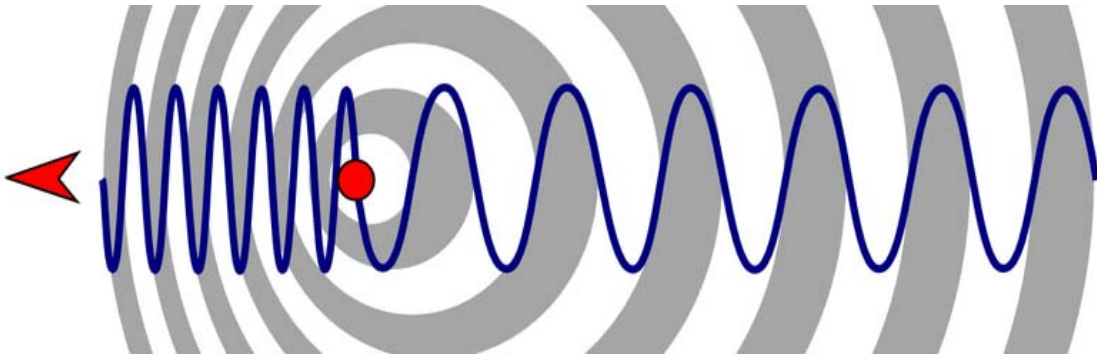


Fig. 2.2 Illustration of the Doppler Effect. The frequency (wavelength) of reflected wave differs from the transmitted wave due to target movement [23].

The Doppler frequency shift can be calculated as follows. If the distance between a radar and a target is R , then the total number of wavelengths λ in the two-way path from radar to target and return is $2R/\lambda$. Each wavelength corresponds to a phase change of 2π radians. The total phase change in the two-way propagation path will be

$$\phi = 2\pi \times \frac{2R}{\lambda} = 4\pi R / \lambda . \quad (2.20)$$

If the target is moving relative to the radar, R is changing and so will the phase. The rate of changing phase can be obtained by differentiating (2.20) with respect to time provides the rate of change of phase, which is the angular frequency

$$\omega_d = \frac{d\phi}{dt} = \frac{4\pi}{\lambda} \frac{dR}{dt} = \frac{4\pi v_r}{\lambda} = 2\pi f_d, \quad (2.21)$$

where $v_r = dR/dt$ is the radial velocity in meters/second, or rate of change of range with time. The rate of change of ϕ with time is the angular frequency $\omega_d = 2\pi f_d$, where f_d is the Doppler frequency shift. Thus from (2.21),

$$f_d = \frac{2v_r}{\lambda} = \frac{2f_t v_r}{c}, \quad (2.27)$$

where f_t is radar frequency and c is the speed of light or 3×10^8 meters/sec.

Doppler effect applies only to the relative motion of the radar and target object. Therefore, if an object is moving at right angle to the radar there will be no Doppler frequency shift. If the angle between the target's velocity vector and the radar line of sight to the target is θ , as shown in Fig. 2.3, then the relative velocity in equation (2.27), $v_r = v \cos \theta$, where v is the speed, or magnitude of the object's vector velocity.

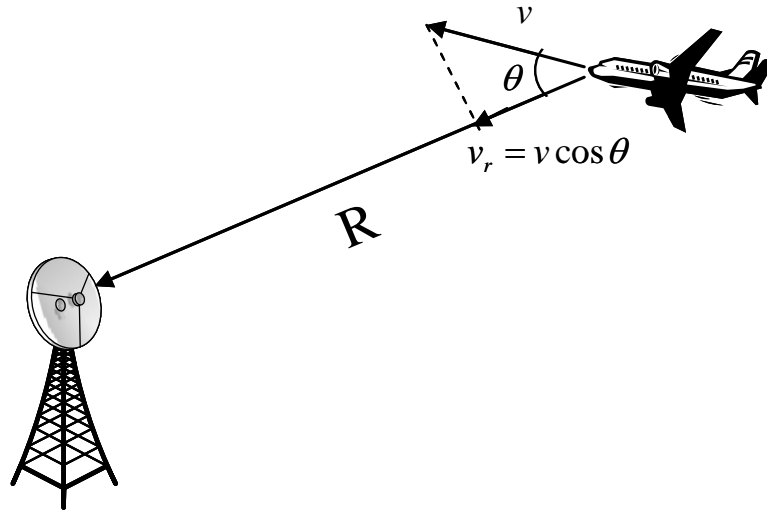


Fig. 2.3. Relative geometry of a radar and target, illustrating the factors influencing the Doppler frequency shift. [21]

In summary, the Doppler effect can be of great use in radar systems. It is possible to determine the target speed, as well as range by binning the receive echoes both over range and Doppler frequency shift, with a Doppler radar. When a target is going away

from the radar, the wavelength of the wave reflected by the target is increased by the Doppler effect, and the Doppler shift is negative. On the other hand, when the target is coming closer to the radar, the wavelength of reflected wave is decreased by the Doppler effect, and the Doppler shift is positive. By measuring this wavelength change, the radar can detect how fast the target is moving with respect to the radar. This allows easy discrimination between moving objects, such as an aircraft or vehicle, and the background clutter, which is generally stationary. However, if the target moves periodically with displacement smaller than the wavelength of the radar, then reflected signal is more phase-modulated rather than frequency-modulated (or frequency shifted).

2.1.4 Continuous Wave (CW) Radar and Pulsed Radar

Radar systems can be classified by their detection purpose, their configuration, or detection method, such as imaging and non-imaging radar, primary and secondary radar, and continuous wave and pulsed radar [24]. For the purpose of this dissertation, this section will only discuss continuous wave (CW) and pulsed radars.

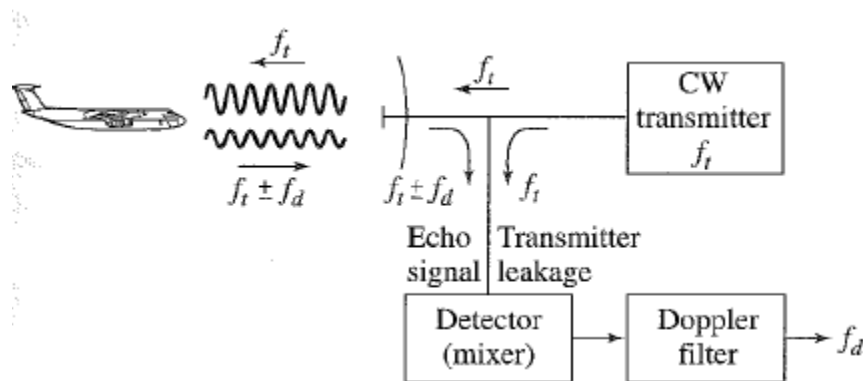


Fig. 2.4 Simple CW radar block diagram that extracts Doppler frequency shift from a moving target [21].

A CW radar system transmits and receives an electromagnetic signal continuously. The transmitted signal of a CW radar is constant in amplitude and frequency. In theory, the operating bandwidth of a CW radar is infinitesimal, since it corresponds to an infinite duration continuous wave. In reality, such systems with infinitesimal bandwidths don't exist. Transmitted CW signals usually have very narrow bandwidths. A CW radar has a simple topology, consisting of a signal source for both transmitting and receiving, and a

receiver, as shown in Fig. 2.4. Due to its continuous nature, range detection is not possible with an unmodulated CW radar.

Since a CW system constantly transmits and receives, there is no need for a switch to control a transmit/receive terminal, which is required in pulsed radar system [25]. Due to its extremely narrow bandwidth, design of the filter at each stage of the receiver becomes very simple. Furthermore, signal processing or demodulation to obtain velocity of a target's motion is quite simple. The main system-level advantage of a pure CW radar system is that it can unambiguously measure the velocity of targets which are at any range and moving at any velocity. In contrast, pulsed and other modulated systems have some ambiguity in both range and velocity measurements. The main disadvantage of CW radar is due to its constant transmission and reception. A portion of the transmitted signal leaks from the transmitter to the receiver, either through coupling between transmit and receive circuitry, or directly through the antennas. Therefore, the radar system receives a large signal at the transmit frequency that has not reflected off the target. Additionally, clutter reflects some of the signal and noise sidebands back to the receiver, adding to the signal at the transmit frequency due to leakage. These unwanted signals result in a dc offset and low-frequency noise if they are not eliminated before the signal is detected.

A pulsed radar system transmits a pulse and then listens for receive signals. It uses switches or duplexers between transmitting and receiving, and the signal has a somewhat wider bandwidth than CW radar signal, because of the nature of pulses. Leakage from the transmitter and strong echoes from short-range clutter are separated temporally from the weaker echoes of long-range targets, and this is the main advantage of pulsed radar over CW radar. Fig. 2.5 shows the block diagram of a pulse radar system [21].

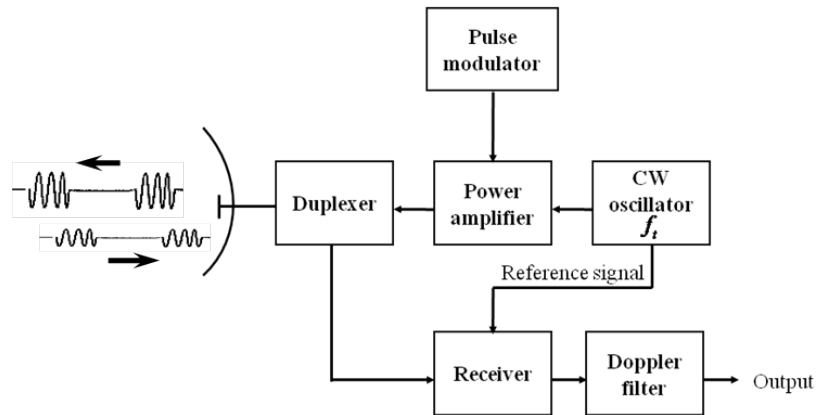


Fig. 2.5 Block diagram of a simple pulse radar that extracts the Doppler frequency shift from a moving target.

Pulse radar waveforms can be completely defined by the following:

- 1) Carrier frequency which may vary depending on the design requirement and radar mission;
- 2) Pulse width, which is closely related to the bandwidth and defines the range resolution;
- 3) Modulation;
- 4) The pulse repetition frequency.

With pulsed radar, the range can be extracted from the two-way time delay between a transmitted and received pulse. Doppler measurements can be made in two ways. If the radar pulse width is long enough and if the target's Doppler frequency is large enough, it may be possible to detect the Doppler frequency shift on the basis of the frequency change within a single pulse. Otherwise, more than one pulse is needed to recognize a change in the echo frequency due to the Doppler effect. This can be seen in Fig. 2.6. Fig. 2.6 (a) represents the echo pulses, Fig. 2.6 (b) is the pulse train when there is a recognizable Doppler frequency shift. To detect a Doppler shift on the basis of a single pulse of width τ generally requires that there be at least one cycle of the Doppler frequency f_d within the pulse, or that $f_d\tau > 1$. Fig. 2.6 (c) is shown that when $f_d\tau < 1$, i.e., the Doppler frequency shift f_d is much smaller than $1/\tau$, the Doppler shift frequency can be sampled at the pulse repetition frequency (prf) with more than one pulse.

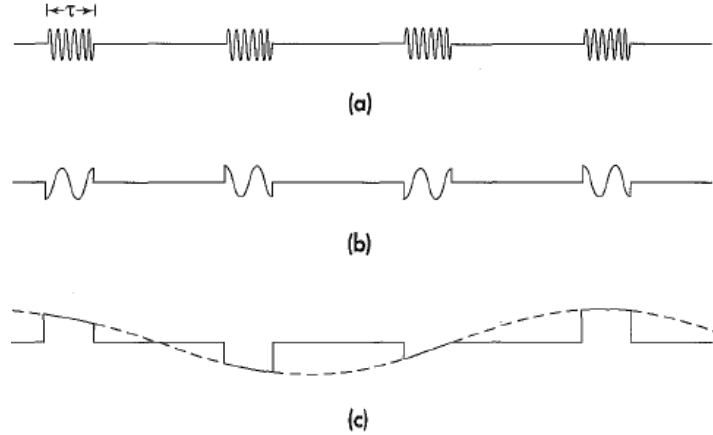


Fig. 2.6 (a) Receive RF echo pulse signals; (b) Base band pulse signals when the Doppler frequency $f_d > 1/\tau$; (c) Base band pulse signals when the Doppler frequency $f_d > 1/\tau$ with the Doppler frequency signal is shown dashed [21].

2.2 Doppler Radar Detection of Cardiopulmonary Signals

Using Doppler effect, human cardiopulmonary signals, including respiration and heart beat rate, can be detected invasively with Doppler radar [9]. The concept of using Doppler radar in non-contact measurement of vital signs was first shown for measurement of human respiration in 1975 and heart beat in 1979, respectively [6, 7]. Over 30 years, the research on Doppler radar cardiopulmonary monitoring has been carried out. Research efforts in this century focus on hardware and software improvements, making the system more compact, more economic, with lower power consumption, longer detection range, better accuracy and more robust operation. For example, in [26] and [27] single chip Doppler radar transceivers were implemented to remove the need for bulky equipment and proved that wireless life signs monitoring can be performed using compact components. Signal processing methods were developed in [28] and [29] for heart rate estimation. Multi Input Multi Output systems were used for multiple subject detection in [30]. In [31] novel signal processing techniques are discussed which include a harmonic canceller for removing respiration harmonic. Demodulation schemes were discussed in [32] and [33]. DC offset and channel imbalance effects on data accuracy were studied in [34] and [35, 36], respectively.

2.2.1 CW Radar Concept of Cardiopulmonary Monitoring

According to Doppler theory, a target moving at velocity $v(t)$ (m/s) will reflect an incident electromagnetic signal, and modulate its frequency by

$$f_d = \frac{2f}{c} v(t), \quad (2.28)$$

where f_d is the Doppler shift in Hz, f is the transmitted frequency in Hz, c is the signal propagation velocity in m/s, and t is the elapsed time in seconds. When a target is in periodic motion with no net velocity, the Doppler shift of the reflected signal can be better described as a phase modulation, which is in proportional to the time-varying position of the target:

$$\varphi_t = \frac{2f}{c} (2\pi x(t)) = \frac{4\pi x(t)}{\lambda}, \quad (2.29)$$

where φ_t is the phase change due to the periodic movement, $x(t)$ is the displacement of the target moving from the original position, and λ is the wavelength of the transmitted signal in meters. A live human subject can be treated as such a target due to his or her periodic cardiopulmonary activity. With Doppler radar technology, the physiological motions resulting from by cardiopulmonary activity can be measured and characterized.

A Doppler radar system performs the sensing function in the technique of Doppler radar detection on human cardiopulmonary signals. The radar transceiver transmits an electromagnetic signal, typically a CW (sometimes frequency modulated) signal in this case. The electromagnetic wave incident upon the body of the human subject under measurement will be scattered in every direction [6], since body tissue acts an inhomogeneity in the air due to differences in permittivity and conductivity. The radar receiver will intercept the reflected or backscattered portion of scattering waves. The waves reflected back by the human body undergoes a phase shift proportional to the small displacements of the skin surface on human chest wall with every heart beat and breath, which contribute to variations in the roundtrip time (or phase delay) of the signal. The phase difference between the transmitted and received signals can be obtained by using a frequency mixer to compare the two signals. This concept is illustrated in Fig. 2.7, where a continuous wave (CW) radar signal illuminates, as expressed in time domain:

$$S_t(t) = \cos(2\pi ft + \phi(t)), \quad (2.30)$$

where f is the frequency of the transmitted microwave signal, and $\phi(t)$ is the phase noise of the oscillator in the transmitter. This transmitted signal will travel until it is incident on the human subject's body, where it is reflected back to the receive antenna. The signal received at the antenna has undergone a phase delay and amplitude variation which can be expressed as:

$$S_r(t) = A_r \cos\left(2\pi ft + \frac{2\pi}{\lambda}(2d_0 + 2d(t)) + \phi\left(t - \frac{2d_0}{c}\right)\right), \quad (2.31)$$

where d_0 is the nominal range between radar antenna and the human subject, $d(t)$ represents chest displacement due to heart beat and respiration, and A_r is the reduced amplitude of the received signal. Comparing the transmitted and received signals, commonly via a mixer, the output of the system is a product of the two signals:

$$\begin{aligned} S_t(t)S_r(t) &= \frac{A_r}{2} \cos\left(\frac{2\pi}{\lambda}(2d_0 + 2d(t)) + \Delta\phi\right) \\ &\quad + \frac{A_r}{2} \cos\left(2\omega_0 t + \frac{2\pi}{\lambda}(2d_0 + 2d(t)) + \Sigma\phi\right), \end{aligned} \quad (2.32)$$

where $\Delta\phi = \phi(t) - \phi\left(t - \frac{2d_0}{c}\right)$ is the residual phase noise, and $\Sigma\phi = \phi(t) + \phi\left(t - \frac{2d_0}{c}\right)$. The second term on the right of above equation has twice the frequency of the transmitted signal. It can be filtered out with a low pass filter (LPF). Therefore, the baseband signal is expressed as:

$$B_r(t) = \frac{A_r}{2} \cos\left(\frac{4\pi d_0}{\lambda} + \frac{4\pi d(t)}{\lambda} + \Delta\phi\right), \quad (2.33)$$

which relates a phase shift of the signal to the displacement of the subject's chest. The radar system detects the phase shift in the form of:

$$\varphi_t = \frac{4\pi}{\lambda} d(t) \text{ [rad]}. \quad (2.34)$$

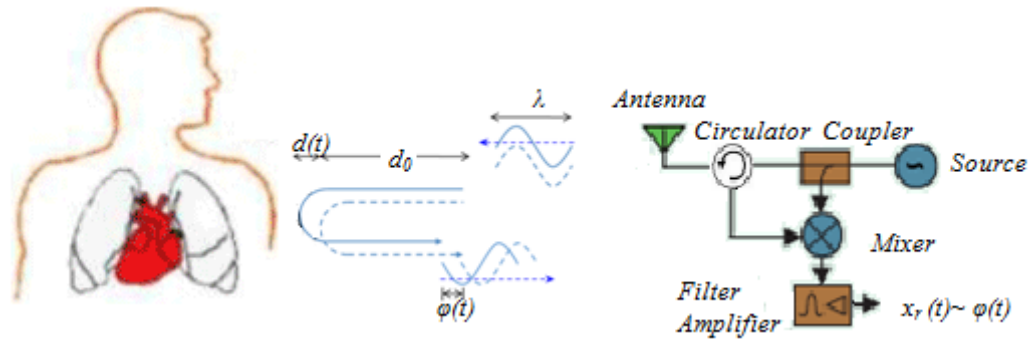


Fig. 2.7 A simple Doppler transceiver architecture denoting transmit and receive antenna, signal source, coupler, circulator and a frequency mixer. Operation Principle of the Doppler radar: the phase shift $\varphi(t)$ of the reflected signal is proportion to the time-varying chest position/displacement $d(t)$ due to heart beat and respiration [19].

2.2.2 Single Channel Receiver

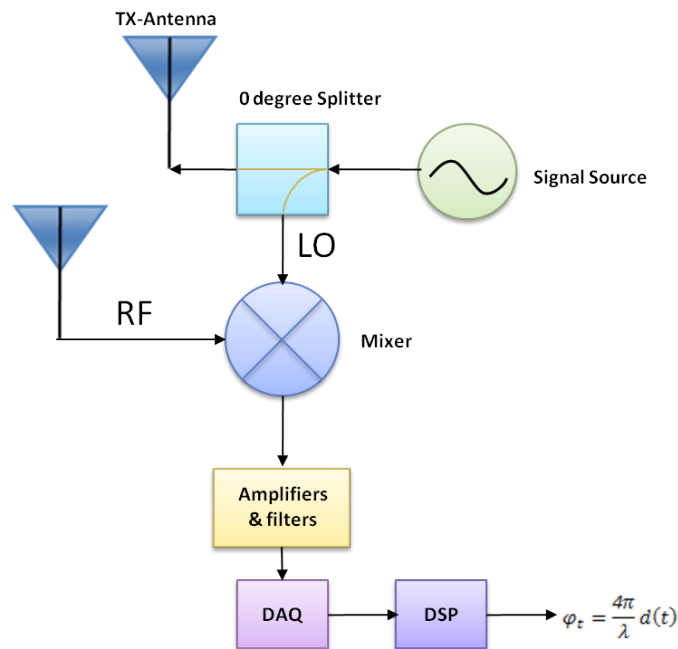


Fig. 2.8 A simple Doppler transceiver architecture, in which a single channel receiver mixes partial transmitted signal and reflected signal with a mixer to produce baseband signal.

Equation (2.33) states that baseband output of the radar is actually cosine of the phase. This implies a phase detector is indeed needed in a Doppler radar system to measure the human cardiopulmonary activities. A simple phase detector can be realized by a single channel receiver, as shown in the Doppler transceiver architecture in Fig. 2.8. A single channel receiver is very simple, requires minimum hardware, and is capable of

producing a baseband signal with sufficient accuracy for extracting vital signs [37]. However, a single channel receiver suffers from varying detection accuracy depending on the location of the subject under test [38].

In equation (2.33), when

$$\frac{4\pi d_0}{\lambda} = k\pi, k = 0,1,2, \dots, \quad (2.35)$$

e.g., d_0 , the nominal distance between radar and the subject under test, is an integer multiple of quarter of wavelength of the transmitted radar signal, the subject is at a null point. In this case, equation (2.33) will become:

$$B_r(t) = \frac{A}{2} \cos\left(k\pi + \frac{4\pi d(t)}{\lambda} + \Delta\phi\right) = \pm \frac{A}{2} \cos\left(\frac{4\pi d(t)}{\lambda} + \Delta\phi\right), \quad (2.36)$$

Applying the small angle approximation and a Taylor series expansion to equation (2.36), the output can be written as:

$$B_r(t) \approx \frac{A}{2} \left[1 \pm \left(\frac{4\pi d(t)}{\lambda} + \Delta\phi\right)^2\right], \quad (2.37)$$

This indicates that the received signal is proportional to the square of the time-varying displacement $d(t)$ and is not very sensitive to physiological motion.

By analogy, when the distance of a subject to the antenna is an odd multiple of an eighth of the wavelength of the transmitted signal, or

$$\frac{4\pi d_0}{\lambda} = \frac{(2k+1)\pi}{2}, k = 0,1,2, \dots, \quad (2.38)$$

the baseband signal will have the form:

$$B_r(t) \approx \pm \frac{A}{2} \left(\frac{4\pi d(t)}{\lambda} + \Delta\phi\right) \quad . \quad (2.39)$$

When the subject is at these locations, the baseband output is proportional to the periodic chest displacement, $d(t)$, and the received signal will be most closely follow physiological motion. These locations are called optimum points.

Equations (2.35) and (2.38) show where the null and optimum points only depends on the distance between radar and the subject, and that null and optimum points are an eighth of a wavelength apart. At a frequency of 2.4 GHz, the null and optimum points will occur every 1.5 cm. Therefore, optimal sensitivity will be hard to maintain

due to variations in the positions of the radar transceiver and the subject. To avoid this problem, a so-called quadrature transceiver can be used.

2.2.3 Quadrature Receiver

The problem of detection sensitivity, and hence accuracy variance with target location in a Doppler radar system using a single channel receiver can be alleviated using a quadrature receiver, with two receive channels. A quadrature receiver [9] is depicted in Fig. 2.9. This is a well known receiver architecture, commonly used in communication systems. In a quadrature receiver, two channels, 90° out of phase with each other, are incorporated. The two channels in such systems are labeled in-phase (I-channel) and quadrature (Q-channel).

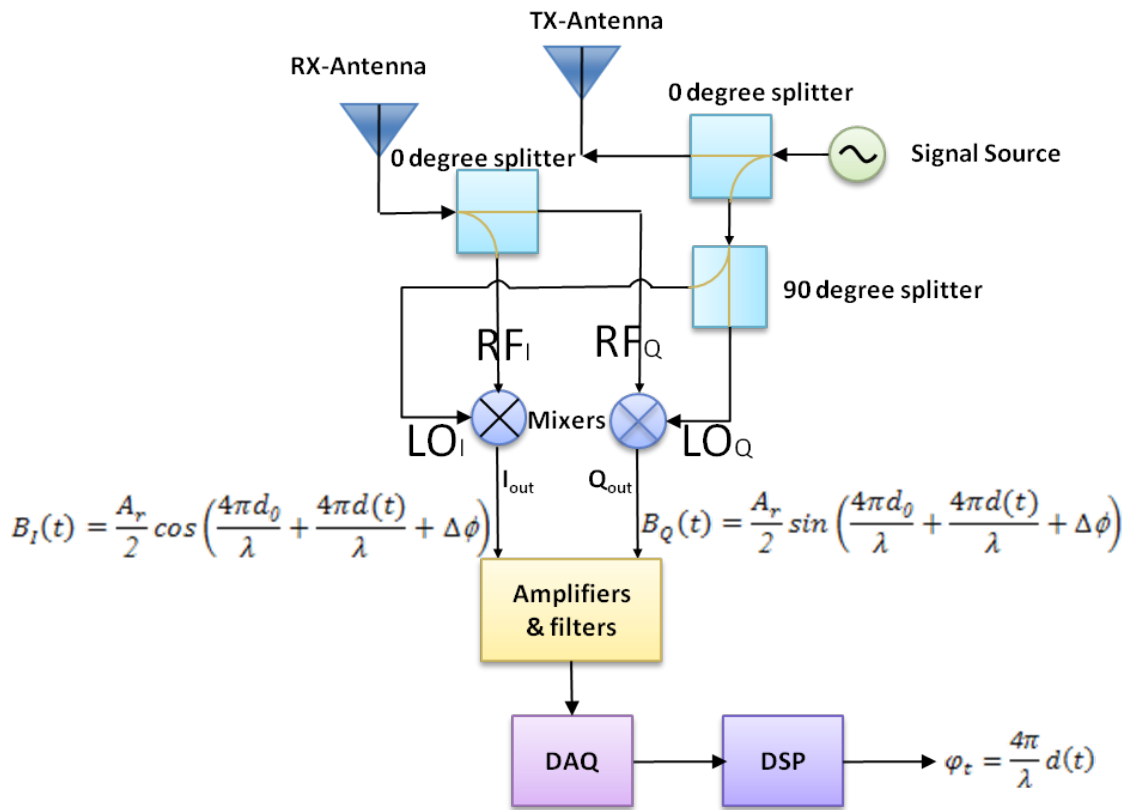


Fig. 2.9 A quadrature Doppler transceiver architecture, in which two receiver chains are 90° out of phase.

As shown in Fig. 2.9, two mixers are used to produce baseband outputs in parallel. The inputs for the two mixers are the transmitted signal generated with Local Oscillator (LO) and the reflected signal received by the receiving antenna. The LO signal

passes a 0° splitter, and then half of it splits again to feed the two mixers. The outputs of the second splitter have a 90° phase difference with each other. The Q-channel goes through a 90° phase-shift and is then mixed with the received signal to generate the quadrature channel output. The I-channel output is in phase with the incoming signals. The two outputs for I-channel and Q-channel can be described individually as:

$$B_I(t) = \frac{A_r}{2} \cos\left(\frac{4\pi d_0}{\lambda} + \frac{4\pi d(t)}{\lambda} + \Delta\phi\right), \quad (2.40)$$

and,

$$B_Q(t) = \frac{A_r}{2} \sin\left(\frac{4\pi d_0}{\lambda} + \frac{4\pi d(t)}{\lambda} + \Delta\phi\right), \quad (2.41)$$

It is obvious from above two equations that if the subject is at the null point for one of the channels the other channel will be at the optimum point. Since there is always one channel at the optimum point, the reduced detection accuracy at a null point can be removed by using a quadrature receiver. At the same time, using a quadrature architecture with two receive chains means more complicated hardware, increased power consumption, and hence increased size, weight, and cost of the radar system. Moreover, to take advantage of complete information from both channels, it requires more complex signal processing compared with a single channel receiver to recover the full spectrum of the cardiopulmonary activities.

Use of the baseband output from a single channel receiver is straightforward. The single channel baseband output is essentially proportional to phase change and hence to the time-varying displacement due to cardiopulmonary activities of the subject. The baseband output data can be directly used for estimating heart and respiration rates with an Fast Fourier Transform (FFT). No further phase demodulation is required, nor possible in this case.

On the contrary, use of the baseband outputs from both I and Q channels requires more work to combine the information to obtain an optimum signal for further processing. This process is called demodulation. There are several known methods to demodulate the I and Q channels [9], [33].

A simple method is to monitor both channels, and select the better output from the two channels. If both channel outputs are comparably strong, simply add them together or

subtract them if I and Q channels have opposite signs. This linear operation of combining the two signals is called linear demodulation.

Another way to combine the I and Q baseband information is called non-linear demodulation. This method, instead of using the small angle approximation, involves calculating the phase directly with the following equation:

$$\varphi_t = \arctan\left(\frac{B_Q(t)}{B_I(t)}\right) = \arctan\left(\frac{\frac{A_r}{2}\sin\left(\frac{4\pi d_0}{\lambda} + \frac{4\pi d(t)}{\lambda} + \Delta\phi\right)}{\frac{A_r}{2}\cos\left(\frac{4\pi d_0}{\lambda} + \frac{4\pi d(t)}{\lambda} + \Delta\phi\right)}\right). \quad (2.42)$$

This method is also called arctangent demodulation [9]. In order for arctangent demodulation to yield desirable results, it is important to estimate the correct value of the signal DC component which has to be removed from the calculations before arctangent demodulation. The effectiveness of arctangent demodulation and its robustness against noise is discussed in [39]. Also, it is important to have perfectly balanced I and Q channels. Both channels have to have same gain/loss and phase shift in RF and baseband components. A survey of the effect of balance imperfections is given in [9].

2.2.4 Sensor Node with Air Coupling

In Doppler radar transceivers that use either single channel or quadrature receivers, the transmitter and receiver are wired together and hence usually physically near to each other. Recent research has shown a Doppler radar system capable of cardiopulmonary detection can be built using an inexpensive, commercially available and off-the-shelf radio units and passive sensor nodes as receivers [40, 41,42]. In [40], a passive sensor node used the RF signal transmitted by a baby monitor to detect heart beat rate. In [42], a radar with a receiver (sensor node), placed in the vicinity of the human subject, was proposed to overcome phase noise appearing in the baseband output due to the phase noise of source signal caused by unintended source movement. The origin of using a passive sensor node as receiver can be traced back to thoughts of making use of the ambient RF signals generated by existing electronic devices. The concept of using an existing telecommunication terminal with an RF transceiver and network connection to monitor human cardiopulmonary motion via Doppler effect was introduced in 2000 [43], and the feasibility demonstrated in 2002 and 2003 [44,45].

The operation of such a radar system with a sensor node is illustrated in Fig. 2.10. A sensor node consists of an antenna and a mixer. It receives both the direct signal from the transmitter, and the signal reflected from a human subject.

The transmitted signal from an ideal CW transmitter has a form shown in equation (2.30),

$$S_t(t) = \cos(\omega_0 t). \quad (2.43)$$

The RF signal received at the sensor node antenna will be the sum of partially transmitted signal and the reflected signal:

$$S_{nRF}(t) = A_t \cos\left(\omega_0 t - \frac{\omega_0}{c} R_{nt}\right) + A_r \left(\omega_0 t - \frac{\omega_0}{c} R_{tb} - \frac{\omega_0}{c} R_{bn}\right), \quad (2.44)$$

where R_{tb} is the time-varying distance of transmitter to the subject, R_{nt} is the distance of transmitter to the node, R_{bn} is the time-varying distance of the subject to the node, and A_t and A_r are the amplitude factor of the transmitted signal and reflected signal. If we neglect amplitude variations due to propagation loss, the baseband output can be produced by splitting $S_{nRF}(t)$ into two halves and passing the splitted signals through a mixer. The resulted baseband signal will have the form:

$$S_n(t) = A_t A_r \cos\left(\frac{2\pi}{\lambda}\right) (R_{tb} + R_{bn} - R_{nt}). \quad (2.45)$$

If the receive node is located close to the RF signal source, such that $R_{tb} \approx R_{bn}$ and R_{nt} is neglected when compared to R_{tb} and R_{bn} , a similar base-band signal expression to equation (2.34) will be obtained:

$$S_n(t) = A_t A_r \cos\left(\frac{2\pi}{\lambda} 2R_{tb}\right). \quad (2.46)$$

The above equation suggests that Doppler radar operation principal with a passive sensor node is eventually as same as the one using single channel receiver. Therefore, this radar system shares the same advantages and disadvantages with radar systems using a single channel receiver architecture. However, due to its nature, this architecture has some extra benefit, including sensing without access to the signal source, and that it potentially can perform energy harvesting with ambient RF sources due to its similar

structure to rectanna, a rectifying antenna that is used to convert RF energy into direct current electricity.

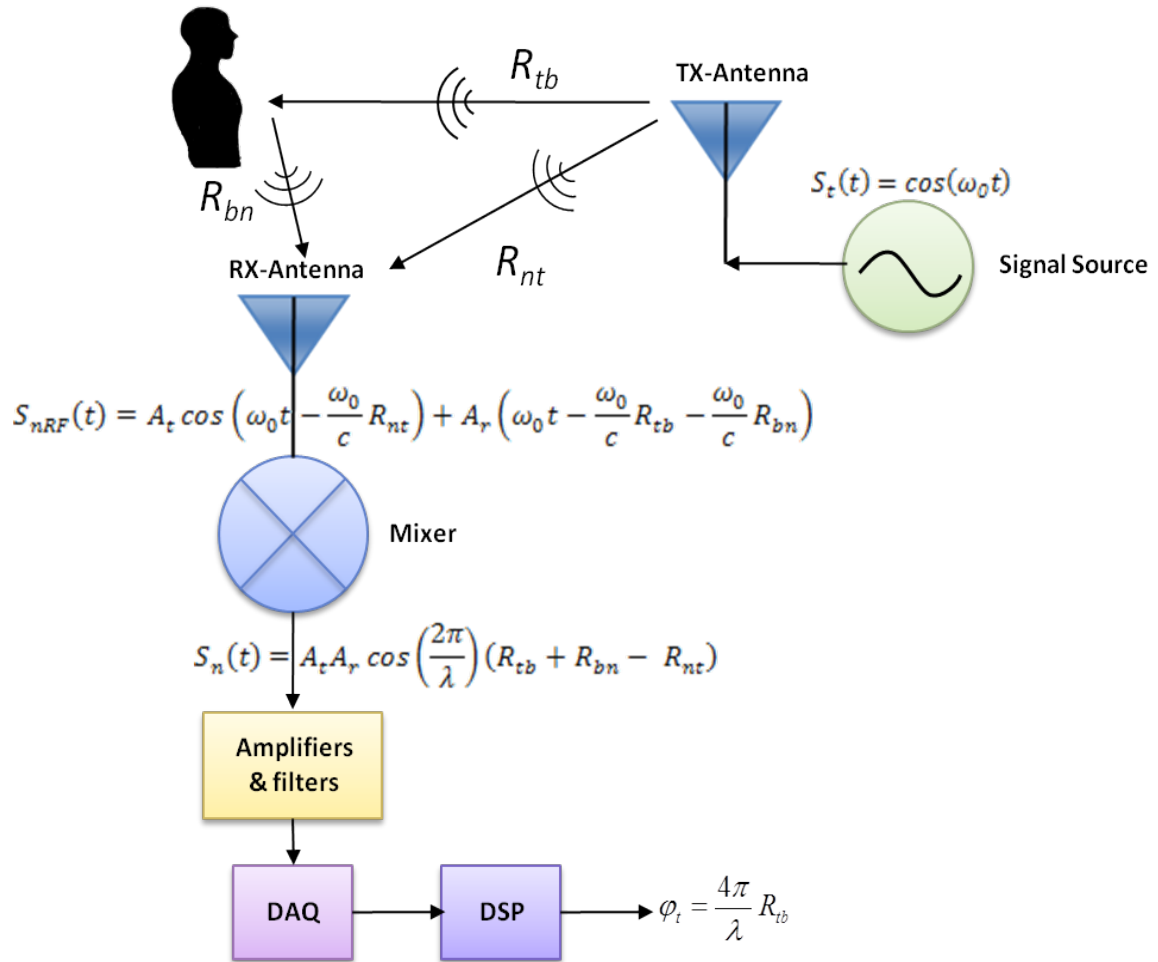


Fig. 2.10 A Doppler radar system with passive sensor node.

Chapter 3 Doppler Radar Occupancy Sensor Hardware Design

A Doppler radar transceiver performs the sensing function in this research. A radar system transmits a radio wave signal and receives a motion-modulated signal reflected from a target. The reflected RF wave from a moving surface undergoes a frequency shift that is proportional to the surface velocity. If the surface is moving periodically and the movement is small compared to the radar carrier wavelength, such as the chest of person breathing or a heart beating, this can be characterized as a phase shift proportional to the surface displacement. A circuit that couples both the transmitted and reflected waves to a mixer can produce an output signal with a low-frequency component that is directly proportional to the movement.

The goal of this dissertation is to develop a Doppler radar-based occupancy sensor that improves upon existing sensor types to meet the needs of smart buildings, such as low-cost, low-power consumption, high intelligence, reduced privacy concerns over camera-based systems, decreased rates of false-positive alarms, and the ability to detect stationary/sleeping persons.

In order for a Doppler radar cardiopulmonary sensing system to become possible in such applications, the research carried out in this dissertation is directed towards achieving the integration of sensing, computation and wireless communication. This is done by adding a low-cost, passive sensor node to an integrated microprocessor/RF-transceiver SoC platform, to build a smart sensor unit.

Fig. 3.1 shows the block diagram of the occupancy sensor, which has been proposed in this dissertation. The transceiver in the SoC is used both as the signal source of Doppler radar, and for wireless communication. The passive sensor node senses the respiration and heart beat rate by listening to the RF signals both directly from the SoC transmitter and the echoes reflected by the subjects. The sensed signal after filtering and amplification will be fed to an A/D converter in the microprocessor, to produce a digital value to use by the processor. The processor performs signal processing on the data and

sends the resulting data to the RF transmitting channel. By processing data locally at the node, only the minimum amount of data is sent out to the network, minimizing the power requirement for wireless communication. In addition the bandwidth required to support each node decreases dramatically, and as a result more sensor nodes can reside in the network.

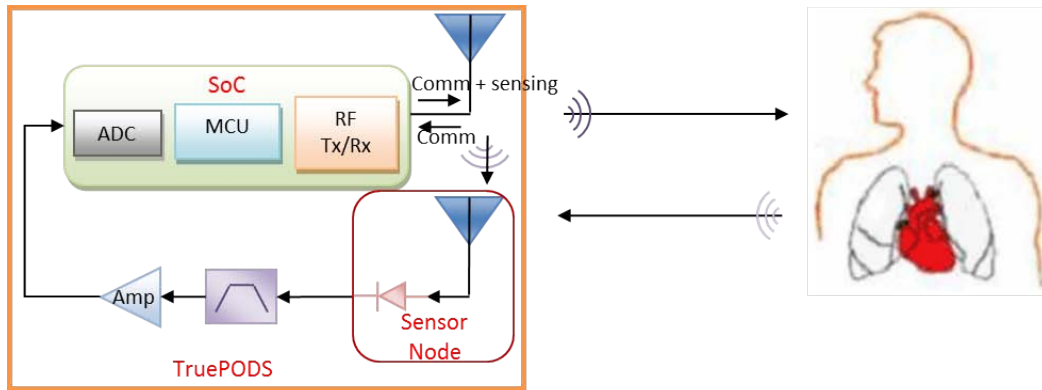


Fig. 3.1 The main components of a Doppler radar based occupancy sensor integrated with off-the-shelf SoC and passive sensor node.

The Doppler radar occupancy sensor platform consists of two cores – a low-cost passive sensor node, and an off-the-shelf, low-power SoC platform which includes microcontroller, RF transceiver and peripherals. The passive sensor node and the RF part of the SoC serves a cardiopulmonary sensing Doppler radar. The detected physiological signals will be pre-processed and stored for short periods of time in the memory of the SoC. Periodically this data is sent via a wireless link to other components in a wireless smart sensor networks (WSSN), such as a base station.

To perform those functions, the SoC must be low cost and compact, offer low power consumption, have enough processing capability to handle DSP and routing, and provide enough RF transmitting power for cardiopulmonary activity detection at reasonable working distance. Commercial available SoCs, such as CC2530 and CC430, products of Texas Instrument have been chosen in this research. The passive sensor node should be able to convert the received RF signal into a baseband signal containing human cardiopulmonary activity information. A mixer is the RF component to implement such conversion. In this dissertation, to test the feasibility of building the Doppler radar occupancy sensor with SoC and passive node, the passive node is built with a commercial

available antenna and mixer. The following two sections will discuss the selected SoCs and the occupancy sensor, which constitutes the passive sensor node made with cable components and those SoCs, respectively. A broadband mixer is designed and tested for future use. It is included in the third section of this chapter.

3.1 System on Chip (SoC)

A system on chip (SoC) is an integrated circuit (IC) that integrates a variety of functional hardware blocks to suit a specific product application in a single chip. It may contain digital, analog, mixed-signal, and/or radio-frequency functions—all on a single chip substrate.

SoC technology has been used by integrated device manufacturers (*e.g.* Intel, AMD and, Samsung, *etc.*), fabless vendors (*e.g.* Apple, Qualcomm, Broadcom, *etc.*) and foundries (*e.g.* TSMC, UMC, TI, *etc.*) for well over a decade. But the rapid proliferation of mobile products in recent years makes this technology to finally realize its full potential. Critical drivers in the mobile market – form-factor, cost and power, for a given function, has increased the importance of on-chip integration of functional hardware (*e.g.* power management, computing, audio/video, graphics, GPS and radio) [46]. Instead of mostly performance-centric chips, the customers and product vendors shift their focus on mostly power-constrained chips, by lowering cost and increasing system-level integration.

A typical SoC consists of:

- A microcontroller, microprocessor or DSP core(s). Some SoCs include more than one processor core.
- Memory blocks, including a selection of ROM, RAM, EEPROM and flash memory.
- Timing sources, including oscillators and phase-locked loops.
- Peripherals, including counter-timers, real-time timers and power-on reset generators.
- External interfaces, including industry standards such as USB, FireWire, Ethernet, USART, or SPI.

- Analog interfaces, including ADCs and DACs.
- Voltage regulators and power management circuits.
- Some SoCs include RF transceiver for wireless functions.

Due to their low cost, low power consumption and high level of integration, the CC2530 and CC430 components from TI containing microprocessor and RF transceiver have been chosen to construct the proposed Doppler radar occupancy sensor conjunction with the passive node.

3.1.1 CC2530

The CC2530 [47] is a true system-on-chip (SoC) solution for IEEE 802.15.4, Zigbee and RF4CE applications. The CC2530 enables the proposed Doppler radar occupancy sensor in this dissertation to be built with very low total bill-of-material costs, by combining many powerful features, such as high performance RF transceiver with an industry-standard, enhanced 8051 MCU, in-system programmable flash memory, and 8-KB RAM. The CC2530 has various operating modes, making it highly suited for achieving the goal of an occupancy sensor with low power consumption. Short transition times between operating modes further ensures low energy consumption.

Fig. 3.2 illustrates the main function blocks of CC2530 [47], which enable this chip to perform many important functions:

- 2.4-GHz IEEE 802.15.4 compliant RF transceiver with programmable output power up to 4.5 dBm
- A compact 6-mm × 6-mm QFN40 package to be laid out with very few external components
- Low power operation modes, with the current consumption from 0.4 μ A at Power Mode 3 (external interrupts) to 29 mA in active transmitting, using a broad 2V – 3.6V voltage supply range
- High-performance and low-power 8051 microcontroller with up to 256-KB in-system-programmable flash and 8-KB RAM
- Various useful peripherals, including a 12-bit ADC, with eight channels and configurable resolution, integrated high-performance Op-Amp and

ultralow-power comparator, battery monitor and temperature sensor, two powerful UARTs with support for several serial protocols, and 21 General-Purpose I/O Pins, *etc.*

Due to these features, CC2530 has been extensively used in home and building automation, lighting systems, industrial control and monitoring, low-power wireless sensor networks, consumer electronics, and health care. However, it is the first time that this research uses it in a Doppler radar cardiopulmonary motion monitoring system to make the system more compact, lower cost, with low power consumption, and eventually fit into occupancy sensor application.

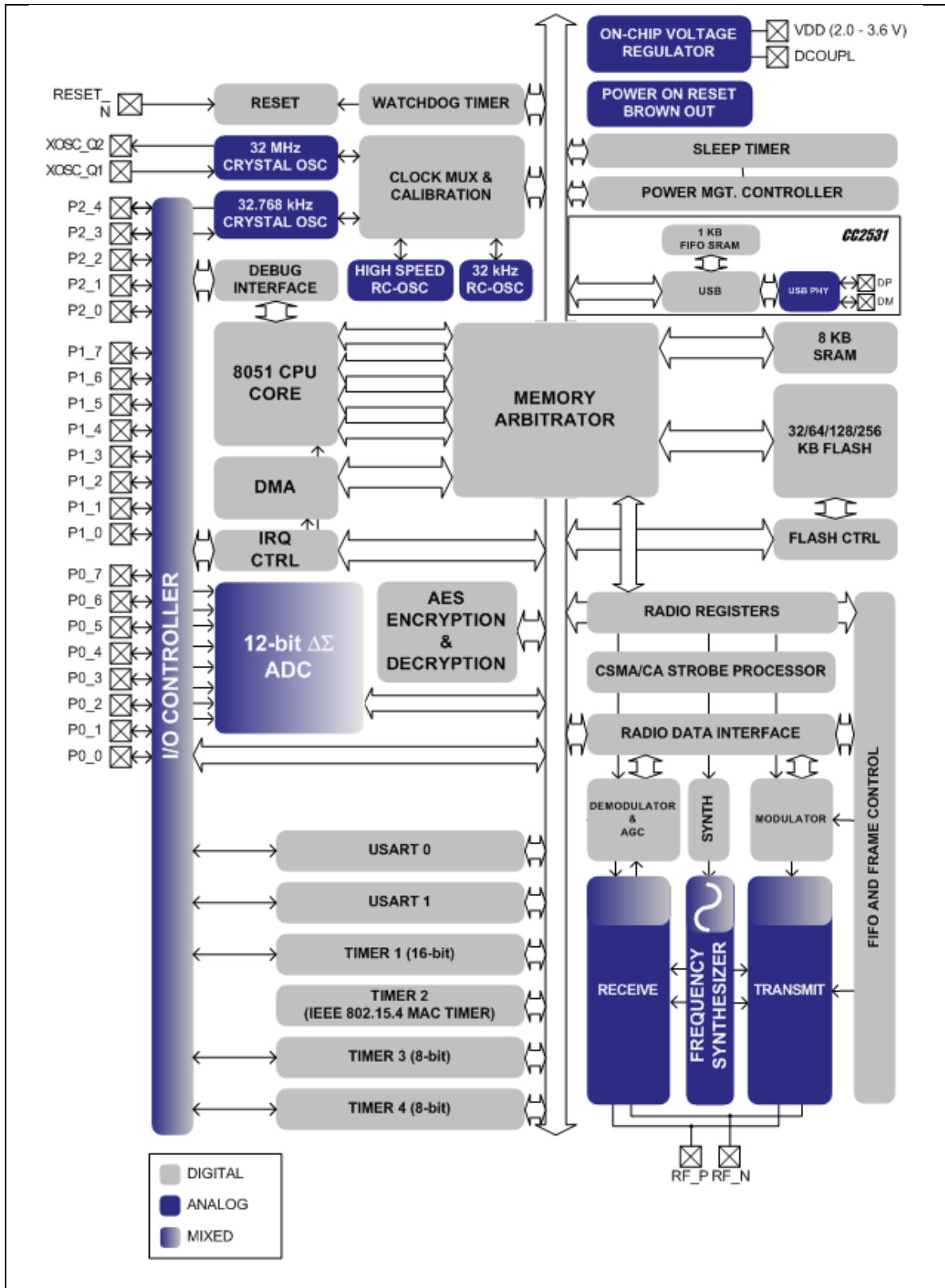


Fig. 3.2 CC2530 function blocks, including MCU, RF function block, and various useful peripherals [47].

3.1.2 CC430

The CC430 [48] family devices include the ultralow-power microcontroller MSP430 integrated with the CC1101 RF transceiver cores, and different sets of intelligent peripherals, targeted for a wide range of applications, all within a compact quad-flat no-lead (QFN) package. The number of pins and package size varies depending on the devices. The unit features 128-bit security encryption and 433-, 865-, and 915-MHz communications, the last two of which are user-selectable. The architecture, combined with seven low-power modes, is optimized to achieve extended battery life in portable measurement applications. Device features include powerful MSP430™ 16-bit RISC CPU, 16-bit registers, and constant generators that contribute to maximum code efficiency. According to TI, the MSP430 is the industry's lowest power-dissipation MCU. It operates from 2.2 to 5.5 V and dissipates a mere 330 μA (at 3 V and 1 MHz). In the standby mode, current drain is only 0.1 μA . Fig. 3.3 is the example of the CC430 family, CC430F614x [49].

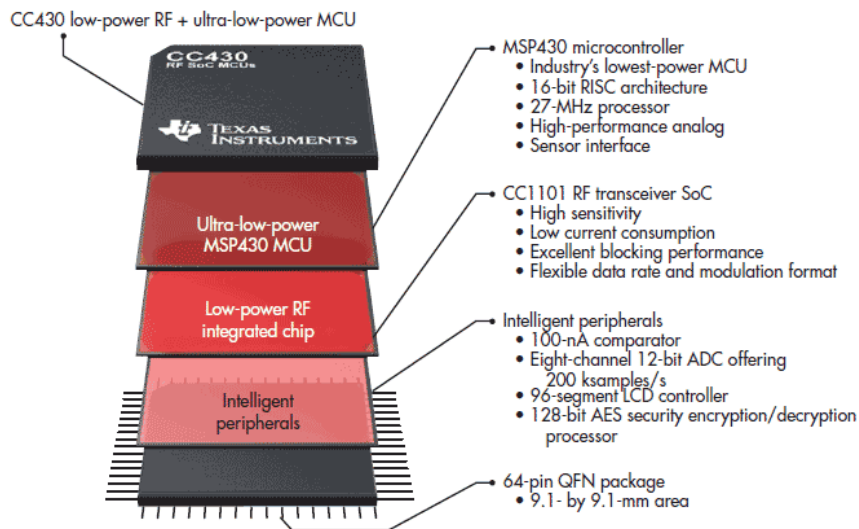


Fig. 3.3 The main components of CC430F614x [49], including MSP430 MCU, CC1101 transceiver, and intelligent peripherals.

The CC 430 makes these true system-on-chip solutions easy to use, as well as improving performance. Typical applications for these devices include wireless analog and digital sensor systems, heat cost allocators, thermostats, metering (AMR, AMI), smart grid wireless networks [48], *etc.* In this dissertation, This SoC is used to build the

proposed Doppler radar occupancy sensor due to its ultralow power consumption and high-level system integration.

3.2 Doppler Radar Occupancy Sensor Built with CC2530 and CC430

In this research, two proposed Doppler radar occupancy sensors are configured. One uses the CC 2530 [50], and the other the CC430. Both comprise the same passive sensor node composed of a receive antenna, coaxial splitter and mixer. The performance of these two occupancy sensors will be discussed in detail, respectively, in what follows.

3.2.1 Doppler Radar Occupancy Sensor with the CC2530

In this section, a TI CC2530 is used to build a Doppler radar occupancy sensor with a passive node. The CC2530 has 16 non-overlapping channels with 5 MHz apart. The center frequencies for these channels are defined by IEEE 802.15.4 [47, 51], beginning at 2.405 GHz and ending at 2.480 GHz. This chip has various operating power modes, making it suited for systems where low power consumption is considered. The CC2530 output power can be programmed from -22 dBm up to +4.5 dBm. At each power level, the CC2530 can transmit signals in one of the following three modes: (1) Continuous Wave (CW) Mode, (2) Modulated Continuous Wave (CW) Mode, and (3) Packet Mode (sending out packet signals in IEEE 802.15.4 frame format).

The CC2530 adopts the direct sequence spread spectrum (DSSS) modulation format defined in IEEE 802.15.4 [51] in both modulated CW mode and packet mode. The DSSS process is performed by a double-balanced mixer to multiply an RF carrier and a pseudo-noise (PN) modulated information signal by offset – quadrature phase shift keying (O-QPSK) [47]. This process causes the RF signal to be replaced with a very wide bandwidth signal with the spectral equivalent of a noise signal. The repetition period of the PN modulated data is 262.14ms.

3.2.1.1 Experiment Setup

As shown in Fig. 3.4, a mechanical target with moving displacement of 1 cm and rate of 0.2 Hz which emulates human respiration (in general, rate of 0.1-0.3 Hz and 0.5-2 cm in chest wall vertical displacement [9]) was used as the subject. RF signals reflected

from the subject are phase modulated by subject periodic motion. Phase demodulation can be performed using a simple mixing device that uses part of the Tx signal as the local oscillator (LO) power. In this experiment, the TI CC2530 provides both the LO (direct path) and RF signals (reflected from the subject), coupled through the air to the sensor node, and sensor node performs phase demodulation, before the signal is digitized for further analysis (movement rate extraction) using offline software.

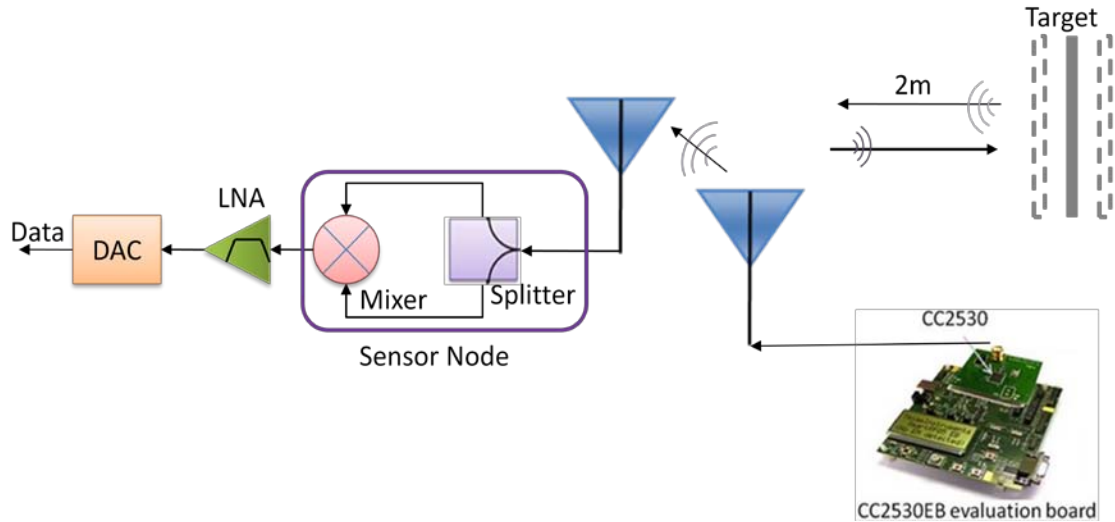


Fig. 3.4 Diagram of a Doppler Radar occupancy sensor using CC2530 and a passive sensor node.

The tests were performed using three waveforms generated by the CC2530 transmitter: CW, modulated CW, and packet modes. Testing was conducted at Channel 11, with a center frequency 2.405 GHz, for all three transmitting modes at the output power of +4.5 dBm. The same passive node and post processing were used for all three waveforms. In all tests, the transmitter and sensor node were located 2m from the subject. Fig. 3.4 shows the arrangement of the test system: CC2530, subject, and node. The CC2530 and node were placed in close proximity to each other to provide a strong reference signal for the node to use as a LO. The sensor node used for receiving and demodulating the radar signal is composed of a Minicircuits splitter (ZFSC-2-2500) and mixer (ZFM4212). A 60° Antenna Specialist patch antenna (ASPPT2988) was used in conjunction with the node. The signal received at the antenna, consisting of direct path signal from the transmitter, and the signal reflected from the target, is split equally to feed the mixer LO and RF ports. The signal from the sensor node output was passed through a

Stanford Research System Model SR560 Low Noise Amplifier for amplification and filtering, before digitization with a NI USB-6259 data acquisition (DAQ) module. The sensor node output, *i.e.* the baseband signal, is amplified by a factor of 500, and subjected to a 6 dB/octave band-pass filtering between 0.03 Hz and 30Hz, for CW and modulated CW inputs, and between 0.03 Hz and 1 kHz, for packet mode to remove DC offset and keep the enough information for further Matlab analysis.

3.2.1.2 Experiment Result

Raw data digitized with DAQ were recorded and processed with Matlab. FFT after low pass filtering was applied to the signals obtained through CW mode and modulated CW mode to find the motion rate of the mechanical target. Fig. 3.5 and Fig. 3.6 show the original and processed data for CW and modulated CW mode, respectively. In both figures, (a) shows the digitized data using NI DAQ, (b) data filtered by FIR low pass filter with cutoff frequency of 2 Hz, and (c) shows motion rate of 0.3 Hz for the periodically moving mechanical target, calculated with an FFT.

Data processing in packet mode is different from the other two modes, which is described in [52]. The raw data first was fed into a local maximum algorithm [52] to find the peak value of pulses and the time at which they occur. Then cubic spline interpolation technique was employed to space the data evenly in time domain since the extracted peaks are not distributed evenly with time. Finally FFT was applied to the reconstructed data to calculate the motion rate of the target. The algorithm to find the target periodic moving rate is illustrated in Fig. 3.7. Fig. 3.8 is the processed result after applying the algorithm in Fig. 3.7. Fig. 3.7(a) shows the raw data and the peaks which are detected by the local maximum algorithm. Fig. 3.7(b) illustrates the result interpolated with spline method. Fig. 3.7(c) shows periodic movement rate of the mechanical target is 0.2 Hz using FFT analysis. The experimental results indicate that in all operation modes, the Doppler radar occupancy sensor using a CC2530 and a passive sensor node can accurately detect the target motion.

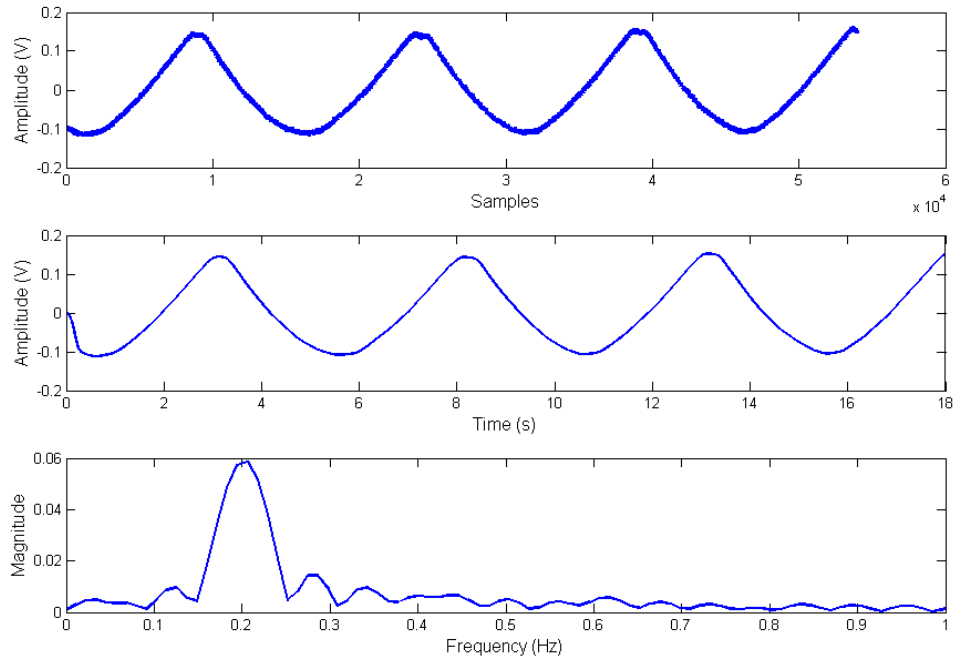


Fig. 3.5 CW mode measurement results at an output power +4.5 dBm: (a) raw data, (b) digital low pass filtered data, and (c) FFT analyzed result: periodic motion rate of the mechanical target at 0.2 Hz.

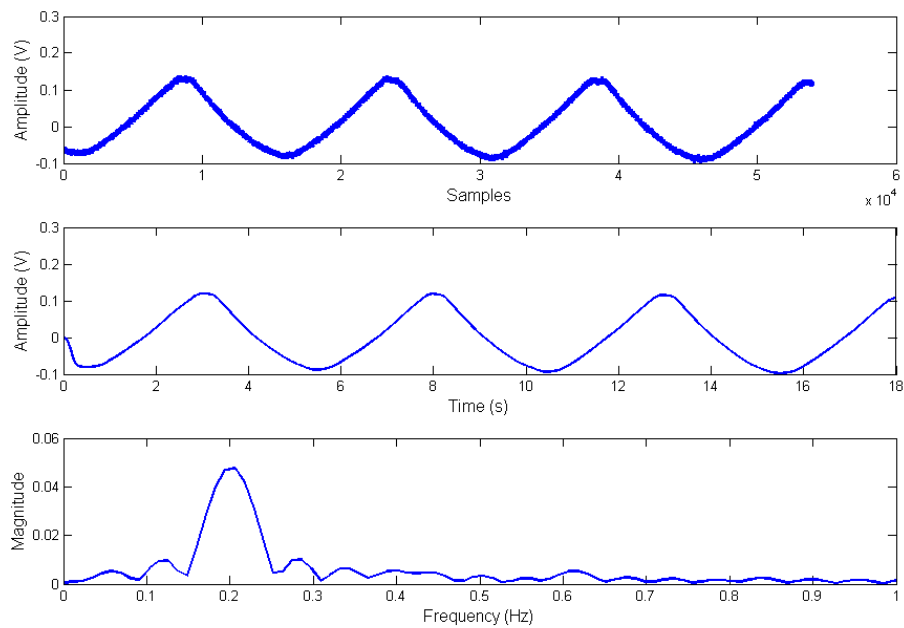


Fig. 3.6 Modulated CW mode measurement result at output power 4.5 dBm: (a) raw data, (b) digital low pass filtered data, and (c) FFT analyzed result: periodic motion rate of the mechanical target at 0.2 Hz.

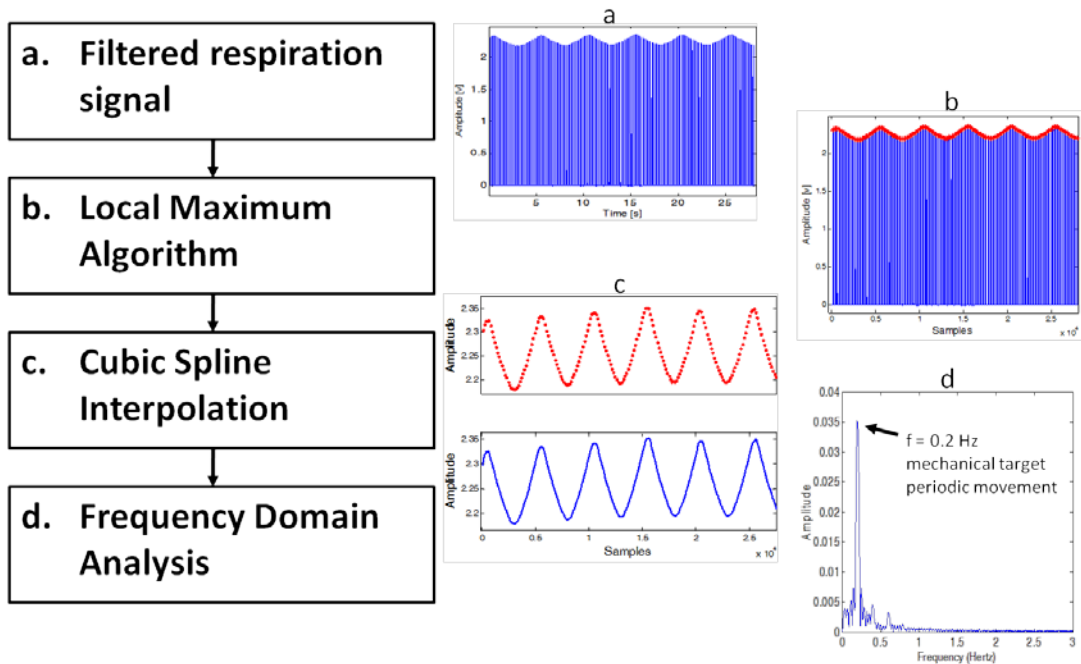


Fig. 3.7 Algorithm for extracting the target motion rate in packet transmitting mode.

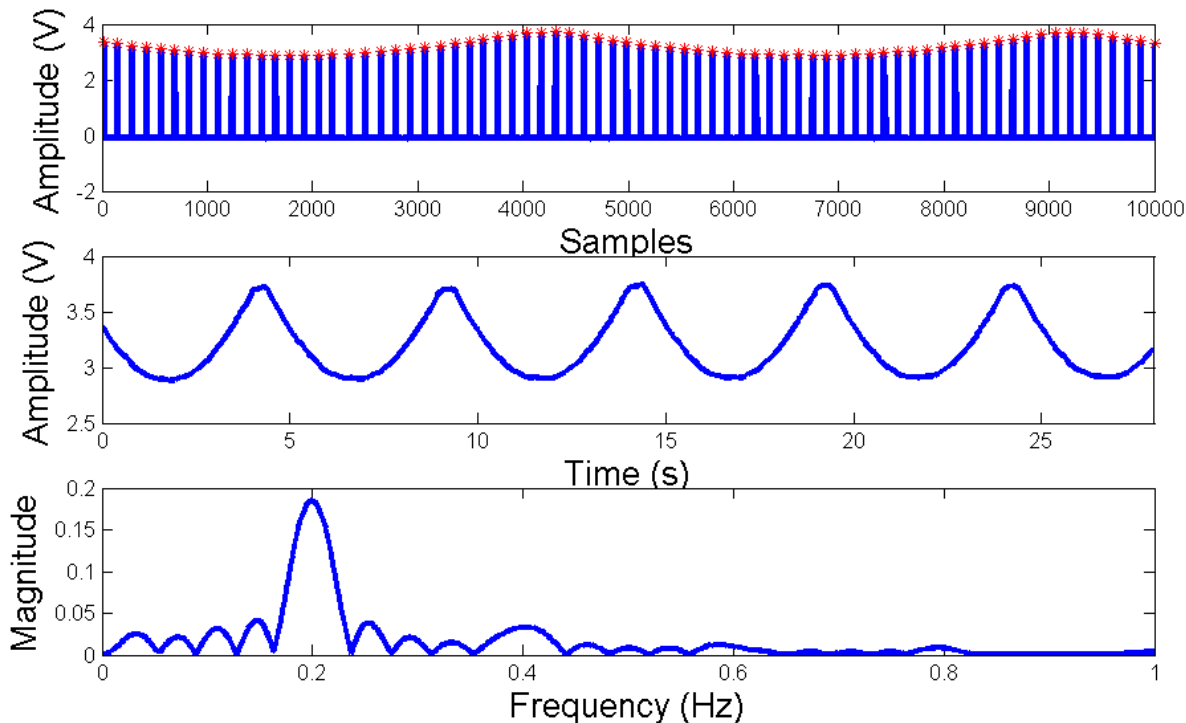


Fig. 3.8 Packet mode measurement result at an output power +4.5 dBm: (a) raw data (only show 10000 samples) with detected peaks marked with red star; (b) peaks interpolated with spline technique; (c) FFT analyzed result: periodic motion rate of the mechanical target at 0.2 Hz.

3.2.2 Doppler Radar Occupancy Sensor with the CC430

In this section, the CC430 replaces CC2530 to build the Doppler radar occupancy sensor. The CC430 is a commercially available SoC solution for sub-1GHz, ultralow-low power, low-cost wireless applications. It offers various sub-1GHz ISM bands, including 300-348 MHz, 389-464 MHz, and 779-928 MHz [48]. This chip has five low-power operation modes, and hence it is well suited to low-power consumption applications. The output power of the CC430 can be programmed up to +12 dBm at all support frequencies. At each power level, the CC430 can transmit signals with the three modes studied earlier in section 3.2.1. The modulation schemes for both modulated CW mode and packet mode include binary frequency-shift keying (2FSK), binary Gaussian frequency-shift keying (2GFSK), minimum-shift keying (MSK), on-off keying (OOK) and flexible amplitude-shift keying (ASK) shaping [48].

3.2.1.1 Experiment Setup

The experiment shown in Fig. 3.4 was rebuilt with CC430 to replace CC2530 as radar signal source and a new passive node with the working frequency range compatible with the CC430, resulting in the new occupancy sensor system, as shown in Fig.3.9. The same mechanical target with same programmed movement – displacement of 1 cm and rate of 0.2 Hz was put 1 m from the radar sensor. The CC430 and node were placed in close proximity to each other, to provide a strong reference signal for the node to use as a LO. The sensor node used for receiving and demodulating the radar signal is composed of a Minicircuits splitter (ZFSC-2-2500) and mixer (ZFM-12). An Omni-directional antenna coming with CC430 evaluation board was used in conjunction with the node. The signal received at the antenna, consisting of direct path signal from the transmitter, and the signal reflected from the target, is equally divided by the splitter to feed the mixer LO and RF ports. The signal from the sensor node output was passed through a Stanford Research System Model SR560 Low Noise Amplifier for amplification and filtering, before digitization with a NI USB-6259 DAQ.

The tests were performed with seven waveforms generated by the CC430 transmitter – CW, three modulated CW, and three packet modes employing the same modulation with the modulated CW modes. Due to the software limitation, only 2FSK,

2GFSK, and MSK modulation schemes were applied in this research. The testing was conducted at a carrier frequency of 868 MHz for all three transmitting modes, at the output power of 10 dBm.

The sensor node output, *i.e.* the base band signal, is amplified by a factor of 500, and subjected to 6 dB/octave band-pass filtering between 0.03 Hz and 30Hz for CW and modulated CW inputs, and between 0.03 Hz and 3 kHz for packet mode to remove DC offset and keep the enough information for further Matlab analysis.

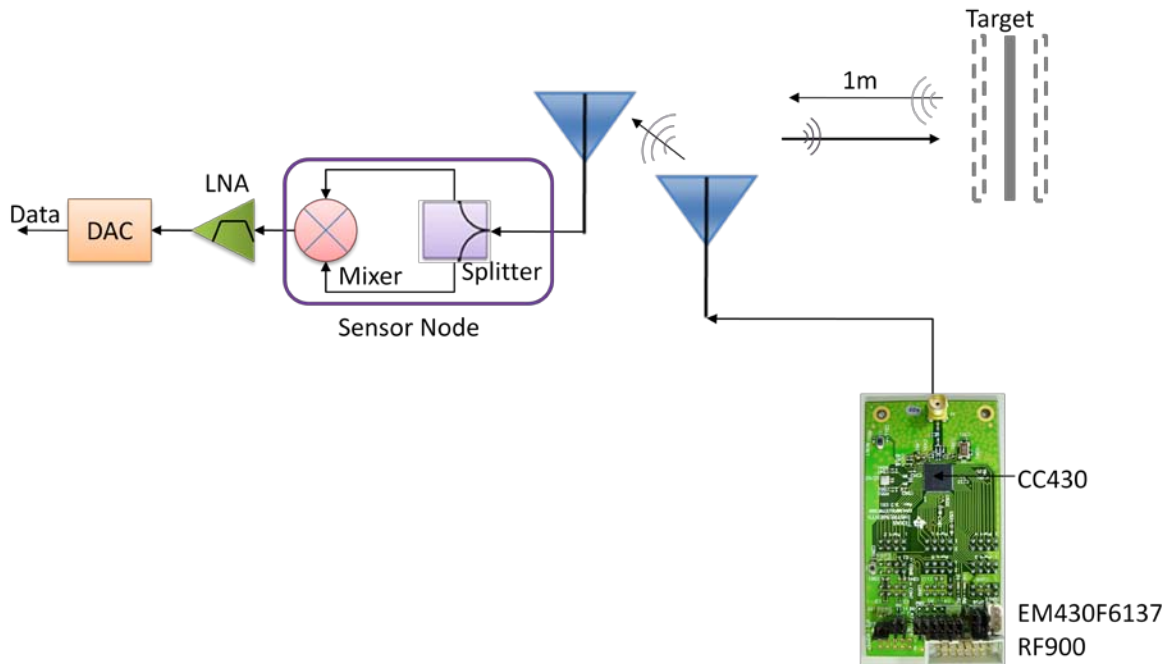


Fig. 3.9 Diagram of Doppler Radar occupancy sensor system using the CC430 and passive sensor node.

3.2.2.1 Experimental results

Raw data digitized with NI DAQ were recorded and processed with Matlab. After low pass filtering the digitized data, FFT was applied to the signals obtained through CW mode and modulated CW mode to find the motion rate of the mechanical target. Fig. 3.10 shows the original data and processed data for CW mode: (a) shows the digitized data using NI DAQ, (b) data filtered by a FIR low pass filter with cut-off frequency of 2Hz, and (c) shows motion rate of 0.2 Hz for the periodic moving mechanical target, calculated using an FFT. Similarly, the data for 2FSK, 2GFSK and MSK modulated CW mode are shown in Fig. 3.11, Fig. 3.12 and Fig. 3.13, respectively. Applying the algorithm

described in Fig. 3.7, the data for the three packet modes with 2FSK, 2GFSK and MSK modulations are also showed in Fig. 3.14, Fig. 3.15 and Fig. 3.16, respectively. Inset (a) shows the raw data and peaks which are detected by the local maximum algorithm, (b) illustrates the result interpolated with spline method, and (c) shows periodic movement rate of the mechanical target is 0.2 Hz using frequency domain analysis.

The experimental results indicate that although using in different frequency ranges and applying different modulation schemes, the Doppler radar sensors built with the CC430 and a passive sensor node can accurately detect the target motion, as the one built with the CC2530.

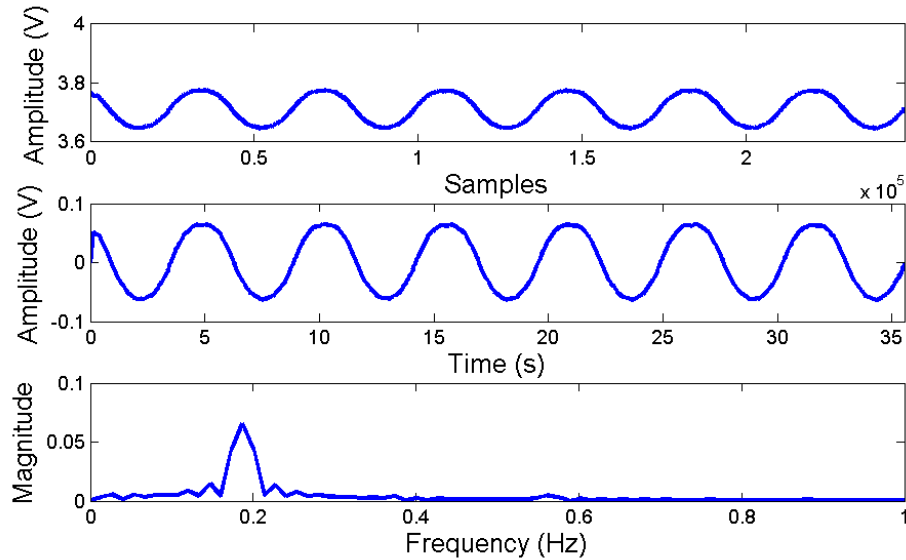


Fig. 3.10 CW mode measurement result at an output power +10 dBm and frequency of 868 MHz. (a) raw data, (b) digital low pass filtered data, and (c) FFT analyzed result: periodic motion rate of the mechanical target at 0.2 Hz.

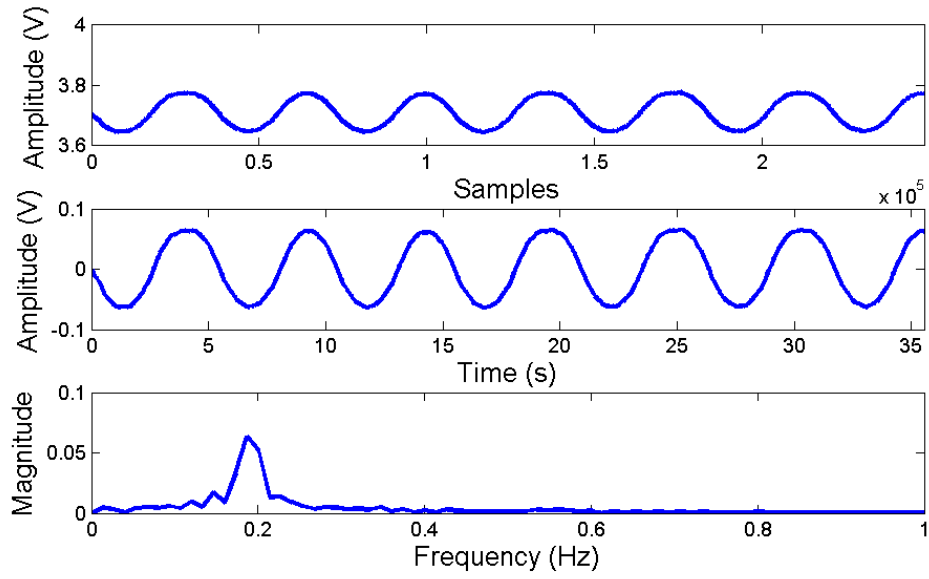


Fig. 3.11 Measurement result for 2FSK modulated CW mode at an output power +10 dBm and carrier frequency of 868 MHz. (a) raw data, (b) digital low pass filtered data, and (c) FFT analyzed result: periodic motion rate of the mechanical target at 0.2 Hz.

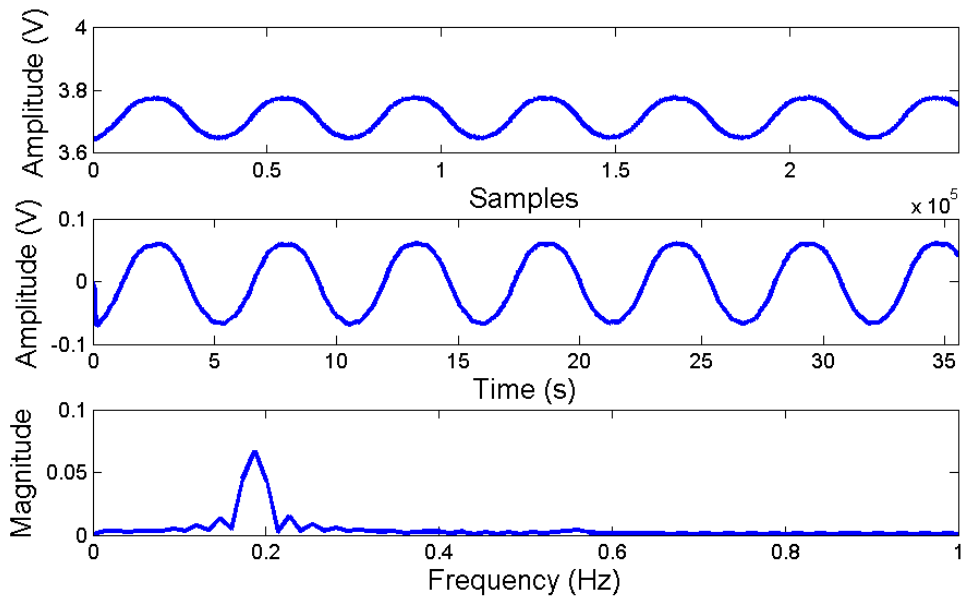


Fig. 3.12 Measurement result for 2GFSK modulated CW mode at an output power +10 dBm and carrier frequency of 868 MHz. (a) raw data, (b) digital low pass filtered data, and (c) FFT analyzed result: periodic motion rate of the mechanical target at 0.2 Hz.

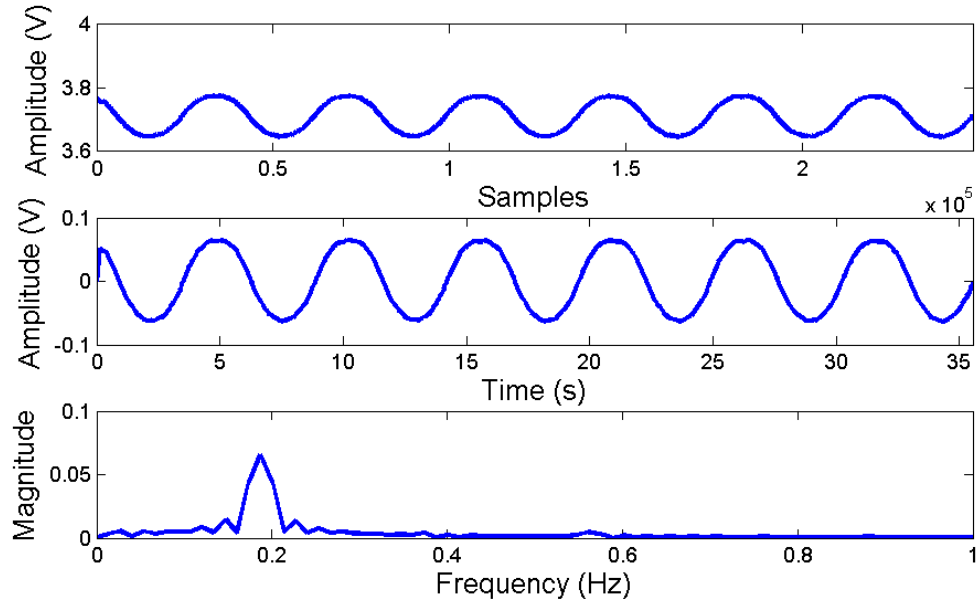


Fig. 3.13 Measurement result for MSK modulated CW mode at an output power +10 dBm and carrier frequency of 868 MHz. (a) raw data, (b) digital low pass filtered data, and (c) FFT analyzed result: periodic motion rate of the mechanical target at 0.2 Hz.

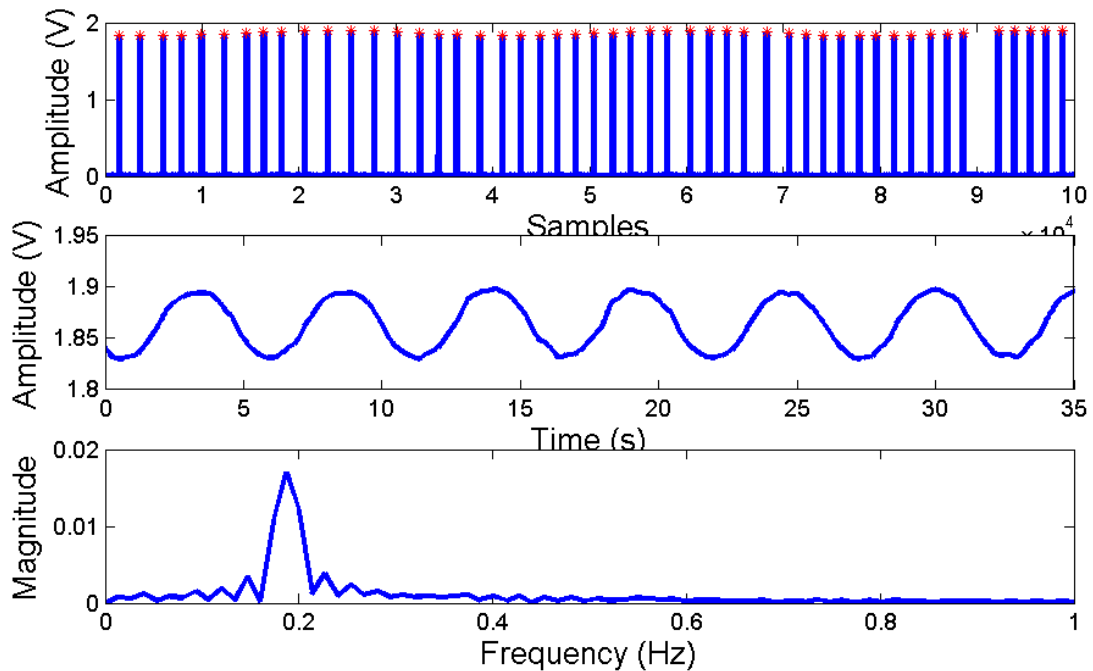


Fig. 3.14. Measurement result for 2FSK Packet mode at an output power +10 dBm and carrier frequency of 868 MHz. (a) raw data with detected peaks marked with red star; (b) peaks interpolated with spline technique; (c) FFT analyzed result: periodic motion rate of the mechanical target at 0.2 Hz.

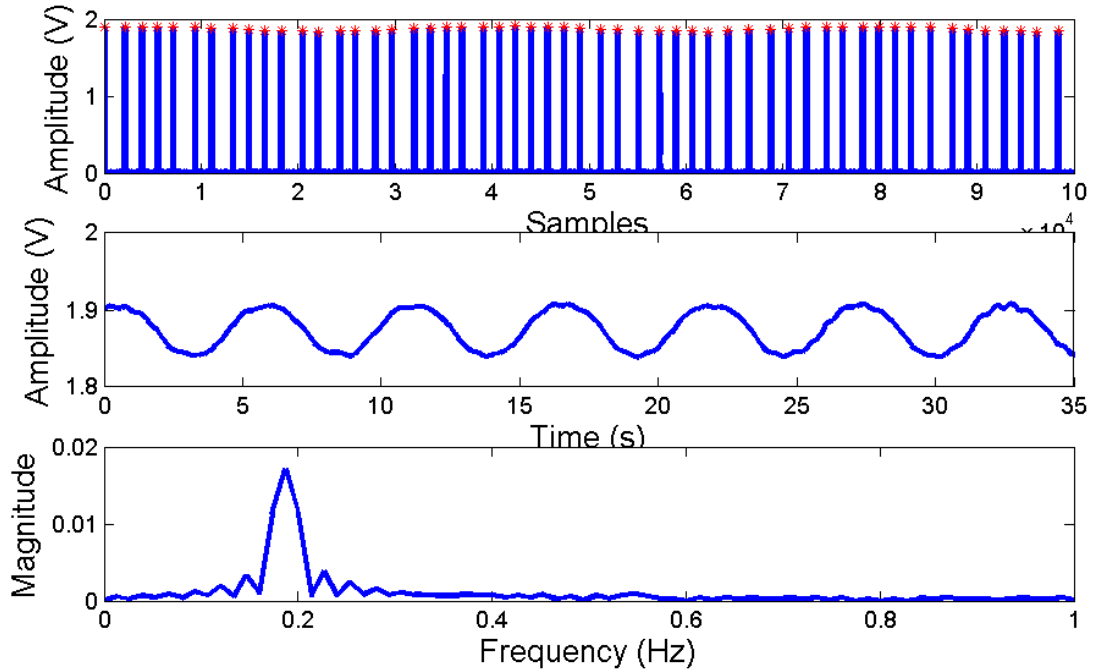


Fig. 3.15 Measurement result for 2GFSK Packet mode at an output power +10 dBm and carrier frequency of 868 MHz. (a) raw data with detected peaks marked with red star; (b) peaks interpolated with spline technique; (c) FFT analyzed result: periodic motion rate of the mechanical target at 0.2 Hz.

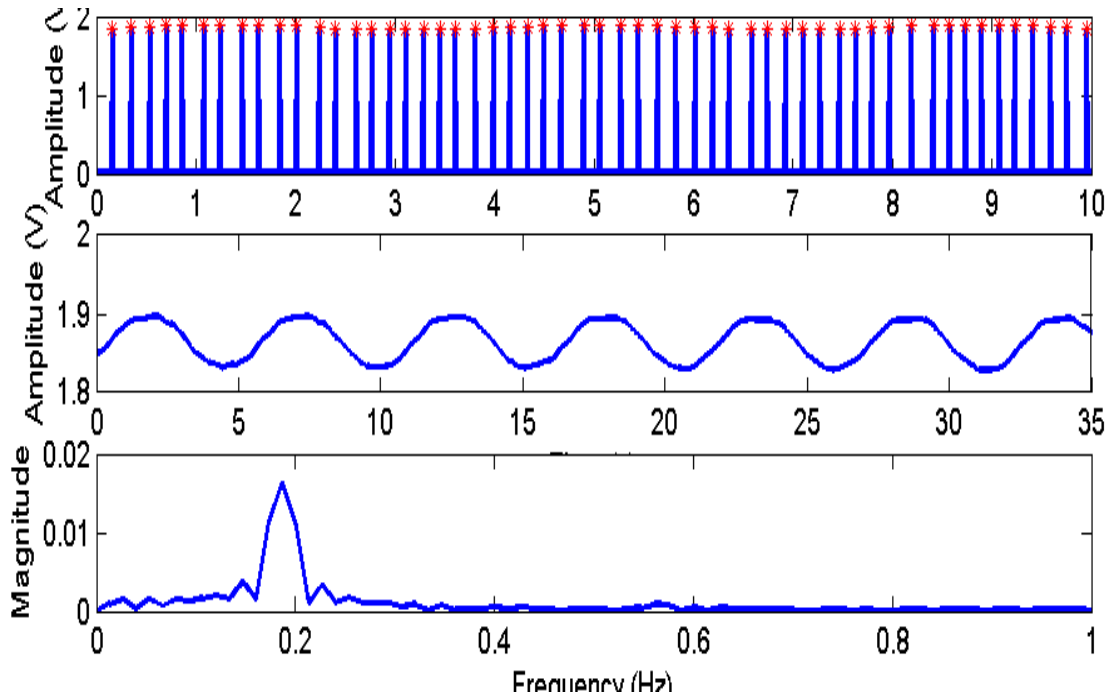


Fig. 3.16 Measurement result for MSK Packet mode at an output power +10 dBm and carrier frequency of 868 MHz. (a) raw data with detected peaks marked with red star; (b) peaks interpolated with spline technique; (c) FFT analyzed result: periodic motion rate of the mechanical target at 0.2 Hz.

3.3 CMOS Wideband Passive Mixers

One of the key building blocks of RF systems used for Doppler radar cardiopulmonary sensing is a frequency mixer. Most modern RF applications require low-cost, compact, and low power consumption mixers. Compared to the traditional “Gilbert Cell” circuit, a passive mixer [53] has the advantage of low Flicker noise and no power consumption, since it operates without DC bias current. A double balanced resistive mixer also exhibits inherent high linearity [54, [55], and it has been shown to be suitable for both homodyne and heterodyne wireless transceivers [56]. Most double-balanced mixers reported to date have been implemented using four MOSFET’s (mixer core) and additional passive elements for RF [57, 58,59], LO [57, 58], and IF matching [5959], and to improve LO efficiency [60]. These passive elements occupy significantly more space on the chip die than the mixer transistor core. In addition, typically, a double-balanced mixer configuration requires single-ended to differential transitions at the RF and LO ports, which are usually implemented off-chip [56] - [61], adding cost, size, and complexity. If used in direct down-conversion receivers, these mixers typically require DC cancellation circuitry to eliminate large DC offset [62, 63].

In this section, a fully integrated resistive mixer that uses baluns both for single-ended to differential conversion and impedance matching is described [64]. With RF and LO baluns integrated on chip, this passive mixer exhibits low conversion loss (CL), excellent linearity, as well as good RF and IF impedance matching, without any matching circuits. This mixer also presents the unique features of extremely low DC offset due to high LO to RF port isolation, and extremely broad bandwidth from single IF output due to the mirror orientation of balun ports at LO and RF inputs [65]. In addition, the mixer core itself is the first reported resistive mixer without any passive elements, and is the smallest double-balanced resistive mixer reported to date with the active chip area of 0.05 mm². Both mixers, the mixer core and the mixer with integrated baluns, were fully integrated in a 0.18μm BiCMOS process. The design process and measurement results for these two mixers are elaborated in the following sections.

3.3.1 Circuit design

The design considerations for the mixer core, balun, and the balun integration with the mixer core will be described in this section.

3.3.1.1 Mixer Core

A schematic of the mixer core circuit with four NMOS transistors in a ring configuration is shown in Fig. 3.17. This is a well-known double-balances resistive mixer configuration [54, 55], that results in high linearity and good port-to-port isolation. Resistive CMOS mixers use the time-varying channel resistance (R) to provide frequency conversion [53]. When the LO signal is applied to the gate, it modulates the depth of the depletion region, which changes the channel resistance (R) under the gate, making the transistor behave like a voltage controlled resistor. For a small drain to source voltage, the channel resistance can be expressed as [66]:

$$R = \frac{1}{\mu_n C_{ox} \frac{W}{L} (V_{gs} - V_{th})}, \quad (3.1)$$

where μ_n is electron mobility, C_{ox} gate oxide capacitance per unit area, W gate width, L gate length, V_{gs} gate to source voltage, and V_{th} threshold voltage. Channel resistance R is directly related to the impedance seen at the RF and IF ports. Since the mixer core structure is completely symmetric, and the same channel resistance is seen from both drain (IF) and source (RF) terminals, RF and IF reflection coefficients are expected to be very similar. Assuming that gate to channel capacitance is small, total resistance seen from either of these two ports will be approximately equal to:

$$R_{in} = R + 50 \Omega. \quad (3.2)$$

Therefore, the best impedance match and conversion loss (CL) can be expected for lowest channel resistance. As W/L increases, channel resistance will decrease. However, increased device size will also result in increased gate to channel capacitance, which may increase CL by providing capacitive feedthrough from LO to RF and IF ports.

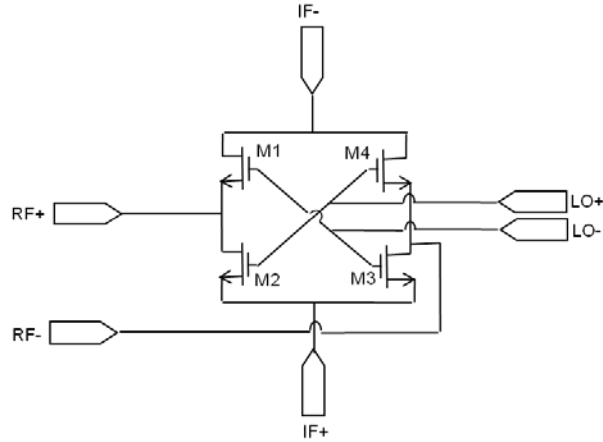


Fig. 3.17 Schematic of the mixer core - four NMOS transistors in ring configuration [54, 55].

The design parameter used in this design is the W/L ratio of NMOS transistors. The size of the NMOS device is chosen for the best CL, RF and IF impedance matching, and minimizing LO capacitive feed-through.

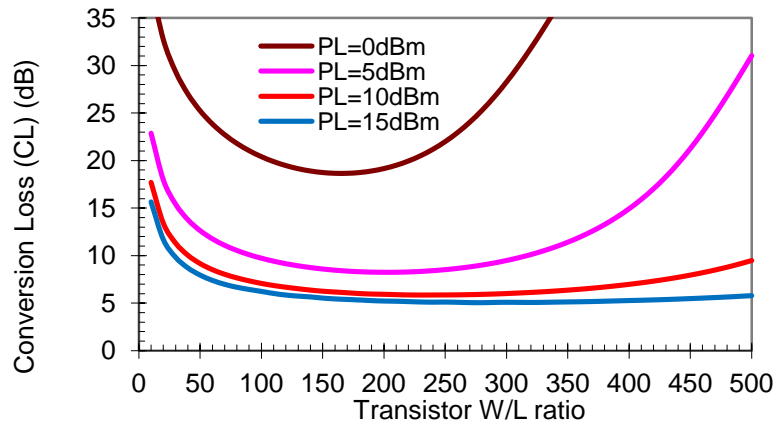


Fig. 3.18 Simulation results for CL as a function of W/L, and LO power at RF frequency of 2.4 GHz.

To define the geometry of the NMOS transistors in Fig. 3.17 and the optimum LO power level, the CL was simulated using Agilent ADS with IBM SiGe 7HP design kit, as the width (W) of the transistors and LO power were swept. The simulation result is shown in Fig. 3.18. The variable n is the ratio of W to, L where L is 180nm. CL as a function of n is shown for the LO power from 0 dBm to +15 dBm with a 5 dB step. The CL simulation result shows that CL decreases with more LO power pumped into the mixer. However, for LO power above +10dBm, no obvious benefit is obtained. The

simulation results indicate that the optimum size for the transistors to achieve the lowest CL of 5.9dB is W/L of 240 at the LO power level of +10 dBm.

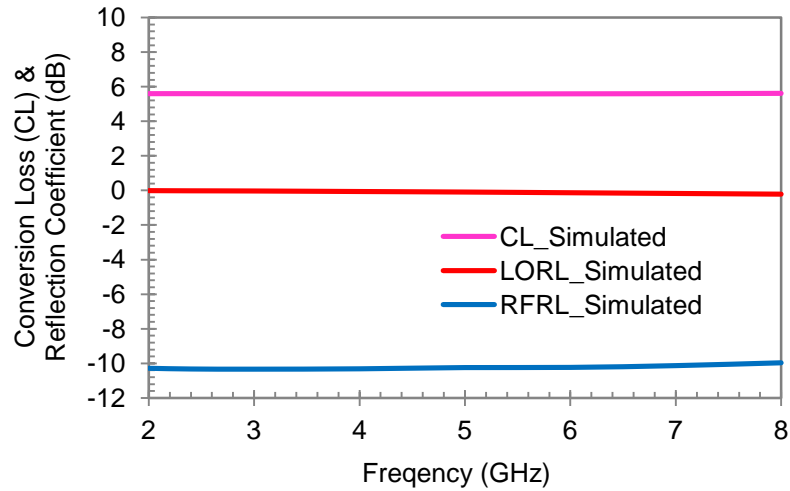


Fig. 3.19 Simulated results of CL, RF and LO reflection coefficient magnitude of the mixer core vs. RF frequency, available LO power = +10 dBm.

The simulated CL and reflection coefficient magnitude at RF and LO ports with transistor W/L ratio of 240 and LO power of +10dBm are shown in Fig. 3.19. The mixer has flat CL performance across a very broad band – greater than 2 – 8 GHz. The RF reflection coefficient also shows broad-band characteristics, and is below -10 dB without any matching elements for the frequency range of 2 – 8 GHz. Since the LO port is connected to the gate of the NMOS transistors, a very high impedance is observed at this port. Since the maximum voltage, and not the power transfer, is required at the LO port to modulate channel resistance, lack of the matching circuit does not affect the efficiency of the mixer [60]. The magnitude of LO reflection coefficient is low, as expected, indicating that the impedance seen at the LO port is almost an open circuit. The results in Fig. 3.19 indicate that this mixer core is very broad-band and matching circuits are not necessary for it to perform efficiently.

3.3.1.2 Passive Balun

Typically, a double-balanced mixer, such as the mixer core described in the previous section, requires single-ended to differential conversion. A passive balun, as shown in Fig. 3.20, is designed with capacitors (C) and inductors (L). The L-C balun uses the fact that the insertion phase through a low pass filter lags the insertion phase through

a high pass filter. It consists of two capacitors and two inductors, which form a low pass filter and a high pass filter that produce ± 90 degree phase shifts. The inductors and capacitors are designed to have a 180-degree phase shift, to provide the differential input signals for the ring mixer core at the RF and LO ports, with minimum loss and equal balanced impedances as well as to improve the RF impedance matching. The capacitor value was chosen to be 0.1 pF, and the inductor value 4.6 nH. Fig. 3.21 shows the simulated balun magnitude and phase imbalance. While the amplitude balance with 3.5 dB in transmission coefficient magnitude was achieved at 2.4 GHz, the phase balance was maintained across the relative wide bandwidth of 1-6 GHz.

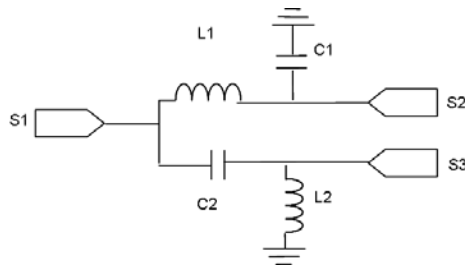


Fig. 3.20 Schematic of the passive balun, implemented using L-C passive elements.

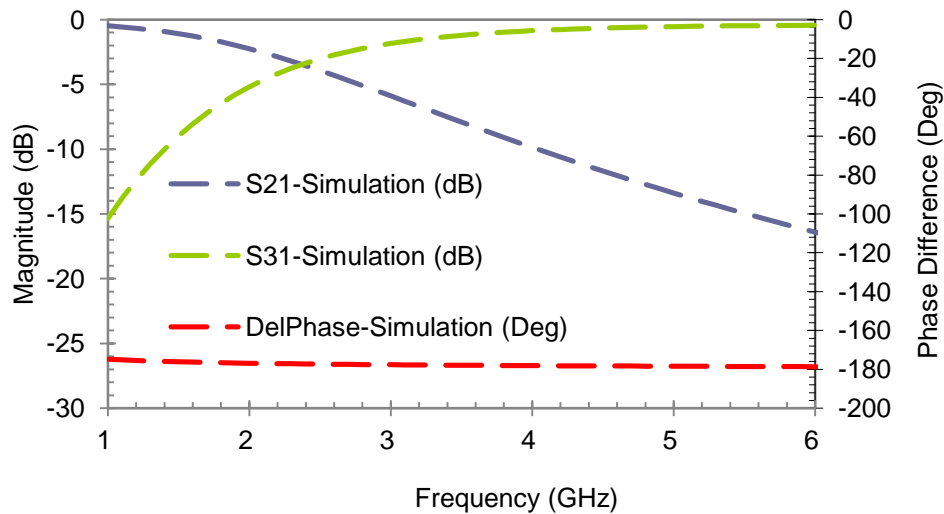
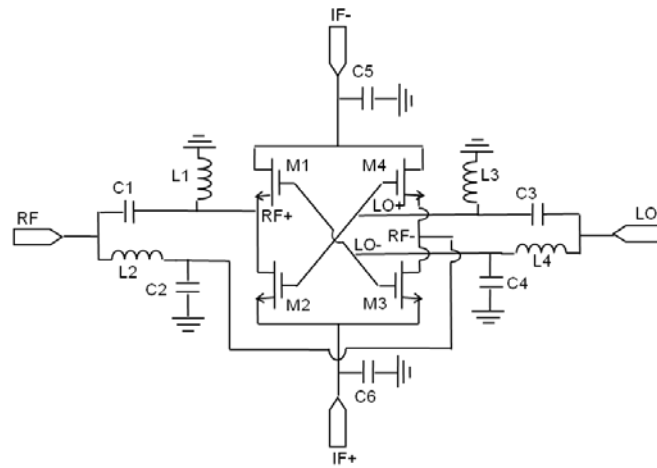


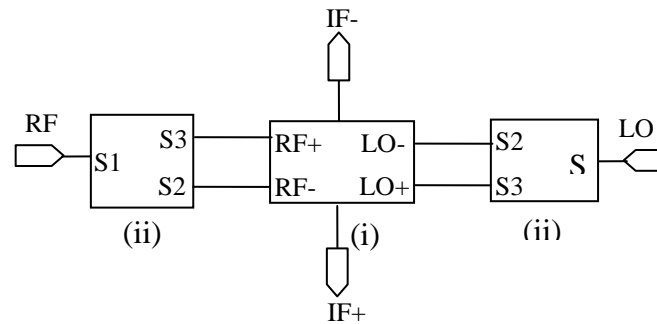
Fig. 3.21 Balun transmission coefficient simulation results: magnitude (S21 and S31) and phase difference (DelPhase) between the ports S2 and S3 in Fig. 3.20.

3.3.1.3 Mixer with Baluns

The mixer core and two baluns described in the previous sections were integrated together to provide single-ended RF and LO inputs. On the IF side, a differential output is provided, since it may be desirable to use differential amplifiers for best noise suppression prior to digitization. Fig. 3.22 shows the schematic of the integrated circuit.



(a)



(b)

Fig. 3.22 (a) Schematic of the mixer with LO and RF baluns. (b) Block diagram of the mixer core (i) integrated with LO and RF baluns (ii).

Balun orientation at the RF and LO ports greatly impacts the performance of the integrated mixer above and below the center frequency of 2.4 GHz. While at the center frequency, the input power is divided almost equally between the two outputs, the magnitude difference increases with the frequency offset from center frequency.

Transistors controlled by the higher LO output power will be on, while the transistors controlled by the lower LO output power will be off.

Simulation results in CL at each IF output versus RF frequency for the mixer with integrated baluns are shown in Fig. 3.23. It was found that the IF+ port exhibits broadband behavior while IF- output is narrow band. The 3-dB CL bandwidth is 1- 12 GHz for IF+ port and 1.5 – 4 GHz for IF- port. Both IF ports have minimum CL of 10.3 dB at 2.4 GHz – the designed center frequency of the RF and LO baluns.

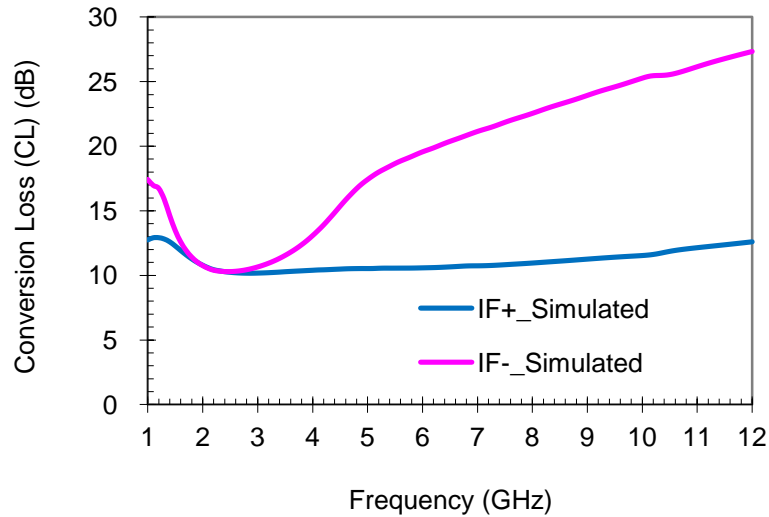


Fig. 3.23 Simulated CL versus RF frequency. The IF frequency = 10 MHz, and LO power = 13 dBm. The CL is calculated with the power level at each IF port versus the power level at the RF input.

The unique behavior of the integrated mixer can be explained based on the insertion loss of the baluns as the function of frequency. As indicated in Fig. 3.21, when operation frequency is significantly lower than the designed center frequency of balun, the power at port LO- (S2) is relatively large compared with the power pumped onto LO+ (S3), since S21 is much higher than S31. This causes transistors M1 and M3 to turn on, while M2 and M4 are off. Due to the same reason, most of power entering RF port flows out from port IF+ through RF- (S2) and M3, with a small portion is coming out from IF- through RF+ (S3) and M1. Assuming the four transistors are identical, CL of IF+ port is indeed the CL of the single IF output of the mixer core plus parasitic resistive loss of the RF balun, while IF- port is smaller than IF+ port when calculated against total RF input

power. As the operation frequency is in proximity 2.4 GHz, the power level is balanced at the differential RF and LO ports of the mixer core, *i.e.* the half of the input RF and LO power, individually. The two pairs of transistors - M1 and M3, and M2 and M4, are alternatively on and off due to the 180° phase difference of the LO balun. This results in almost equal CL, ideally the CL of the mixer core, at both IF ports with the assumption that the four transistors are identical. When the operation frequency is significantly above the balun center frequency, most of the LO power goes into port LO+ (S3), while the power at port LO- (S2) is very small. As the result, transistor M2 and M4 will be turned on, while the other two transistors will be off. In this case, the CL of two IF ports are similar to the one under the frequencies much lower than 2.4 GHz, since most of power entering RF port flows out from port IF+ through RF+ (S3) and M2, while little portion of that RF power comes out from IF- through RF- (S2) and M4. Therefore, the overall effect of the balun integration on mixer performance makes IF+ very broad-band and its CL similar to the single IF output of the mixer core across the whole band, while IF- exhibits much narrower band with CL almost equal to that of mixer core at frequencies at and near 2.4 GHz.

This mixer can be used with single IF output for broadband applications with 3-dB reduction in CL, which is due to the fact that transistors are on only half of the period, or with differential output at 2.4 GHz.

3.3.2 Measured Results

The mixer core and the mixer with integrated baluns were fabricated in IBM 7HP process. This is a 0.18 μm SiGe process with 7 metal layers. Chip layout and verification were performed using the Cadence Virtuoso Layout editor. Fig. 3.24 shows the chip micrographs of the mixer core (a) and mixer with baluns (b). The total chip size for the mixer with integrated baluns is $1.4 \times 1.3 \text{ mm}^2$. It is determined largely by the passive elements and the mixer core only occupies about 0.05 mm^2 of active area. The capacitor size is $20 \mu\text{m} \times 50 \mu\text{m}$, and the inductor size is $0.25 \text{ mm} \times 0.25 \text{ mm}$. The total chip size for the mixer core is $1.01 \times 1.1 \text{ mm}^2$.

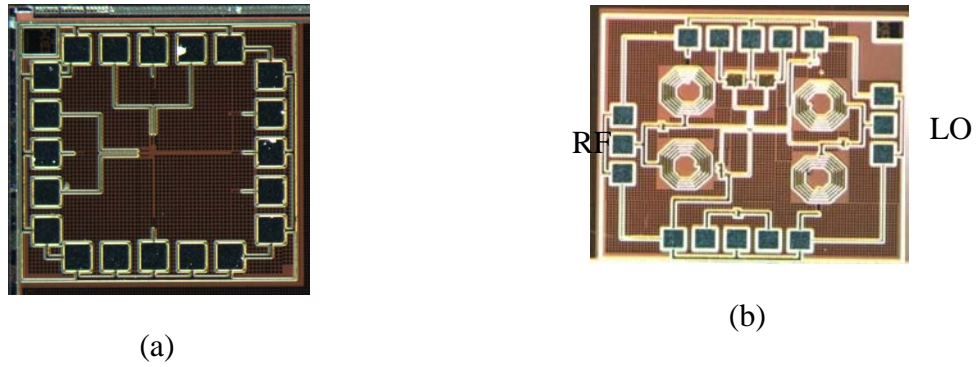


Fig. 3.24 Die photograph of mixer core (a), and the mixer with integrated RF and LO baluns (b). Chip size is $1.01 \times 1.1 \text{ mm}^2$ for mixer core (a) and $1.4 \times 1.3 \text{ mm}^2$ for mixer integrated with balun (b).

3.3.2.1 Mixer Core

The mixer core was characterized using a Cascade probe station and three GSGSG probes. External coaxial baluns with bandwidth of 2 – 8 GHz were used on the RF and LO ports during the CL and linearity measurements. Fig. 3.25 shows the measured and simulated CL for the mixer core as a function on LO power at 2.4 GHz. The lowest CL of 6.8 dB was measured for LO power of +10 dBm. CL increases at lower LO power is steeper than predicted by the simulations, likely due to LO feed-through. For the balanced mixer core LO feed-through is underestimated in the simulation due to assumption, that perfectly balanced structure provides perfect port-to-port isolation. Fig. 3.26 shows measured and simulated CL as a function of frequency. As expected, due to the absence of any passive elements, this mixer exhibits broad-band performance. The measured mixer CL is within 1-1.5 dB of the simulated CL. Fig. 3.26 also shows the RF and LO reflection coefficient magnitude, respectively. RF reflection coefficient is very broadband, due to the absence of any matching elements. Due to parasitics, RF and LO reflection coefficient magnitude decreases at higher frequencies. The RF reflection coefficient magnitude is higher than simulated, indicating that channel resistance is likely higher than predicted. As indicated in Fig. 3.27, by adding a small gate bias, channel resistance can be lowered, and the RF reflection coefficient magnitude improves significantly. Similarly, the IF reflection coefficient magnitude is also lowered with the gate bias, as shown in Fig. 3.28. This way the mixer core can provide broadband performance with excellent RF and IF return loss without any passive elements.

Other measured results, such as power at 1dB gain compression point (IP1dB), input third-order point (IIP3), LO port to RF port (LO-to-RF) and LO port to IF port (LO-to-IF) isolations, are summarized with CL and reflection coefficient magnitude in Table 3.1. This mixer core can provide very broadband performance without any passive elements.

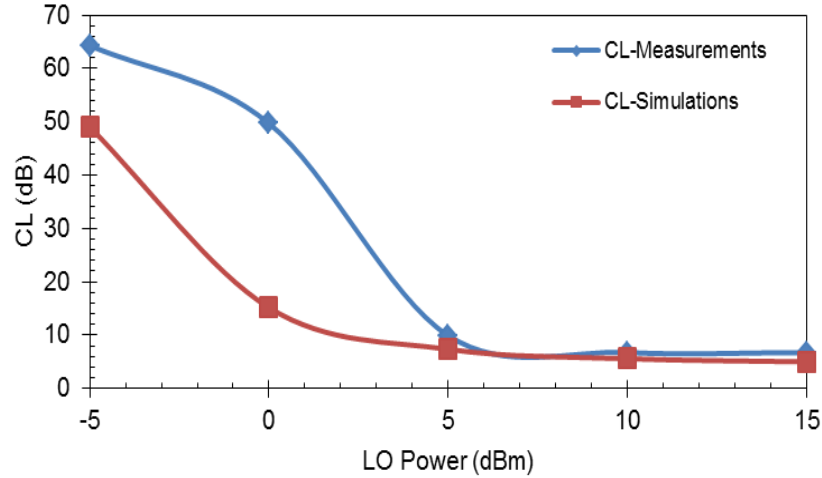


Fig. 3.25 Simulated and measured CL of the mixer core vs. LO power. RF frequency is 2.4 GHz, and IF frequency 10 MHz.

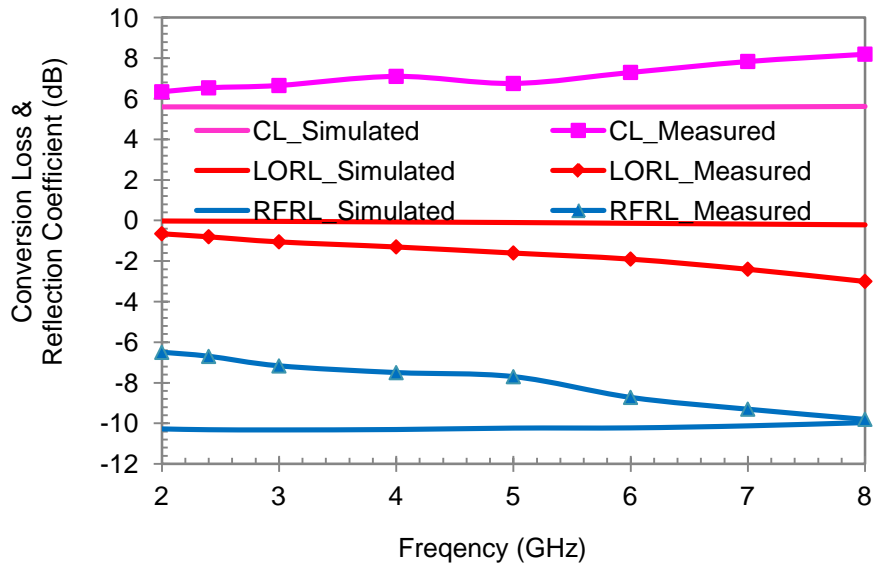


Fig. 3.26 Simulated and measured results of CL, RF and LO reflection coefficient magnitude of the mixer core vs. RF frequency, available LO power = 10 dBm.

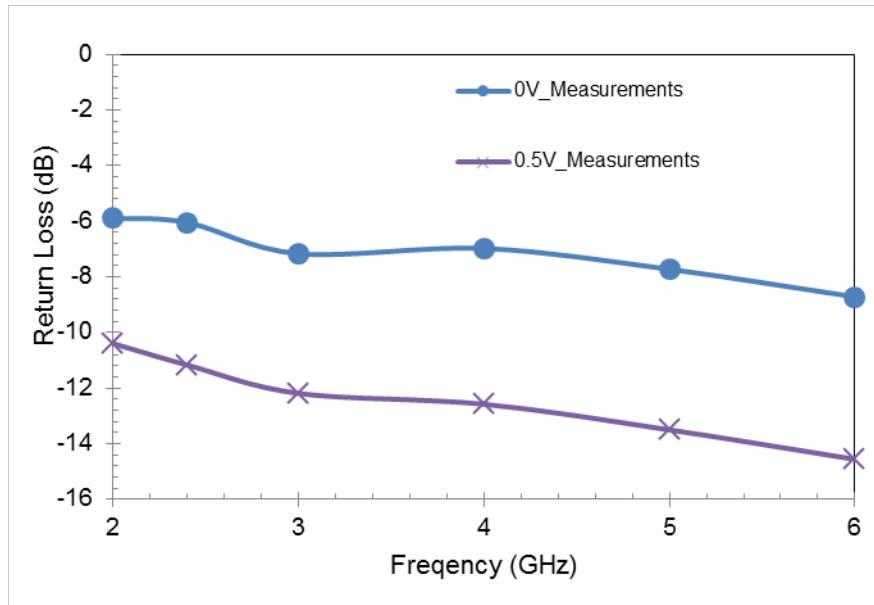


Fig. 3.27 Measured RF reflection coefficient magnitude of the mixer core with no gate bias, and with a gate bias of 0.5 V, for available LO power = 10 dBm.

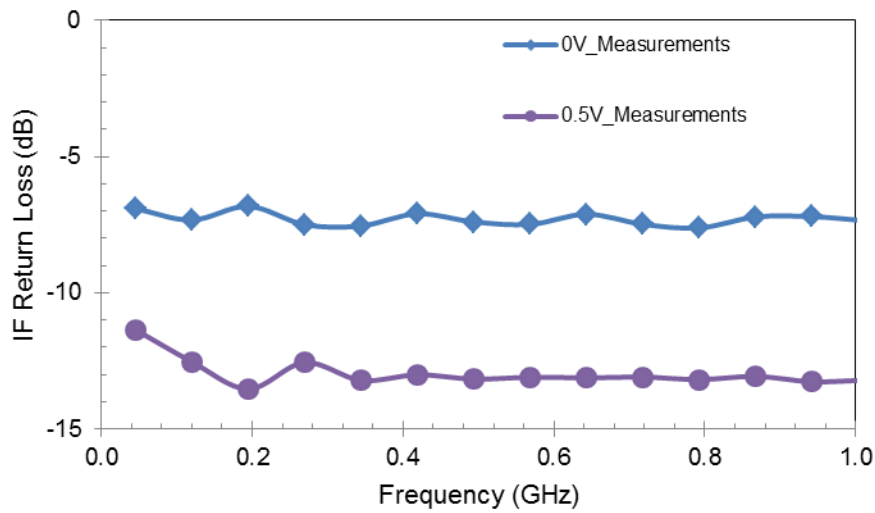


Fig. 3.28 Measured IF reflection coefficient magnitude of the mixer core with no gate bias, and with a gate bias of 0.5 V, for available LO power = 10 dBm.

3.3.2.2 Passive Balun

To verify the port balance, the S-parameters of the balun tester were measured separately using a Cascade probe station with a GSG probes for single-ended input, and a GSGSG probe for differential outputs. It was found that the operating center frequency was slightly shifted to 2.35 GHz, with transmission coefficient magnitude of -4.3 dB and phase difference of -181.9 degree at this frequency. Measured balun transmission

coefficient for the two output ports as a function of frequency is shown in Fig. 3.29. At 2.4 GHz, the transmission coefficient magnitude imbalance is 0.3dB and the phase imbalance 1.8 degrees.

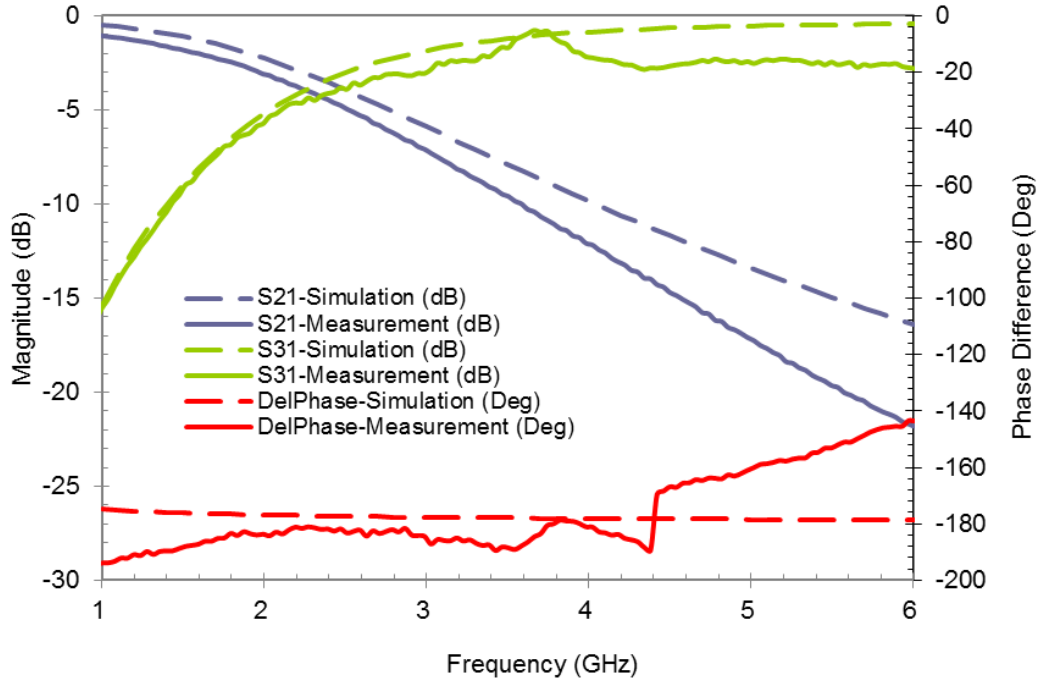


Fig. 3.29 Balun transmission coefficient magnitude and phase difference: measurement vs. simulation.

3.3.2.3 Mixer with Baluns

The mixer with integrated baluns was characterized using a Cascade probe station with two GSG probes, for RF and LO ports, and a GSGSG probe for the differential IF ports. The mixer measurements were taken with the LO power level of +13dBm, and the RF power level of -40dBm, unless specified otherwise. The measured results will be reported for 3-dB bandwidth for both ports, unless specified otherwise.

The measured results of CL versus the frequency are shown in Fig. 3.30. The CL was measured at a fixed IF frequency of 10 MHz, while both RF and LO frequencies were swept between 1 and 12 GHz for IF+ port, and 1 – 6 GHz for IF- port. The loss of the cables at different frequencies were measured and compensated for. According to Fig. 3.30, it can be seen that the IF+ port shows the wide-band performance (CL of 10.1 – 12.9 dB at the RF frequency range from 1 – 12 GHz) with CL of 10.3 dB at 2.4 GHz, and

the IF- port shows 3-dB bandwidth approximately from 1.8 – 2.8 GHz with minimum CL of 10.8 dB at 2.4 GHz. The difference between measured and simulated CL for IF+ is in 1.5 dB. For IF- ports, as the frequency increases, the discrepancy between the measurement and simulation increases. This is likely caused by the decreased measured magnitude of transmission coefficient of the balun compared with the simulation as frequency increases (Fig. 3.29), resulting in lower delivered LO power to the transistors.

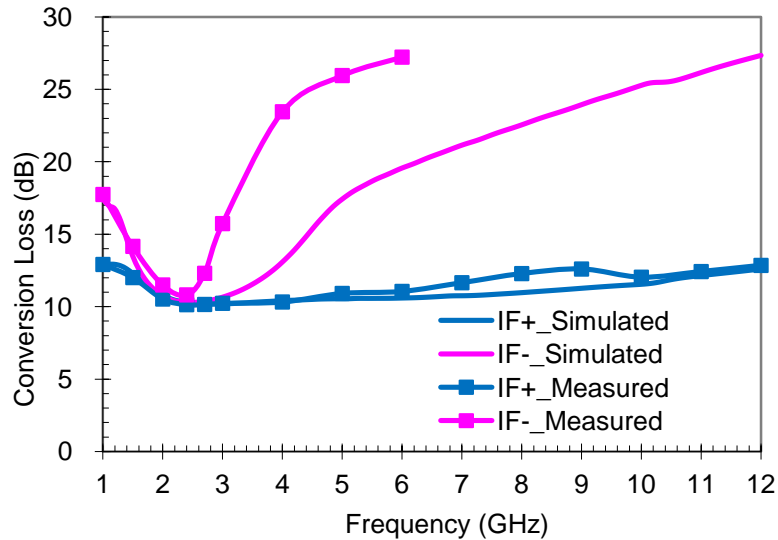


Fig. 3.30 Simulated and measured CL versus RF frequency. IF frequency = 10 MHz, and LO power = 13 dBm. The CL is calculated with the power level at each IF port versus the power level at the RF input.

Fig. 3.31 and Fig. 3.32 show the measured RF, LO, and IF reflection coefficient magnitude of the mixer. The input reflection coefficient of each port was measured using Agilent 8510C vector network analyzer. The magnitude of RF reflection coefficient is better than -9.6 dB in the frequency range of 1 to 12 GHz. The broadband RF reflection coefficient is achieved through the optimization of the NMOS device size, with balun reactive elements used to enhance the matching. At the LO port, the magnitude of reflection coefficient is above -5 dB from 1 to 7 GHz. This implies a high reflection coefficient at the LO port which leads to a considerable high available V_{gs} , since the LO port is nearly open. However, at frequencies higher than 7 GHz, the LO reflection coefficient magnitude decreases to -8 dB at 12 GHz. This is due to the increased parasitic gate to channel capacitance at the higher frequencies. At the IF port, the magnitude of reflection coefficient is better than -8 dB at the frequencies lower than 100 MHz.

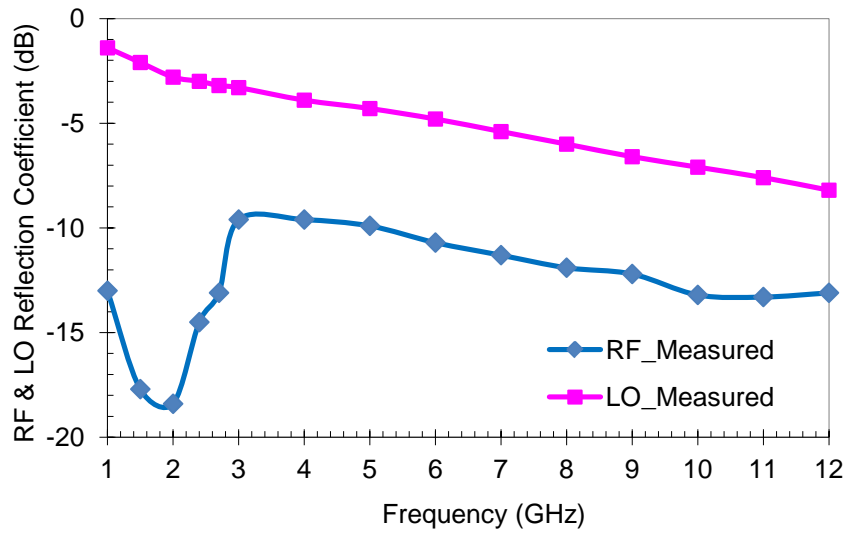


Fig. 3.31 RF and LO reflection coefficient magnitude of the mixer with baluns, with available LO power = 13 dBm.

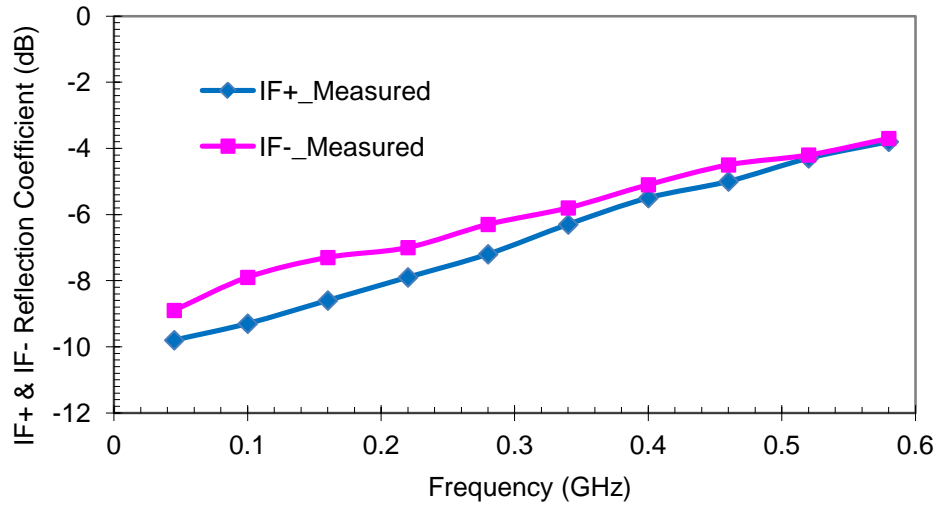


Fig. 3.32 IF reflection coefficient magnitude of the mixer with baluns, available LO power = 13 dBm.

Fig. 3.33 shows mixer with integrated baluns LO-RF and LO-IF isolation. Across the frequency of 1 – 12 GHz, LO-RF isolation achieves the best performance of -51.9 dB at 2.4 GHz. Highest LO-IF+ isolation of -63.6 dB is achieved at 3 GHz, and highest IF- isolation of -51.5 dB is achieved at 2 GHz. Due to the low reflection coefficient magnitude at the LO port, this mixer exhibits excellent LO-RF and LO-IF isolation.

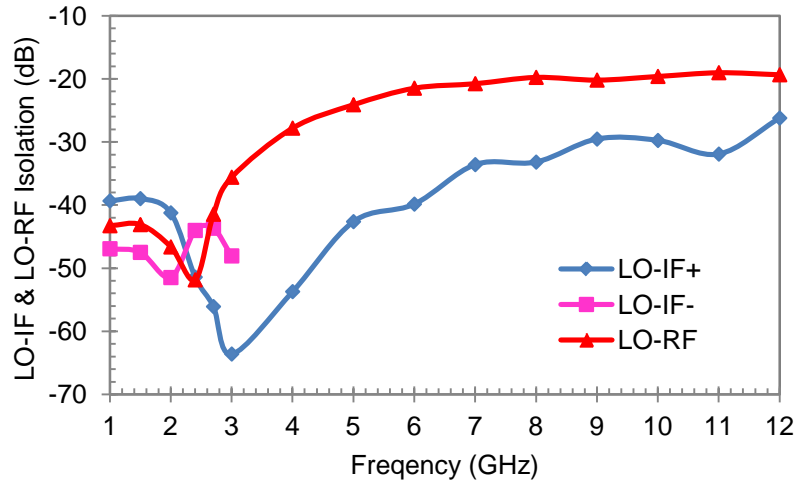


Fig. 3.33 Measured LO-RF and LO-IF isolation of the mixer with baluns versus RF frequency. IF frequency = 10 MHz, and LO power = 13 dBm.

The important figures of the linearity for a mixer are the 1 dB compression point (P1dB) and the third-order intercept point (IP3). The input P1dB (IP1dB) and input IP3 (IIP3) of the mixer were measured and the results are shown in Fig. 34 and Fig. 35. The input power range was from -20 dBm to +15 dBm for the IP1dB testing. To determine the IIP3, a two-tone test was employed. The tone spacing was set at 100 kHz.

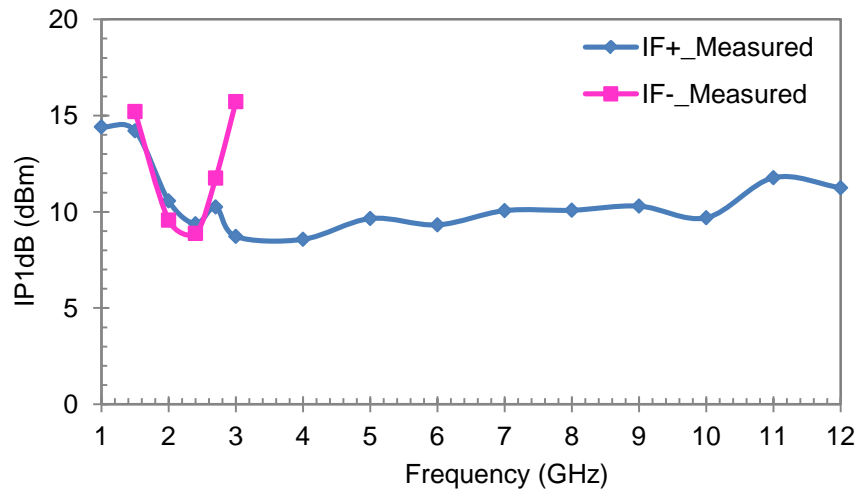


Fig. 3.34 IP1dB of the mixer with baluns versus RF frequency. IF frequency = 10 MHz, and LO power = 13 dBm.

Measured IP1dB as the function of the RF frequency is shown in Fig. 3.34. IF+ has IP1dB of 8.5 – 14.4 dBm from 1-12 GHz, and IF- has IP1dB of 8.9 dBm at 2.4 GHz. As indicated by Fig. 3.35, the tendency of the measured IP1dB follows the measured CL results.

Fig. 3.35 shows IF+ port of the mixer has IIP3 of 16 – 22.2 dBm in the frequency range of 1 – 12 GHz, and IF- port has IIP3 of 16.5 – 18.5 dBm in the 3-dB bandwidth of 1.8 – 2.8 GHz. Due to the bandwidth limitation of the power combiner used in the testing, the IIP3 measured results are only shown up to 10 GHz here.

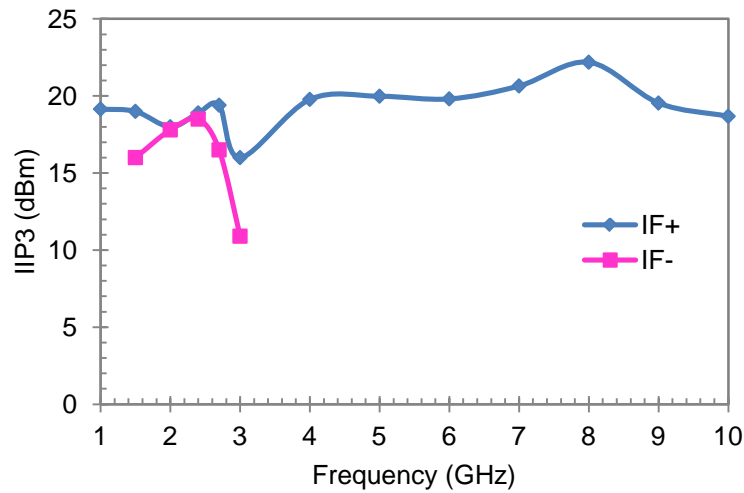


Fig. 3.35 Measured IIP3 of the mixer with baluns versus RF frequency. IF frequency = 10 MHz, and LO power = 13 dBm.

Recently, the direct-conversion receiver (DCR) has attracted a lot of attention. An important parameter of the mixer used in a DCR is DC offset at the IF ports. DC offset is mainly attributed to self-mixing of LO leakage to RF port. Therefore, high LO-RF isolation is an prerequisite for low DC offset.

DC offset measurements were taken for both IF ports simultaneously using Tektronix TDS3014B oscilloscope, with RF-port terminated by a 50 Ω resistor and the LO-port pumped with power of 13 dBm. Due to the high RF-LO isolation at frequencies between 2-2.4 GHz, this mixer shows low DC offset, with less than 3 mV for both IF ports and the lowest DC offset of 0.7 mV at 2.4 GHz. As the frequency increases, the DC offset increases since the LO-to-RF leakage increases. Unlike the direct conversion

mixers reported in [6262] and [63], this mixer does not employ a DC offset cancellation technique. Without adding extra DC offset cancellation circuitry, this mixer still shows excellent DC offset behavior at the frequencies of 2-2.4 GHz, while saving the space. Excellent DC offset performance makes this mixer a good candidate for zero-IF applications, such as Doppler radar cardiopulmonary sensing.

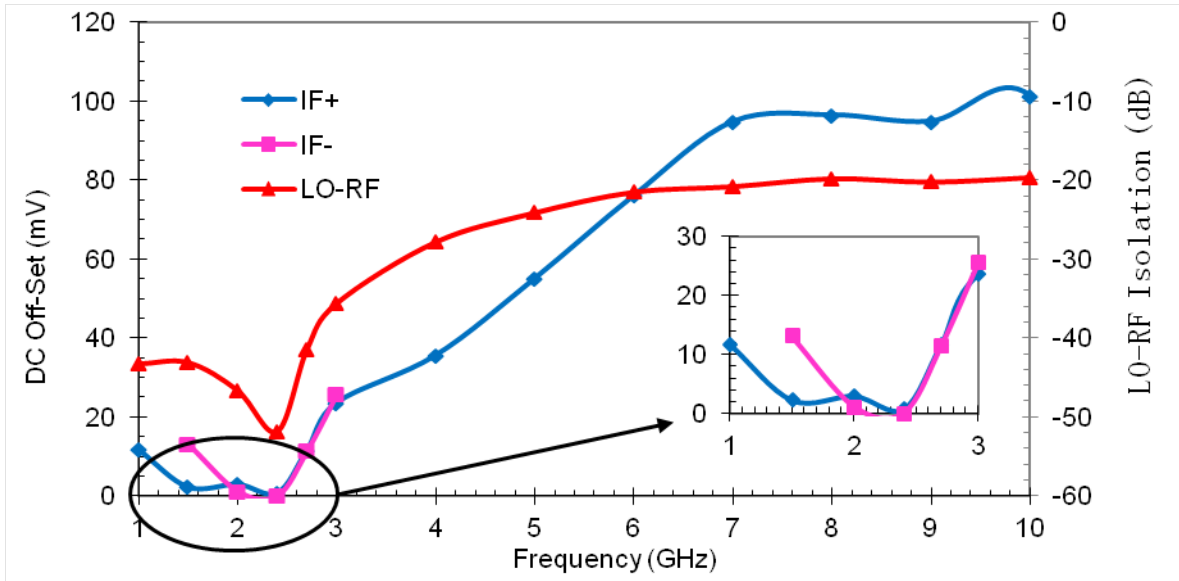


Fig. 3.36 Measured DC offset of the mixer with baluns versus LO frequency. LO power = 13 dBm.

The overall performance of the mixer with integrated baluns, and the mixer core by itself, is summarized and compared with other published CMOS resistive mixers in Table 3.1

3.4 Conclusion

In this chapter, two hardware platforms for the SoC-based Doppler radar occupancy sensor are formed using CC2530, CC430 and custom passive nodes. The passive nodes are composed of a receive antenna, a splitter and a mixer. The experimental results demonstrate that both platforms employing the architecture integrating SoC and passive node can successfully and accurately detect human respiration-like movement. Hence, it is feasible to build an SoC-based Doppler radar occupancy sensor with an add-on passive node by detecting the human cardiopulmonary activities.

Two 0.18 μm CMOS miniature wideband passive mixers fully integrated in IBM7HP process are also discussed in this chapter. The mixer core is the first reported resistive mixer without any passive elements, and is the smallest double-balanced resistive mixer reported to date with the active chip area of 0.05 mm². This mixer with integrated baluns, exhibits wideband operation, despite the intrinsic narrow-band magnitude balance of the passive baluns. By using the size of the NMOS as a design parameter, the mixer core exhibits a broadband characteristics in RF and IF impedance matching, without any matching circuits. The mixer with integrated baluns exhibits an RF reflection coefficient magnitude better than -9.6 dB over the RF frequency range of 1 – 12 GHz. The IF reflection coefficient magnitude is lower than -8 dB at the IF frequency below 100 MHz. The unique features of this mixer include extremely low DC offset due to high LO to RF isolation, and broadband performance of single IF output, despite the balun narrowband magnitude balance. If single IF output is used, the mixer exhibits CL of 10.1 – 12.9 dB at the frequencies of 1 – 12 GHz, IP1dB of 8.6 – 14.4 dBm, and IIP3 of 16 – 22.2 dBm. With differential IF outputs combined, at the operating RF frequency of 2.4 GHz and with the LO power of 10 dBm, the CL is 7.5 dB, the IP1dB is 6.2 dBm, and IIP3 is 15.5 dBm. The LO-RF isolation of -51.9 dB, and the LO-IF isolation of -47.7 dB is achieved at 2.4 GHz. Due to its excellent RF-LO isolation between 2 - 2.4 GHz, both IF ports exhibit DC-offset of less than 3 mV, with the lowest DC-offset of 0.7mV at 2.4 GHz. This is the first reported double-balanced passive resistive mixer with integrated RF and LO baluns, with the best RF reflection coefficient, lowest DC offset for harmonic mixer without dc cancellation, and widest bandwidth reported to date. This compact integrated design is suitable for Doppler radar respiration and heartbeat detection.

Table 3.1 Summarized performances of this mixer and its comparison with previously published data

	This work			[56]	[60]	[61]	[58]	[59]
	Mixer Core	Mixer + Balun						
Technology	BiCMOS 0.18 μ m	BiCMOS 0.18 μ m		BiCMOS 0.25 μ m	CMOS 130nm	CMOS 130nm	CMOS 0.25 μ m	CMOS 0.18 μ m
Topology	Double balanced	Double balanced ¹	Single ended	Double balanced	Double balanced	Double balanced	Double balanced	Double balanced
Matching Circuit	No	No	No	RF and LO	No	No	RF and LO	RF and IF
On-Chip Balun	No	Yes	Yes	No	No	No	No	No
RF Frequency (GHz)	2 – 8	1.8 – 2.8	1-12	1.8	2 – 3	5 – 6	2 – 9	1 – 11
IF Frequency (MHz)	10	10	10	170	~0	2500	0.1	500
LO Power (dBm)	10	10	13	14	0	0	10	9
Gate bias (V)	0	0	0	0	0.33	0.3	0.45	—
CL (dB)	6.3 – 8.2	7.5 @ 2.4 GHz	10.1-12.9	5.8 ²	5.6 ²	6 ²	6.4 ²	6.5 ²
IP1dB (dBm)	7.1 – 8.6	6.2 @ 2.4 GHz	8.6-14.4	10	0 @ 2.5 GHz	—	4 – 6.5	4 – 6 ³
IIP3 (dBm)	14.1 – 17.9	15.4 @ 2.4 GHz	16 – 22.2	19.5	10 @ 2.5 GHz	10 – 14	11.4 – 14.3	9 – 13 ³
LO-RF Isolation (dB)	-24.7 – -40.3	-51.9 @ 2.4 GHz	-19 – -51.9	—	-48	-45	-51	-36
LO-IF Isolation (dB)	-19.9 – 40.4	-47.7 @ 2.4 GHz	-63.6 – -26.2	-43	-52	-44	-36	—
RF Return Loss ⁴ (dB)	-6 – -8	-14.5 @ 2.4GHz	-18.4 - -9.8	—	—	< -15	-18 – -8.6	-32 – -4
IF Return Loss ⁴ (dB)	< -6.9	< -8	< -8	—	—	—	< -8	—
Power Consumption (mW)	@ DC – 1 GHz	@ DC – 100 MHz	@ DC – 100 MHz				@ DC – 135 MHz	
Power Consumption (mW)	0	0	0	0	0	0	0	3
Die Size (mm \times mm)	1.01 \times 1.1 <i>0.22 \times 0.23</i>	1.45 \times 1.27		3.5 \times 3.5	\times	<1 mm ² <i>0.5 \times 0.5</i>	1.24 \times 0.8	0.95 \times 0.65

¹ The combination average result of both IF ports.² Lowest conversion loss (CL) versus RF frequency.³ IP1dB and IIP3 were measured between 1 and 12 GHz.⁴ The magnitude of RF and IF reflection coefficient in the text is listed as return loss here.

— Not specified.

Italic: the active die area.

Chapter 4 Sensitivity Study of Doppler Radar Based Occupancy Sensor

In this chapter, the Doppler radar based occupancy sensor built with the CC2530 and an add-on passive node in Chapter 3 was tested under various operation modes, finding the optimum operation condition of the sensor system to achieve the best efficiency .

4.1 Detection Sensitivity and Power Consumption vs. Operation Modes

Chapter 3 proves that cardiopulmonary motion monitoring Doppler radar occupancy sensors can be realized by adding a passive sensor node into a commercially available SoC. In particular, these occupancy sensors must be power efficient so that they are cost effective to deploy and can run on batteries for long life time, ideally for years. The SoC's selected for the Doppler radar occupancy sensor in this dissertation transmit RF signals in three wave forms, and at various programmable output power levels. In Chapter 3, all testing was done at maximum power output. This might not be a power efficient way to operate the sensor. Therefore, the goal of this section is to find the most cost and power-saving operation point of the occupancy sensor built in previous chapter by comparing the detection sensitivity, room coverage, and power consumption. The system under study is the one built with the CC2530 TI SoC, due to the easy access to the pins to measure the current consumption. The research result will provide a significant guideline for sensor deployment in “smart home” or “smart building” wireless sensor networks.

4.1.1 Experiment Setup

The experiment setup is similar to the one in section 3.2.1.1, except an attenuator is added in the system to find the lowest detectable transmitted power, as shown in Fig. 4.1. A mechanical target with moving displacement of 1 cm and rate of 0.2 Hz, which emulates human respiration, was placed 2m away from the transmitter and node which are close to each other to provide a strong LO reference signal. A CC2530 is used as the

transmitter to provide both the LO (direct path) and RF signals (reflected from the subject) coupled through the air to the sensor node, and sensor node performs phase demodulation before the signal is digitized for further analysis (movement rate extraction) with software. The sensor node is composed of a Minicircuits splitter (ZFSC-2-2500) and mixer (ZFM4212). A 60° Antenna Specialist patch antenna (ASPPT2988) was used in conjunction with the node. The signal from the sensor node was passed through a Stanford Research System Model SR560 Low Noise Amplifier for amplification and filtering, before digitization with a NI USB-6259 DAC. The mixer's output is amplified by a factor of 500, and subjected to 6 dB/octave band-pass filtering between 0.03 Hz and 1 kHz to remove DC offset and keep the enough information for packet mode operation.

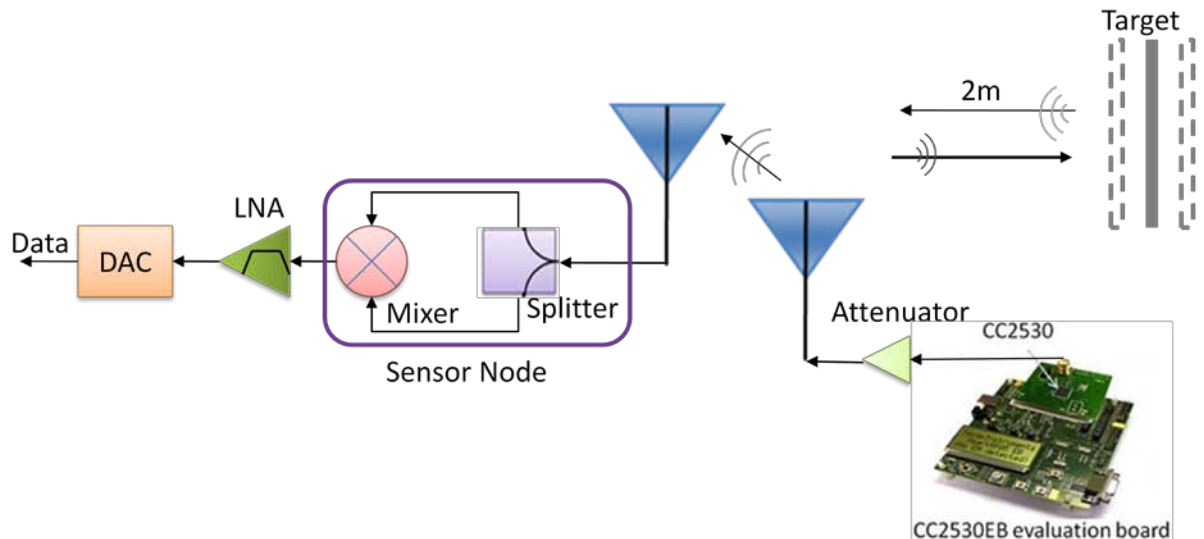


Fig. 4.1 Diagram of Doppler Radar system using CC2530 and passive sensor node.

The testing was conducted at Channel 11 with center frequency 2.405 GHz for all three transmitting modes varying the output power from -22 dBm to +4.5 dBm. Since the lowest detectable output power could be lower than the lowest programmable transmitted power of CC2530, a Broadwave tunable attenuator 751-002-030 was used to extend the transmitted power to be lower than -22 dBm to find the lowest detectable output power. During testing, a BK Tool Kit 2706A multimeter was used to record the current consumption.

4.1.2 Experiment Result

To find the lowest detectable transmitting power for each mode, the output power of CC2530 was set at its upper limit at +4.5 dBm first, and then decreased gradually. At each power level, raw data digitized with DAQ were recorded and processed in Matlab using DSP algorithms described in section 3.2.1.2. FFT (FFT on the low-pass filtered CW and modulated CW signals; for the packet mode data, FFT on the extracted envelop) were applied to seek the peak corresponding to the target moving frequency until no obvious peak was found. The lowest detectable output power level is defined as the power level at the previous stage of the one in which no peak is found. The lowest detectable output power for CW and modulated CW mode is -22 dBm, and -18 dBm for packet mode. The results for the lowest detectable output power for these three transmit modes are shown in Fig. 4.2. – Fig. 4.4.

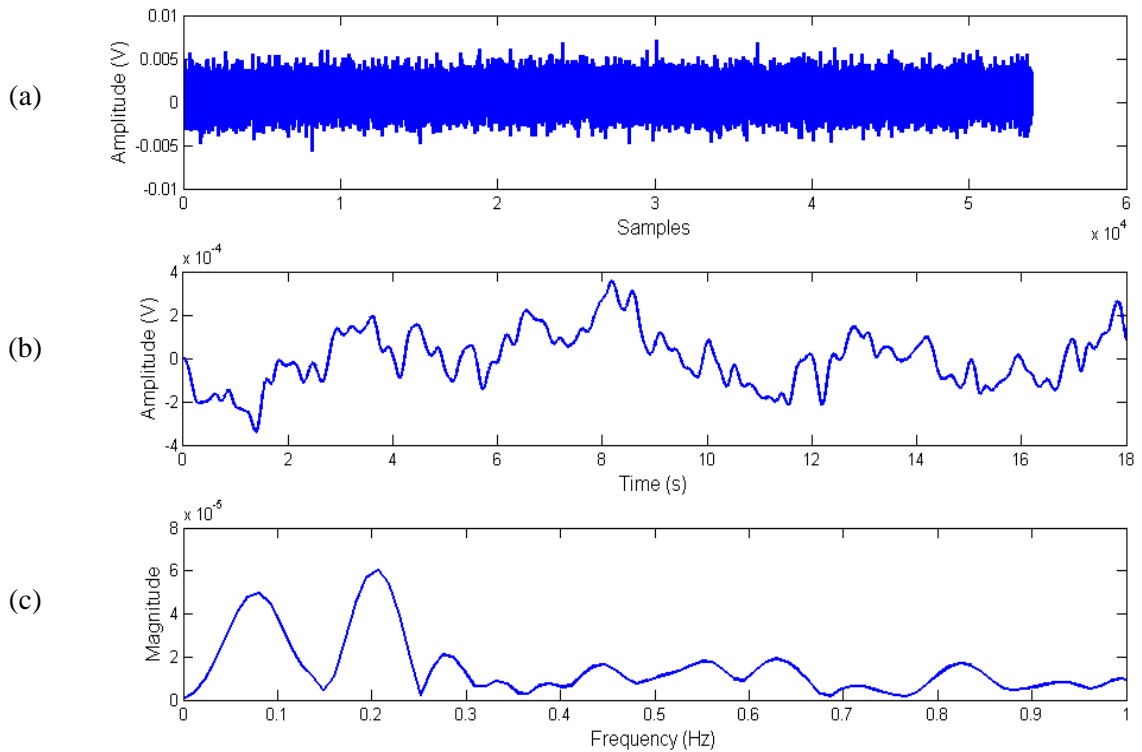


Fig. 4.2 Measurement result for CW mode at an output power of -22 dBm. (a) raw data, and (b) FFT analysis (a) result: periodic motion rate of the mechanical target at 0.2 Hz.

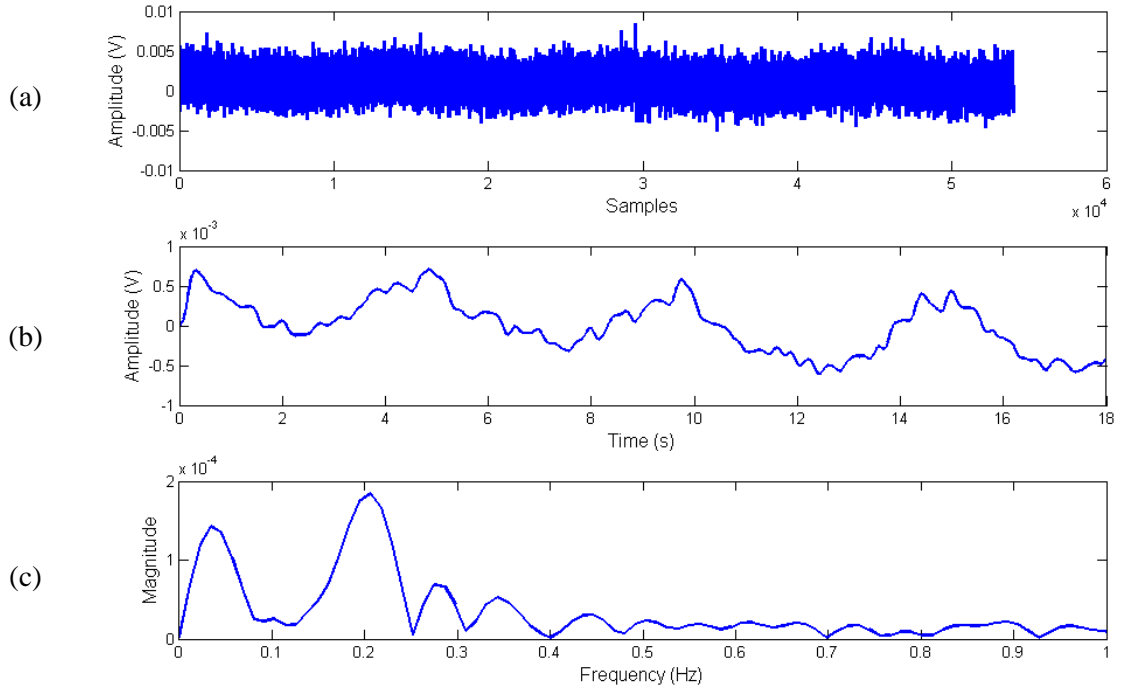


Fig. 4.3 Measurement result for modulated CW mode at an output power of -22 dBm. (a) raw data, and (c) FFT analyzed result: periodic motion rate of the mechanical target at 0.2 Hz.

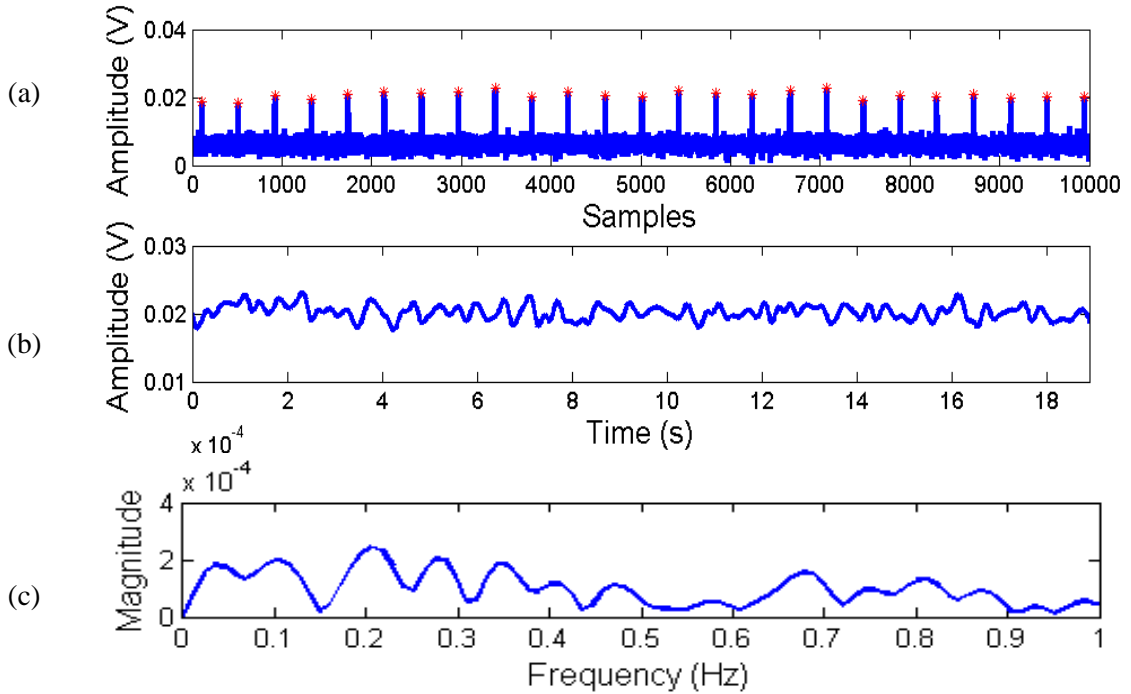


Fig. 4.4. Measurement result for Packet mode at an output power of -18 dBm. (a) raw data with detected peaks marked with red star; (b) peaks interpolated with spline technique; (c) FFT analyzed result: periodic motion rate of the mechanical target at 0.2 Hz.

Fig. 4.2 and Fig. 4.3 are the results for CW and modulated CW mode at lowest detectable output power of -22 dBm: (a) shows the digitized data using NI DAQ, (b) shows data filtered by a FIR low pass filter with cut-off frequency of 2Hz, and (c) shows motion rate of 0.2 Hz for the periodical moving mechanical target, calculated with FFT. Fig. 4.4 is the result for packet mode at lowest detectable output power of -18 dBm: (a) shows the raw data and peaks which are detected by the local maximum algorithm, (b) illustrates the result interpolated with cubic spline method, and (c) shows periodic movement rate of the mechanical target is 0.2 Hz using FFT.

The minimum detectable received signal power $P_{r,\min}$ can be estimated using the following equation (Equation (2.16)) with the measured lowest detectable transmitted power level and correspondingly maximum coverage range R_{\max} , which is 2m here:

$$R_{\max} = \sqrt[4]{\frac{P_t G^2 \lambda^2 \sigma}{P_{r,\min} (4\pi)^3}} \quad [\text{m}], \quad (4.1)$$

where P_t is the known transmitted power, G is antenna gain of transmitting and receiving antenna, λ is the signal wavelength, and σ is the radar cross section of the target. Hence, the minimum detectable received signal power can be expressed as:

$$P_{r,\min} = \frac{P_t G^2 \sigma \lambda^2}{(4\pi)^3 R_{\max}^4}. \quad (4.2)$$

For a given radar system, the minimum detectable received signal is a constant. Therefore, the maximum working distance at one transmitted power level and the one at another transmitted power have the following relationship:

$$P_{r,\min} = \frac{P_{t,1} G^2 \sigma \lambda^2}{(4\pi)^3 R_{\max,1}^4} = \frac{P_{t,2} G^2 \sigma \lambda^2}{(4\pi)^3 R_{\max,2}^4}, \quad (4.3)$$

which can be simplified to:

$$\frac{P_{t,1}}{R_{\max,1}^4} = \frac{P_{t,2}}{R_{\max,2}^4}, \quad (4.4)$$

where, in this experiment, $P_{t,1}$ and $R_{max,1}$ are the measured minimum detectable transmitted power (for example, -22 dBm for CW mode) and corresponding maximum coverage range (2m), and $P_{t,2}$ and $R_{max,2}$ are the other known transmitted power and maximum coverage range to be calculated at this power.

With a calculated maximum working distance of the occupancy sensor for a corresponding transmitted power level, it can be estimated that how many sensor units will be deployed within a given space by the following procedures:

1. The number of sensor units will be resulted for a given area, in which the sensors will be deployed divided by the coverage area of each sensor
2. The coverage area of each sensor will be equal to the area of a circle with radius of R_{max}
3. The power consumption for each sensor unit will be the product of the power voltage supply on CC2530 evaluation board, 3.3 V here, and the measured current consumption
4. The total power consumption for all the sensor units deployed in the given area is the product of number of sensor units and the power consumption of each sensor

Table 4.1 compares the calculated maximum working distance at various power levels for the three operation modes considered, the required number of sensor nodes and the total power consumption, given a typical 400 ft² hotel room.

According to Table 4.1, although CW and modulated CW operating modes are more sensitive than packet mode, packet mode has the advantage of the greater power efficiency, since it sends out signals intermittently. Compared with the other two modes, packet mode can save up to 82% of power. Therefore, the most power efficient and deployment cost efficient way is running CC2530 at packet mode with -6 dBm output power or above.

Table 4.1 Comparison of max. working distance, sensor node number, and power consumption for three modes

Output Power (dBm)	Max. Working Distance (m)			No. of Required Sensor Units			Total Power Consumption (mW)		
	CW Mode	Modulated CW Mode	Packet Mode	CW Mode	Modulated CW Mode	Packet Mode	CW Mode	Modulated CW Mode	Packet Mode
4.5	9.2	9.2	7.4	1	1	1	115.8	117.2	19.8
-0.5	7	7	5.4	1	1	1	96.4	97.7	19.5
-6	5	5	4	1	1	1	86.8	88.4	19.1
-12	3.6	3.6	2.8	1	1	2	83.8	85.8	37.6
-18	2.6	2.6	2	2	2	3	162.7	168.3	56.4
-22	2	2	1.6	3	3	5	236.6	241.6	94

4.2 Sensitivity Comparison between Sensor Node and Quadrature Architecture

In this section, we will compare the sensitivity of the Doppler radar occupancy sensor built with the simple add-on sensor node architecture with the one using quadrature receiver when the target is at non-null points.

4.2.1 Experiment Setup

Two Doppler radar occupancy sensors were built for this testing. One is as same as the one used in section 4.1.1, using receive architecture of passive sensor node with air coupling. The other one adopts quadrature receiver architecture. Both the sensors employ same CC2530 evaluation board as radar signal source. A mechanical target with moving displacement of 1 cm and rate of 0.3 Hz which emulates human respiration was used as the target subject. The distance between the target and the receiving antennae of the both sensors are 2 meters. The experiment arrangement for the two sensors is shown in Fig. 4.5.

In sensor node testing setup, as same as in section 4.1.1, the transmitting and receiving antennae were set next to each other to provide a strong LO reference signal. The sensor node consists of an Antenna Specialist (ASPPT2988) antenna, a Minicircuits splitter (ZFSC-2-2500) and mixer (ZFM4212). It receives both the direct signal from

CC2530 (LO) and the signal reflected from the mechanical target (RF), which mix with themselves down to base band.

In quadrature receiver setup, Minicircuits ZFSC-2-2500 coupler was used to split the signal source output into the transmitter antenna and local oscillator paths with 90 degree phase difference. The Antenna Specialist (ASPPT2988) antenna with 8 dBi gain and 60 degree E-plane beamwidth was used for transmitting and receiving antenna. The received signal which is scattered from the target is fed into a Minicircuits ZFM4212 mixer. It was mixed down to baseband, using small portion of the transmitted signal hardwired to the LO ports of the mixers.

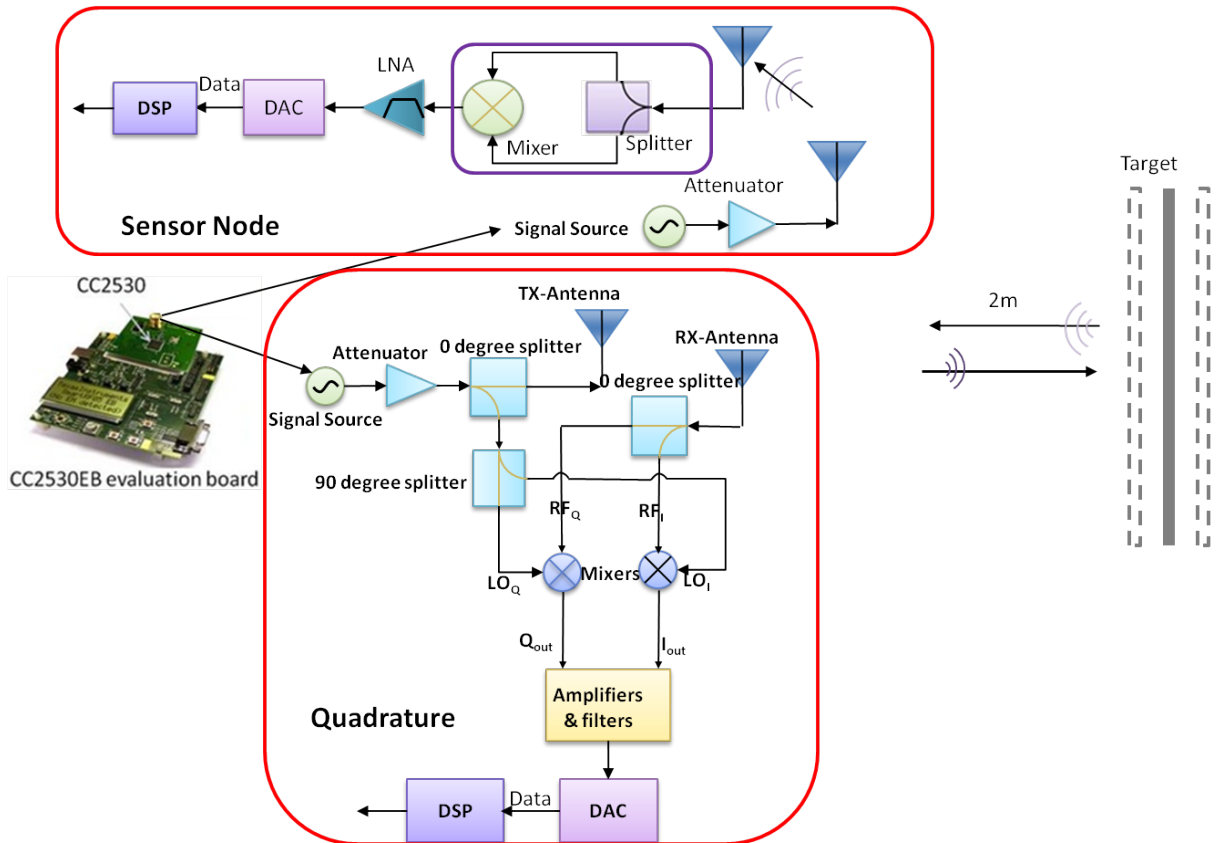


Fig. 4.5. The illustration of experiment setup for the sensitivity testing of Doppler radar occupancy sensors with sensor node and quadrature receiver, respectively.

In both of the sensor node and quadrature setups, the baseband signals were passed through Stanford Research System Model SR560 Low Noise Amplifiers for amplification and filtering, before digitization with a NI USB-6259 data acquisition device. The mixers' output were amplified by a factor of 500, and subjected to 6

dB/octave high-pass filtering at 0.03 Hz to remove DC offset. Then, 6 dB/octave low-pass filtering with 1 kHz cutoff frequency was applied. Finally, signal was recorded by a NI USB-6259 to the PC with the sampling rate of 3kHz.

The testing was conducted at Channel 11 with center frequency 2.405 GHz for all three transmitting modes varying the output power from -22 dBm to 4.5 dBm. Similarly to section 4.1, the output power of CC2530 was set at its upper limit at 4.5 dBm first, and then decreased gradually to find the lowest detectable transmitting power for each mode. Broadwave tunable attenuator 751-002-030 was used to extend the transmitted power, in case if it is lower than -22 dBm.

4.2.2 Experimental Results

For both passive sensor node and quadrature receiver Doppler radar occupancy sensor setup, raw data digitized with the DAQ were recorded and processed in Matlab. The data was cleaned with FIR low pass filtering first for both CW and modulated CW modes. The motion rate of the mechanical target was then calculated by applying FFT to the filtered data. For packet mode data, DSP algorithms described in section 3.2.1.2, low pass filtering, local maximum detection, cubic spline interpolation, and FFT were applied to calculate the motion rate of the target.

Figures 4.6 through 4.11 are the results for both sensor node and quadrature architecture at output power of +4.5 dBm, respectively operated at CW, modulated CW, and packet modes. In Fig. 4.6 – Fig. 4.9, top shows the raw data digitized with NI DAQ, middle shows data filtered by a FIR low pass filter with cut-off frequency of 2Hz, and the bottom shows the filtered data in frequency domain by applying FFT. Fig. 4.10 top shows the raw data and peaks which are detected by the local maximum algorithm, middle illustrates the result interpolated with spline method, and bottom shows frequency domain analysis result on the spline interpolated data. In Fig. 4.11, the raw data with extracted peak envelop for I and Q channels are presented in top, the spline interpolated data for the two channels are combined in the bottom left graph, and the FFT results for both channels are shown in the bottom right graph.

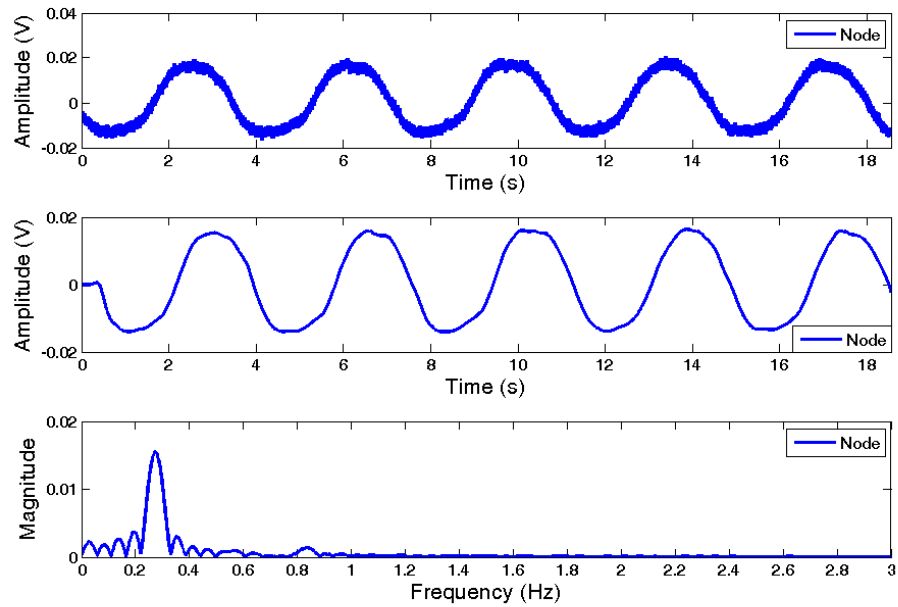


Fig. 4.6 Measured result for passive sensor node at an output power of +4.5 dBm and frequency of 2.405 GHz when operated at CW mode. Top: raw data, Middle: digital low pass filtered data, and Bottom: FFT analyzed result: periodic motion rate of the mechanical target at 0.3 Hz.

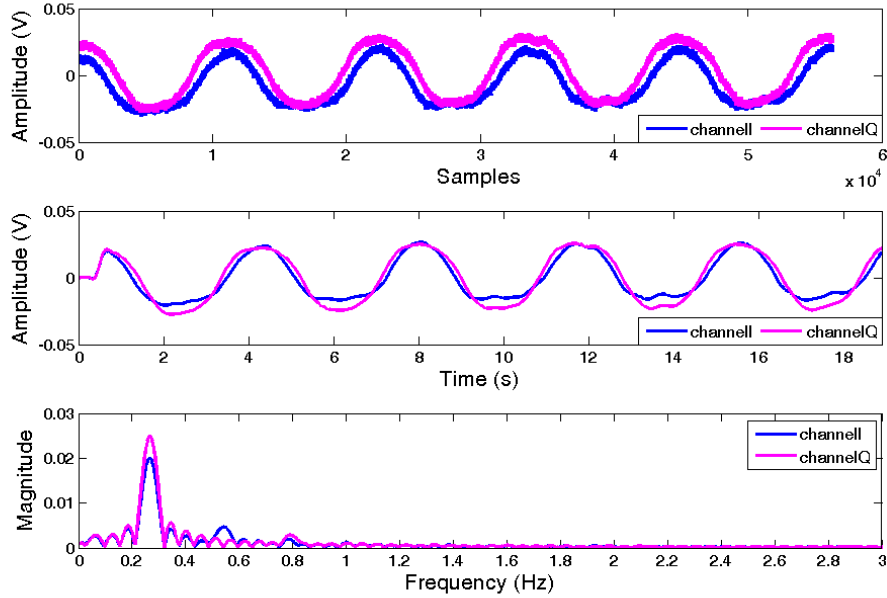


Fig. 4.7 Measured result for quadrature sensor at an output power of +4.5 dBm and frequency of 2.405 GHz when operated at CW mode. Top: raw data, Middle: digital low pass filtered data, and Bottom: FFT analyzed result: periodic motion rate of the mechanical target at 0.3 Hz.

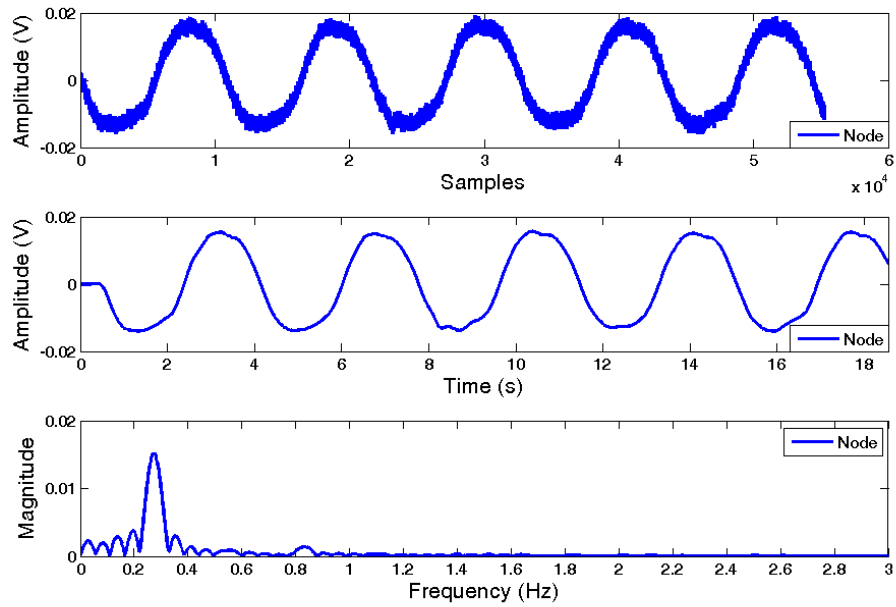


Fig. 4.8 Measured result for passive sensor node at an output power of +4.5 dBm and frequency of 2.405 GHz when operated at modulated CW mode. Top: raw data, Middle: digital low pass filtered data, and Bottom: FFT analyzed result: periodic motion rate of the mechanical target at 0.3 Hz.

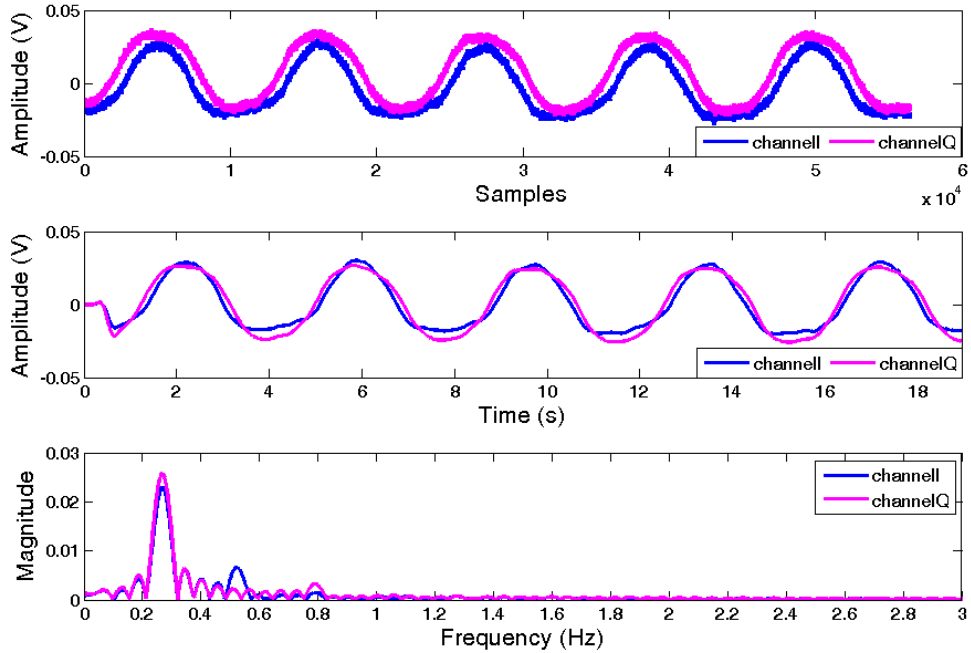


Fig. 4.9 Measured result for quadrature sensor at an output power of +4.5 dBm and frequency of 2.405 GHz when operated at modulated CW mode. Top: raw data, Middle: digital low pass filtered data, and Bottom: FFT analyzed result: periodic motion rate of the mechanical target at 0.3 Hz.

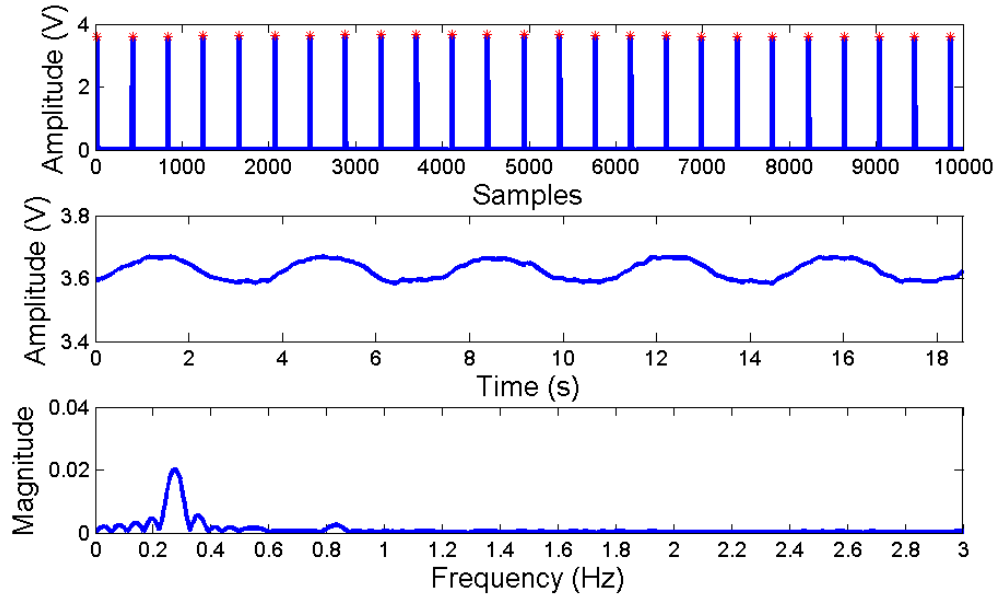


Fig. 4.10 Measured result for sensor node at an output power of +4.5 dBm and frequency of 2.405 GHz when operated at packet mode. Top: raw data with detected peaks marked with red star; Middle: peaks interpolated with spline technique; Bottom: FFT analyzed result: periodic motion rate of the mechanical target at 0.3 Hz.

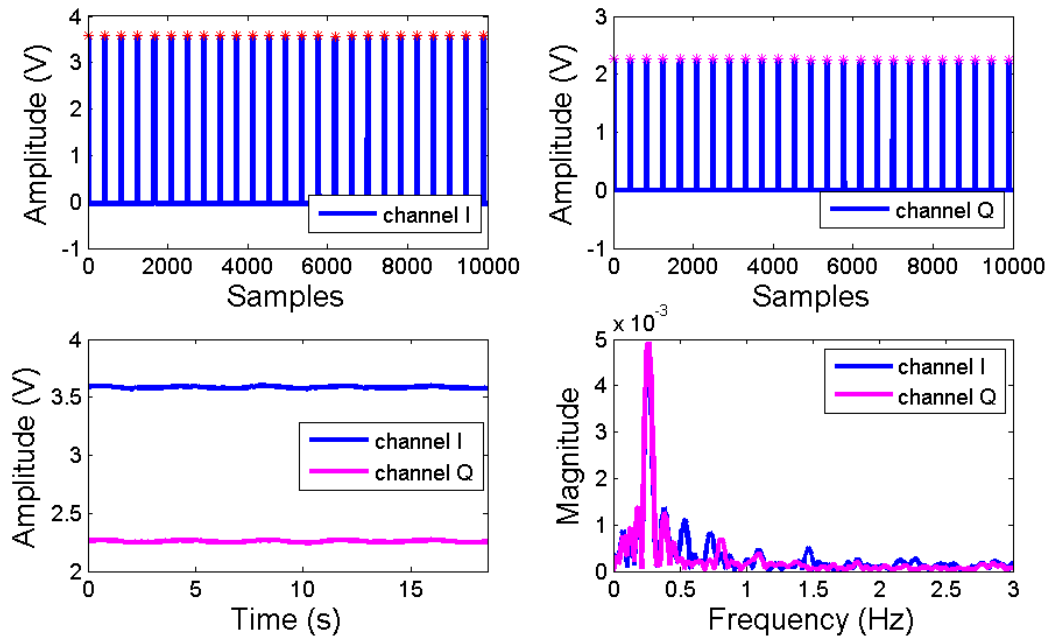


Fig. 4.11 Measured result for quadrature sensor at output power +4.5 dBm and frequency of 2.405 GHz when operated at packet mode. Top: raw data with detected peaks marked with red star for I-channel (left) and Q-channel (right); Bottom left: peaks interpolated with spline technique; Bottom right: FFT analyzed result: periodic motion rate of the mechanical target at 0.3 Hz.

Passive sensor node shows the similar results with both I and Q channels, indicating the sensors are located at the position between null and optimum points. At an output power of +4.5 dBm, both sensors can accurately extract the motion rate of 0.3 Hz for the periodical moving mechanical target under all three transmission modes.

The same testing and analysis were conducted at various output power levels. FFT was employed to seek the peak corresponding to the target moving frequency at each power level, until no obvious peak was found in the spectrum. The lowest detectable output power level is defined as the power level at the previous stage of the one in which no peak is found. The lowest detectable output power for the Doppler radar sensor built with passive sensor node when it is operated at CW mode is -23 dBm, -22 dBm at modulated CW mode, and -20 dBm at packet mode. This result is very close to the one built with quadrature receiver, which has the lowest detectable output power at -22 dBm for all three transmitting modes. The results at the lowest detectable transmitted power are shown in Fig. 4.12 through Fig. 4.17. The comparison between sensor node and quadrature receiver indicates the sensitivity of the system is not sacrificed by employing simple passive sensor node architecture when the sensor is at non-null points.

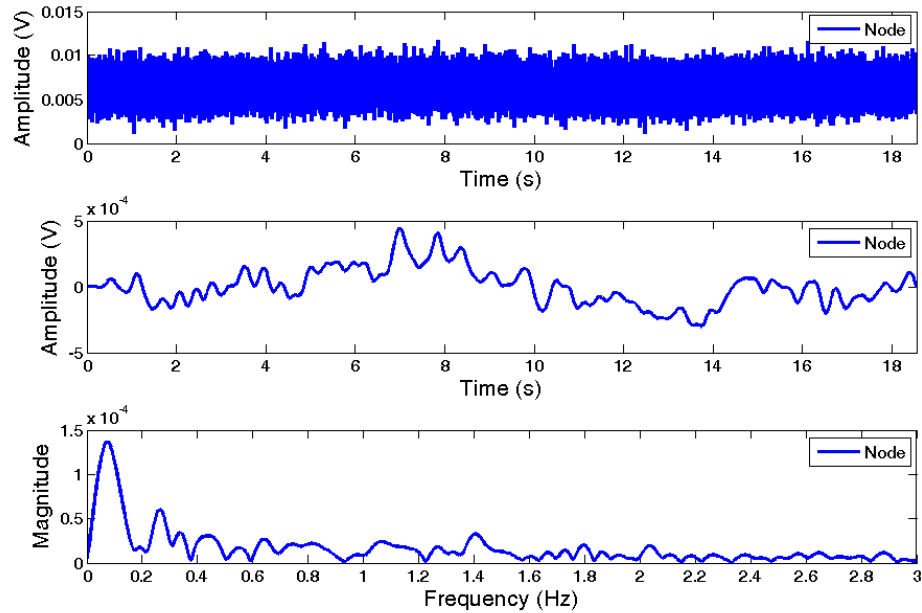


Fig. 4.12 Measured result for passive sensor node at an output power of -23 dBm and frequency of 2.405 GHz when operated at CW mode. Top: raw data, Middle: digital low pass filtered data, and Bottom: FFT analyzed result: 0.3 Hz periodic motion rate peak is buried in other peaks.

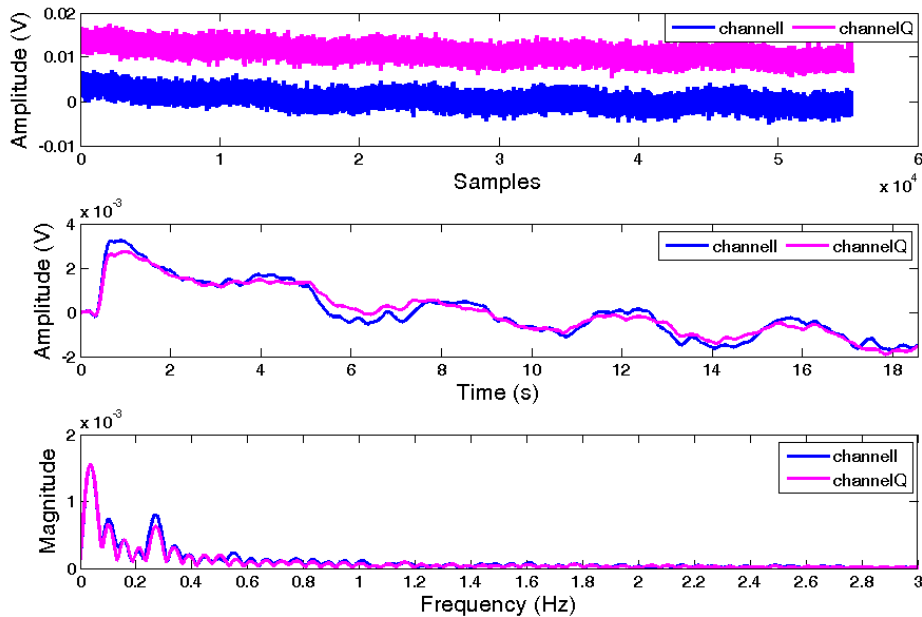


Fig. 4.13 Measured result for quadrature sensor at an output power of -22 dBm and frequency of 2.405 GHz when operated at CW mode. Top: raw data, Middle: digital low pass filtered data, and Bottom: FFT analyzed result: 0.3 Hz periodic motion rate peak is buried in other peaks.

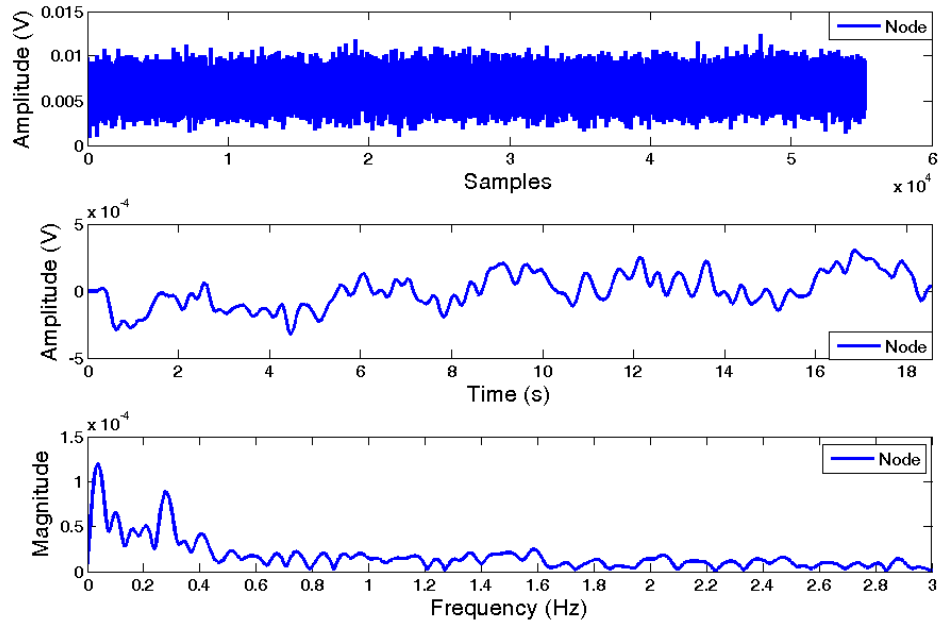


Fig. 4.14 Measured result for sensor node at an output power of -22 dBm and frequency of 2.405 GHz when operated at modulated CW mode. Top: raw data, Middle: digital low pass filtered data, and Bottom: FFT analyzed result: 0.3 Hz periodic motion rate peak is buried in other peaks.

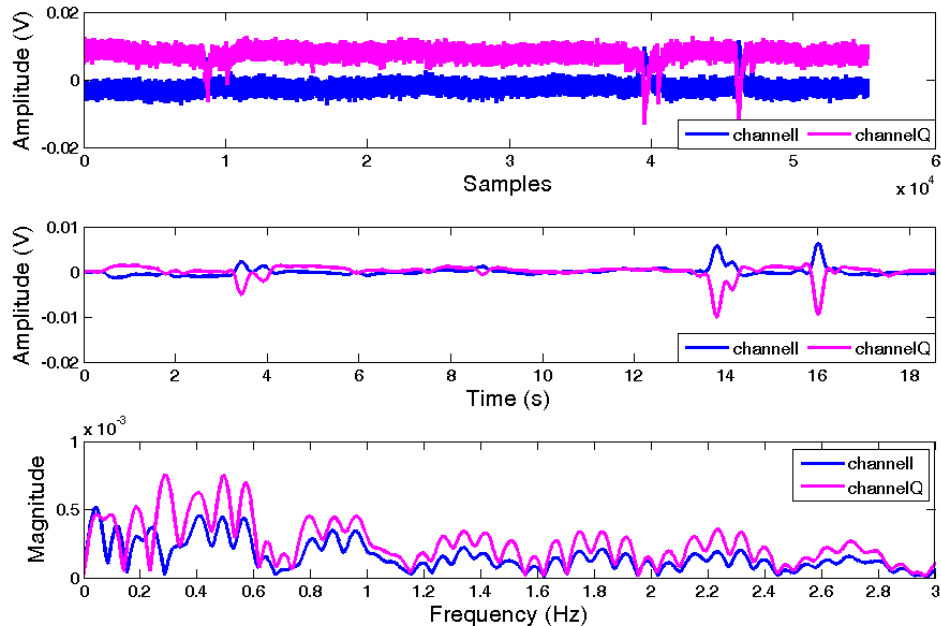


Fig. 4.15 Measured result for quadrature sensor at an output power of -22 dBm and frequency of 2.405 GHz when operated at modulated CW mode. Top: raw data, Middle: digital low pass filtered data, and Bottom: FFT analyzed result: 0.3 Hz periodic motion rate peak is buried in other peaks.

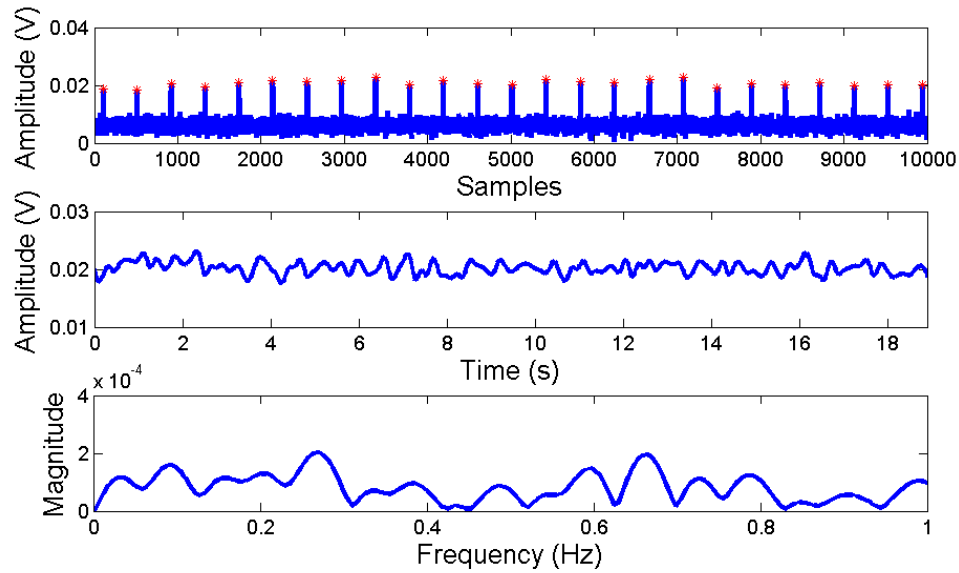


Fig. 4.16 Measured result for sensor node at an output power of -20 dBm and frequency of 2.405 GHz when operated at packet mode. Top: raw data with detected peaks marked with red star; Middle: peaks interpolated with spline technique; Bottom: FFT analyzed result: 0.3 Hz periodic motion rate peak is buried in other peaks.

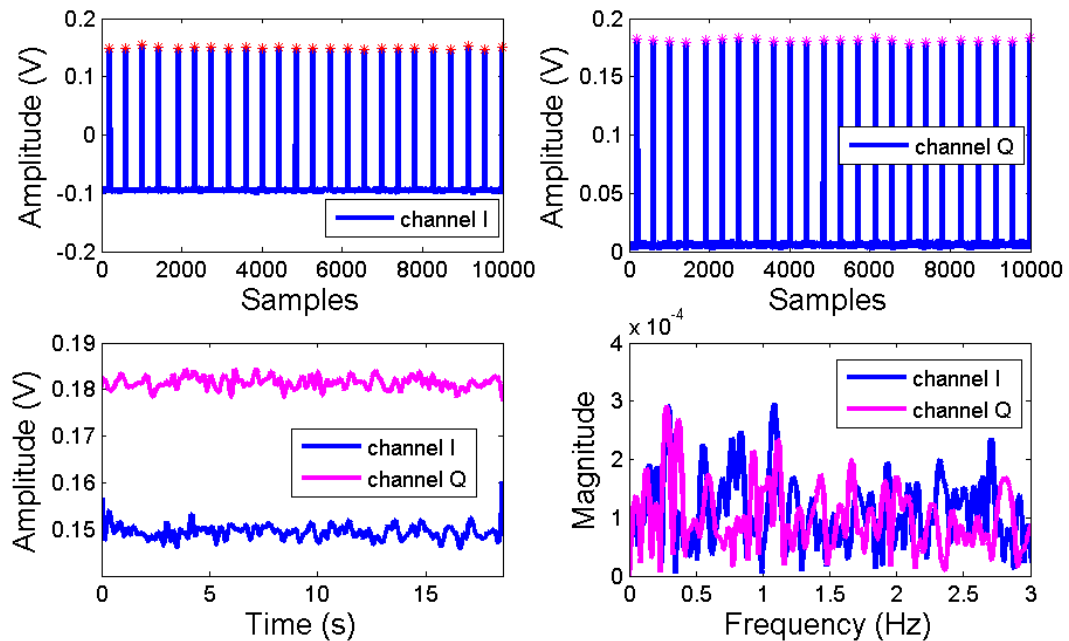


Fig. 4.17 Measured result for quadrature sensor at output power -22 dBm and frequency of 2.405 GHz when operated at packet mode. Top: raw data with detected peaks marked with red star for I-channel (left) and Q-channel (right); Bottom left: peaks interpolated with spline technique; Bottom right: FFT analyzed result: 0.3 Hz periodic motion rate peak is buried in other peaks.

4.3 Sensitivity Comparison between Null Point and Optimum Point

Previous section proves that when Doppler radar occupancy sensor locates at non-null points, no obvious difference between the architectures of passive sensor node and quadrature receiver has been observed.

However, passive sensor node is essentially a single-channel receiver. Its sensitivities will vary with the position depending on when it is at null or optimum points. When the sensor node is at the optimum points, the baseband signal $B_r(t)$ will have the form of

$$B_r(t) \approx \pm A \left(\frac{4\pi d(t)}{\lambda} + \Delta\phi \right) \quad , \quad (4.5)$$

in which it is linearly proportional to the displacement $d(t)$ of periodic movement. When the sensor node is at the null points, the base band signal will be proportional to the square of the time-varying displacement:

$$B_r(t) \approx \frac{A}{2} \left[1 \pm \left(\frac{4\pi d(t)}{\lambda} + \Delta\phi \right)^2 \right], \quad (4.6)$$

and its sensitivities will decrease.

The null and optimum points will occur one after the other every eighth of a wavelength. For example, at a frequency of 2.405 GHz used for CC2530 in the previous sections, the null and optimum points are only 1.5 cm apart. Therefore, it is very important to know how the signals look like and what the sensitivities would be when the Doppler radar occupancy sensor with passive sensor node is at optimum and null points. This section will explore what will happen when the sensor is at those positions.

4.3.1 Experiment Setup

In this experiment, a same Doppler radar occupancy sensor as the one used in previous sections was made with CC2530 evaluation board and a passive sensor node. Again, a 3-dB Minicircuits ZFSC-2-2500 power splitter and a Minicircuits ZFM4212 mixer were assembled conjunctionally with an 8 dBi gain and 60 degree E-plane beamwidth Antenna Specialist (ASPPT2988) antenna to form the passive sensor node receiver. The transmitter was constructed with CC2530 and another ASPPT2988

antenna. The transmitting and receiving antennae were put next to each other to provide strong coupling signal for LO port of the mixer. A mechanical target was placed 2m from the radar sensor originally. Then the mechanical target was brought closer to the radar sensor at a step with one sixteenth of a wavelength at the radar operational central frequency of 2.405 GHz. At every location for each step, the mechanical target was programmed to move periodically with 0.2 Hz rate and 1 cm displacement, and the signal modulated by this movement was recorded and analyzed until a null point was found. Once a null point was confirmed, an optimum point can be located by moving the target one eighth of a wavelength forward or backward from the null point. Fig. 4.18 illustrates how to find the null and optimum point.

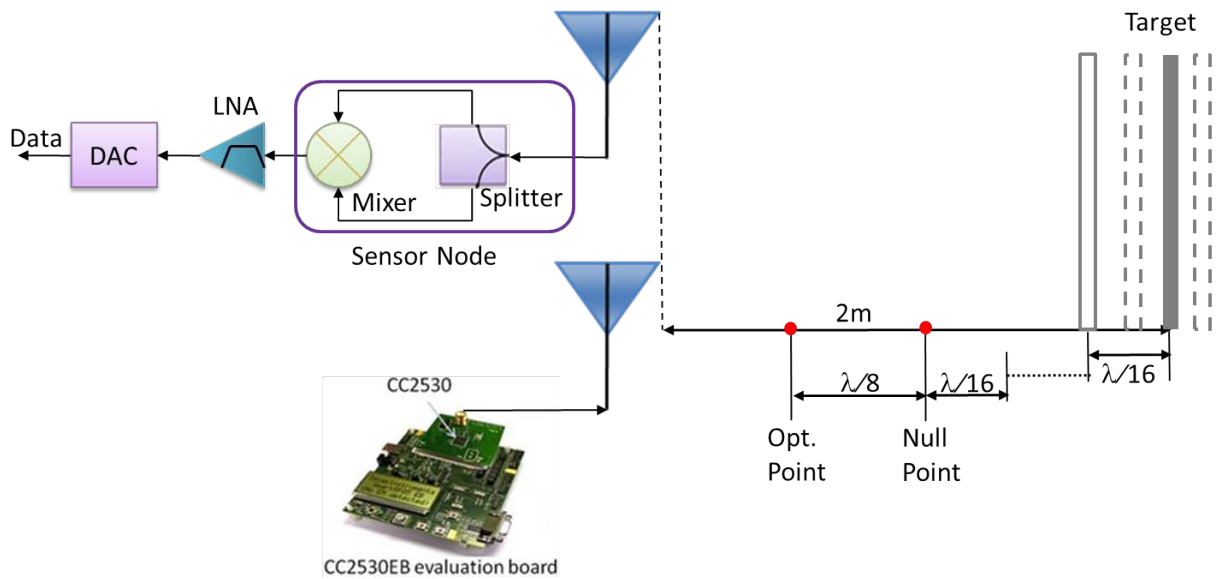


Fig. 4.18. The illustration of experiment setup for the sensitivity testing of Doppler radar occupancy sensor with sensor node at null and optimum points.

The testing was performed under various programmed output power for each of the three transmitted waveforms – CW, modulated CW and packet mode. The purpose to test various output power level is to find the lowest detectable output power, *i.e.*, the minimum operational output power. In all the testing, the baseband signals were passed through Stanford Research System Model SR560 Low Noise Amplifiers for amplification and filtering. The mixers' output were amplified by a factor of 500, and subjected to 6 dB/octave high-pass filtering at 0.03 Hz to remove DC offset. After the high-pass filter, 6

dB/octave low-pass filtering with 1 kHz cutoff frequency was applied. Finally, signals were recorded by a NI USB-6259 to the PC with the sampling rate of 3kHz.

4.3.2 Experimental Results

At original position and after each step with the movement of sixteenth of a wavelength, raw data digitized with DAQ were recorded and processed with Matlab. For CW and modulated CW modes, the data were filtered with FIR low pass filter first and then fed with FFT to extract the periodic motion rate of the mechanical target. For packet mode data, FFT will be applied to the spline interpolated envelop signal which was extracted from the raw data by peak detection.

Figures 4.19 through Fig. 4.24 are the results for both null and optimum points at output power of +4.5 dBm, respectively operated at CW, modulated CW, and packet modes. In all the figures for CW and modulated CW modes, top shows the raw data digitized with NI DAC, middle shows data filtered by a FIR low pass filter with cut-off frequency of 2Hz, and the bottom shows the filtered data in frequency domain by applying FFT. In Fig. 4.23 and Fig. 4.24 for packet mode, top shows the raw data and peaks which are detected by the local maximum algorithm, middle illustrates the result interpolated with spline method, and bottom shows the FFT result in frequency domain.

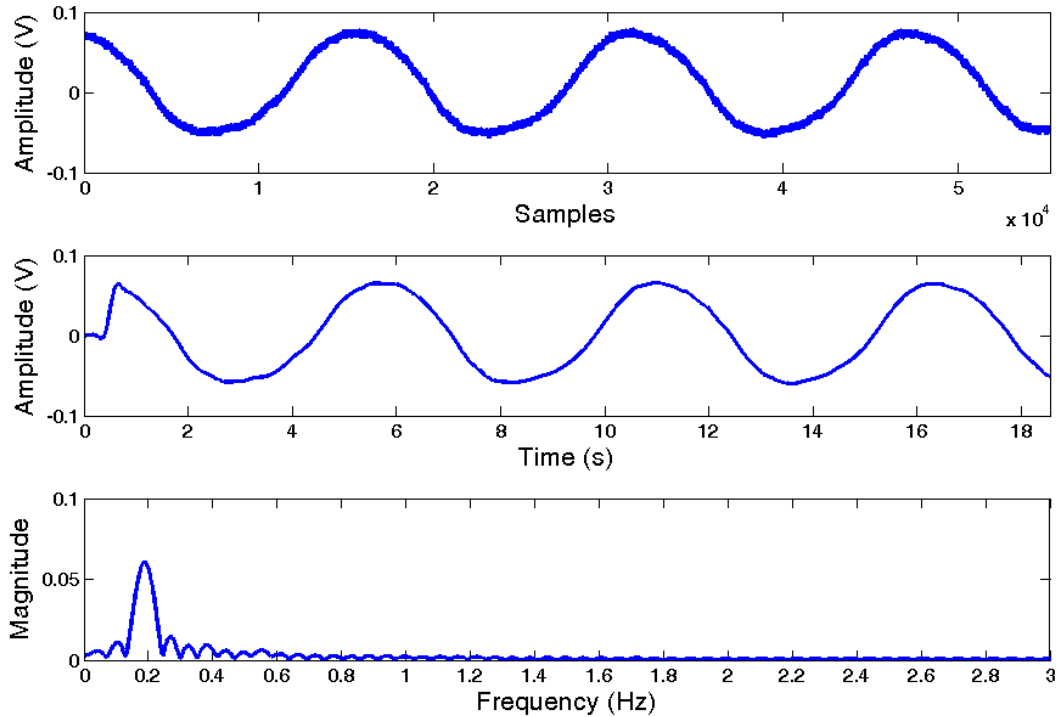


Fig. 4.19 Measured result for optimum point at an output power of +4.5 dBm and frequency of 2.405 GHz when operated at CW mode. Top: raw data, Middle: digital low pass filtered data, and Bottom: FFT analyzed result: periodic motion rate of the mechanical target at 0.2 Hz.

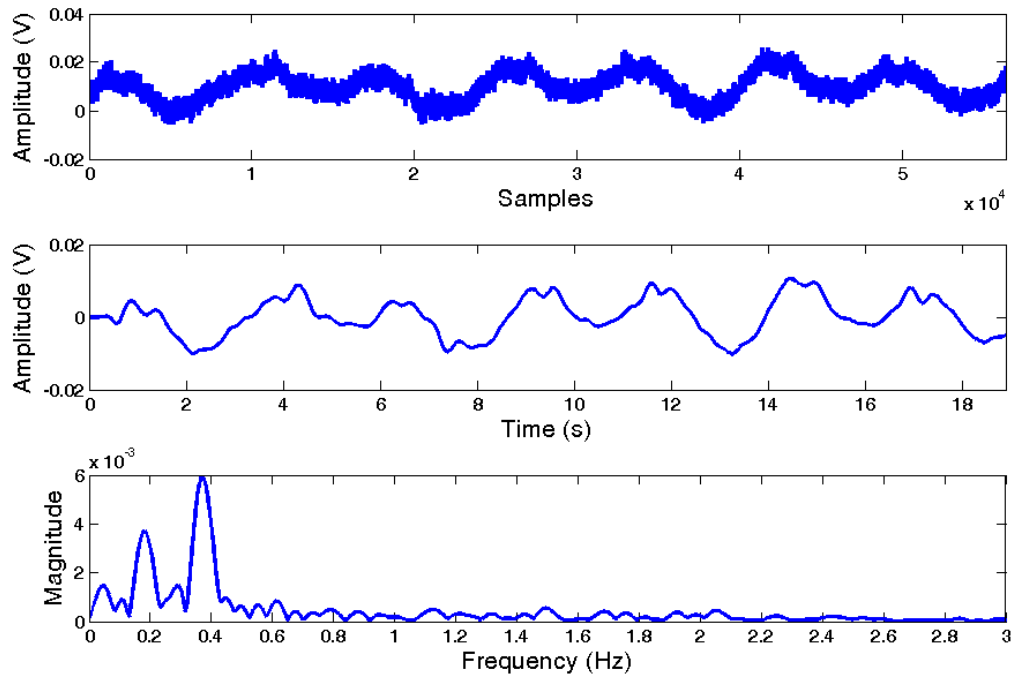


Fig. 4.20 Measured result for null point at an output power of +4.5 dBm and frequency of 2.405 GHz when operated at CW mode. Top: raw data, Middle: digital low pass filtered data, and Bottom: FFT analyzed result: two peaks appear at original motion rate of 0.2 Hz and 0.4 Hz.

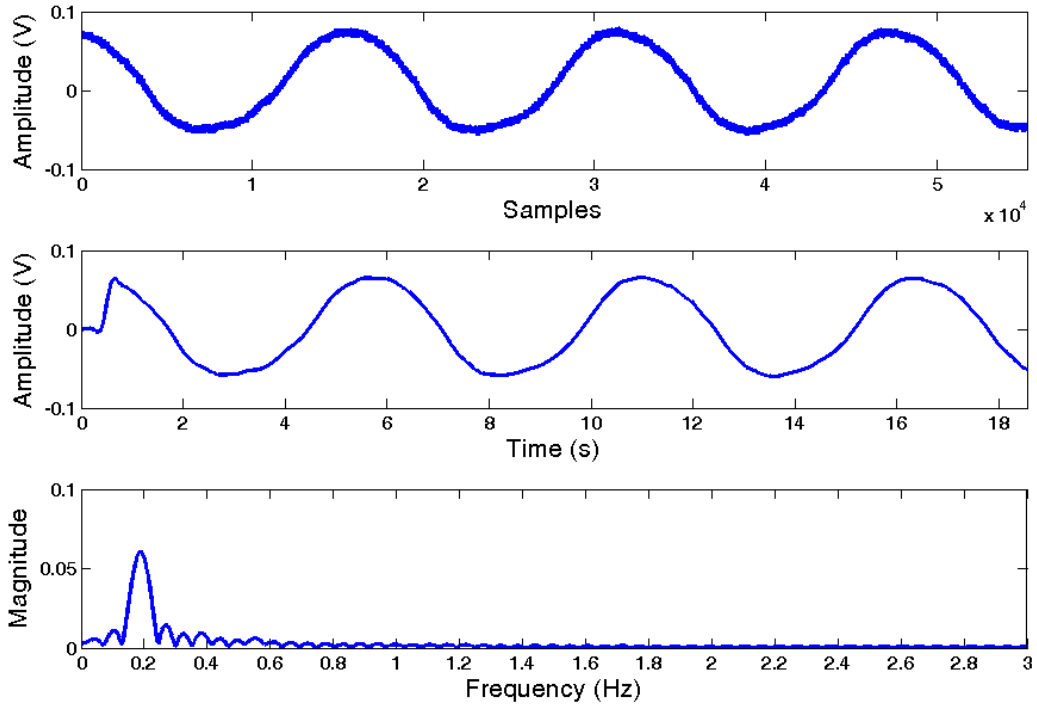


Fig. 4.21 Measured result for optimum point at an output power of +4.5 dBm and frequency of 2.405 GHz when operated at modulated CW mode. Top: raw data, Middle: digital low pass filtered data, and Bottom: FFT analyzed result: periodic motion rate of the mechanical target at 0.2 Hz.

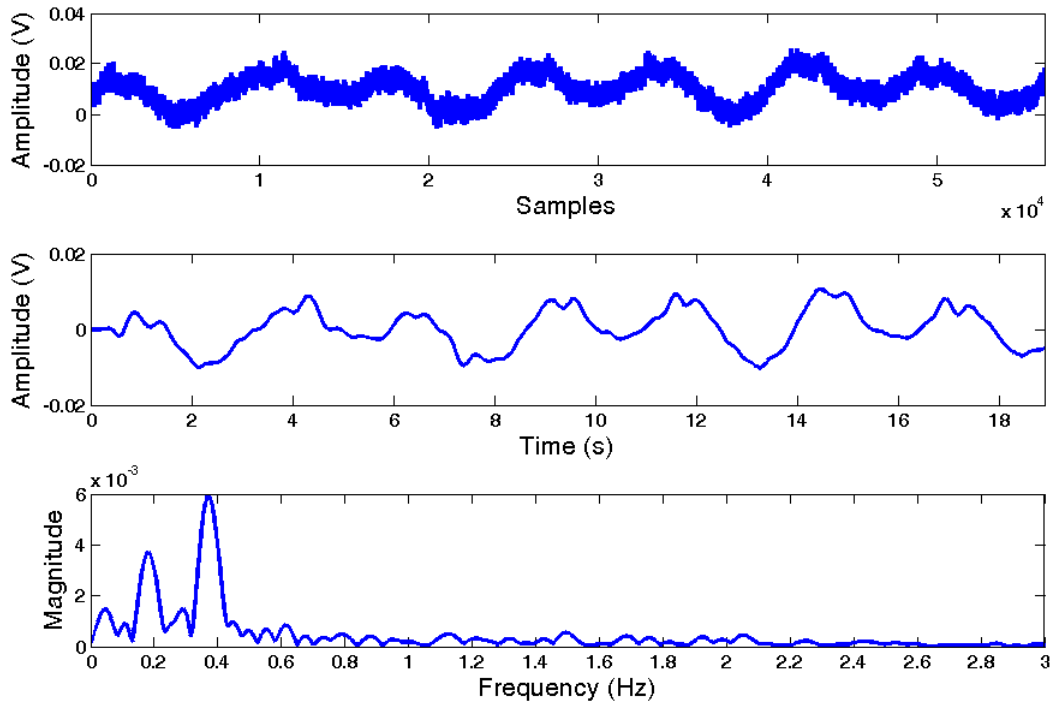


Fig. 4.22 Measured result for null point at an output power of +4.5 dBm and frequency of 2.405 GHz when operated at modulated CW mode. Top: raw data, Middle: digital low pass filtered data, and Bottom: FFT analyzed result: two peaks appear at 0.2 Hz original motion rate and 0.4 Hz.

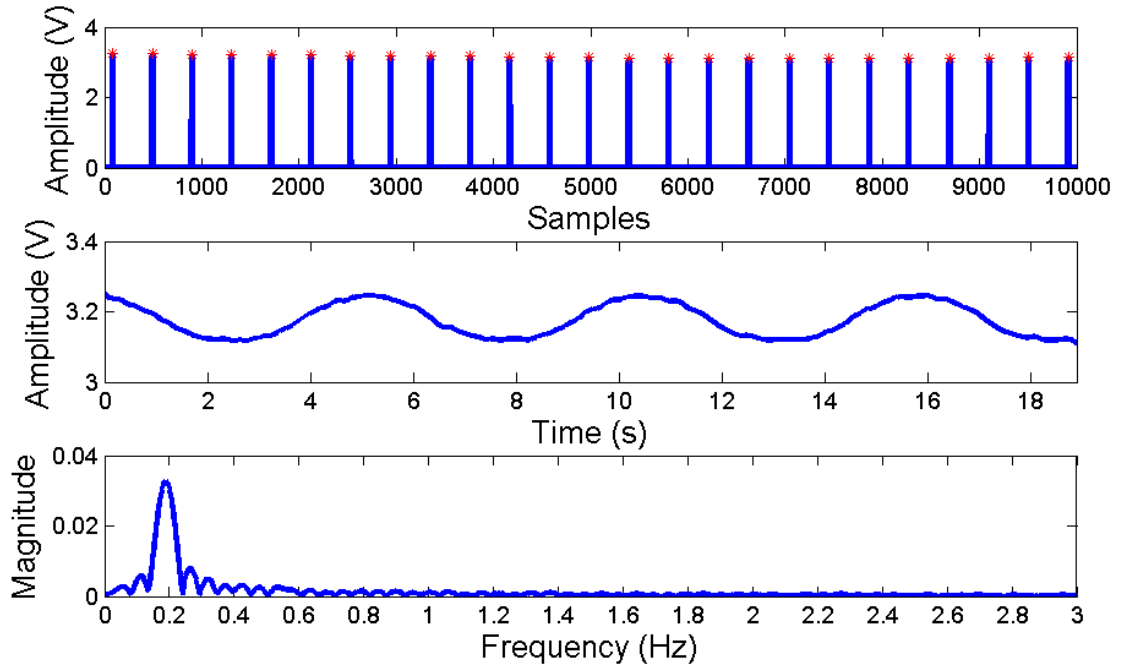


Fig. 4.23 Measured result for optimum point at an output power of +4.5 dBm and frequency of 2.405 GHz when operated at packet mode. Top: raw data, Middle: digital low pass filtered data, and Bottom: FFT analyzed result: periodic motion rate of the mechanical target at 0.2 Hz.

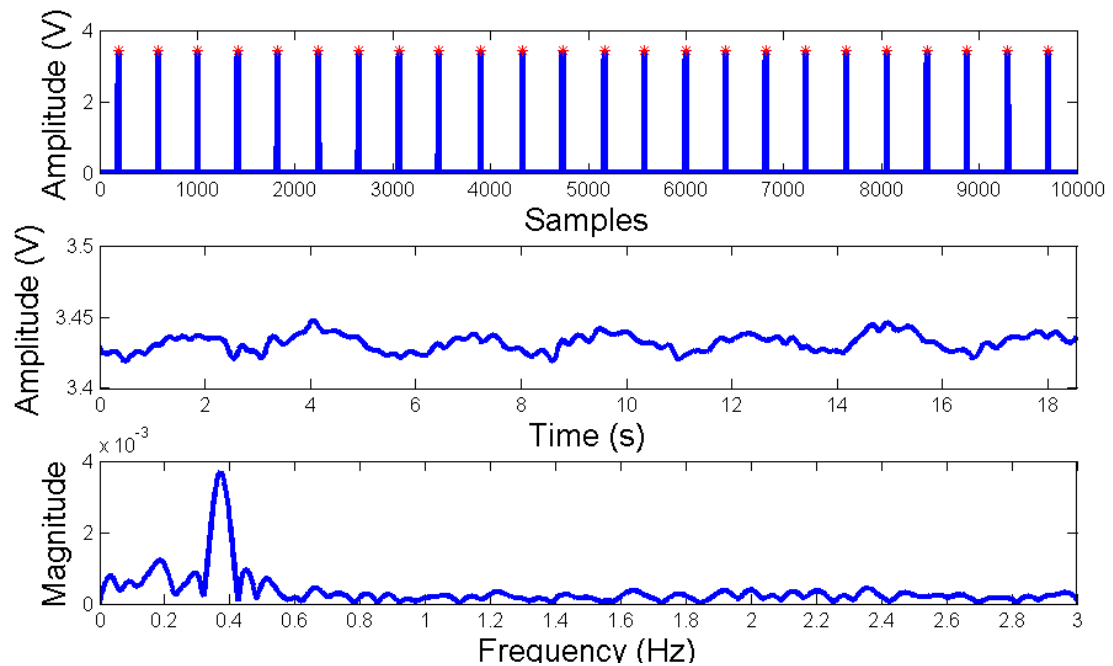


Fig. 4.24 Measured result for null point at an output power of +4.5 dBm and frequency of 2.405 GHz when operated at packet mode. Top: raw data, Middle: digital low pass filtered data, and Bottom: FFT analyzed result: one peak appears at 0.4 Hz.

Compared with the optimum point, the amplitude of the signal at a null point is much smaller, and a peak with frequency doubled of the original motion appears in the spectrum. This means at null points, in addition to the decreased sensitivity, the frequency information could be misinterpreted by the sensor.

The same testing and analysis were repeated at various output power levels for both null and optimum points until the lowest detectable transmitted power was found. The lowest detectable output power level is defined as the power level at the previous stage of the one at which no peak at the corresponding frequency is found. The lowest detectable output power for the sensor at the null point when it is operated at CW mode is -10.5 dBm at both CW and modulated CW modes, and -9.5 dBm at packet mode. When the sensor is at the optimum point, the lowest detectable output power is -22 dBm for all three transmitting modes. The results are shown in Fig. 4.25 through Fig. 4.30.

The experimental results show that a reduction in sensitivity appears at the null points, as well as a distortion in the motion frequency for the Doppler radar occupancy sensor built with passive sensor node. However, the distorted frequency occurs at double of the original motion frequency alone or accompanied with the original frequency. This clear pattern can still provide useful information for developing an occupancy algorithm.

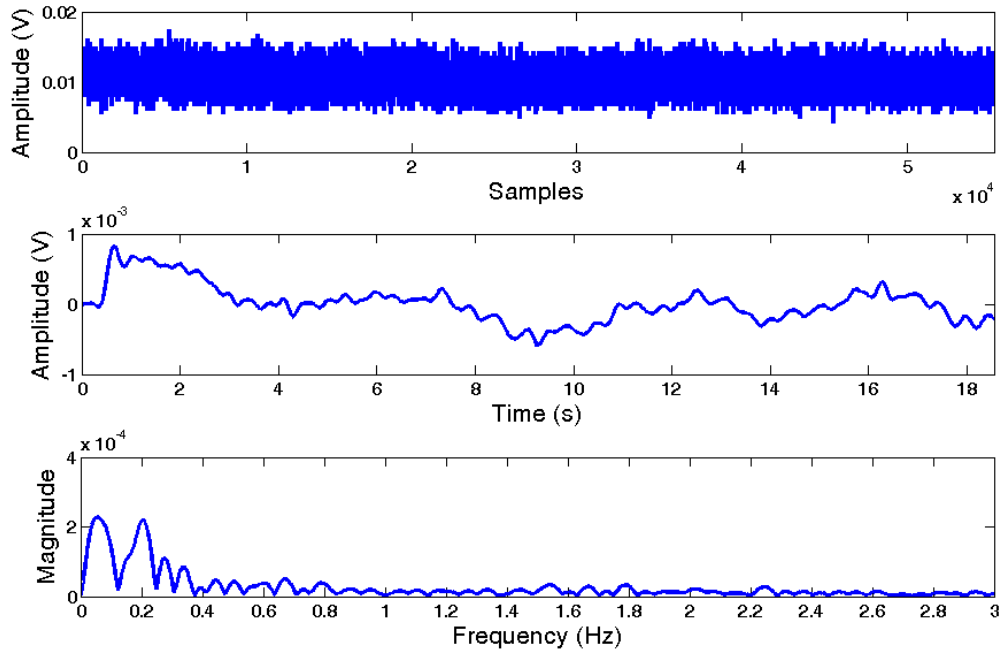


Fig. 4.25 Measured result for optimum point at output power -22 dBm and frequency of 2.405 GHz when operated at CW mode. Top: raw data, Middle: digital low pass filtered data, and Bottom: FFT analyzed result: 0.2 Hz periodic motion rate peak is buried in other peaks.

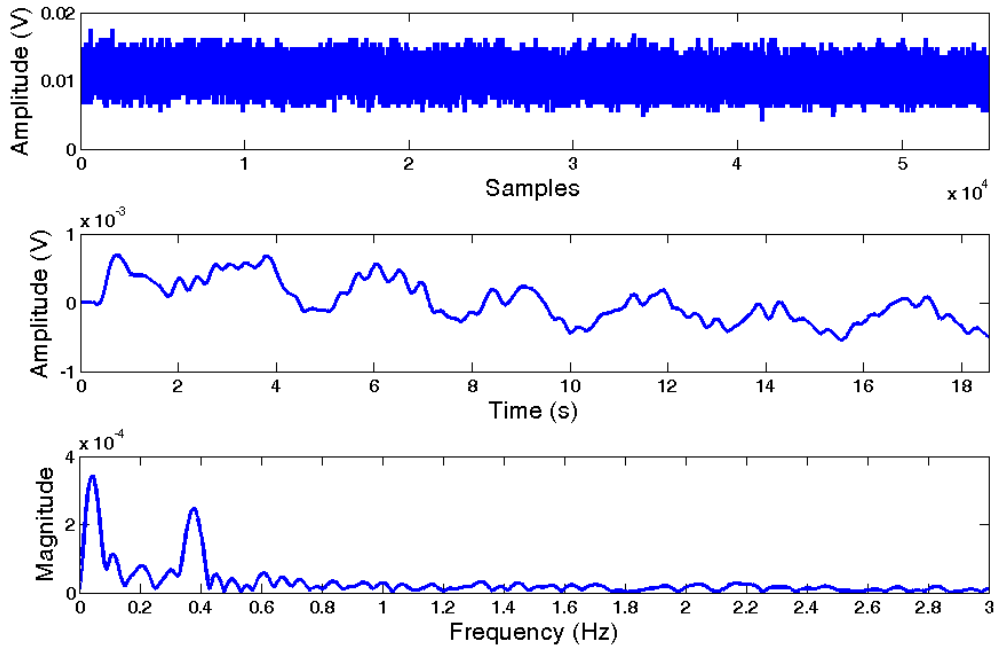


Fig. 4.26 Measured result for null point at output power -10.5 dBm and frequency of 2.405 GHz when operated at CW mode. Top: raw data, Middle: digital low pass filtered data, and Bottom: FFT analyzed result: periodic motion rate of the mechanical target appears at 0.4 Hz.

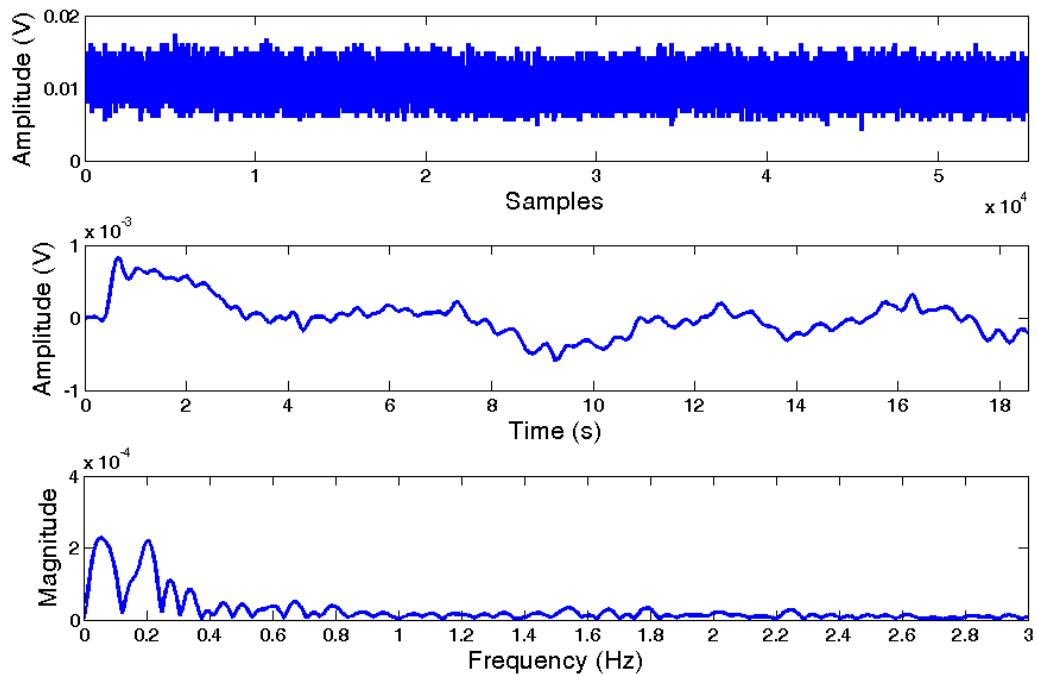


Fig. 4.27 Measured result for optimum point at output power -22 dBm and frequency of 2.405 GHz when operated at modulated CW mode. Top: raw data, Middle: digital low pass filtered data, and Bottom: FFT analyzed result: 0.2 Hz periodic motion rate peak is buried in other peaks.

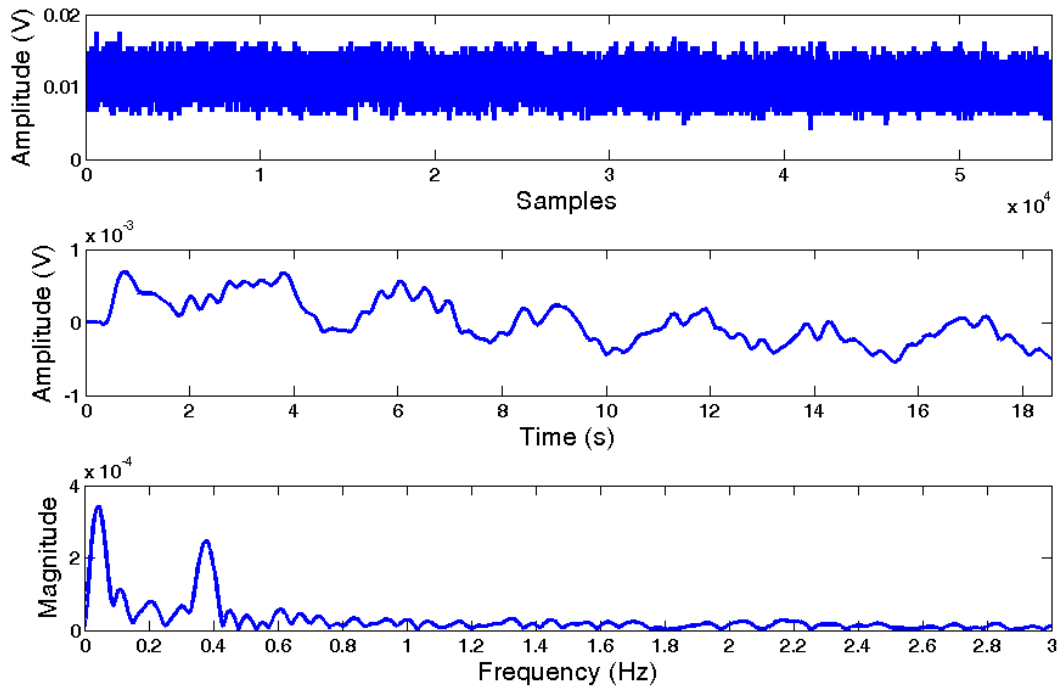


Fig. 4.28 Measured result for null point at an output power of -10.5 dBm and frequency of 2.405 GHz when operated at modulated CW mode. Top: raw data, Middle: digital low pass filtered data, and Bottom: FFT analyzed result: periodic motion rate of the mechanical target appears at 0.4 Hz.

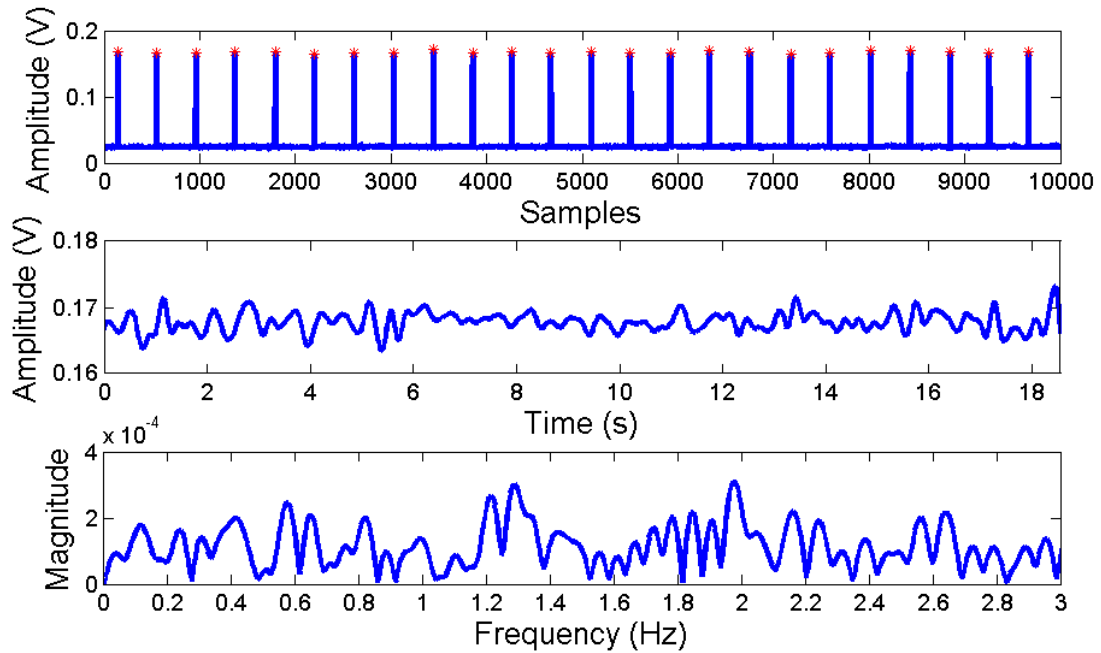


Fig. 4.29 Measured result for null point at an output power of -9.5 dBm and frequency of 2.405 GHz when operated at CW mode. Top: raw data, Middle: digital low pass filtered data, and Bottom: FFT analyzed result: 0.2 Hz periodic motion rate peak is buried in other peaks.

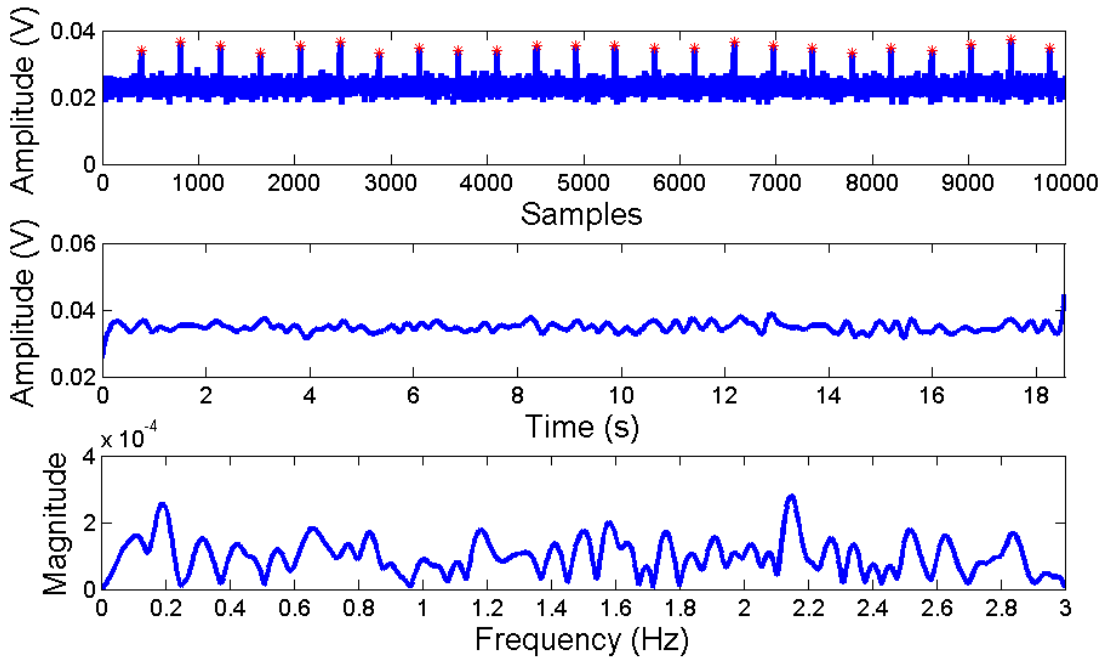


Fig. 4.30 Measured result for optimum point at output power -22 dBm and frequency of 2.405 GHz when operated at CW mode. Top: raw data, Middle: digital low pass filtered data, and Bottom: FFT analyzed result: 0.2 Hz periodic motion rate peak is buried in other peaks.

4.4 Conclusion

This chapter shows the feasibility of building a Doppler radar occupancy sensor with off-the-shelf SoC's and a passive sensor node. By considering the combination of power consumption, working range and cost, we choose TI's CC2350 and CC430 were chosen to provide radar signal source and computation platform. The passive sensor node consists of a splitter and mixer conjunctional with a receive antenna.

Sensitivity and power consumption of its three operation mode have been measured and compared. Though the packet mode is slightly inferior to CW and modulated CW mode in sensitivity, it is superior in power efficiency (up to 82% less power consumption) to the other two modes. Low cost and power efficient Doppler radar occupancy sensor built with CC2530 can be achieved with packet mode operation at the programmed optimum output power level.

This sensor shows similar sensitivity in lowest detectable output power to the quadrature receiver at non-null points: -23 dBm for CW mode, -22 dBm for modulated CW mode, and -20 dBm for packet mode by using passive sensor node vs. -22 dBm for all three transmitting mode by using quadrature receiver. Comparing with optimum points, the sensitivity of the sensor deceases by 10dB and its spectrum pattern is off from original one in the way where a peak appears at the double of the original motion rate. However, the characteristics of the double of original frequency can still provide useful information to build occupancy algorithm.

Chapter 5 Algorithm of True Presence Occupancy Detection

The Doppler radar occupancy sensor detection algorithm is developed based on monitoring respiration patterns. Doppler radar senses all motion in the field of view, and the phase modulation generated by a human subject typically consists of locomotion, fidgeting, respiratory effort, and heartbeat signals [68]. Locomotion and fidgeting produce large amplitude signals that are easily discerned using Doppler radar, as well as commercially available PIR and ultrasonic sensors [68]. Therefore, the algorithm development will focus on stationary subject detection based on detected cardiopulmonary motion.

As references [67] and [68] indicate the successful true presence detection of proposed Doppler radar occupancy sensor is based on the detection of cardiopulmonary activity and its patterns. The respiration is usually in the frequency range 0.1-0.8 Hz and heartbeat in the range of 0.8-2 Hz. Since the chest motion associated with respiration is typically two orders of magnitude stronger signal than that of the heartbeat, this chapter will explore how to characterize the respiration pattern and apply it for subject detection.

5.1 Respiration Signal Pattern Analysis of Doppler Radar Occupancy Sensor with SoC and Passive Node

5.1.1 Analysis with Sinusoidal model

5.1.1.1 Simulation

Assuming the RF transmitter on the SoC sends out a single-tone CW signal,

$$S_t(t) = \cos(2\pi f_0 t + \phi(t)), \quad (5.1)$$

where f_0 is the frequency of the transmitted microwave signal, t is the elapsed time and $\phi(t)$ is the phase noise of the oscillator in the transmitter. Once this signal illuminates a

subject at a nominal distance d_0 from the SoC radar sensor, it will be phase-modulated by the periodic chest movement, and the reflected signal can be expressed as:

$$S_r(t) = \cos\left(2\pi f_0 t + \frac{2\pi}{\lambda}(2d_0 + 2d(t)) + \phi\left(t - \frac{2d_0}{c}\right)\right), \quad (5.2)$$

where $d(t)$ represents chest displacement.

The chest movement is caused by two physiological activities – respiration and heart beat. Assuming respiration and heart beat are two independent time-varying motion with displacements given by $x(t)$ and $y(t)$, then the round trip distance of radar signal is

$$2d(t) = 2d_0 + 2x(t) + 2y(t). \quad (5.3)$$

Replacing $2d(t)$ in equation (5.2) with (5.3), when the chest movement period $T \gg d_0/c$, where c is the velocity of the microwave signal, and $x(t) \ll d_0$, $y(t) \ll d_0$, the received signal can be approximated as

$$S_r(t) = \cos\left(2\pi f_0 t + \frac{4\pi d_0}{\lambda} + \frac{4\pi x(t)}{\lambda} + \frac{4\pi y(t)}{\lambda} + \phi\left(t - \frac{2d_0}{c}\right)\right) \quad (5.4)$$

Since the passive sensor node in the sensor mixes the sum of air-coupled transmitted and reflected signal with itself, the resulting low-pass-filtered mixer output signal, e.g. the base band signal will be

$$B_r(t) = \cos\left(\theta + \frac{4\pi x(t)}{\lambda} + \frac{4\pi y(t)}{\lambda} + \Delta\phi(t)\right), \quad (5.5)$$

where $\Delta\phi(t)$ is the residual phase noise, and θ is the constant phase shift related to the nominal distance to the subject with a factor θ_0 which compensates for the phase change at the surface of a target and phase delay between the mixer and antenna. Each is expressed as

$$\Delta\phi(t) = \phi(t) - \phi\left(t - \frac{2d_0}{c}\right), \quad (5.6)$$

$$\theta = 2\pi f_0 t + \frac{4\pi d_0}{\lambda} + \theta_0. \quad (5.7)$$

Since the passive sensor node in this research is essentially a single channel receiver, the output signal from it will vary with respect to θ for a certain motion of $x(t)$ and $y(t)$. For a given radar system, such as the occupancy sensor in this research, f_0 and

θ_0 have fixed value. The change of the output signal respect to θ eventually projects on the nominal distance d_0 between the subject and the radar.

When θ is an odd multiple of $\pi/2$, *i.e.*, the subject is at optimum points, we can apply the small-angle approximation to equation (5.5), which will turn the equation into

$$B_r(t) = \frac{4\pi x(t)}{\lambda} + \frac{4\pi y(t)}{\lambda} + \Delta\phi(t). \quad (5.8)$$

As a first order approximation, the displacements associated with respiration and heart activity, $x(t)$ and $y(t)$ can be replaced by sinusoidal waves with corresponding frequencies and amplitudes. Hence, the base band signal $B_r(t)$ will become

$$B_r(t) \approx A\sin 2\pi f_1 t + B\sin 2\pi f_2 t + \Delta\phi(t), \quad (5.9)$$

where f_1 is the frequency of respiration, f_2 the heartbeat frequency, A and B are corresponding amplitude, and $f_1 < f_2$, and $A \gg B$. This expression shows that the output signal is linearly proportional to the chest motion. Therefore, with appropriate filtering, information on the respiration and heartbeat will be obtained.

When θ is an integer multiple of π , *i.e.*, the subject is at null points, the base band output data is in the form of

$$B_r(t) \approx 1 - [A\sin 2\pi f_1 t + B\sin 2\pi f_2 t + \Delta\phi(t)]^2, \quad (5.10)$$

which can be further expanded into the expression of

$$\begin{aligned} B_r(t) \approx 1 - \frac{1}{2} [(A^2 + B^2) - A^2 \cos(4\pi f_1 t) - B^2 \cos(4\pi f_2 t) \\ - 2AB \cos 2\pi(f_1 + f_2)t + 2AB \cos 2\pi(f_1 - f_2)t], \end{aligned} \quad (5.11)$$

by neglecting $\Delta\phi(t)$, if it is much smaller than the other components in the bracket.

As indicated by equation (5.10), the output signal is no longer linearly proportional to the displacement of the chest. Instead, it is proportional to the square of the chest movement and becomes much less sensitive to both respiration and heart motion. In addition to the reduced sensitivity, equation (5.11) suggests that frequency obtained in this way no longer reflects the real rate of the subject's movement.

Depending on the magnitudes of A and B and bandwidth of the filter, the remained information could include one or more of the following: the doubled the original frequencies, the sum of the respiration and heartbeat frequencies, and the difference of them. Since the amplitude of respiration A is usually much greater than the one of heartbeat, double of the real respiration frequency will be expected to dominate in the spectrum after filtering is applied.

When a subject is at a position between null and optimum points, the phenomenon will be too complicated to describe with simple mathematical expression. Therefore, simulation has been done with Matlab to study on how the position of the subject impacts the phase demodulated output of the occupancy sensor in this research.

In simulation, the mathematical models are built with equation (5.5), using the two sinusoidal signals to represent the motion of respiration and heart. The respiration frequency is set at 0.25 Hz, and heartbeat 1.25 Hz. The Doppler radar signal frequency is 2.045 GHz, which is corresponding to the operation frequency of CC2530. The nominal distance between the subject and the sensor is set at 1 m first, then decreased with 64^{th} of wavelength ($\lambda/64$) at the radar operation frequency at each step for total of 36 steps. This simulates the subject moving toward the occupancy sensor.

The simulated results are presented in both time domain and frequency domain in Fig. 5.1 – Fig. 5.7. In these figures, the top graphs show how the waveforms of the phase demodulated output change with the target nominal distance to the radar sensor in the time domain, and the bottom ones tell at which frequencies the corresponding peaks appear in the spectrum as the nominal position of the target varies. In Fig. 5.1, there is a obvious peak at the 0.5 Hz, double of the real simulated respiration rate. This means the target is at a null points. Fig. 5.4 indicates that the target is at an optimum point, since the dominant peak shows up at 0.25 Hz, the programmed respiration frequency. The distance between where the results in Fig. 5.1 and Fig. 5.4 show is $\lambda/8$, which further confirm the two position with these results above are null and optimum points, respectively. Fig. 5.2 and Fig. 5.3 shows both peaks at programmed 0.25 Hz, and double of that frequency. The difference is the amplitude of these two peaks. In Fig. 5.2, the amplitude of 0.25 Hz peak is lower than the one of 0.5 Hz. In Fig. 5.3, the amplitude of 0.25 Hz peak increases,

while the one of 0.5 Hz decreases, resulting the higher peak of 0.25 Hz than the one of 0.5 Hz. The position in Fig. 5.3 is $\lambda/64$ closer to the optimum point in Fig. 5.4, than the position in Fig. 5.2, or equally saying $\lambda/64$ farther to the null point in Fig. 5.1. The results in Fig. 5.1 – Fig. 5.4 implies there is a connection between change in the amplitude of 0.25 Hz and 0.5 Hz peaks and the position relative to the null or optimum point. That is as the subject moves away from null point to optimum point, the amplitude of false frequency (0.5 Hz) peak decreases, while the amplitude of the real respiration frequency (0.25 Hz) increases, until no obvious 0.5 Hz peak is found in the spectrum, while 0.25 Hz reaches the highest value. Correspondingly, as the subject moves further from the null point and closer to the optimum point, the amplitude of the output signal in the time domain keeps increase to the biggest value. This means the increases of the sensitivity from the null point to the optimum point. Once the target from one null point reaches the optimum point, and continues to move beyond the optimum point in the same direction, the change of the amplitude of the signal in both time domain and frequency will be with the reverse tendency, since the target moves away from the optimum point to the next null point, as shown in Fig. 5.1 – Fig. 5.7. Then the amplitude of the real motion frequency peak and the double (of the real one) frequency peak repeats as the target continues get closer to the sensor.

The simulation results on the amplitude at the two frequency peaks and where these peaks appear in the number of $\lambda/64$ steps are summarized in Fig. 5.2. From Fig. 5.8, we can also tell that the optimum and null point are $\lambda/8$ apart, and they repeatedly appear every $\lambda/4$, respectively.

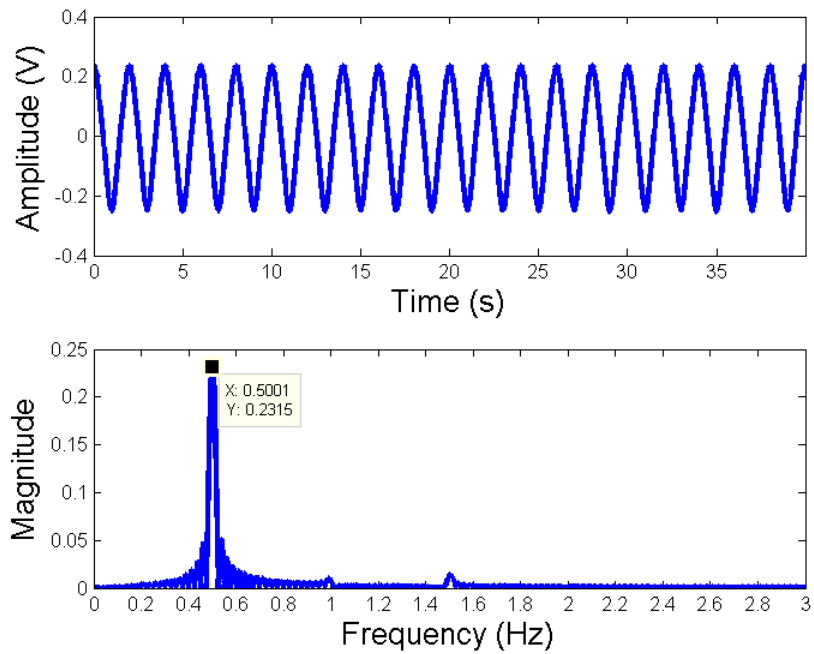


Fig. 5.1 Simulation results on the amplitude of misinterpreted frequency at 0.5 Hz, with data shown in time domain (Top) and frequency domain (Bottom), at nominal distance of 1m (null point).

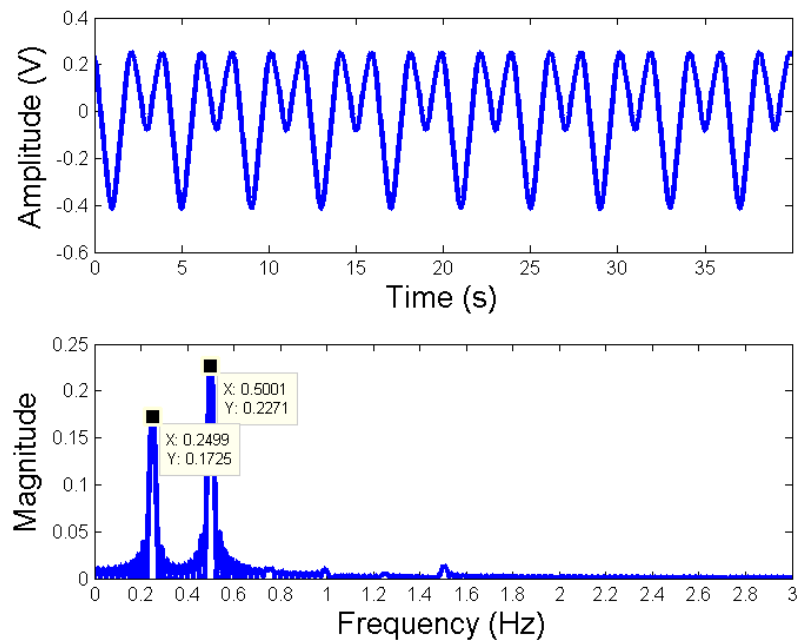


Fig. 5.2 Simulation results on the amplitude of real motion frequency at 0.25 Hz and misinterpreted frequency at 0.5 Hz, with data shown in time domain (Top) and frequency domain (Bottom), at nominal distance of 1m - $\lambda/64$.

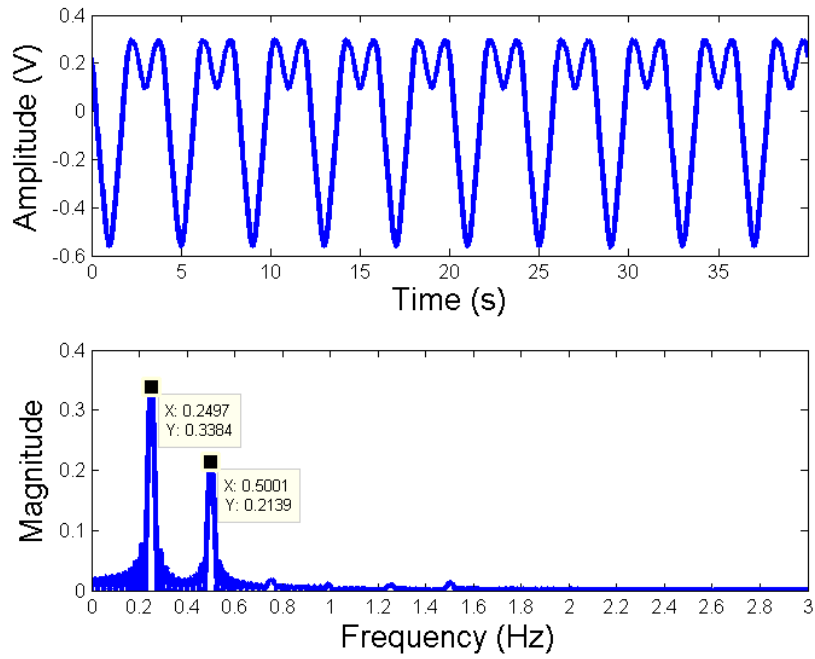


Fig. 5.3 Simulation results on the amplitude of real motion frequency at 0.25 Hz and misinterpreted frequency at 0.5 Hz, with data shown in time domain (Top) and frequency domain (Bottom), at nominal distance of 1m - 2 of $\lambda/64$.

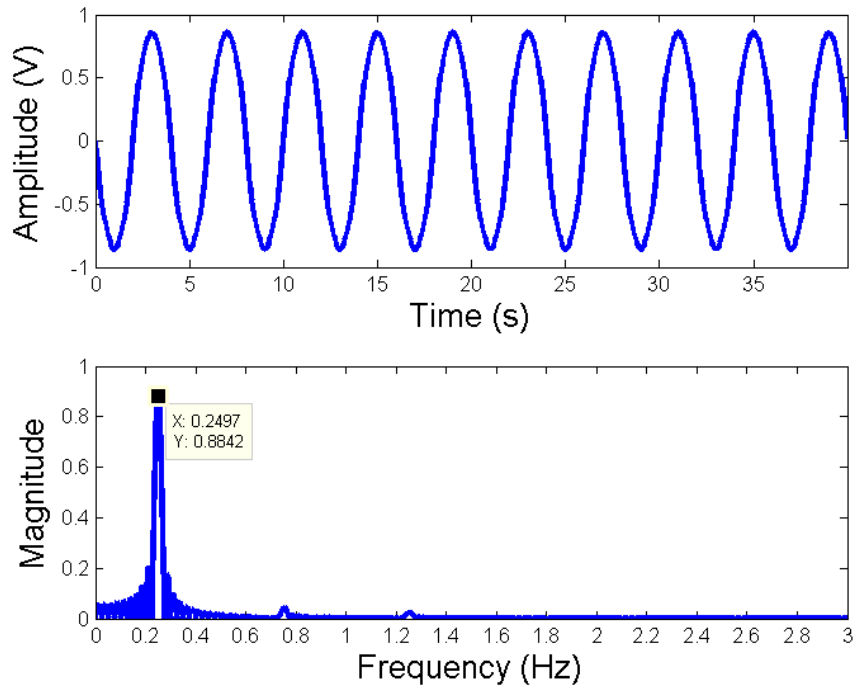


Fig. 5.4 Simulation results on the amplitude of real motion frequency at 0.25 Hz, with data shown in time domain (Top) and frequency domain (Bottom), at nominal distance of 1m - 8 of $\lambda/64$ (optimum point).

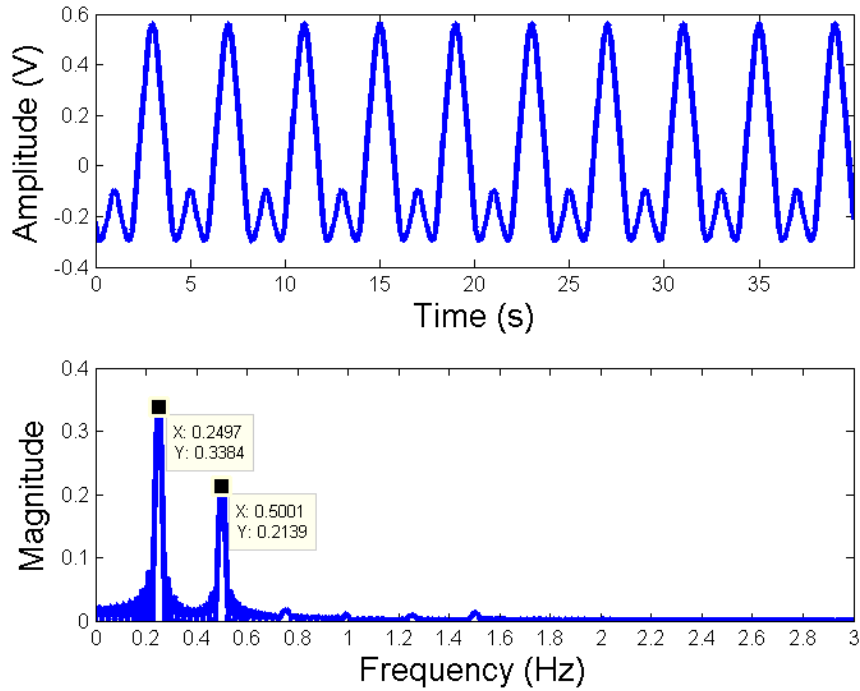


Fig. 5.5 Simulation results on the amplitude of real motion frequency at 0.25 Hz and misinterpreted frequency at 0.5 Hz, with data shown in time domain (Top) and frequency domain (Bottom), at nominal distance of 1m - 14 of $\lambda/64$.

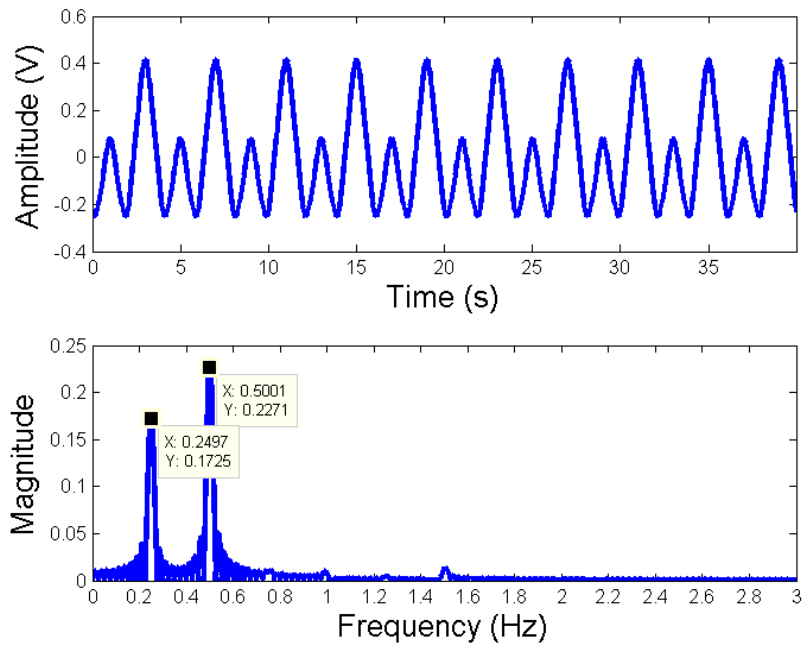


Fig. 5.6 Simulation results on the amplitude of real motion frequency at 0.25 Hz and misinterpreted frequency at 0.5 Hz, with data shown in time domain (Top) and frequency domain (Bottom), at nominal distance of 1m - 15 of $\lambda/64$.

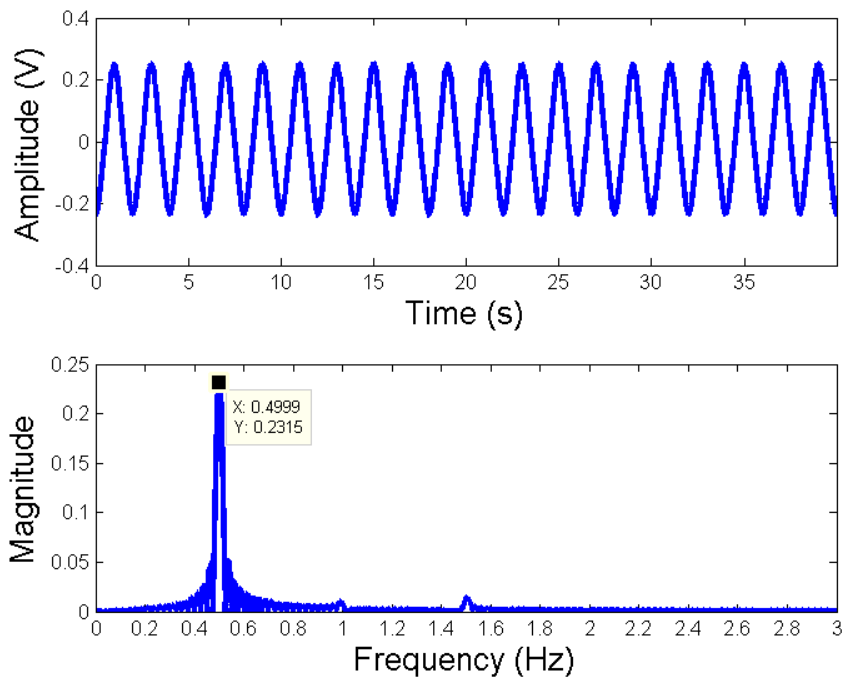


Fig. 5.7 Simulation results on the amplitude of misinterpreted frequency at 0.5 Hz, with data shown in time domain (Top) and frequency domain (Bottom), at nominal distance of 1m - 16 of $\lambda/64$ Null point.

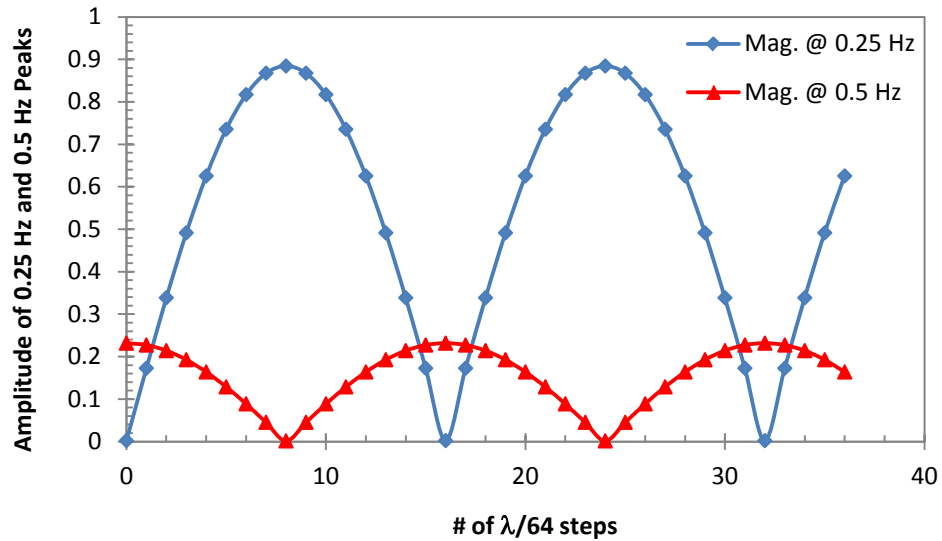


Fig. 5.8 Amplitude of real motion frequency peak at 0.25 Hz and the one at 0.5 Hz changes with the position of the target tells where the target is relative to the null or optimum point.

5.1.1.2 Experiment

In this section, a mechanical target programmed to oscillate with combination of two sinusoidal waveforms at the frequencies of 1.25 Hz and 0.25 Hz and the maximum

displacements of 1 cm and 0.03 cm, respectively, is employed to examine the validity of the simulation in the previous section.

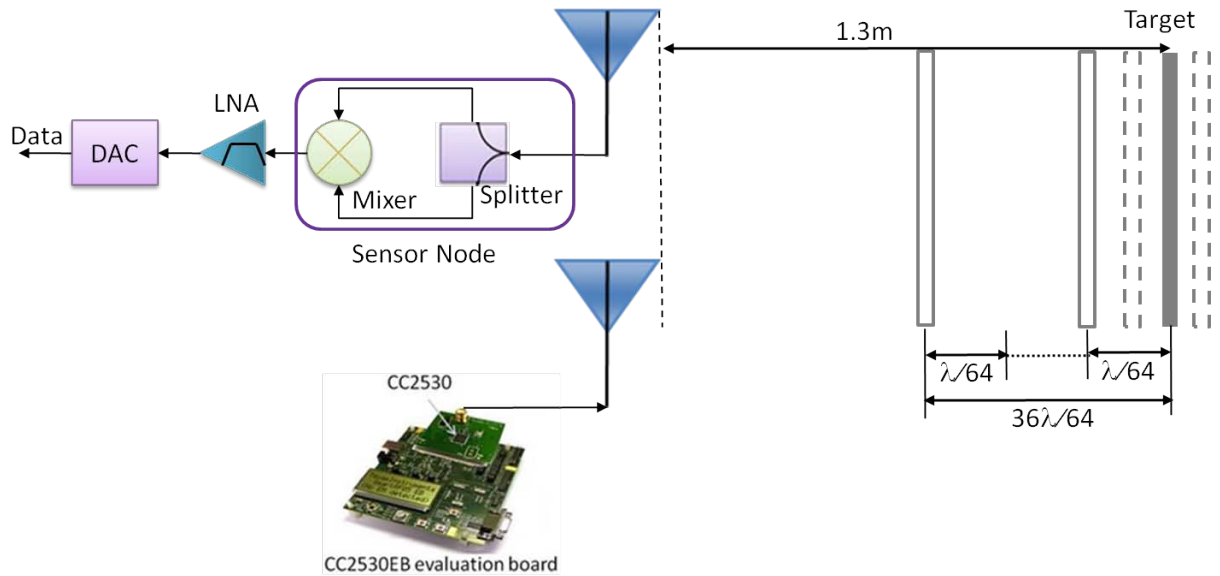


Fig. 5.9 The illustration of experiment setup for the impact of position of periodic moving target on the phase demodulated output.

Fig. 5.9 shows how the experiment is setup for verifying the simulation. A Doppler radar occupancy sensor was built with CC2530 evaluation board and a passive sensor node which is composed of a 3-dB Minicircuits ZFSC-2-2500 power splitter, a Minicircuits ZFM4212 mixer. Two Antenna Specialist (ASPPT2988) antennae with 8 dBi gain and 60 degree E-plane beamwidth used for transmitter and receiver were located close to each other to provide strong coupling signal for LO port of the mixer. The mechanical target was placed 1.3 m from the radar sensor originally. Then the mechanical target was brought closer to the radar sensor by 36 of total incremental with 64^{th} of one wavelength at the operation frequency of 2.405 GHz for each step. At each new position, the mechanical target repeats the programmed movement. The sensor under test was operated at output power of 4.5 dBm for CW mode at each nominal position.

In all the testing, the baseband signals were passed through Stanford Research System Model SR560 Low Noise Amplifiers for amplification and filtering. The mixer's output was amplified by a factor of 200, and subjected to 6 dB/octave low-pass filtering with cutoff frequency of 30 Hz. Finally, signals were recorded by a NI USB-6259 to the PC with the sampling rate of 100 Hz.

Fig 5.10 shows where the peak of real motion frequency and its doubled frequency peak occur, and the amplitude of these two peaks normalized by the maximum value of real frequency peak. For comparison, the simulation data normalized to its maximum amplitude of 0.25 Hz peak is also included in this figure. The experiment data shows the measured oscillation frequency at 0.2568 Hz, very close to the programmed real motion frequency of 0.25 Hz. The locations where the measured double of real frequency peaks and its amplitude relative to 0.2568 Hz peak also follow the simulated closely, e.g. as the nominal position of the target is moving away from null point towards the optimum point, the amplitude of the real motion frequency peak increases, and the misinterpreted frequency at double decreases; while the nominal position of the target is getting closer towards null point from the optimum point, the amplitude of the real motion frequency peak decreases, and the misinterpreted frequency at double increases. The maximum amplitude of the real motion frequency peak presents with the minimal value of the double of it where the target is at optimum points, and vice versa where the target is at null points. The optimum and null points are $\lambda/8$ apart, and they repeat themselves every quarter wavelength.

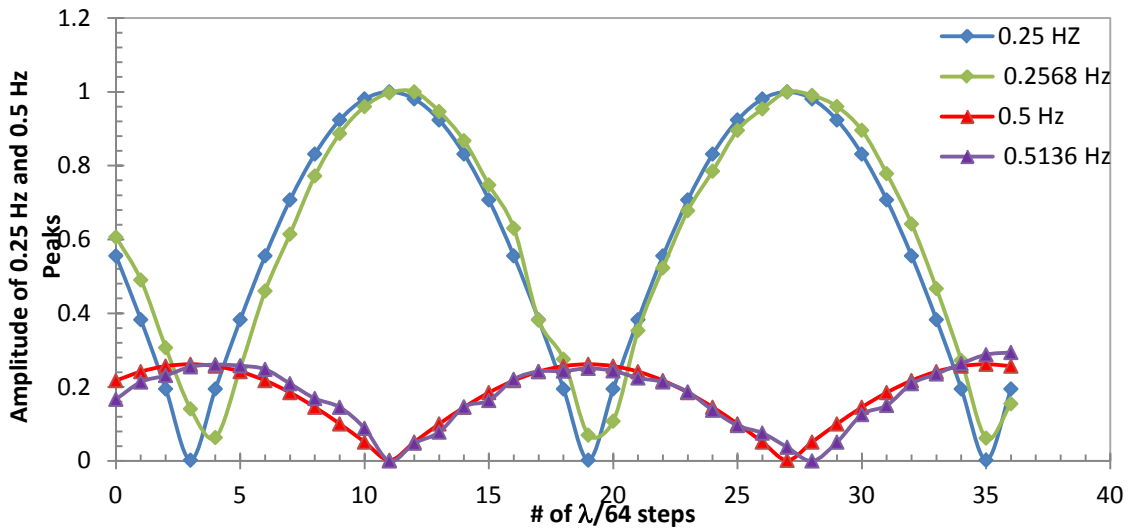


Fig. 5.10 Comparison between simulation and experiment data for the position impact on the phase demodulated sensor output.

Fig. 5.11 – Fig. 5.13 show the detailed information in the time domain and frequency domain for the typical data set at the null point, optimum point and between. At the null point, 0.5136 Hz peak dominates. At the optimum point, the real motion

frequency at 0.2568 Hz dominates. In between, both peaks appear. Which one is higher depends on the target position relative to the null or optimum points.

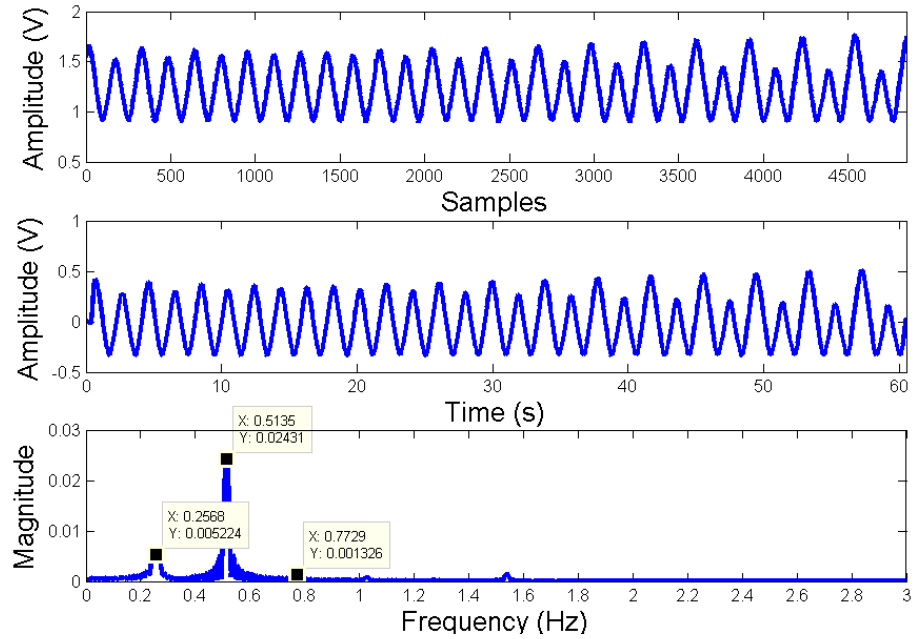


Fig. 5.11 Experimental results on the impact of subject location on phase demodulated sensor output, with raw data shown in time domain (Top), filtered data shown in time domain (Middle) and data in frequency domain (Bottom), at a null point.

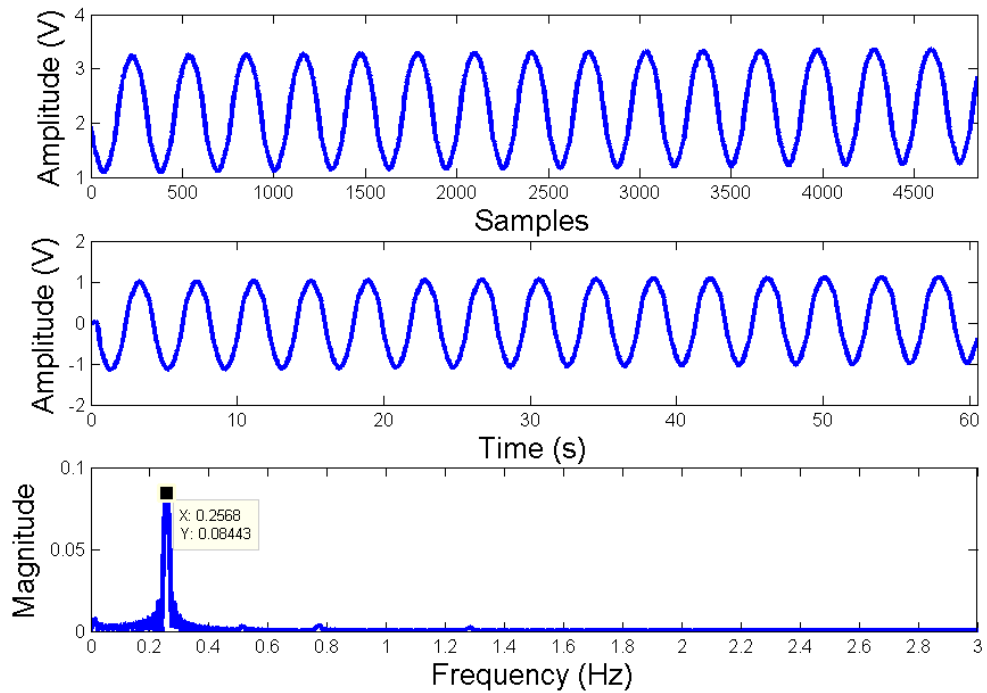


Fig. 5.12 Experimental results on the impact of subject location on phase demodulated sensor output, with raw data shown in time domain (Top), filtered data shown in time domain (Middle) and data in frequency domain (Bottom), at an optimum point.

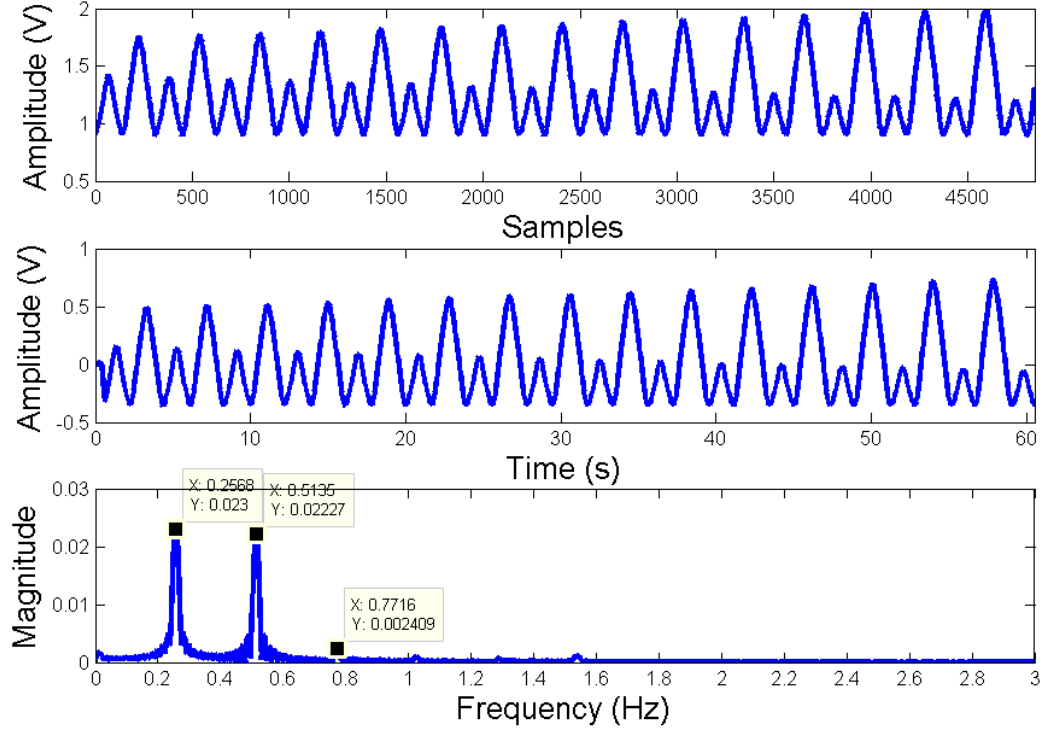


Fig. 5.13 Experimental results on the impact of subject location on phase demodulated sensor output, with raw data shown in time domain (Top), filtered data shown in time domain (Middle) and data in frequency domain (Bottom), at a point between a null point and an optimum point.

Both simulation and experimental results suggest that though the sensitivity and the extracted motion frequency vary with the target position, either the peak representing the real motion frequency or the peak at the double of the real one or both will appear in the spectrum after appropriate filtering. This can be used as the baseline of the occupancy algorithm design.

5.1.2 Analysis with complex model

5.1.2.1 Simulation

In reality, human respiration and heart beat are not in the form of sinusoidal wave. Therefore, in this section, more realistic models are adopted for respiration and heart signals.

An idealized chest motion due to respiration can be modeled with a sinusoidal half-cycle with rounded cusp [69]:

$$p_R(t) = \sin^p \pi f_R t, \quad (5.12)$$

where f_R is respiratory frequency and p controls the rounding of the cusp and the general shape of the signal. Modeling respiratory signals with raised sinusoid has prolonged and narrow halves which are closer to real respiratory signals detected by radar [70].

The heart signal is modeled with an analog pulse of an exponential $e^{t/\tau}$, with time constant τ , filtered by a critically damped second-order Butterworth filter with cutoff frequency f_0 . The the pulse shape repeats at $1/f_H$ with heartbeat frequency f_H . This model has been developed based on the fact of discharging heart ventricles during the systolic phase generates impulsive motion that is subsequently filtered by the bone and tissue to chest wall where radar senses the motion [69]. The resulting characteristic pulse shape is expressed as:

$$p_H(t) = e^{t/\tau} + \left[\left(\frac{\sqrt{2}}{\omega_0\tau} - 1 \right) \sin \frac{\omega_0 t}{\sqrt{2}} - \cos \frac{\omega_0 t}{\sqrt{2}} \right] e^{-\omega_0 t / \sqrt{2}}. \quad (5.13)$$

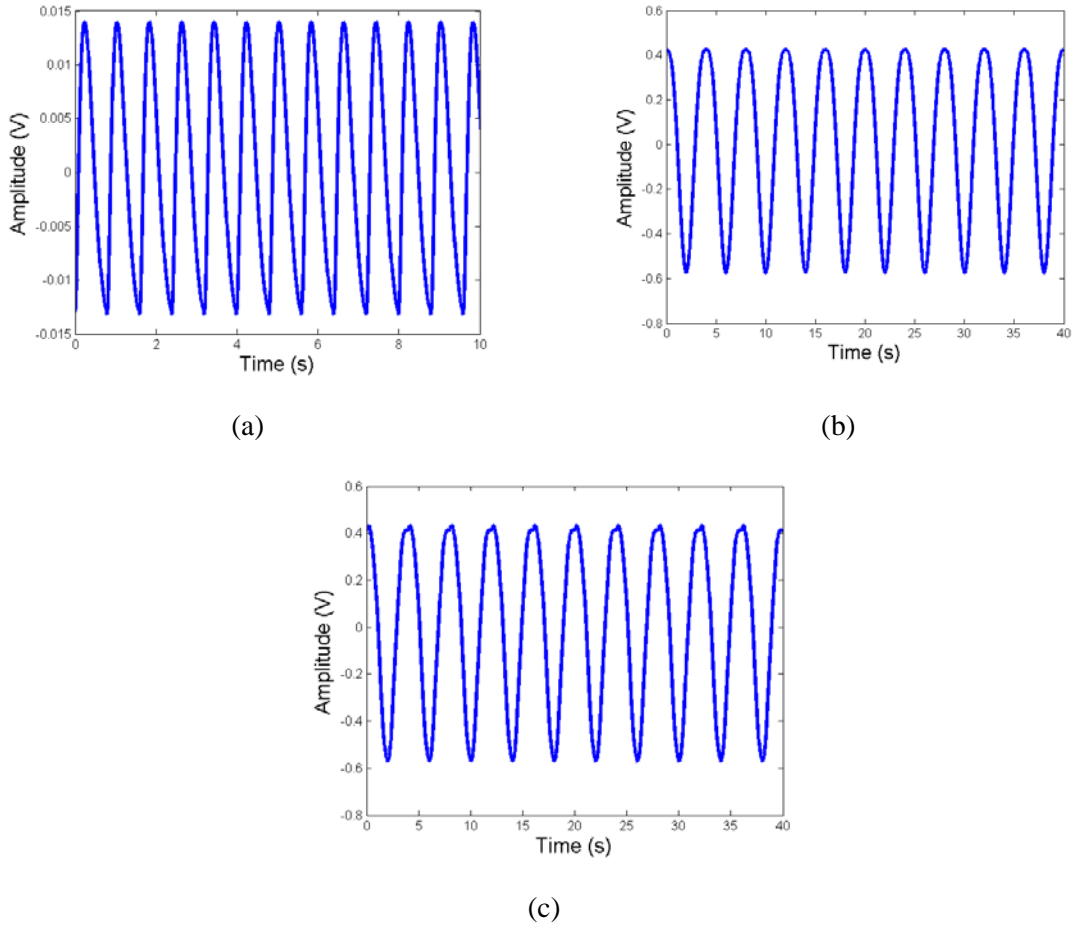


Fig. 5.14 Modeled chest wall motion waveform: (a) heartbeat signal; (b) respiration signal; (c) combination of heartbeat and respiration.

Fig. 5.14 shows the components of the test signal for parameter values that simulate a typical real signal from a live subject. In this simulation, a total of 4000 samples (40 s) are generated at a sampling rate of 100 Hz. The peak-to-peak amplitude of heartbeat signal is 3% of the one for respiration ($A_R = 1$). The heart rate is f_H 1.25Hz and the respiration rate is f_R 0.25Hz. The other parameters, $\tau = 0.05$, $f_0 = 1$ Hz, and $p = 3$ are chosen to best present typical real data. Fig. 5.14 (a) shows the heartbeat signal for 10 seconds, Fig. 5.14 (b) shows the respiration component, and Fig. 5.14 (c) shows the combined signal.

Using the test signal in Fig. 5.9, how the subject location affects the demodulated output data is examined with the same process described in section 5.1.1. The same CW radar signal with frequency of 2.045 GHz, sample frequency 100 Hz, and nominal distances from 1m to $36\lambda/64$ closer to the radar than 1m with $\lambda/64$ incremental at each step were used in the simulation. Figures 5.15 – 5.21 show the time domain and frequency domain patterns of the output signal from null point to optimum point.

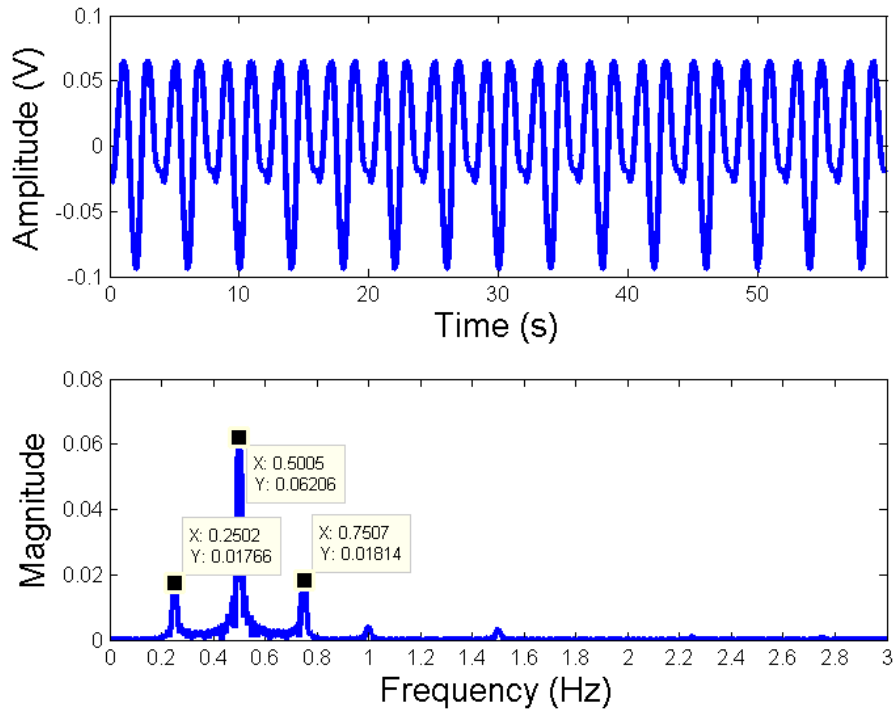


Fig. 5.15 Simulation results on the impact of subject location on demodulated output, with demodulated data shown in time domain (Top) and frequency domain (Bottom), at the distance of 1m (null point).

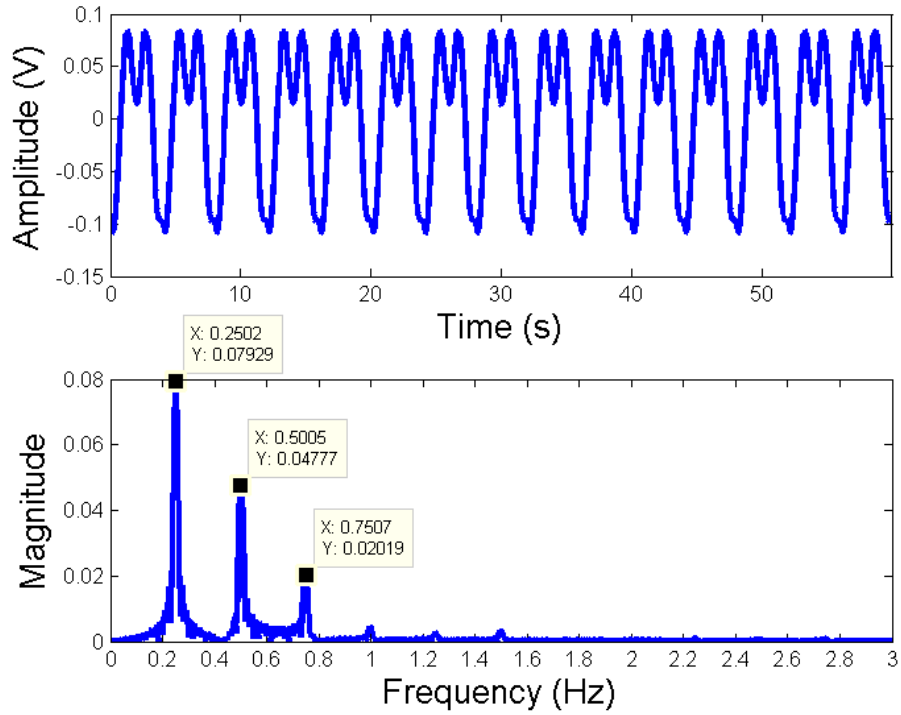


Fig. 5.16 Simulation results on the impact of subject location on demodulated output, with demodulated data shown in time domain (Top) and frequency domain (Bottom), at incremental nominal distance of $1\text{m} - \lambda/64$.

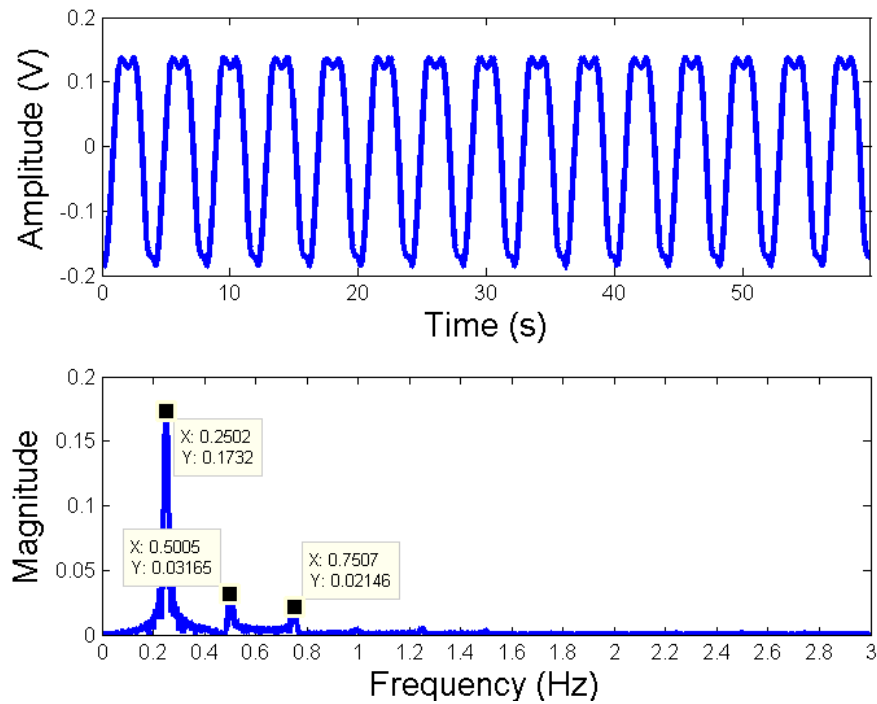


Fig. 5.17 Simulation results on the impact of subject location on demodulated output, with demodulated data shown in time domain (Top) and frequency domain (Bottom), at the nominal distance of $1\text{m} - 2$ of $\lambda/64$.

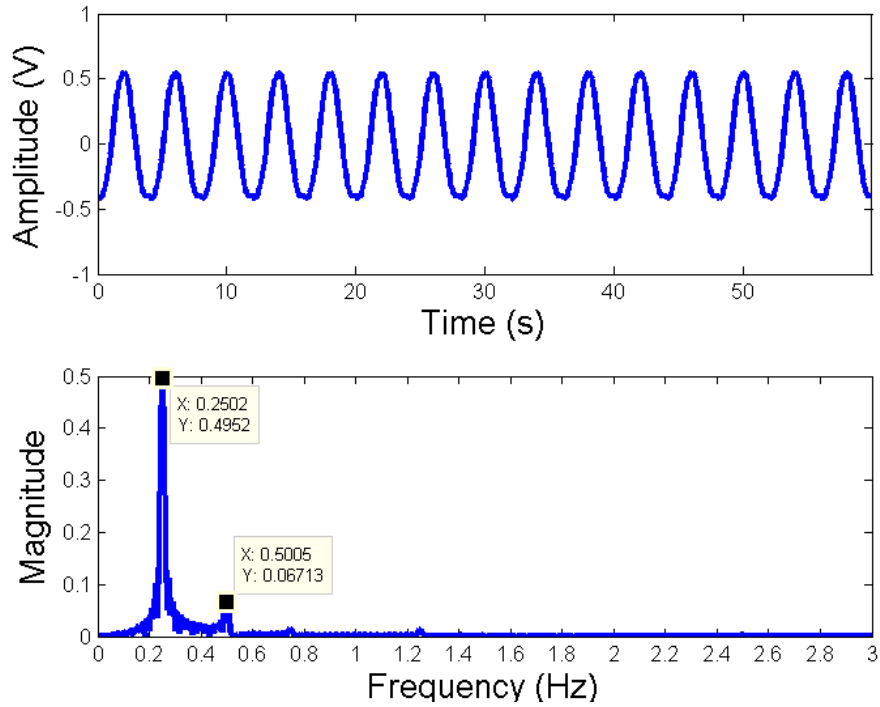


Fig. 5.18 Simulation results on the impact of subject location on demodulated output, with demodulated data shown in time domain (Top) and frequency domain (Bottom), at incremental nominal distance of 1m - 8 of $\lambda/64$ (optimum point).

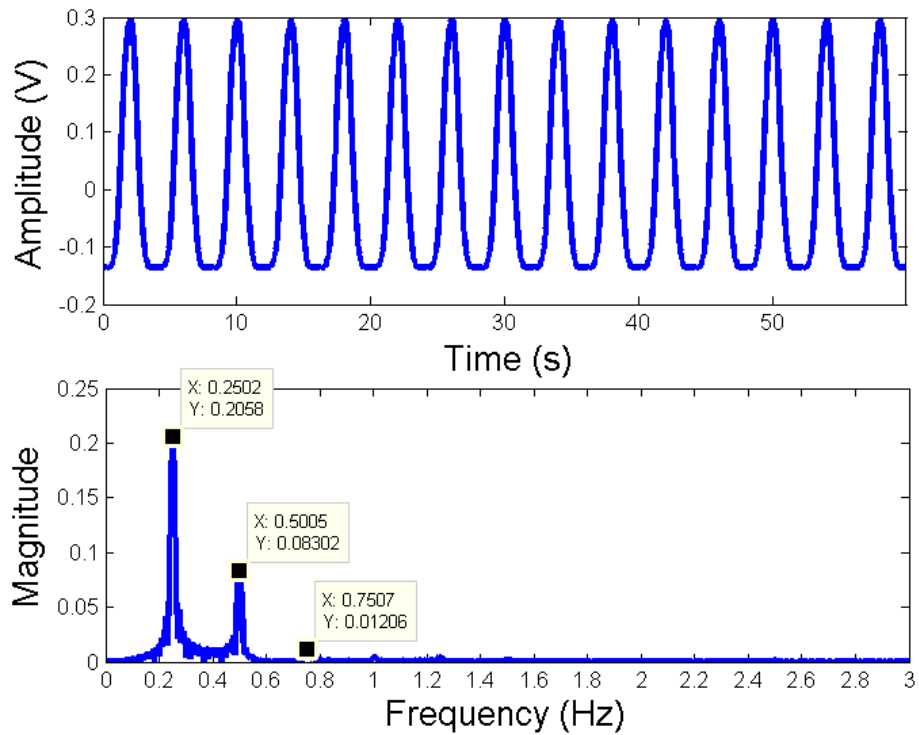


Fig. 5.19 Simulation results on the impact of subject location on demodulated output, with demodulated data shown in time domain (Top) and frequency domain (Bottom), at the nominal distance of 1m - 14 of $\lambda/64$.

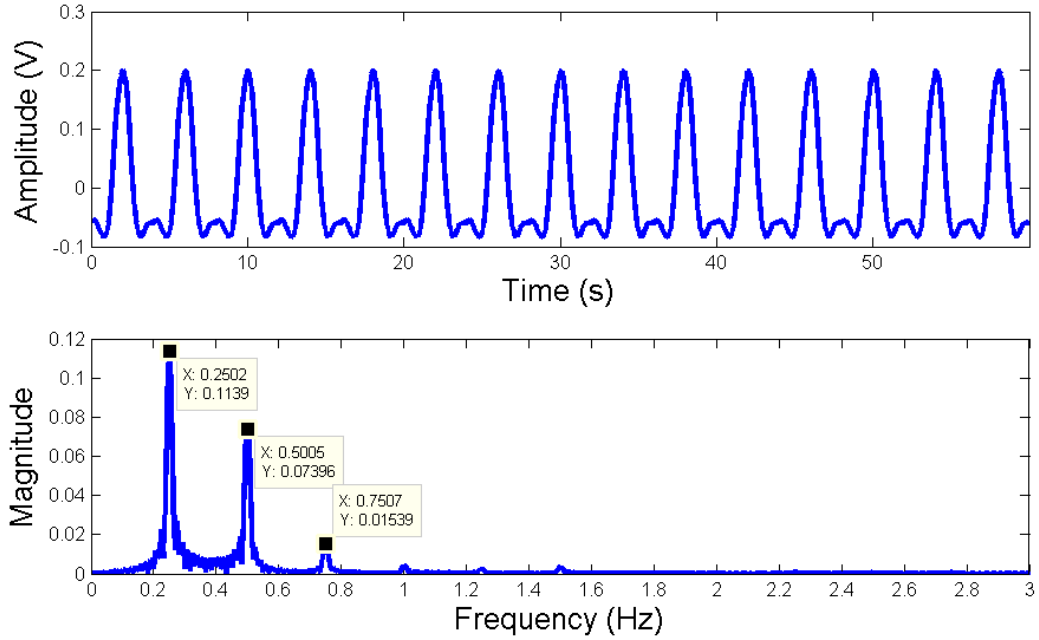


Fig. 5.20 Simulation results on the impact of subject location on demodulated output, with demodulated data shown in time domain (Top) and frequency domain (Bottom), at incremental nominal distance of 1m - 15 of $\lambda/64$.

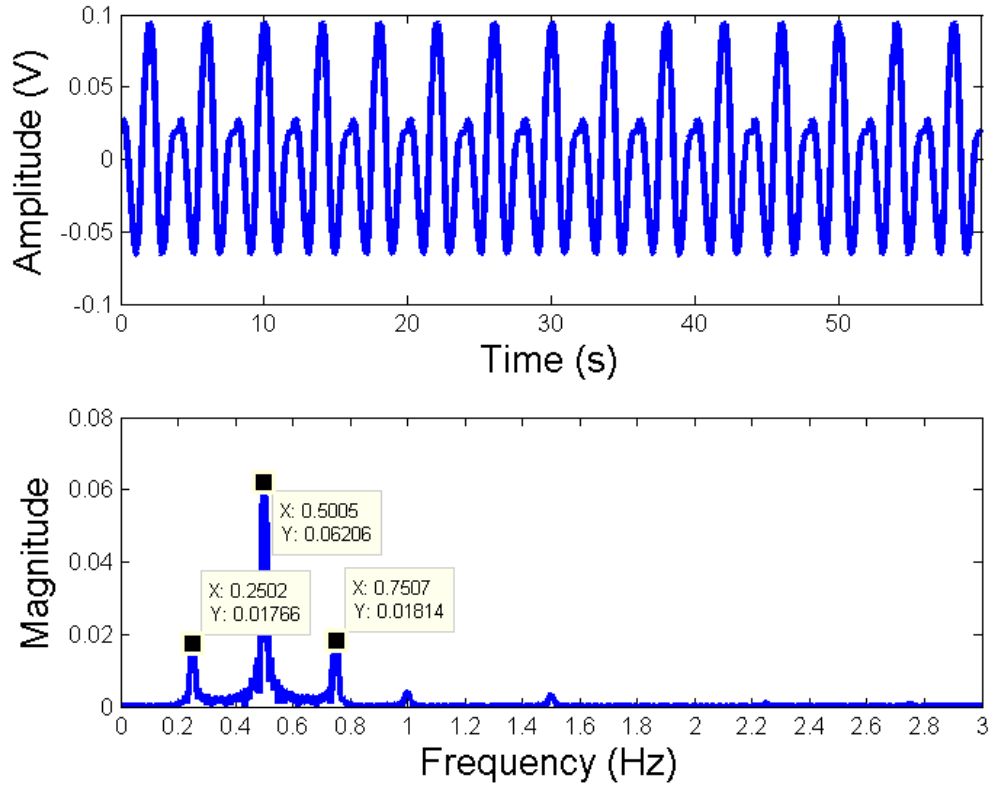


Fig. 5.21 Simulation results on the impact of subject location on demodulated output, with demodulated data shown in time domain (Top) and frequency domain (Bottom), at incremental nominal distance of 1m - 16 of $\lambda/64$ (null point).

Fig. 5.15 shows that the subject is at the null point where the extracted respiration frequency is at 0.5Hz, the double of the preset real one at 0.25 Hz. Also there are very small peaks at fundamental frequency and third harmonic. As the nominal distance decreases, the subject moves away from null point to optimum point. The amplitude of mispresenting 0.5 Hz peak decreases, while the amplitude of the real respiration frequency increases, until no obvious 0.5 Hz peak is found in the spectrum and 0.25 Hz reaches the highest value. Also, as the subject moves further from the null point and closer to the optimum point, the amplitude of the output signal in the time domain keeps increase to the biggest value. Once the target passes the first optimum point, the opposite tendency on the change in amplitude of the peaks of 0.5 Hz and 0.25 Hz was observed in frequency domain, and the amplitude of output data in the time domain gradually decrease until it reaches the lowest value, since the distance between the target and the optimum point increases as the subject moves closer to the next null point. The amplitude variation of each peak with the position is summarized in Fig. 5.22, which shows the similar pattern as in Fig. 5.10. However, in Fig. 5.22, the occurrence of crest of 0.25 Hz is not accompanied with the valley of 0.5 Hz. This is due to the model itself has relative strong harmonics [6969]. Therefore, where the double of real motion frequency shows up is affected by both the target position relative to null or optimum points and 2^{nd} harmonic of the signal itself.

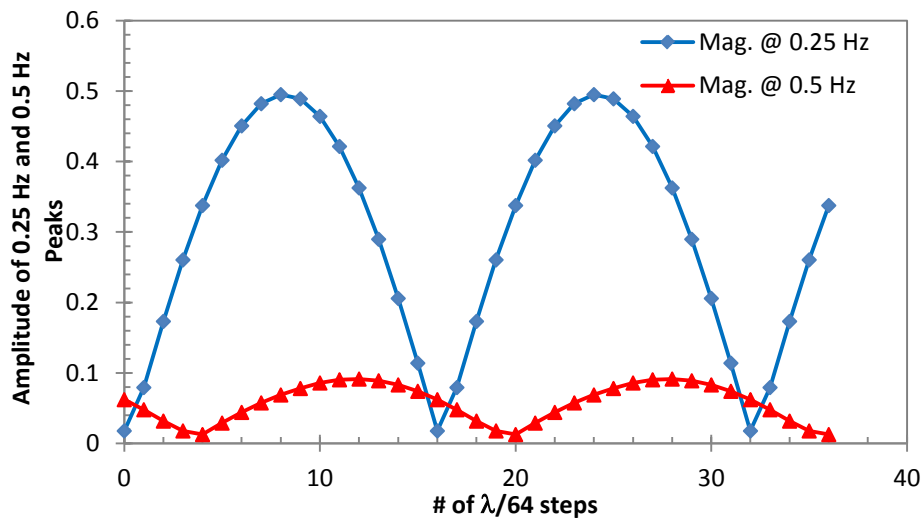


Fig. 5.22 Amplitude of real motion frequency peak at 0.25 Hz and the one at 0.5 Hz changes with the position of the target tells where the target is relative to the null or optimum point.

5.1.2.2 Experiment

In this section, a series of experiments with the same setup as shown in Fig. 5.3 were run to prove the authenticity of simulation using the models expressed by Equations (5.12) and (5.13). Different from the experiment in section 5.1.1, the mechanical target moves along the contour programmed with the sum of these more realistic models, instead of the sinusoidal signals. The motion frequencies are kept the same, 1.25 Hz for heart beat and 0.25 Hz for respiration.

Fig. 5.23 summarizes with the experiment data where the peaks of real frequency and double of that occur, and how big the amplitude is relative to the null or optimum position. It also compares the measurement and simulation results by normalizing the data at each point to the maximum amplitude of real frequency peak in measurement and simulation, respectively. With the more complex but more realistic models, the occupancy sensor can accurately measure the respiration frequency at 0.2568 Hz at optimum points, which is the same as the one obtained with sinusoidal models, and very similar to the programmed 0.25 Hz. The pattern with experiment data follows the simulated one closely, which proves the simulation result is correct.

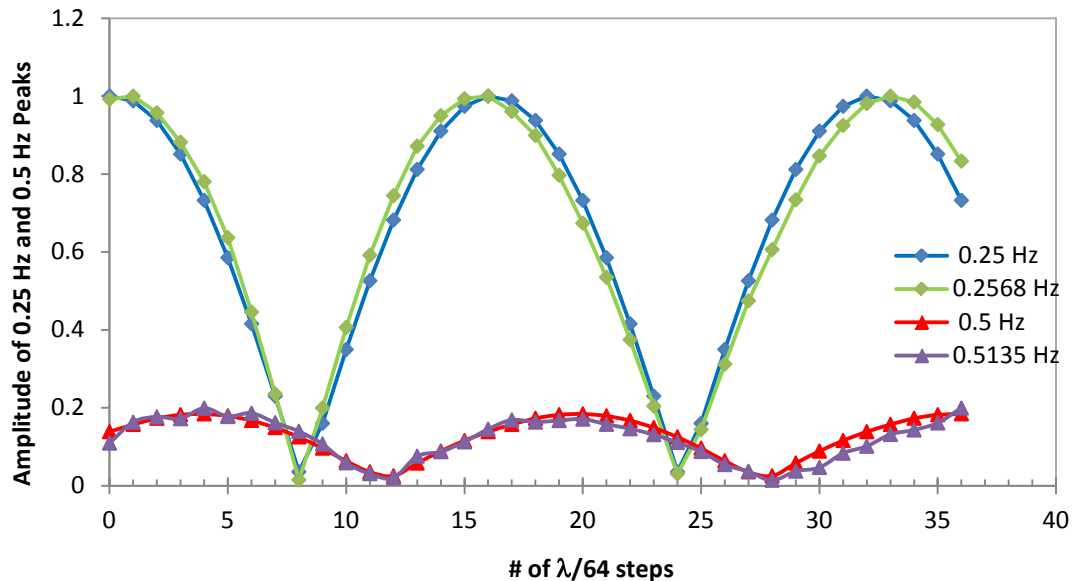


Fig. 5.23 A comparison between simulation and experiment data.

Fig. 5.24 – Fig. 5.26 show the detailed information in the time domain and frequency domain for the typical data set at the null point, optimum point and between.

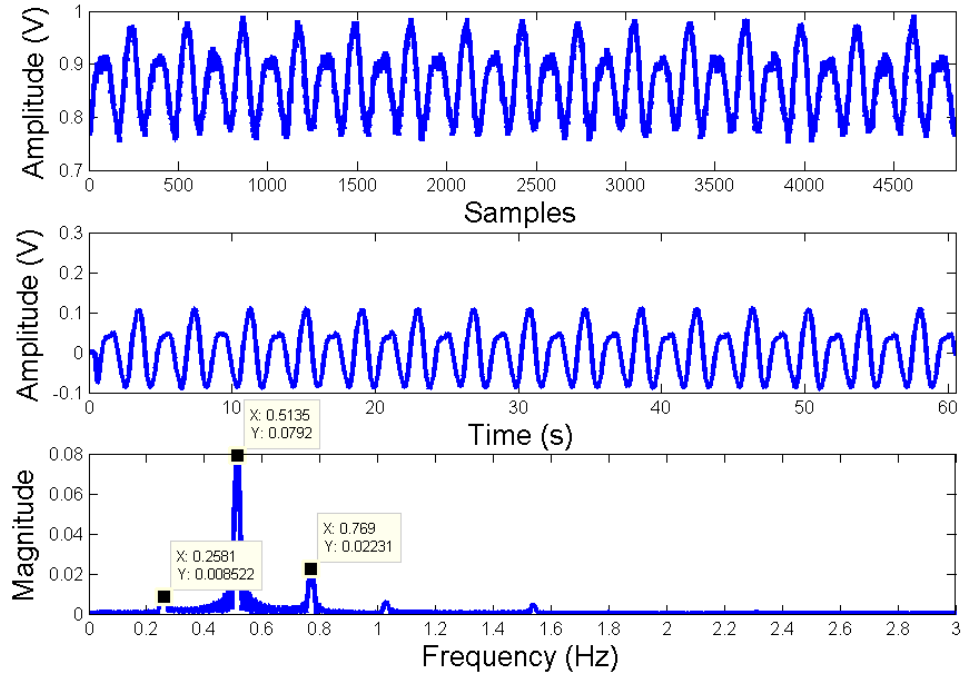


Fig. 5.24 Experimental results on the impact of subject location on phase demodulated sensor output, with raw data shown in time domain (Top), filtered data shown in time domain (Middle) and data in frequency domain (Bottom), at a null point.

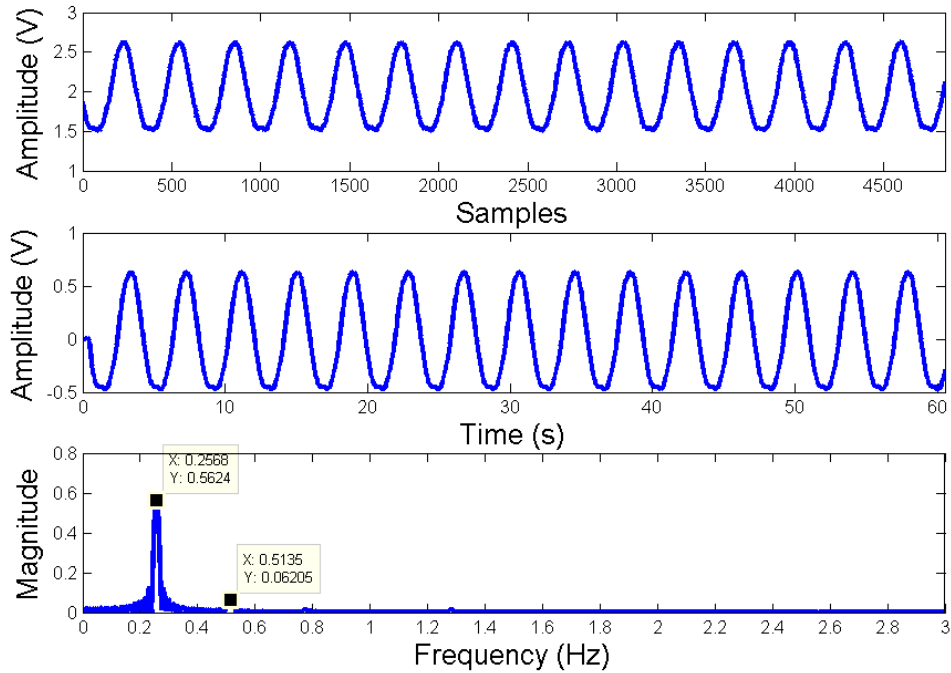


Fig. 5.25 Experimental results on the impact of subject location on phase demodulated sensor output, with raw data shown in time domain (Top), filtered data shown in time domain (Middle) and data in frequency domain (Bottom), at an optimum point.

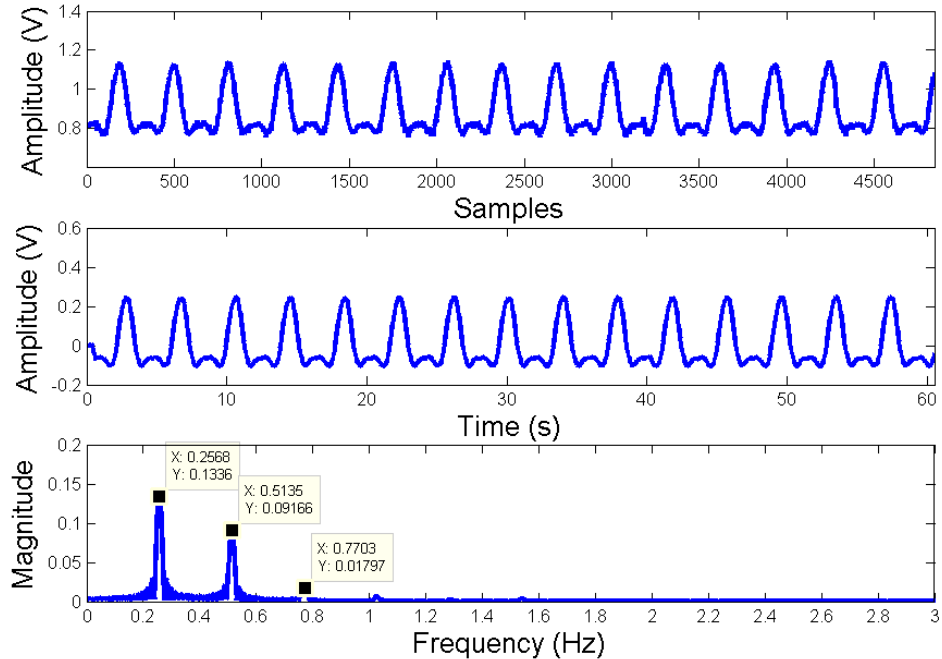


Fig. 5.26 Experimental results on the impact of subject location on phase demodulated sensor output, with raw data shown in time domain (Top), filtered data shown in time domain (Middle) and data in frequency domain (Bottom), in between a null point and an optimum point.

The experiment and simulation with complex models repeat the result what is obtained with the sinusoidal model. It confirms that although at the null point, the moving rate of a target could be misrepresented with the proposed occupancy sensor since its single channel receiver nature, the uncorrected frequency is always the double of the real one. Depending on where is the target relative to the null or optimum point, either one of the two frequency peaks or both will be observed in the spectrum analysis.

5.2 Algorithm

In this section, details of algorithm to detect true presence occupancy based on respiration pattern of stationary subject will be presented.

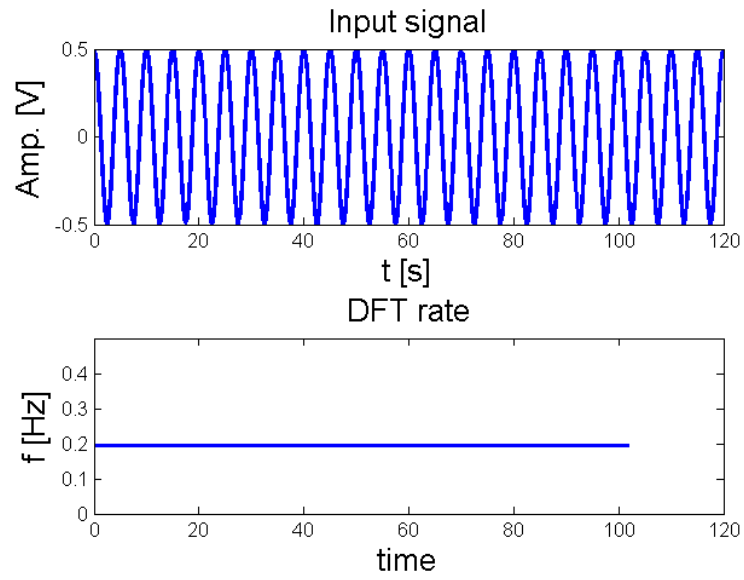
The simulation and experimental results in previous section tell us in the range where the subject is closer to the optimum points, the output data from the Doppler radar occupancy sensor built in this dissertation can keep the information in the original signal, and as the subject leaves further from the optimum points, i.e., approaches closer to the null points, the extracted information from the output of the sensor will be deviated from the original one, including decreased sensitivity and misinterpreted motion rate.

However, the incorrect frequency peak always appears at the double of the real one, either alone or with the real peak, depending how far or how close the subject is to the null or optimum points. Due to the human respiration frequency range is usually in 0.1 – 0.8 Hz, we can search for the peaks between 0.1 – 1.6 Hz as our occupancy detection baseline. To improve the efficiency, we can scan the frequency between 0.1 – 0.8 Hz first, if find nothing, then expand the searching scope to 0.8 – 1.6 Hz.

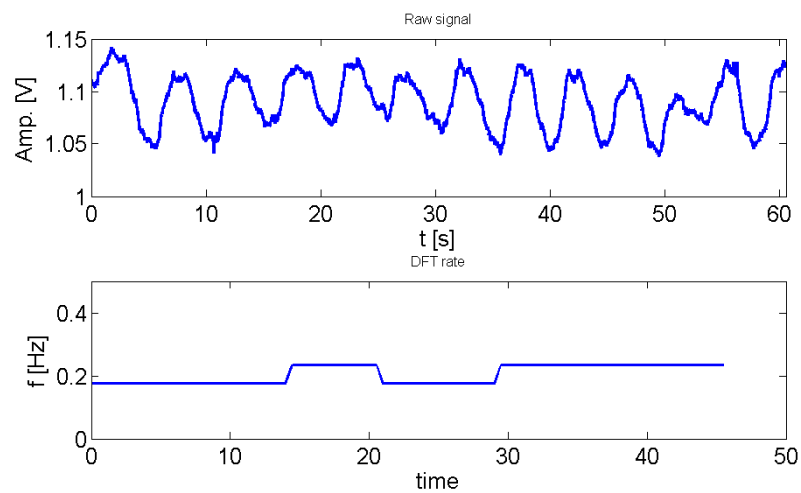
In addition, to differentiate the mechanical target periodically moving with the rate in the same frequency range, the nature of time varying quantities in the human respiration rates will be employed. Fig. 5.27 shows the difference between the mechanical target programmed to oscillate at 0.2 Hz and a subject with respiration rate around 0.2 Hz. Fig. 5.27 (a) indicates the mechanical target moves with even displacement and rate, while Fig 5.27 (b) implies the subject breathes with varied depth and rate.

To extract the inherent variability in the respiration rate, a windowed method is required. The short time Fourier transform method divides the data into chunks of proper length (windows), calculates the FFT of each window of data, average the FFT over multiple windows to yield a representation of Power Spectral Density (PSD) of a segment of data and ultimately find the peak in the PSD. The window length is determined depending on the application. Rule of thumb is to have a window long enough to accommodate 5-10 periods of the signal. This results in a 10-18 s window length for respiration due to its low frequency nature [9,10].

The overall flow chart of the proposed algorithm is presented in Fig. 5.28.



(a)



(b)

Fig. 5.27 Comparison of radar signals between the mechanical target (a) moves at 0.2 Hz and subject (b) breath with rate around 0.2 Hz.

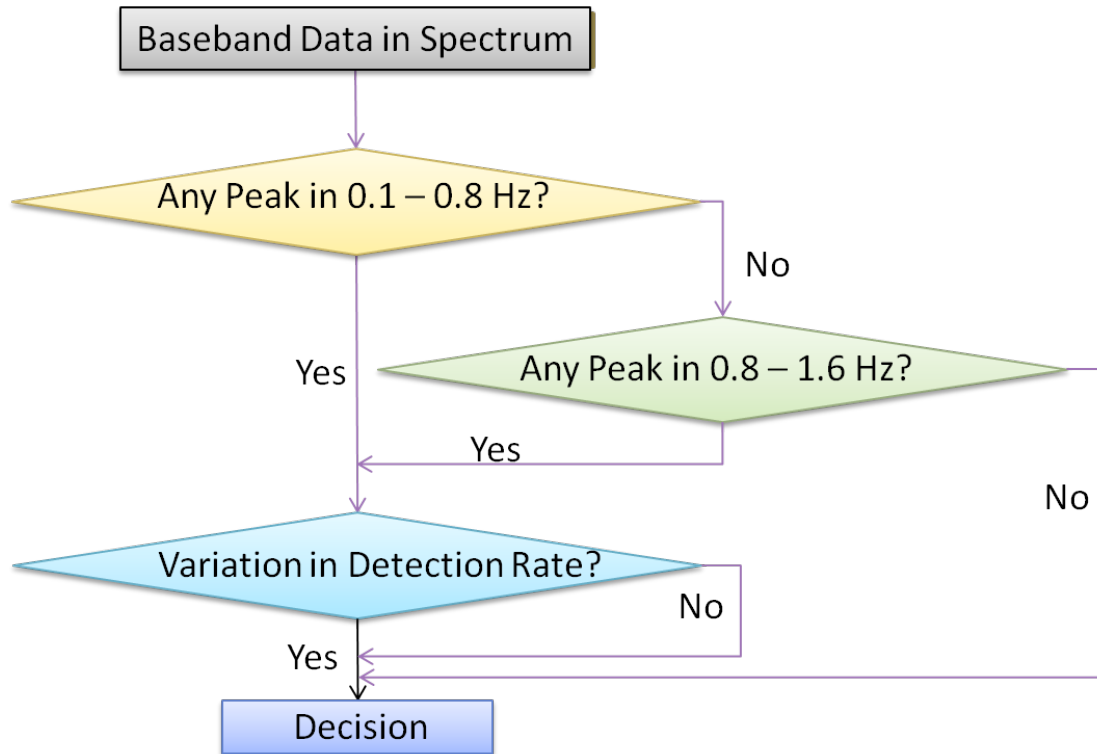


Fig. 5.28 Flow chart of the algorithm to detect human presence occupancy.

5.3 Human Testing

To examine the concept of the proposed algorithm, human tests with the Doppler radar occupancy sensor were run. As mentioned before, since Doppler radar can easily pick up large signal generated by locomotion and fidgeting, such as body moving, the test focused on stationary subjects sitting in front of radar. Total of 19 subjects were tested by following the protocol CHS 14884.

5.3.1 Experiment Setup

In this experiment, the SoC based Doppler radar occupancy sensor is assembled with CC2530 evaluation board, passive sensor node, transmit and receive antennae, and other laboratory equipment and off-the-shelf coaxial components. The testing was conducted at Channel 11 with center frequency 2.405 GHz for both CW and packet modes. The transmitted power was programmed to be 4.5dBm. The subjects were seated at a distance of 1.2 meters away from the cabled occupancy sensor.

The RF transmitter on CC2530 generates the active radar signal, which will be phase-modulated by the cardiopulmonary activities of the subject after it incidents on and is reflected by the human body. The passive sensor node, constructed with an Antenna Specialist (ASPPT2988) receive antenna, a Minicircuits splitter (ZFSC-2-2500) and mixer (ZFM4212), converts the sum of air-coupled transmitted and reflected signals to the base band output, which will be fed into Stanford Research System Model SR560 Low Noise Amplifiers for amplification and filtering, and then digitized with a NI USB-6259 data acquisition device. The base band output is amplified by a factor of 200, and subjected to 6 dB/octave low-pass filtering at 30 Hz for CW mode, and 1 kHz for packet mode. Finally, signals out of DAQ are recorded by a NI USB-6259 to the PC with the sampling rate of 120 Hz for CW mode and 3 kHz for packet mode.

Parallel with the Doppler radar sensor test setup, an Infrared camera system monitoring the movement of the chest activity was running to take the same measurement for reference. Fig. 5.29 is the experiment arrangement for occupancy sensor testing.

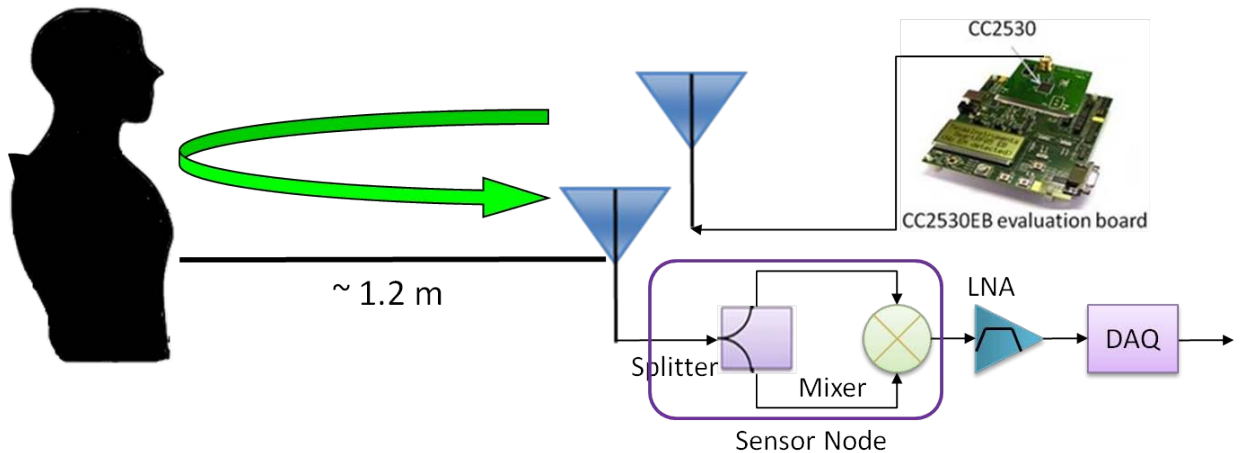


Fig. 5.29 Human testing with Doppler radar occupancy sensor.

5.3.2 Experiment Result

For all the human testing, raw data digitized with DAQ were recorded and processed with Matlab. The data was cleaned with FIR low pass filtering first for CW mode. The motion rate of the mechanical target was then calculated by applying FFT to the filtered data. For packet mode data, DSP algorithms described in section 4.1 were

applied to calculate the motion rate of the subject, *i.e.*, low pass filtering, local maximum detection, cubic spline interpolation, and FFT.

The data collected from subject #16 is shown in Fig.5.30 for CW operation mode and Fig. 5.31 for packet operation mode, as an example to show the test result in time and frequency domain for the use of the proposed detection algorithm. Since the camera measures the displacement directly, different from the radar measurement, for comparison purpose, both raw data were normalized to their maximum measured value. For CW mode, a dominant frequency at 0.13Hz and its second harmonic were found in the preset searching frequency range of 0.1 – 1.6 Hz. For packet mode, only one peak appears at 0.16 Hz. Although the radar data don't follow the reference data in the time domain exactly, the frequency domain result match with each other very well. The radar detects the movement of broader area than the camera. Therefore, it is reasonable that there is phase discrepancy between radar and reference.

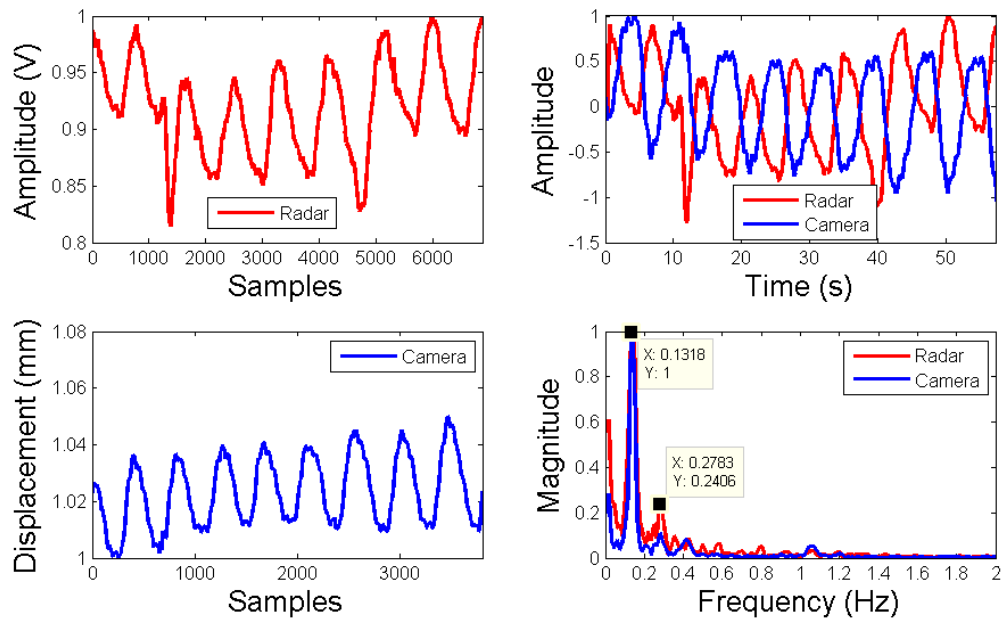


Fig. 5.30 CW Data from Subject #16. The top left trace is the occupancy sensor raw data, the bottom left trace is IR camera raw data, the top right trace is the comparison between sensor and camera after filtering and normalization, and the bottom right trace is the frequency spectrum after FFT.

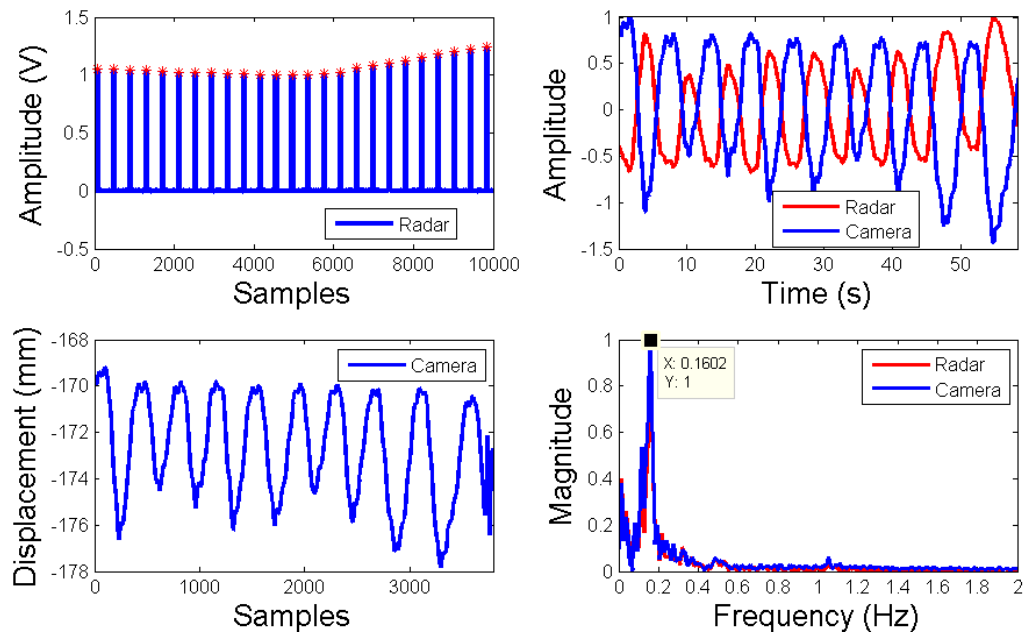


Fig. 5.31 Packet mode Data from Subject #16. The top left trace is the occupancy sensor raw data (only show 10000 samples), the bottom left trace is IR camera raw data, the top right trace is the comparison between sensor and camera after filtering and normalization, and the bottom right trace is the frequency spectrum after FFT.

The testing results are summarized in Fig. 5.32 through Fig. 5.35. The frequencies of the dominant peaks and their harmonics for each subject are presented in Fig. 5.32 and Fig. 5.33 when the occupancy sensor is operated with CW mode and packet mode, respectively. Both figures clearly indicate that all the detected dominant respiration frequencies fall into the range of 0.1 – 0.8 Hz. Some of the dominant peaks are accompanied with second harmonics. According to what is observed in Fig. 5.32 and Fig. 5.33, we can make a preliminary judgment that the human presence is detected. However, to further exclude the interference of the periodic mechanic movement, such as the one has been used through the dissertation, the time-varying respiration needs to be verified. This is done by performing FFT analysis of the collected baseband data in a window size of 10s. Since checking if the collected baseband signal is a periodic data set with time-varying rate is the purpose for occupancy sensing, instead of tracking the respiration rate with continuous time in medical application, segment windows, not the continuous sliding windows are taken to calculate the FFT. The results for CW operation and packed mode are illustrated in Fig. 5.34 and Fig. 5.35, individually, which confirm the preliminary judgment of human presence. As a comparison, the testing results on the

mechanical target (subject #20) is also included in these figures. Although it is programmed to oscillate at 0.25Hz on purpose, its constant value of rate with the time excludes the possibility of false positive alarm.

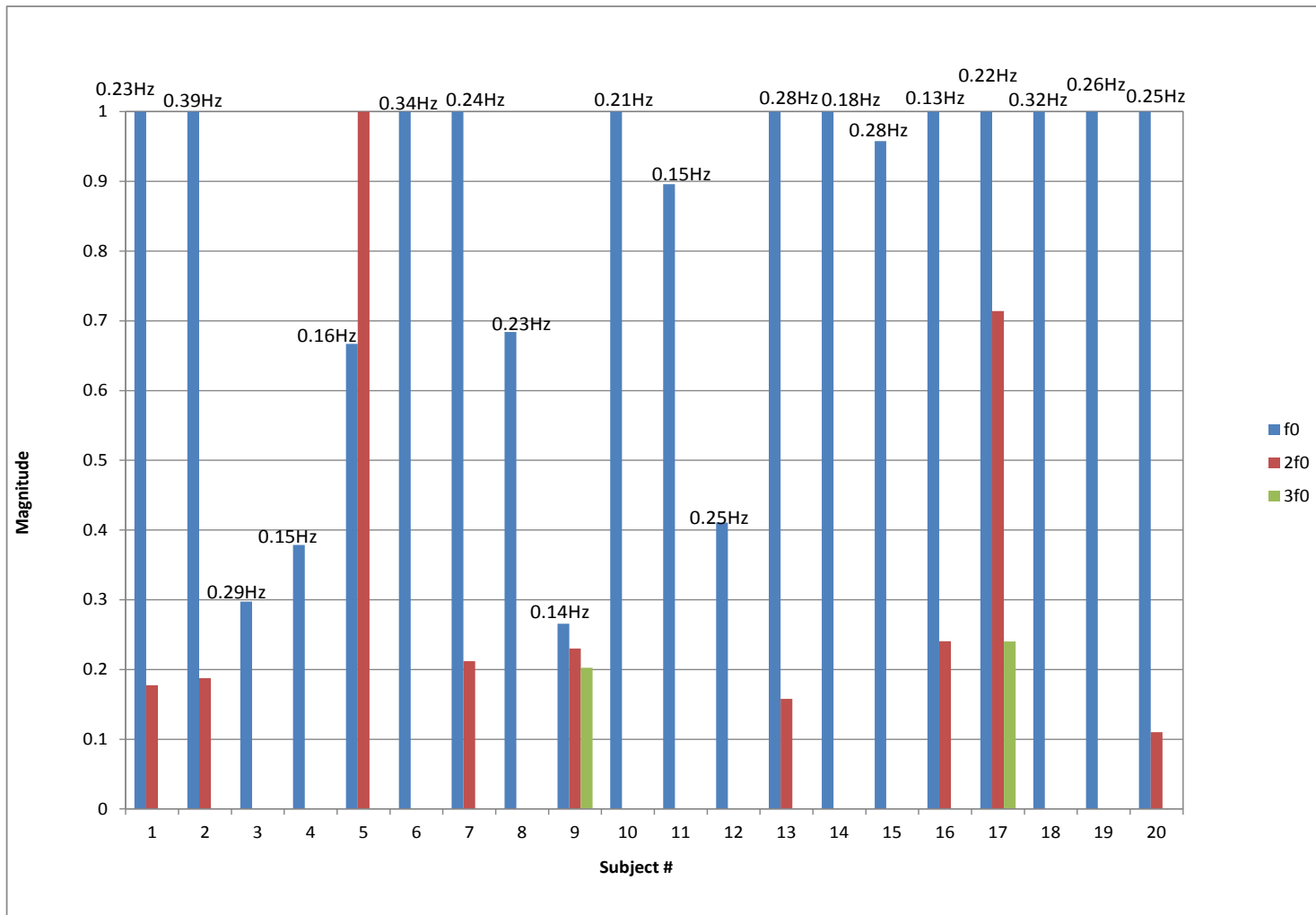


Fig. 5.32 Detected dominant frequency and its harmonics for respiration of subject #1 – 20 at CW mode.

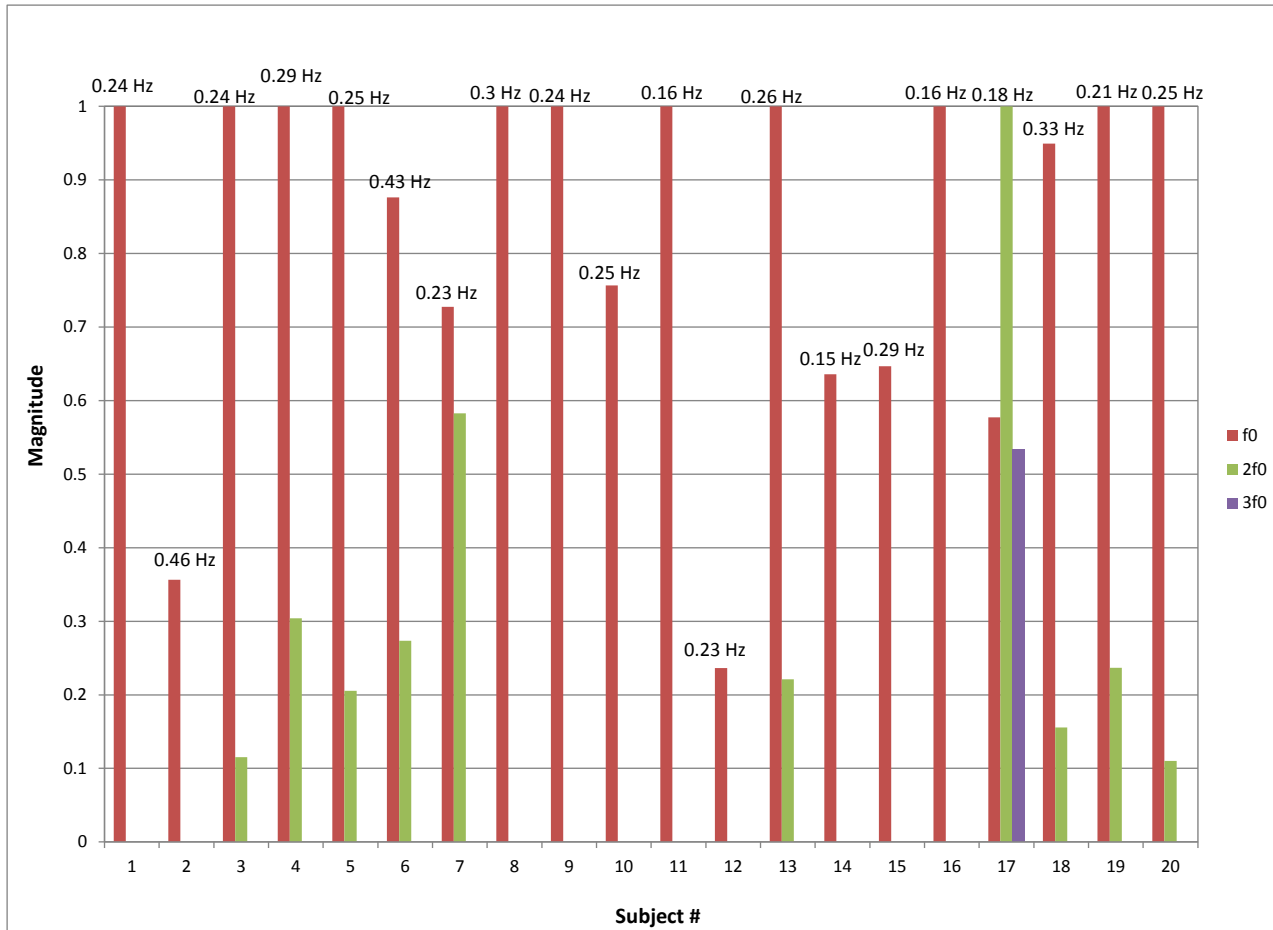


Fig. 5.33 Detected dominant frequency and its harmonics for respiration of subject #1 – 20 at packet mode.

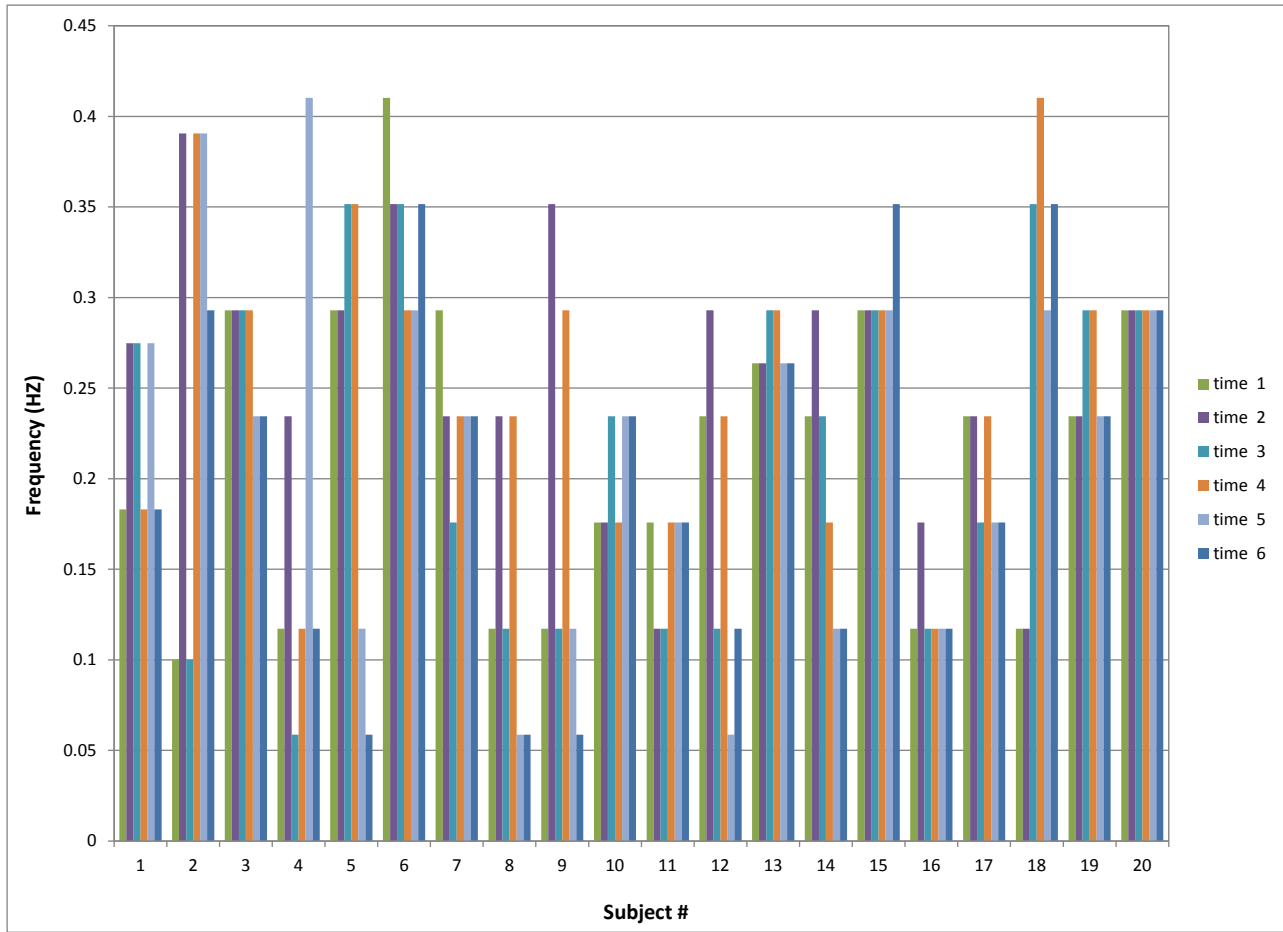


Fig. 5.34 Detected respiration rate vs. time for subject # 1 – 20 at CW mode.

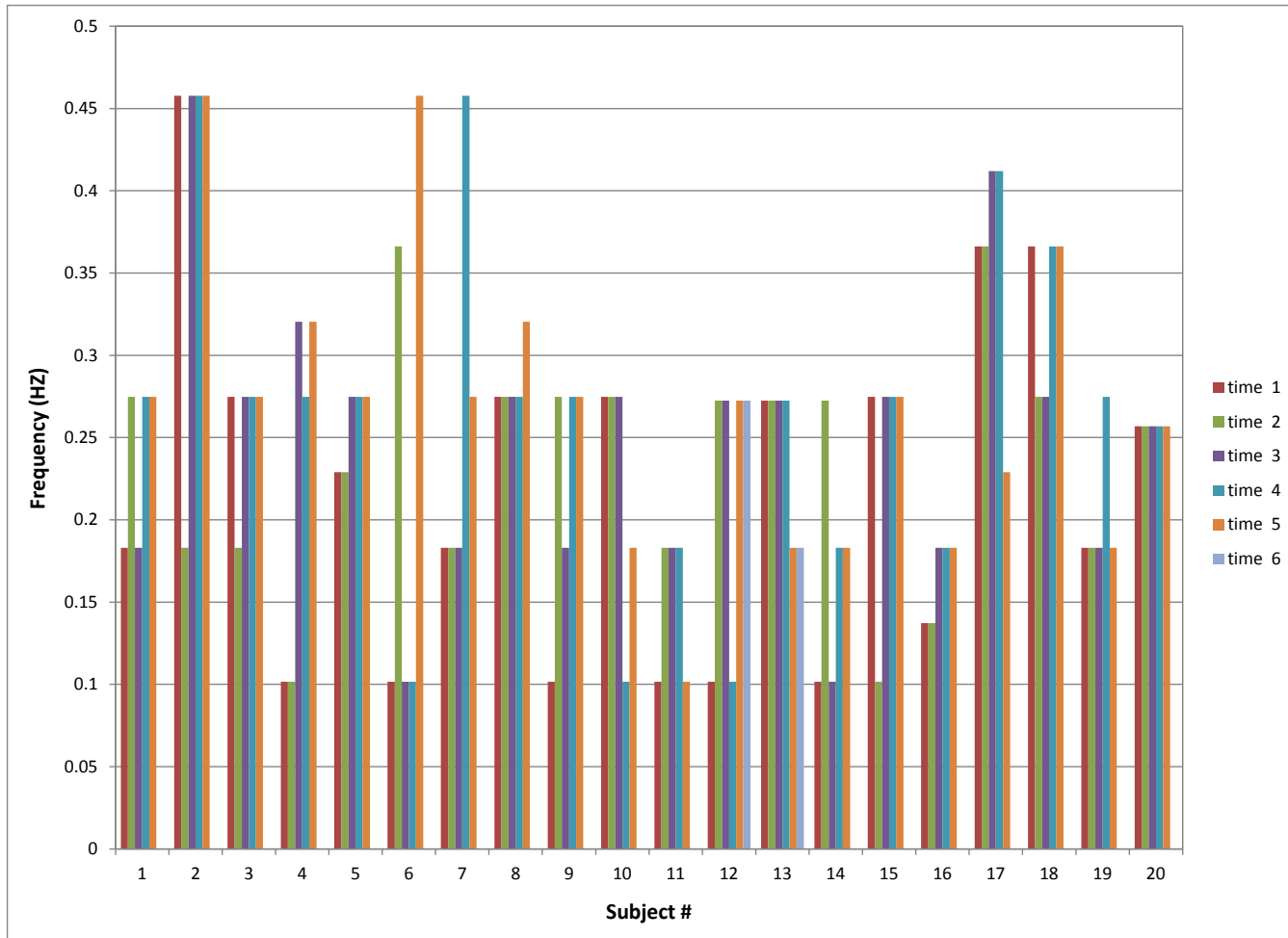


Fig. 5.35 Detected respiration rate vs. time for subject # 1 – 20 at packet mode.

5.4 Conclusion

This chapter analyzes the spectral pattern of the received signals by using the passive node in the SoC based Doppler radar occupancy sensor for both simulation and experiment. The results show that the accuracy of the extracted motion rate of the target varies with the where the target is. At the optimum points or nearby, the original moving frequency peak dominates, while at the null points or nearby, the double of original frequency peak takes over.

With this spectrum characteristics in mind, searching for the peaks in the typical respiration frequency range of 0.1 – 0.8 and double of it is the baseline of the occupancy detection algorithm as well as looking for the variation of the rate in this range.

Human testing with 19 subjects proves the validity of the occupancy detection algorithm with 100% accuracy.

Chapter 6 Future Work and Conclusions

The goal of this dissertation is to realize a Doppler radar occupancy sensor, which can detect the true presence of a human subject, by integrating a passive node into an off-the-shelf SoC platform to sense the human respiration. A lot of effort has been put into the development of a broadband mixer for the proposed sensor. Study of the operation conditions, and design of occupancy decision algorithm, in order to realize low power, low cost and accurate detection for this sensor. During the research, some interesting area has been located and left for future work, which will be described in the following section.

6.1 Periodic Motion Measurement with Single Channel Doppler Radar

As shown in [71], for ideal Doppler radar sensing of physical movements, the normalized detected baseband signal is

$$B_r(t) = \cos\left(\theta + \frac{4\pi x(t)}{\lambda} + \Delta\phi(t)\right), \quad (6.1)$$

where $\Delta\phi(t)$ is the residual phase noise, λ is the wavelength at the operation frequency, $x(t)$ is the time varying displacement of the target, and θ is the constant phase shift generated on the transmission path and at the surface of the target.

If the target moves with a single sinusoidal tone,

$$x(t) \approx m \times \sin 2\pi f t, \quad (6.2)$$

where m is the movement amplitude and f is the moving frequency.

When m is much smaller than λ , a linear approximation can be applied [Line, 4] to Equation (6.1). However, due to the nature of the single channel, the detected output, including both amplitude and frequency, by linear approximation varies with the position of the target relative to the radar system from the null points to optimum points.

Simulation shows two peaks appear at the frequencies with the ratio of 2 between the higher one and lower one. The amplitude of the fundamental peak and second harmonic changes as the location of the target varies. As shown in Fig. 6.3, the ratio of the amplitude between the fundamental frequency and its second harmonic has unique value at each point. Using these unique values, we will know where the target is relative to the null or optimum points. The movement frequency f can be accurately obtained from the fundamental frequency of $B_r(t)$ whether the target is at null, optimum or between points.

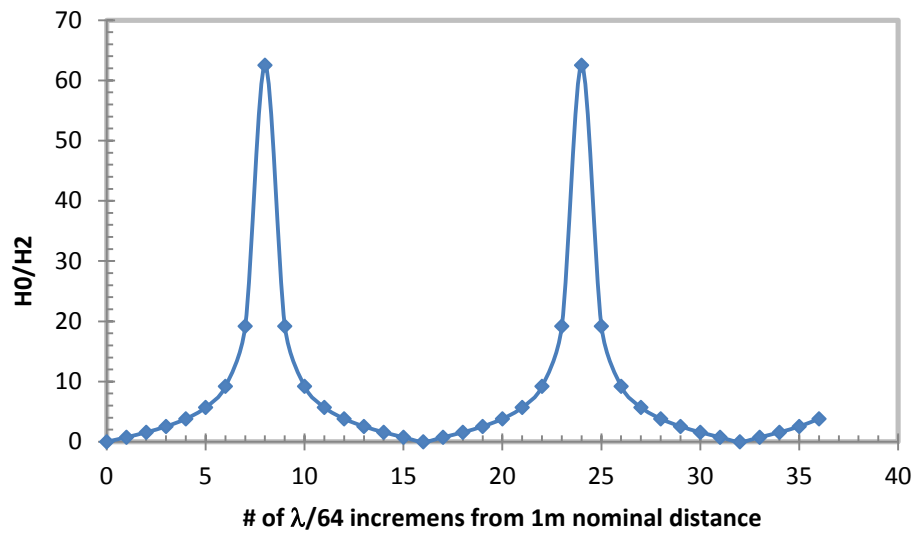


Fig. 6.1 The amplitude ratio between fundamental frequency and second harmonic varies with the position of a periodically moving mechanical target.

Also, by calibrating the received signal with the receiver gain and distance to the target, from one point, we can retrieve the information at the opposite point, i.e., from known null points to unknown optimum points or vice versa, and recover the moving displacement which can't be obtained by single channel receiver radar system.

6.2 Harvesting Ambient RF Energy with the Passive Sensor Node

In this dissertation, the passive sensor node is constructed by receive antenna, a splitter and a mixer. To further simplify the circuit and reduce the size and cost, a diode can replace the splitter and mixer in the future. This architecture is called rectenna, which is most popular harvester used to scavenge the ambient RF energy. According to

reference [72], a 2.4 GHz dual polarized patch rectenna can harvest 8 – 420 μW out of an input with energy density 30 - 70 $\mu\text{W}/\text{cm}^2$.

Due to the similar structure of the passive sensor node to the rectenna, we propose to design a rectenna array to provide partial power for the occupancy sensor. In the proposed rectenna array, each rectenna consists of a zero-biased rectifying Schottky diode and a multi-frequency antenna which will receive the signals in the frequency range of sub-GHz to 5.8 GHz. Any of the rectenna in the array can perform the cardiopulmonary sensing function with the active Radar signal or the RF source already operating in the environment. The concept is as shown in Fig. 6.2.

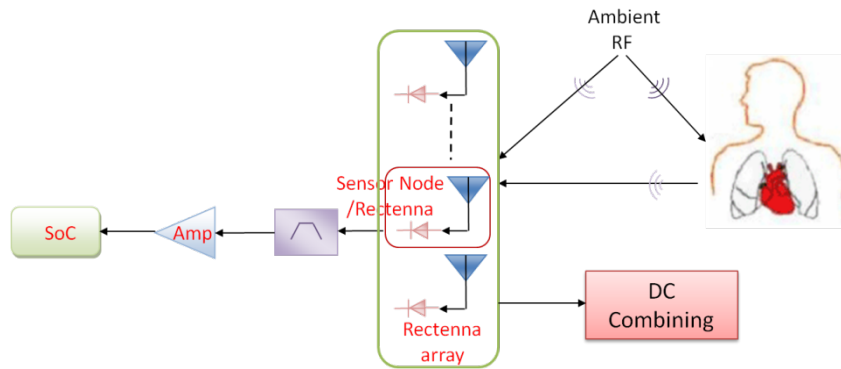


Fig. 6.2 The basic components which provide cardiopulmonary remote sensing and RF energy harvesting, including the passive sensor node/rectenna.

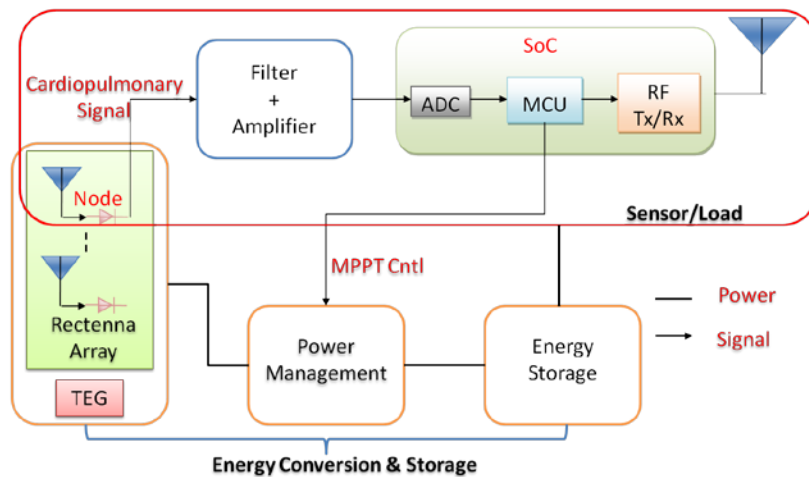


Fig. 6.3 Block diagram for proposed occupancy sensor unit, consisting of: energy harvester, power management, energy storage, and sensor/load.

The variation of power density and overall low power levels of available energy source for the energy harvester may limit integrated sensor operation. To overcome this, a power management and maximum power point tracking (MPPT) circuitry employing a boost converter will be developed to obtain the maximum possible power from the energy harvester of non-linear behaviour. The converter will be intelligently controlled by the microcontroller in the SoC to perform MPPT and hence optimize the power conversion efficiency. A supercapacitor will be employed for storage in this work because it has superior characteristics over batteries.

Fig. 6.3 shows the block diagram for the proposed sensor unit with RF harvester. It includes an energy harvester, a power management circuit, an energy storage device, and an Doppler radar occupancy sensor load.

6.3 Conclusion

Doppler radar cardiopulmonary sensing technology has many applications, including medical, military, security, first responder, *etc.* This dissertation expands its applications in energy saving for “smart building” and “smart home”, by building a Doppler radar occupancy sensor with off-the-shelf SoC and custom passive sensor node and developing an algorithm for true presence occupancy detection. Simulation and measurements were performed that demonstrate that the radar system can make use of a characteristic spectrum pattern of receive respiration signal to detect a stationary subject with 100% accuracy. The contributions of this dissertation include:

1. The first demonstration of applying Doppler radar detection on vital signs in occupancy sensing with off-the-shelf SoC and sensor nodes (Chapter 3). The transmitter on the SoC is used as the radar signal source, the sensor node is the add-on receiving module. In the future, the sensor node can be used for passive physiological monitoring with ambient RF signals, as well as ambient RF energy harvester.
2. A unique CMOS passive mixer with extremely low DC offset and broadband performance of single IF output, despite the integrated balun narrowband magnitude balance (Chapter 3). This mixer can be used at 2.4 GHz for narrow

band application, with the differential IF outputs combined, or for broad band application using single IF output.

3. The first efforts on the operation modes of the Doppler radar occupancy sensor to optimize the energy and operation efficiency of the sensor (Chapter 4).
4. Demonstration of the true presence occupancy detection using the occurrence of the original respiration frequency peak and/ or the peak at doubled original frequency depending on the position of the subject relative to the optimum and null points, and time-varying nature of the respiration rate (Chapter 5). The respiration spectrum pattern changing with the position will be used to predict the location and displacement in the future.

Appendix A

MatLab Codes for Human Presence Occupancy Detection Algorithm at CW Mode

```
% File: cw_radar_camera_variation.m
clc
close all
clc

%% Pre-process radar raw data

% Synchronise radar data with referece carmera data
% by discarding non-sync data
sync = data(:,2);
input = data(:,4);
total_sample = data(:,1);
total_sample_num = length(total_sample);
for i =1:total_sample_num;
    if sync(i) < 0.5 %find the index of first sync data
        break
    end
end

Input_Radar = input(i:total_sample_num);
%Input_Radar = input(1:30*fs_radar);
sample_Radar =0:length(Input_Radar)-1;
%truncRadar=Input_Radar(240:length(Input_Radar));
%sample_Radar = 0:length(truncRadar)-1;
fs_radar = 120;

%DC cancellation
Radar=Input_Radar-mean(Input_Radar);
%Radar=truncRadar-mean(truncRadar);
%filter the raw data
[filtRadar]=BPF(Radar,fs_radar);

%% Pre-process reference camera data

%Importing datacamera data from drf file
fileID = fopen('../Raw Data/camera/cw/8.drf');
%Read data into seperate cells
C = textscan(fileID,'%s %s %s %7s %s %s %7s');

% Extracting cell and converting to num type
Input_Cam = str2num(char(C{1,2}));
sample_Cam = 0:length(Input_Cam)-1;
%truncCam=Input_Cam(240:length(Input_Cam));
%sample_Cam = 0:length(truncCam)-1;

% Centering amplitude data at 0
Cam = Input_Cam-mean(Input_Cam);
%Cam = truncCam-mean(truncCam);
% Apply filtering
```

```

fs_cam = 60;
[filtCam]=BPF(Cam,fs_cam);

% interpolate data with scale of radar fs and camerer fs
coe = 120/fs_cam;
interpCam = interp (Cam, coe);

%% Fourier Transform Calculation
fs = fs_radar;
[freq_Radar, fft_Radar,time_Radar] = fourier_cw(filtRadar,fs);
[freq_Cam,fft_Cam,time_Cam] = fourier_cw(interpCam,fs);

%% Check the variation of fft in different time segment for radar
signal
[segment_num,freq_peak]=radar_variation(input,fs);

%% Plot

%Normalize the data with max. value
Input_Radar=Input_Radar/max(Input_Radar);
Input_Cam=Input_Cam/max(Input_Cam);
filtRadar=filtRadar/max(filtRadar);
interpCam=interpCam/max(interpCam);
fft_Radar=fft_Radar/max(fft_Radar);
fft_Cam=fft_Cam/max(fft_Cam);

figure;
% Plot original data in time domain
subplot (2,2,1)
plot (sample_Radar, Input_Radar,'r','LineWidth',2)
%plot (sample_Radar, truncRadar,'r','LineWidth',2)
%title ('Original Data')
hleg1 = legend('Radar');
xlabel('Samples','FontSize',16)
ylabel('Amplitude (V)','FontSize',16)
xlim([0 max(sample_Radar)])

subplot (2,2,3)
plot (sample_Cam, Input_Cam,'LineWidth',2)
%plot (sample_Cam, truncCam,'LineWidth',2)
%title ('Original Data')
hleg3 = legend('Camera');
xlabel('Samples','FontSize',16)
ylabel('Displacement (mm)','FontSize',16)
xlim([0 max(sample_Cam)])

subplot (2,2,2)
plot(time_Radar,filtRadar,'r',time_Cam, interpCam,'LineWidth',2)
%title ('Data in Time Domain')
xlim([0 max(time_Radar)]);
hleg2 = legend('Radar','Camera');
xlabel('Time (s)','FontSize',16)
ylabel('Amplitude','FontSize',16)

```

```

% Plot FFT data in frequency domain
subplot(2,2,4)
%plot(freq(1:50), A(1:50))
plot(freq_Radar, fft_Radar, 'r', freq_Cam, fft_Cam, 'LineWidth', 2)
%grid on
xlim([0 3]);
hleg4 = legend('Radar', 'Camera');
%title ('FFT Data')
xlabel('Frequency (Hz)', 'FontSize', 16)
ylabel('Magnitude', 'FontSize', 16)
set(gca, 'XTick', 0:0.2:3)

figure (2);
clf;
% Plot original data in time domain
plot (segment_num, freq_peak, 'ro')
%plot (sample_Radar, truncRadar, 'r', 'LineWidth', 2)
%title ('Original Data')
%hleg1 = legend('Radar');
xlabel('Time Segment', 'FontSize', 16)
ylabel('frequency (Hz)', 'FontSize', 16)
xlim([0 max(segment_num)])

%% Band-Pass filtering raw data
function [filtData]= BPF(input,fs)

B=fir1(fs,[.1/(fs/2) 3/(fs/2)]);

filtData=filter(B,1,input);

end

%% Fourier Transform Calculation and Plot
function [freq,A,time]= fourier_cw(input,fs)

% Creating time vector
sample_num=length(input);
x=0:sample_num-1; % x-axis vector
time = x/fs; % real time vector

window=hamming(sample_num);
input_window=window.*input;
N=2^nextpow2(sample_num);
L=N/2;
ft=fft(input_window,N);
absft=abs(ft); % symmetric duplicate of the real FT
A=absft(1:L+1); % reject the duplicated half
A=A/sample_num; % Rescale to real amplitude for infinite
waveform
freq=fs*(0:L)/N; % real frequency

```

```

end
%% Check the variation of fft in different time segment for radar
signal
function [segment_num,freq_peak]=radar_variation(input,fs)

freq_peak = [];
segment_num = [];
sample_num=length(input);
time = sample_num/fs;
segment_length = 15; % in seconds
segment_start = 0;
segment_step = fs*segment_length;

for l=1:floor(time/segment_length)
    segment_end=segment_start+segment_step;
    Radar_segment=input(segment_start+1:segment_end);
    Radar_segment=Radar_segment-mean(Radar_segment);
    %filt_segment=BPF(Radar_segment,fs);
    [freq_segment, fft_segment,time_segment] =
fourier_packet(Radar_segment,fs);
    [max_magnitude max_index]= max(fft_segment);
    freq_peak(l)=freq_segment(max_index);
    segment_num(l)=l;
    segment_start=segment_end;
end

```

Appendix B

MatLab Codes for Human Presence Occupancy Detection Algorithm at Packet Mode

```
clc
close all
clc

%% Pre-process radar raw data

% Synchronize radar data with referece carmera data
% by discarding non-sync data
sync = data(:,2);
input = data(:,4);
total_sample = data(:,1);
total_sample_num = length(total_sample);
for i =1:total_sample_num;
    if sync(i) < 0.5 %find the index of first sync data
        break
    end
end

Input_Radar = input(i:total_sample_num);
sample_Radar =0:length(Input_Radar)-1;
fs_radar = 3000;

subplot(2,2,1)
%subplot(3,1,1)
plot (Input_Radar, 'LineWidth', 2.5)
xlim([0 max(sample_Radar)])

% Eatract the envolp with peak detection
[maxtab, mintab] = peakdet(Input_Radar, 0.8);
hold on;
plot(maxtab(:,1), maxtab(:,2), 'r*');
hleg1 = legend('Radar');
xlabel('Samples', 'FontSize', 16)
ylabel('Amplitude (V)', 'FontSize', 16)

%DC cancellation
Radar=maxtab(:,2)-mean(maxtab(:,2));
interpRadar = interp1(maxtab(:,1), Radar, sample_Radar, 'spline');

%filter the raw data
%[filtRadar]=BPF(Radar, fs_radar);

%% Pre-process reference camera data

%Importing datacamera data from drf file
fileID = fopen('../Raw Data/camera/pk/7.drf');
%Read data into seperate cells
C = textscan(fileID, '%*s %*s %*s %7*s %s %s %7s');
```

```

% Extracting cell and converting to num type
Input_Cam = str2num(char(C{1,2}));
sample_Cam = 0:length(Input_Cam)-1;

% Centering amplitude data at 0
Cam = Input_Cam-mean(Input_Cam);

% Apply filtering
fs_cam = 60;
[filtCam]=BPF(Cam,fs_cam);

% interpolate data with scale of radar fs and camerer fs
coe = fs_radar/fs_cam;
interpCam = interp (Cam, coe);

%% Fourier Transform Calculation
fs = fs_radar;
[freq_Radar, fft_Radar,time_Radar] = fourier_packet(interpRadar,fs);
[freq_Cam,fft_Cam,time_Cam] = fourier_packet(interpCam,fs);

%% Check the variation of fft in different time segment for radar
signal
[segment_num,freq_peak]=radar_variation(interpRadar,fs);

%% Plot

%Normalize the data with max. value
%Input_Radar=Input_Radar/max(Input_Radar);
%Input_Cam=Input_Cam/max(Input_Cam);
interpRadar=interpRadar/max(interpRadar);
interpCam=interpCam/max(interpCam);
fft_Radar=fft_Radar/max(fft_Radar);
fft_Cam=fft_Cam/max(fft_Cam);

subplot (2,2,3)
plot (sample_Cam, Input_Cam,'LineWidth',2)
%title ('Original Data')
hleg3 = legend('Camera');
xlabel('Samples','FontSize',16)
ylabel('Displacement (mm)','FontSize',16)
xlim([0 max(sample_Cam)])

subplot (2,2,2)
plot(time_Radar,interpRadar,'r',time_Cam, interpCam,'b','LineWidth',2)
%plot(time_Radar,interpRadar,'LineWidth',2)
%title ('Data in Time Domain')
xlim([0 max(time_Radar)]);
hleg2 = legend('Radar','Camera');
xlabel('Time (s)','FontSize',16)
ylabel('Amplitude','FontSize',16)

% Plot FFT data in frequency domain

```

```

subplot(2,2,4)
%plot(freq(1:50), A(1:50))
plot(freq_Radar, fft_Radar,'r',freq_Cam, fft_Cam,'b','LineWidth',2)
%grid on
xlim([0 3]);
hleg4 = legend('Radar','Camera');
%title('FFT Data')
xlabel('Frequency (Hz)','FontSize',16)
ylabel('Magnitude','FontSize',16)
set(gca,'XTick',0:0.2:3)

figure (2);
clf;
% Plot original data in time domain
plot (segment_num,freq_peak,'ro')
%plot (sample_Radar, truncRadar,'r','LineWidth',2)
%title ('Original Data')
%hleg1 = legend('Radar');
xlabel('Time Segment','FontSize',16)
ylabel('frequency (Hz)','FontSize',16)
xlim([0 max(segment_num)])

function [maxtab, mintab]=peakdet(v, delta, x)
%PEAKDET Detect peaks in a vector
% [MAXTAB, MINTAB] = PEAKDET(V, DELTA) finds the local
% maxima and minima ("peaks") in the vector V.
% MAXTAB and MINTAB consists of two columns. Column 1
% contains indices in V, and column 2 the found values.
%
% With [MAXTAB, MINTAB] = PEAKDET(V, DELTA, X) the indices
% in MAXTAB and MINTAB are replaced with the corresponding
% X-values.
%
% A point is considered a maximum peak if it has the maximal
% value, and was preceded (to the left) by a value lower by
% DELTA.

% Eli Billauer, 3.4.05 (Explicitly not copyrighted).
% This function is released to the public domain; Any use is allowed.

maxtab = [];
mintab = [];

v = v(:); % Just in case this wasn't a proper vector

if nargin < 3
    x = (1:length(v))';
else
    x = x(:);
    if length(v)~= length(x)
        error('Input vectors v and x must have same length');
    end
end

```

```

end

if (length(delta(:))>1
    error('Input argument DELTA must be a scalar');
end

if delta <= 0
    error('Input argument DELTA must be positive');
end

mn = Inf; mx = -Inf;
mnpos = NaN; mxpos = NaN;

lookformax = 1;

for i=1:length(v)
    this = v(i);
    if this > mx, mx = this; mxpos = x(i); end
    if this < mn, mn = this; mnpos = x(i); end

    if lookformax
        if this < mx-delta
            maxtab = [maxtab ; mxpos mx];
            mn = this; mnpos = x(i);
            lookformax = 0;
        end
    else
        if this > mn+delta
            mintab = [mintab ; mnpos mn];
            mx = this; mxpos = x(i);
            lookformax = 1;
        end
    end
end
end

%% Fourier Transform Calculation and Plot
function [freq,A,time]= fourier_cw(input,fs)

% Creating time vector
sample_num=length(input);
x=0:sample_num-1;           % x-axis vector
time = x/fs;                % real time vector

>window=hamming(sample_num);
window.*input;
N=2^nextpow2(sample_num);
L=N/2;
ft=fft(input,N);
absft=abs(ft);              % symmetric duplicate of the real FT
A=absft(1:L+1);            % reject the duplicated half
A=A/sample_num;            % Rescale to real amplitude for infinie
waveform
freq=fs*(0:L)/N;           % real frequency

```

References

-
- [1] WBCSD, “Facts and trends to 2050,” [on line], available at <http://www.wbcd.org/DocRoot/juCBrdwIQLnI5bIo6TdI/Basic-Facts-Trends-2050.pdf>
- [2] <http://newscenter.lbl.gov/feature-stories/2009/06/02/working-toward-the-very-low-energy-consumption-building-of-the-future/>
- [3] <http://ecmweb.com/lighting-amp-control/occupancy-sensors-101>
- [4] M. Levy, “Low-cost occupancy sensor saves energy, ” [on line], available at http://www.atmel.com/dyn/resources/prod_documents/mega88_3_04.pdf
- [5] The Energy Observer, “Occupancy sensors for lighting control,” [on line], available at http://www.michigan.gov/documents/dleg/EO_12-07_218809_7.pdf
- [6] J.C. Lin, “Non-invasive microwave measurement of respiration,” *Proc. IEEE*, vol. 63, p. 1530, 1975.
- [7] J.C. Lin, “Microwave apexcardiography,” *IEEE Trans. Microwave Theory Tech.*, vol. 27, pp. 618-620, 1979.
- [8] K.M. Chen, D. Mirsa, H. Wang, H.R. Chuang, and E. Postow, “An X-band microwave life detection system,” *IEEE Trans. Biomed. Eng.*, vol. 33, pp. 697-70, 1986.
- [9] A. D. Droitcour, “Non-contact measurement of heart and respiration rates with a single-chip microwave doppler radar,” Ph.D. dissertation, Stanford University, 2006.
- [10] W. J. Massagram, “A Study of feasibility in long-term cardiopulmonary monitoring via Doppler radar,” Ph.D. dissertation, University of Hawaii at Manoa, 2008.
- [11] B. Park, “Cardiopulmonary monitoring using Doppler radar,” Ph.D. dissertation, University of Hawaii at Manoa, 2007.
- [12] <http://www.ti.com/corp/docs/landing/cc2530/index.htm>
- [13] <http://www.ti.com/corp/docs/landing/cc430/index.htm>
- [14] “Occupant Sensors,” in *Advanced Lighting Guidelines, 2nd Ed.*, California Energy Commission, 1993, pp. 2.

-
- [15] <http://embedsoftdev.com/tag/pir-based-remote-thermometer/>
- [16] <http://en.wikipedia.org/wiki/Ultrasound>
- [17] “Sensors-Ultrasonic Sensing.” *Rockwell Automation*. ab.com, inc, 2013. Web. 22 Nov. 2013. <http://www.ab.com/>
- [18] http://www.mge.com/saving-energy/business/bea/escrc_0013000000DP22YAAT-2_BEA1_PA_PA_Lighting_PA-10.html
- [19] O. Boric-Lubecke and V.M. Lubecke, “Wireless house calls: using communications technology for health care monitoring,” *IEEE Microwave Mag.*, v.3, pp.43-48, September 2002.
- [20] http://www.eetimes.com/document.asp?doc_id=1278779.
- [21] M. I. Skolnik, “An Introduction to Radar,” in Radar handbook, Second Edition (M. I. Skolnik, Ed.), San Francisco: McGraw-Hill, Inc., 1990, pp. 1.1-1.21.
- [22] S. Kingsley and S. Quegan, *Understanding radar systems*. London: McGraw-Hill, 1992.
- [23] <http://astro.unl.edu/naap/esp/dopplereffect.html>
- [24] C. Wolff, “Classification of radar systems,”
<http://www.radartutorial.eu/02.basics/rp04.en.html#1>
- [25] D. S. Banks, “Continuous wave (CW) radar,” *Electronic Progress*, vol. 17, no. 2, pp. 34-41, 1975.
- [26] A. Droitcour, V.M. Lubecke, J. Lin, and Olga Boric-Lubecke, “A Microwave Radio for Doppler radar Sensing of Vital Signs,” *IEEE MTT-S Int. Microwave Symp. Dig.*, Phoenix, AZ, USA, vol. 1, pp. 175-178, May 2001.
- [27] A. Droitcour, O. Boric-Lubecke, V. M. Lubecke, and J. Lin, “0.25 μm CMOS and BiCMOS single chip direct conversion Doppler radars for remote sensing of vital signs,” *IEEE ISSCC Digest of Technical Papers*, pp. 348-349, February 2002.

-
- [28] B. Lohman, O. Boric-Lubecke, V. M. Lubecke, P. W. Ong, and M. M. Sondhi, "A Digital Signal Processor for Doppler Radar Sensing of Vital Signs," in *Proc. IEEE 23rd annu. Engineering in Medicine and Biology Society Conf.*, vol. 4, 2001, pp. 3359-3362.
- [29] A. Host-Madsen, N. Petrochilos, O. Boric-Lubecke, V. M. Lubecke, B.-K. Park, and Q. Zhou, "Signal Processing Methods for Doppler Radar Heart Rate Monitoring," in *Signal Processing Techniques for Knowledge Extraction and Information Fusion*, Springer, 2008.
- [30] D. Samardzija, B.-K. Park, V. M. Lubecke, and O. Boric-Lubecke, and T. Sizer, "MIMO Doppler Radar Detection of Physiological Motion," *IEEE MTT-S International Microwave Symposium*, June 2007.
- [31] Dennis R. Morgan, Michael G. Zierdt, "Novel signal processing techniques for Doppler radar cardiopulmonary sensing," *Signal Processing* 89 (2009) pp. 45-66.
- [32] C. Li, and J. Lin, "Complex signal demodulation and random movement body cancellation techniques for non-contact vital sign detection," *IEEE IMS, Atlanta, GA*, June 2008.
- [33] B.-K. Park, O. Boric-Lubecke, and V. M. Lubecke, "Arctangent demodulation with DC offset compensation in quadrature Doppler radar receiver systems," *IEEE Trans. on Microwave Theory Tech.*, Vol. 55, No.5, pp.1073-1079, May 2007.
- [34] X. Zhao, C. Song, V. Lubecke, and O. Boric-Lubecke, "DC Coupled Doppler Radar Physiological Monitor", *IEEE EMBC, 2011*.
- [35] M. Valkama, M. Renfors and V. Koivunen, "Advanced methods for I/Q imbalance compensation in communication receivers," *IEEE Transactions on Signal Processing*, Vol. 49, Issue 10, pp. 2335-2344, 2001.
- [36] B. K. Park, S. Yamada, V. Lubecke, "Measurement method for imbalance factors in direct-conversion quadrature radar systems," *IEEE Microwave and Wireless Components Letters, IEEE* , Vol.17, No.5, pp.403-405, May 2007.

-
- [37] A. Droitcour, V.M. Lubecke, J. Lin, and Olga Boric-Lubecke, "A Microwave Radio for Doppler radar Sensing of Vital Signs," *IEEE MTT-S Int. Microwave Symp. Dig.*, Phoenix, AZ, USA, vol. 1, pp. 175-178, May 2001.
- [38] B.-K. Park, S. Yamada, O. Boric-Lubecke, V. Lubecke, "Single-Channel Receiver Limitations in Doppler Radar Measurements of Periodic Motion," *IEEE Radio and Wireless Symposium*, vol. 1, pp. 17-19, Jan 2006.
- [39] A. Host-Madsen, B-K. Park, N. Petrochilos, O. Boric-Lubecke, V. Lubecke, "Demodulation for a Doppler radar system for vital signs extraction with unknown DC offset," submitted to *IEEE Signal Processing Letters*.
- [40] N. Hafner, I. Mostafanezhad, V. M. Lubecke, O. Boric-Lubecke, and A. Host-Madsen, "Non-Contact Cardiopulmonary Sensing with a Baby Monitor," *Proc. IEEE 29th annu. Engineering in Medicine and Biology Society Conf.*, pp.2300-2302, August 2007.
- [41] I. Mostafanezhad, B.K. Park, O. Boric-Lubecke, V. Lubecke and A. Host-Madsen, "Sensor Nodes for Doppler Radar Measurements of Life Signs," *IEEE MTT-S Int. Microwave Symp. Dig.*, Honolulu, HI, USA, vol. 1, pp. 1241-1244, June 2007.
- [42] I. Mostafanezhad, O. Boric-Lubecke, V. Lubecke and A. Host-Madsen, "Cancellation of Unwanted Motion in a Handheld Doppler Radar Used for Life Sign Monitoring," *IEEE MTT-S Int. Microwave Symp. Dig.*, Atlanta, GA, USA, June 2008
- [43] V.M. Lubecke, O. Boric-Lubecke, G. Awater, P.-W. Ong, P. Gammel, R.-H. Yan, J.C. Lin, "Remote sensing of Vital Signs with Telecommunications Signals," (*Invited Presented at the World Congress on Medical Physics and Biomedical Engineering (WC2000)*), Chicago, IL, USA, July 2000.
- [44] V. Lubecke, O. Boric-Lubecke and E. Beck, "A Compact Low-Cost Add-On Module for Doppler Radar Sensing of Vital Signs Using a Wireless Communications Terminal," *IEEE MTT-S Int. Microwave Symp. Dig.*, vol. 3, pp. 1767-1770, June 2002.
- [45] O. Boric-Lubecke, G. Awater, and V. M. Lubecke, "Wireless LAN PC Card Sensing of Vital Signs," *IEEE TCWCT*, pp.206-207, October 2003.

-
- [46] Pushkar Ranade, "System-on-chip technology comes of age", http://www.eetimes.com/document.asp?doc_id=1279975
- [47] CC2530 datasheet, <http://www.ti.com/lit/ds/symlink/cc2530.pdf>
- [48] CC430 datasheet, <http://www.ti.com/lit/ds/symlink/cc430f5123.pdf>
- [49] Roger Allan, "Medical devices get ready to make house calls", *Electronic Design*, [on line], <http://electronicdesign.com/medical/medical-devices-get-ready-make-house-calls>
- [50] C. Song, E. Yavari, A. Singh, V. Lubecke, and O. Boric-Lubecke, "Detection Sensitivity and Power Consumption vs. Operation Modes Using System-on-Chip Base Doppler Radar Occupancy Sensor", *IEEE RWS*, 2012.
- [51] IEEE std. 802.15.4 – 2003, "Wireless Medium Access Control (MAC) and Physical Layer (PHY) specifications for Low Rate Wireless Personal Area Networks (LR-WPANs)", [on line], available at <http://standards.ieee.org/getieee802/download/802.15.4-2003.pdf>
- [52] E. Yavari, C. Song, V. Lubecke, and O. Boric-Lubecke, "System-on-Chip Based Doppler Radar Occupancy Sensor", *IEEE EMBC*, 2011.
- [53] W. Redman-White, D. M. W. Leenaerts, "1/f noise in passive CMOS mixers for low and zero IF integrated receivers," *IEEE ESSCIRC 2001, Proceedings of*, pp. 41-44, September, 2001.
- [54] S. A. Mass, *Microwave Mixers*, Boston. London: Artech House, Second Edition, pp. 338-339, 1993.
- [55] S. A. Maas, "A GaAs MESFET mixer with very low intermodulation," *IEEE Trans. Microwave Theory Tech.*, vol. MTT-35, pp. 425-429, April, 1987.
- [56] O. Boric-Lubecke, J. Lin, A. Verma, I. Lo, and V. M. Lubecke, "Multi-Band 0.25 μm CMOS Base Station Chip-Set for Indirect and Direct Conversion Receivers," *IEEE Trans. on Circuits and Systems*, Volume 55, Issue 7, Aug. 2008 Page(s):2106 - 2115.

-
- [57] P. Gould, C. Zelle, and J. Lin, "A CMOS resistive ring mixer MMICS for GSM 900 and DCS 1800, base station applications," 2000 IEEE MTT-S Int. Microwave Symp. Dig., vol. 1, pp. 521-524, June 2000.
- [58] I. Lo, X. Wang, O. Boric-Lubecke, Y. Hong, and C. Song, "Wide-band 0.25 μ m CMOS passive mixer," RWS 2009, Jan. 2009.
- [59] T. Chang, and J. Lin, "1-11 GHz ultra-wideband resistive ring mixer in 0.18 μ m CMOS technology," IEEE RFIC Symp., June 2006.
- [60] R. Circa, D. Pienkowski, and G. Boeck, "Integrated 130nm CMOS passive mixer for 5 GHz WLAN applications," 2005 SBMO/IEEE MTT-S Int. Conf., pp. 103-106, July 2005.
- [61] R. Circa, D. Pienkowski, G. Boeck, R. Kakerow, M. Mueller, and R. Wittmann, "Resistive mixers for reconfigurable wireless front-ends," IEEE RFIC Symp., pp. 513-516, June 2005.
- [62] Y. Furuta, T. Heima, H. Sato, and T. Shimizu, "A Low Flicker-Noise Direct Conversion Mixer in 0.13 μ m CMOS with Dual-Mode DC offset Cancellation Circuits," Silicon Monolithic Integrated Circuits in RF Systems, 2007 Topical Meeting on, pp.:265 – 268, 2007.
- [63] S. Zhou and M. Chang, "A CMOS passive mixer with low flicker noise for low-power direct-conversion receiver," IEEE J. Solid Circuits, vol. 40, No. 5, pp. 1084 – 1093, May 2005.
- [64] C. Song, I. Lo, and O. Boric-Lubecke, "2.4 GHz 0.18 μ m CMOS Passive Mixer with Integrated Baluns," 2009 IEEE MTT-S Int. Microwave Symp. Dig., pp. 409-412, June 2009.
- [65] C. Song, I. Lo, O. Boric-Lubecke, "0.18 μ m CMOS Wideband Passive Mixer", *Microwave and Optical Technology Letters*, pp.23-27, Vol. 55, No. 1, January 2013.
- [66] B. Razavi, Design of Analog CMOS Integrated Circuits, New York, McGraw-Hill, pp. 18, 2001.

-
- [67] E. Yavari, H. Jou, V. Lubecke, O. Boric-Lubekce, "Doppler Radar Sensor for Occupancy Monitoring," *Radio Wireless Symposium*, 20-23 Jan. 2013.
- [68] E. Yavari, C. Song, V. Lubecke, O. Boric-Lubekce, "Is there anybody in there?: Intelligent radar occupancy sensors," *IEEE Microwave Magazine*, Vol. 15, pp 57-64, Mar. – Apr., 2014.
- [69] D. Morgan, and M. Zierdt, "Novel signal processing techniques for Doppler radar cardiopulmonary sensing," *Signal Processing*, vol. 89, issue 1, Jan. 2009.
- [70] M. Zakrzewski, H. Raittinen, J. Vanhala, "Comparison of center estimation algorithms for heart and respiration monitoring with microwave Doppler radar," *IEEE Sensors J.*, vol. 12, issue 3, pp. 627–634, March 2012.
- [71] C. Li and J. Lin. "Non-Contact Measurement of Periodic Movement by a 22-40 GHz Radar Sensor Using Nonlinear Phase Modulation". *IEEE MTT-S International Microwave Symposium*, pp. 579-582, Honolulu, June, 2007.
- [72] T. Paing, J. Shin, R. Zane and Z. Popovic, "Resistor Emulation Approach to Low-Power RF Energy Harvesting," *IEEE Transactions on Power Electronics*, vol. 23, no. 3, May, 2008.